Universiteit Antwerpen

Faculteit Wetenschappen
Department Fysica

Search for longlived Heavy Neutral Leptons using a displaced jet tagger in the CMS experiment

Haifa Rejeb Sfar

Promoters:
Prof. Dr. Albert De Roeck
Prof. Dr. Nick Van Remortel

Submitted in part fulfilment of the requirements
for the degree of Doctor of Philosophy at
University of Antwerp, November 2023

During my PhD, I was involved in several tasks within the CMS collaboration; I played the role of Detector Control System and Central Data acquisition system shifter and shift crew leader at the CMS experiment control room. I have also been one of the shift leaders and DCS shifter's trainers. I have been involved in Strip Tracker Detector operations and data acquisition systems. I served as Monte Carlo contact, responsible for central Monte Carlo samples generation and generator operator, i.e., solving issues related to central MC production within the MC Generator group.

I hereby declare that this results on Heavy Neutral Leptons presented in this thesis was composed by and originated from me based on my work during my PhD. Information derived from the published and unpublished work of others has been acknowledged in the text and references are given in the list of sources.

Haifa Rejeb Sfar

Abstract

This thesis presents a search for long-lived heavy neutral leptons (HNLs) using proton-proton collision events, with a focus on the νMSM model for HNL production. The νMSM model is a theoretical framework that extends the Standard Model of particle physics to include right-handed neutrinos and provides a possible explanation for the observed neutrino masses and mixing angles. We have analyzed a data sample containing two leptons (electron or muon) and jets, with an integrated luminosity of 138 fb^1 collected from 2016 to 2018, which corresponds to the full RunII dataset, and have developed a novel jet tagger based on a deep neural network to identify displaced jets from the HNL decay.

To estimate the contribution from background processes, we used an ABCD method, which is a data-driven technique that relies on the correlation between two independent variables to separate signal and background events. We applied this method to the data in sideband regions and determined the expected background in the signal region. No excess in data over the expected background is observed. Limits on the HNL production cross section are derived as a function of the HNL mass and the three coupling strengths ($V_{\ell N}$) to each lepton generation (ℓ).

Our results provide the best limit on the coupling strength for pure muon coupling scenarios, excluding values of $|V_{\mu N}|^2 > 5(4) \times 10^7$ for Dirac (Majorana) HNLs with a mass of 10 GeV at 95% CL. This has important implications for the viability of the νMSM model and other theoretical models that propose the existence of HNLs. Our methodology, including the use of the jet tagger and the ABCD method, can be applied to future searches for HNLs at higher energies and luminosities. However, our study has limitations, such as the assumption of a specific HNL production mechanism and the use of simplified background models. Future research could focus on improving the sensitivity of the jet tagger, exploring alternative HNL production scenarios, developing more sophisticated background estimation techniques, and combining the results from existing HNL searches to improve the sensitivity and coverage of the parameter space.

Part I

title

I extend my sincere gratitude to my supervisor, Prof. Albert de Roeck, for his invaluable help, patience, and steadfast support throughout the entire duration of my thesis. I would also like to express my appreciation to Prof. Nick Van Remortel for dedicating his time and energy to resolving all my administrative issues. I would also like to thank the Imperial College team and alumni, particularly Alex Tapper, Matthias Komm, Matthew Citron, and Rob Bainbridge, for their constructive feedback, fruitful discussions, and guidance. A big thank you goes to the technical and run coordination team for their support, especially Gaelle Boudoul. Lastly, I saved the best for last, thank you to the people I love. You gave me the energy to persevere through the dark moments ... and it is because of you that this has become possible...

To myself first...and to the people I love second...

Once I said to my supervisor "One day, I will write a book", He answered "Yes, It will be your PhD Thesis..."
So here we go...

- Haifa's life(2023).

Contents

Declaration 2

Abstract 3

I title 4

Acknowledgements 5

1 Theoretical Overview 18
- 1.1 The Standard Model . . . 18
  - 1.1.1 Matter Particles . . . 18
  - 1.1.2 Fundemental forces . . . 20
  - 1.1.3 Dirac and Majorana Fermions . . . 22
- 1.2 The structure of the standard model . . . 24
- 1.3 Successes and limitations of the standard model . . . 28
- 1.4 Heavy Neutral Leptons in the νMSM theory . . . 29
  - 1.4.1 Introduction . . . 29
  - 1.4.2 Heavy Neutral Leptons production and decay modes . . . 31
  - 1.4.3 Previous experimental results . . . 33

2 The CMS experiment at the large hadron collider 37
- 2.1 The Large Hadron Collider (LHC) . . . 37
  - 2.1.1 Accelerator Complex . . . 38
  - 2.1.2 Accelerator parameters . . . 38
- 2.2 CMS experiment . . . 39
  - 2.2.1 Tracker . . . 40
  - 2.2.2 Electromagnetic Calorimeter . . . 42
  - 2.2.3 Hadronic Calorimeter . . . 43
  - 2.2.4 Solenoid Magnet . . . 45
  - 2.2.5 Muon System . . . 45
  - 2.2.6 Trigger . . . 45

3 Event Reconstruction 47
- 3.1 Introduction . . . 47
- 3.2 Charged Particles Track finding . . . 48
- 3.3 Vertex finding . . . 49
- 3.4 Particle flow algorithm . . . 50
- 3.5 Jets . . . 52

3.6 Isolation . . . 52
3.7 Muon Identification . . . 53
3.8 Electron Identification . . . 54
3.9 Missing Transverse Momentum . . . 55
3.10 Pileup . . . 56

4 The HNL search in the CMS experiment 58
4.1 HNLs Analysis overview . . . 58
4.2 Data samples . . . 60
4.3 HNL samples production . . . 60
4.3.1 Signal kinematic . . . 63
4.3.2 Event observables . . . 63
4.4 Background simulation samples . . . 66

5 QCD Dynamics, and Pythia Tuning in HNL Analysis 68
5.1 Introduction . . . 68
5.2 Pythia8.2 Monash Tune at Low CM Energies . . . 71
5.2.1 Measurements of $< n_{cp} >$ in data . . . 71
5.2.2 Measurements of $< n_{cp} >$ in simulation . . . 72
5.2.3 Comparison of $< n_{cp} >$ measurements from pythia 8.2 and data . . . 74
5.2.4 Particles composition in e^+e^- annihilation events . . . 76
5.3 Summary . . . 77

6 Analysis strategy 78
6.1 Introduction . . . 78
6.2 Objects selection for HNL search . . . 78
6.3 Signal Region (SR) . . . 82
6.4 Control Regions (CRs) . . . 86
6.5 Corrections to simulation . . . 90
6.5.1 Pileup reweighting . . . 90
6.5.2 Jet energy corrections . . . 90
6.5.3 Prompt leptons trigger, identification and isolation efficiency . . . 91
6.5.4 Displaced Track reconstruction efficiency . . . 91
6.5.5 Displaced jet tagger efficiency . . . 96
6.5.6 Displaced leptons reconstruction and identification efficiency . . . 96
6.6 Event categorisation . . . 99
6.6.1 Event topologies . . . 99
6.6.2 Event displacement . . . 100
6.6.3 Summary . . . 105

7 Neural-network-based displaced jet tagger 107
7.1 Introduction . . . 107
7.2 Neural Network architecture . . . 107
7.2.1 Input features . . . 108
7.2.2 NN training . . . 117
7.2.3 Domain adaptation . . . 117
7.2.4 NN outputs configuration . . . 118
7.2.5 Jet labelling: Truth level . . . 118

7.2.6 output classes . . . 120
7.2.7 NN performance and validation . . . 121

8 Background estimation for the HNLs search 126
8.1 Introduction . . . 126
8.2 ABCD method . . . 126
8.3 Tagger threshold optimisation . . . 129
8.4 Background studies in validation regions . . . 132
8.4.1 Standard model background suppression . . . 137
8.4.2 Residual type-I background suppression . . . 142
8.4.3 Residual Type-II background suppression . . . 149
8.4.4 Miscategorised displaced leptons . . . 155
8.4.5 Summary . . . 156
8.5 Closure tests . . . 157
8.5.1 Validation regions . . . 157
8.5.2 Goodness of fit . . . 170

9 Systematic uncertainties 175
9.1 systematic uncertainties on signal . . . 175
9.2 systematic uncertainties on background . . . 176
9.3 summary . . . 178

10 Results and interpretation 179
10.1 Likelihood model . . . 179
10.2 Results of the fit to data . . . 180
10.3 Procedure for deriving the limits . . . 184
10.4 Interpretation . . . 185
10.5 Impacts and pulls . . . 186
10.6 Flavour-dependent limits . . . 191
10.7 Summary . . . 191

List of Tables

1.1 The fundamental forces vector bosons mediators and their characteristics. 21

3.1 Jet identification criteria for 2016 and 2017/2018 data-taking scenarios. 52
3.2 The applied modified loose cut-based electron identification (94X-V2) criteria. . 55
3.3 MET filters applied to data and MC for 2016, 2017 and 2018 data taken periods. 56

4.1 Trigger names and the corresponding ℓ_1 p_T threshold for the three years. 60

5.1 $< n_{cp} >$ from past experiments, their corresponding CM energies and uncertainties. 73
5.2 e^+e^- event composition from past experiments and two event generators pythia8.2 and HERWIG++. 76

6.1 Overview of selection requirements in signal and control regions for the dilepton categories. The tight lepton requirements are shown per year of data-taking. . . 83
6.2 The fitted fractions of $t\bar{t}$ and W+jets events with respect to data for muon and electron events per year of data taking. 92

7.1 Features of charged PF features. 111
7.2 Features of neutral PF candidates. 111
7.3 Features of secondary vertices. 112
7.4 Features of PF electrons (part 1). 113
7.5 Features of PF electrons (part 2). 114
7.6 Features of PF muons. 115
7.7 Global jet features. 116

8.1 Boosted and resolved signal regions. 127
8.2 Signal samples used to optimise thresholds. For each mass and lifetime five couplings are considered: pure electron, pure muon, electron and muon, electron and tau, and muon and tau 130
8.3 Signal samples used for the signal efficiency study. 148
8.4 Fraction thresholds for combined flavour categories except $\mu\mu$ OS per year of data taken. 156

9.1 Measured κ parameter per category derived from fits to the VR1. 177
9.2 Systematic uncertainty applied per category based on the measured κ parameters. 177
9.3 Measured κ parameter per $\mu\mu$ OS category derived from fits to the VR5. 178
9.4 Sources of systematic uncertainties considered in the HNL search. 178

List of Figures

1.1 Fundemantal particles of the standard model and their caracteristics. 21
1.2 The Higgs potential V(ϕ) for $\lambda > 0$ and $\mu^2 < 0$ conditions. 27
1.3 Fundemantal particles of the SM including its minimal extension by N_1, N_2 and N_3 in the neutrino sector and their caracteristics[21]. 30
1.4 Contour lines for the HNL proper decay length $c\tau_0$. Shaded areas correspond to approximate current exclusion by different experiments. 32
1.5 Existing limits on the mixing angle between HNLs and active neutrinos as a function of the HNL mass m_N in the mass range from 100 MeV to 500 GeV [41]. 33
1.6 Limits at 95% CL in the $|V_{Ne}|^2$ as a function of m_N (left) and $|V_{N\mu}|^2$ as a function of m_N (right) planes. The dashed black curve is the expected upper limit, with one and two standard-deviation bands shown in dark green and light yellow, respectively. The solid black curve is the observed upper limit, while the dotted black curve is the observed limit in the approximation of prompt HNL decays. Also shown are the best upper limits at 95% CL from other collider searches in L3 [10], DELPHI [9], ATLAS [4], and CMS [49]. 34
1.7 The 95% Confidence Level (CL) exclusion limits on the mixing angle of HNLs with active electron and muon neutrinos, $|V_{Ne}|^2$ (left) and $|V_{N\mu}|^2$ (right) respectively, as functions of m_N for a Dirac HNL. The area inside the solid (dashed) black curve indicates the observed (expected) exclusion region [67]. 35
1.8 The 95 % confidence level (CL) exclusion limits on the mixing angle of HNL to ν_μ i.e $|U_\mu N|^2$ as a function of HNL mass m_N. for the prompt and displaced signatures, the region above the black line and the region enclosed by the red line are exluded respectively. Majorana HNL limits are shown with solid lines, where half of the events contain decays assuming Leptonic number violation (LNV) and the second half consides HNL decays with Leptonic number conservation (LNC). The Dirac limits are shown with long dashed line assuming only events with LNC. These results are taken from[5]. 35
1.9 The 95% CL exclusion limits on $|U_{N\mu}|^2$ as a function m_N for HNL Majorana case. The green and yellow bands are ± 1 and ± 2 standard deviation (σ) spreads respectively for the expected limits. This figure is taken from [35] 36

2.1 The structure of the CERN accelerator complex.The protons are accelerated through the following chain LINAC4 $\rightarrow$ BOOSTER $\rightarrow$ Proton Synchrotron (PS). The protons are then injected in the LHC. [54] 38
2.2 The integrated luminosity delivered to CMS experiment since 2010. 40
2.3 Overview of the full CMS detector compared with the size of a human. 41
2.4 2D view of the CMS tracker detector. 42
2.5 A comparison between the original and the phase-I upgrade version of the pixel detector. 42

2.6 Overview of the CMS hadronic calorimeter system [30]. 44
2.7 Overview of the CMS muon system by the end of LHC Run 2 taken fro [63] . . 46

3.1 Transverse view of the CMS detector. Figure taken from **??**. 48
3.2 Tracking reconstruction efficiency as a function of track η using simulated $t\bar{t}$ events and 2017 conditions. 49
3.3 CMS average Pileup distribution for 2016, 2017 and 2018. 57

4.1 Left (Right): Feynman diagrams of the production and decay processes of Dirac(Majorana) HNL considered in this search. 59
4.2 The produced signal scenarios with $\mid V_e \mid = \mid V_\mu \mid = \mid V_\tau \mid$ in the mass-coupling plane for Majorana. Scenarios with the same proper lifetime, $c\tau_0$, as calculated by MadGraph, are colour-coded and connected by dashed lines. 62
4.3 The 67 relative coupling points considered in the analysis for reweighting each signal sample generated with equal couplings to all three generations of standard model neutrinos. The relative coupling points are plotted in barycentric coordinates, where $(f_e + f_\mu + f_\tau) = 1$. 62
4.4 Kinematic distribution of signal events at the generator level. 65

5.1 Charged particle multiplicity (n_{cp}) distribution for data and simulation with different hadronisation tunes at $\sqrt{(s)} = 91.2$ GeV [59]. 70
5.2 Average charged particles multiplicity (n_{cp}) as a function of CM energy for data and several tunes including "Monash" on the (left). Average $K^{\pm}$ multiplicity as a function of CM energy (right) [59]. 71
5.3 The fitted average charged particle multiplicity distribution from past experiments covering CM energy range from 1 to 50 GeV [53]. 72
5.4 Charged particle multiplicity from e^+e^- annihilation events using pythia8 for different CEM values. 73
5.5 Charged particle multiplicity from HNL decaying to W^* or Z^* events using pythia8 for different CM energies. 73
5.6 Comparison between $n_{cp} >$ measurements in e^+e^- annhilation events in simulation and in data. 74
5.7 Comparison between $< n_{cp} >$ measured in e^+e^- annhilation events in data and HNL decays producing Z^* and W^* in simulation. 75
5.8 Particles composition in e^+e^- annihilation simulated events with Pythia8.2 . . 76

6.1 Muon (left) and electron (right) ($\ell_2 = \mu, e$) reconstruction and identification efficiency as a function of generator-level lab frame displacement (top) and generator-level p_T (bottom) [28]. 80
6.2 $\Delta R(\ell_2, \mathrm{j}^\star)$ distributions for signal events (a) before and (b) after applying the jet overlap removal. 81
6.3 Fraction of non isolated ℓ_2 in resolved event. 81
6.4 Distributions of reconstructed quantities for OS $\mu\mu$ final state background and signal events ($m_{\mathrm{N}} = 4.5$, $c\tau_0 = 100$, $V_e = V_\mu$) and ($m_{\mathrm{N}} = 10$, $c\tau_0 = 10$, $V_e = V_\mu$). The distributions are shown for p_T^{miss}, min $\Delta R(\ell_2, \mathrm{jets})$, ℓ_1 p_T, ℓ_2 p_T, $m(\ell_1, \ell_2)$ and $m(\ell_1, \ell_2, \mathrm{j}^\star)$(simulation only). 84

6.5 Distributions of reconstructed quantities for OS μe final state background and signal events ($m_{\mathrm{N}} = 4.5$, $c\tau_0 = 100$, $V_e = V_\mu$) and ($m_{\mathrm{N}} = 10$, $c\tau_0 = 10$, $V_e = V_\mu$). The distributions are shown for p_T^{miss}, $\min \Delta R(\ell_2, \mathrm{jets})$, ℓ_1 p_T, ℓ_2 p_T, $m(\ell_1, \ell_2)$ and $m(\ell_1, \ell_2, \mathrm{j}^\star)$(simulation only). 85
6.6 Modelling of reconstructed quantities for OS $\mu\mu$ boosted final state events in high dilepton mass CR for 2016, 2017 and 2018 on the left, middle and right respectively. The distributions are shown for ℓ_1 p_T, ℓ_2 p_T and $p_T(\mathrm{j}^\star)$(data and simulation). 87
6.7 Modelling of reconstructed quantities for OS $\mu\mu$ resolved final state events in high dilepton mass CR for 2016, 2017 and 2018 on the left, middle and right respectively. The distributions are shown for ℓ_1 p_T, ℓ_2 p_T and $p_T(\mathrm{j}^\star)$(data and simulation). 88
6.8 Modelling of reconstructed quantities for OS $\mu\mu$ boosted final state events in high dilepton mass CR for 2016, 2017 and 2018 on the left, middle and right respectively. The distributions are shown p_T^{miss} and $\min \Delta R(\ell_2, \mathrm{jets})$(data and simulation). 89
6.9 Modelling of reconstructed quantities for OS $\mu\mu$ resolved final state events in high dilepton mass CR for 2016, 2017 and 2018 on the left, middle and right respectively. The distributions are shown for p_T^{miss} and $\min \Delta R(\ell_2, \mathrm{jets})$(data and simulation). 89
6.10 data monte carlo agreement for track d_{xy} for the three years of data taking . . . 92
6.11 Displaced Track reconstruction scale factors for the year 2016, 2017 and 2018 before and after the fit. 93
6.12 Displaced track reconstruction scale factors for the year 2016 during the HIP, post-HIP and combined periods. 94
6.13 The comparison of the displaced track reconstruction scale factors for the year 2016 post-HIP, 2017 and 2018 on the left and for the year 2016 total , 2017 and 2018 on the right. 95
6.14 Example of the loose muon identification SFs binned as a function of its p_T and d_{xy}^{sig} for the year 2018 97
6.15 Example of the customised electron identification SFs binned as a function of its p_T and d_{xy}^{sig} for the year 2018 98
6.16 Fraction of signal events classified as resolved for different HNL mass points using the ΔR approach. 100
6.17 Distributions of the three displacement variables L_{xy}(top), $|d_{xy}|l_2$(middle) and $|d_{xy}^{sig}|(l_2)$(bottom) for background and signal processes ($m_{\mathrm{N}} = 8, c\tau_0 = 0.1, 1$ and 10) 101
6.18 Distribution of $d_{xy}(\ell_2)$, $d_{xy}^{sig}(\ell_2)$ and $\sigma_{d_{xy}}(\ell_2)$ in high $M(\ell_1, \ell_2)$ control region. the distribution are shown in two different lepton categories for 2018 datasets. . . . 102
6.19 Significance scan for benchmark signal processes ($m_{\mathrm{N}} = 4.5, 6, 8$ and $10, c\tau_0 = 10, 10, 1$ and 1 respectively, for OS $\mu\mu$ (left) and OS ee (right) final states. 104
6.20 Categorisation of background and benchmark signal processes ($m_{\mathrm{N}} = 10, c\tau_0 = 1$ for $V_e = V_\mu$, pure muon and pure electron couplings.) 106

7.1 The default architecture of the neural network for identifying displaced jets from the HNL decay. 109
7.2 Confusion matrix quoting the normalized occurrence of how often a jet class is predicted (x axis) for each possible true jet class (y axis). 122

7.3 An example of ROC curves of the trained tagger for displaced HNL jet classes(LLP_Q, LLP_QMU and LLP_QE)(columns), for HNL samples with mass $m_N = 4.5$ GeV and several lifetimes, against SM jets (mu, pileup and udsg) (rows), selected from an inclusive sample of W+jets production in 2016 conditions. An example Figure (h): For HNL with $c\tau = 0.1$ m, True $LLP_Q Ejetareidentifiedwithefficiency\ 70\%whileTrueUDSje$ 123
7.4 Data/MC agreement of the tagger score in the high dilepton mass control region, boosted muon class (LLP_QMU). The distributions are shown for the 2016, 2017, and 2018 scenarios in the left, middle and right columns, respectively. The distributions are shown for the OS dimuon category in the first row, and the SS electron-muon mixed flavor category in the bottom row. Only Statistical uncertainty is considered in these plots. 125

8.1 2D plots of the three body mass as a function of the displaced jet tagger information for two different SR categories with inclusive displacement. Signal (top row) and background from simulation (bottom row). 128
8.2 Cartoon showing sideband method for chosing thresholds without unblinding. . . 130
8.3 The optimised thresholds on the jet tagger. These thresholds are used as cuts on the tagger score per category. 131
8.4 The $m(\ell_1, \ell_2, \mathrm{j}^\star)$distribution in data in low and high tagger score VR regions [0. , 0.2] and [0.2 , 0.4] respectively, for $\mu\mu$ OS boosted prompt category for 2016, 2017 and 2018. 133
8.5 The tagger score distribution in signal and sideband $m(\ell_1, \ell_2, \mathrm{j}^\star)$regions, for $\mu\mu$ OS boosted prompt category for 2016, 2017 and 2018. 134
8.6 The $m(\ell_1, \ell_2, \mathrm{j}^\star)$distribution in data in low and high tagger score VR regions [0. , 0.2] and [0.2 , 0.4] respectively for 3 prompt categories for 2018. 135
8.7 The tagger score distribution in signal and sideband $m(\ell_1, \ell_2, \mathrm{j}^\star)$regions for 3 prompt categories for 2018. 136
8.8 Background distribution in low and high tagger score regions for $\mu\mu$ OS and ee OS prompt bins in data. 138
8.9 Background distribution in low and high tagger score regions for $\mu\mu$ OS prompt bin in simulation. 139
8.10 The distribution in data of the 3 body mass in two high tagger score VR regions [0.2 , 0.3] and [0.3 , 0.4] for $\mu\mu$ OS boosted prompt category for 2016, 2017 and 2018. 140
8.11 The distribution in data of the 3 body mass in two (low and high) tagger score VR regions $[0., 0.2]$ and $[0.2, 0.4]$ respectively, for 3 prompt categories for 2018. 141
8.12 The distribution of the 3 body mass in two high tagger score VR regions [0.2 , 0.3] and [0.3 , 0.4] including the fraction cuts for $\mu\mu$ OS boosted prompt category for 2016, 2017 and 2018. 143
8.13 The distribution of the 3 body mass in two high tagger score VR regions [0.2 , 0.3] and [0.3 , 0.4] including the fraction cuts respectively, for 3 prompt categories for 2018. 144
8.14 The fraction distribution for signal events in the signal region and data in the mass sideband regions for 3 displaced lepton flavor resolved for the year 2018. . 145
8.15 The fraction distribution for signal events in the signal region and data in the mass sideband regions for 3 displaced lepton flavor boosted categories for the year 2018. 146

8.16 The distribution of the fraction variable for $\mu\mu$ OS category for the year 2018. . 147
8.17 Signal efficiency after applying the fraction cuts for HNL mass = 8 and $c\tau = 10$ for the year 2018. 147
8.18 Signal efficiency as a function of the $l_2 p_T$ after applying the fraction cuts for HNL mass = 8 GeV and $c\tau = 10$ mm for the year 2018. 148
8.19 MC distributions for $m(\ell_1, \ell_2, \mathrm{j}^\star)$ in SR and sidebands for Z/γ^*+jets (left) and inclusive no Z/γ^*+jets (right) for the year 2018. 150
8.20 MC distributions for tagger score in $m(\ell_1, \ell_2, \mathrm{j}^\star)$ SR and sidebands for Z/γ^*+jets and inclusive no Z/γ^*+jets separately for the year 2018. 151
8.21 MC distribution for the dilepton mass and HNL jet hadronic fraction at high and low tagger score separately for boosted medium(top) and displaced (bottom) categories for the year 2018. 152
8.22 MC distribution for the dilepton mass and HNL jet hadronic fraction at high and low tagger score separately for boosted medium(top) and displaced (bottom) categories for the year 2018. 153
8.23 MC distribution for tagger score and $m(\ell_1, \ell_2, \mathrm{j}^\star)$ in SR and sidebands for Z/γ^*+jets for the year 2018 after applying the fraction and dilepton mass cuts. . 154
8.24 d_{xy}^{sig}, d_{xy} and d_{xy}^{err} MC distribution in $\mu\mu$ OS and ee OS prompt categories. 155
8.25 Cartoons of the SR on the left and of the three validation regions VR1, VR2 and VR3 on the right. 158
8.26 Closure test in VR1 data sideband $m(\ell_1, \ell_2, \mathrm{j}^\star) > 90$ with loose tagger thresholds for boosted (left) and resolved (right) categories. 161
8.27 Closure test in VR2 data sideband $m(\ell_1, \ell_2, \mathrm{j}^\star) < 70$ with loose tagger thresholds for boosted (left) and resolved (right) categories. 162
8.28 Closure test in VR3 data sideband for boosted (left) and resolved (right) categories. 163
8.29 Closure test in VR4 simulation sideband for boosted (left) and resolved (right) categories. 164
8.30 Closure test in VR5 data sideband for boosted (left) and resolved (right) categories. 165
8.31 Closure test in VR1 data sideband $m(\ell_1, \ell_2, \mathrm{j}^\star) > 90$ with optimised tagger thresholds for boosted (left) and resolved (right) categories. 167
8.32 Closure test in VR2 data sideband $m(\ell_1, \ell_2, \mathrm{j}^\star) < 70$ with optimised tagger thresholds for boosted (left) and resolved (right) categories. 168
8.33 Closure test in VR5 data sideband $m(\ell_1, \ell_2, \mathrm{j}^\star) < 70$ with optimised tagger thresholds for boosted (left) and resolved (right) categories 169
8.35 Goodness of fit in VR2 in data sideband for boosted (up) and resolved (bottom) categories. 172
8.36 Goodness of fit in VR3 data sideband for boosted (up) and resolved (bottom) categories. 172
8.37 Goodness of fit in VR5 data sideband for boosted (up) and resolved (bottom) categories. 173
8.38 Goodness of fit in VR1 with tagger optimized thresholds data sideband for boosted (up) and resolved (bottom) categories. 173
8.39 Goodness of fit in VR2 with tagger optimised thresholds data sideband for boosted (up) and resolved (bottom) categories. 174
8.40 Goodness of fit in VR5 with tagger optimised thresholds data sideband for boosted (up) and resolved (bottom) categories. 174

10.1 Expected background and signal yields for boosted (left) and resolved (right) categories per year and combined obtained from a fit to the Asimov dataset. Two signal Majorana models are superimposed. 182
10.2 Expected background and signal yields for boosted (left) and resolved (right) categories for combined years obtained from a fit to the Asimov dataset. Two signal Majorana models are superimposed. 183
10.3 Combined limits for Dirac (top) and Majorana(bottom) HNLs for pure and equal muon and electron couplings. 188
10.4 Combined limits for Dirac (top) and Majorana(bottom) HNLs for equal coupling to muon and tau, electron and tau, and electron, muon, and tau. 189
10.5 Impacts ranked by decreasing significance for the 2016, 2017 and 2018 data-taking scenarios. Only the first sixty are shown. Signal model used: $m_{\mathrm{N}} = 10\mathrm{GeV}$, $c\tau_0 = 1\mathrm{mm}$, $V_\mu = V_e$ 190
10.6 Minimum excluded mass for each flavour combination for Dirac HNLs for (left column) Majorana and (right column) Dirac HNLs with a fixed lifetime of (top row) with $c\tau_0 = 0.1$ mm and (bottom row) $c\tau_0 = 1$ mm. 192
10.7 Minimum excluded proper lifetime for each flavour combination for (left col- umn) Majorana and (right column) Dirac HNLs with a fixed mass of (top row) 4.5 GeV and (bottom row) 8.0 GeV. 193

Chapter 1

Theoretical Overview

In this chapter, the Standard Model (SM) theory of particle physics is outlined. A detailed description of fundamental particles and their interactions, the structure of the SM, its success and limitations, as well as physics beyond the SM are given in the following.

1.1 The Standard Model

The SM is the best theory that describes fundamental matter particles and their interactions prescisely. It is constructed based on quantum field theory (QFT) which describes the quantum behavior of relativistic particles by predicting their observables such as their cross section or decay rate. Many experimental measurements show an excelent agreement with the SM theoretical predictions validating its success. However, there are still several key questions that remain unanswered. The SM is then an incomplete theory that needs to be improved.

1.1.1 Matter Particles

All the matter around us is made up of fundamental particles that form the Standard Model (SM) of particle physics. These particles are the smallest observed entities and are indivisible into smaller ones. The SM has two categories of matter particles: leptons and quarks.

Leptons are particles that do not experience strong interactions, and they can be either charged particles like electrons ($e^{\pm}$), muons ($\mu^{\pm}$), or taus ($\tau^{\pm}$), or their associated neutral

particles called electron neutrinos (ν_e), muon neutrinos (ν_μ), and tau neutrinos (ν_τ), respectively. Each lepton doublet (ℓ, ν_ℓ) is called a generation, and the first generation, consisting of electrons and electron neutrinos, is the lightest and most stable. The second and third generations, consisting of muons, tauons, and their respective neutrinos, are heavier and less stable and decay eventually to the first generation.

Leptons have a conservative additive quantity called lepton number under the SM, which is conserved in all physical processes. The sum of the number of leptons n_ℓ and the number of antileptons $\bar{n_\ell}$ must always be equal the same before and after the interaction.

Quarks are particles that experience strong interactions and are always bound within composite particles called hadrons, such as protons and neutrons. There are six types of quarks in the SM, which are grouped into three generations. The lightest generation consists of the up and down quarks, while the other two generations contain the heavier charm, strange, top, and bottom quarks.

Quarks have an additional quantum number called "color charge," which can be red, green, or blue. This degree of freedom was introduced to explain the existence of particles like the Δ^{++}, which has three up quarks in the same quantum state that would otherwise violate the Pauli exclusion principle. The color confinement rule states that quarks can only exist in bounded composite particles that are colorless.

The study of different hadron interactions led to the discovery of an additive number conserved during these interactions, called the baryonic number B. It is defined as the difference between the number of quarks N_q and the number of antiquarks $N_{\bar{q}}$ in the hadron, divided by three:

$$B = \frac{N_q - N_{\bar{q}}}{3}$$

Baryons, such as protons and neutrons, are fermions with a baryonic number of $B = 1$, while mesons, such as pions, are bosons with a baryonic number of $B = 0$. There are also exotic hadrons like tetraquarks and pentaquarks, which have four and five quarks ($\mathrm{qq\bar{q}\bar{q}}$ and $\mathrm{qqq\bar{q}}$), respectively, and have been observed in recent experiments.

In summary, matter particles in the SM are divided into two categories: leptons and quarks.

Leptons have three generations, and the lightest generation is stable and forms ordinary matter. Quarks come in six flavors and are always bound within composite particles called hadrons, which have a conserved baryonic number and the lightest quarks (u,d) for the ordinary matter.

1.1.2 Fundemental forces

As far as we know, there are four fundamental forces in the universe: the strong, weak, electromagnetic, and gravitational forces. These forces are necessary to describe the structure and behavior of matter particles. In the framework of QFT, the vector bosons are the mediators of the fundamental forces. All vector bosons together with fundamental matter particles are shown in figure 1.1. The strong interaction is responsible for binding quarks together into protons and neutrons through gluons. It is also called the nuclear force or residual strong interaction when it acts on binding protons and neutrons into atomic nuclei. Gluons, the mediators of the strong interaction, are massless particles, and there are eight different gluons in total.

The weak interaction is responsible for the radioactive decay of atoms. These interactions are mediated by $W^{\pm}$ and Z^0 bosons. Due to the relatively high mass of these bosons, the weak interaction has a short range.

The electromagnetic interaction is mediated by the photon (γ) and is responsible for the binding between electrons and nuclei, leading to composite matter structures such as atoms and molecules. It is also responsible for all electromagnetic phenomena, including light and electromagnetic radiation.

The gravitational interaction is the weakest among the four forces, approximately 10^{38} times weaker than the strong interaction and 10^{29} times weaker than the weak interaction. At the particle level, the effect of the gravitational force is negligible, and it is not included in the SM of particle physics. However, it is the dominant force at the macroscopic level, determining the motion of celestial objects such as planets, stars, and galaxies. Understanding the behavior of gravity at the quantum level is a major challenge in modern physics, and many theoretical physicists are working to unify it with the other fundamental forces. A summary of the three SM fundamental forces is given in table 1.1.

Table 1.1: The fundamental forces vector bosons mediators and their characteristics.

Force	Strength	Mediator	Mass (GeV)	Electric charge	Spin
Strong	1	8 gluons	0	0	1
Electromagnetism	$\frac{1}{137}$	γ	0	0	1
Weak	10^{-5}	$W^{\pm}$	80.4 GeV	$\pm$ 1	1
	10^{-5}	Z^0	91.2 GeV	0	1

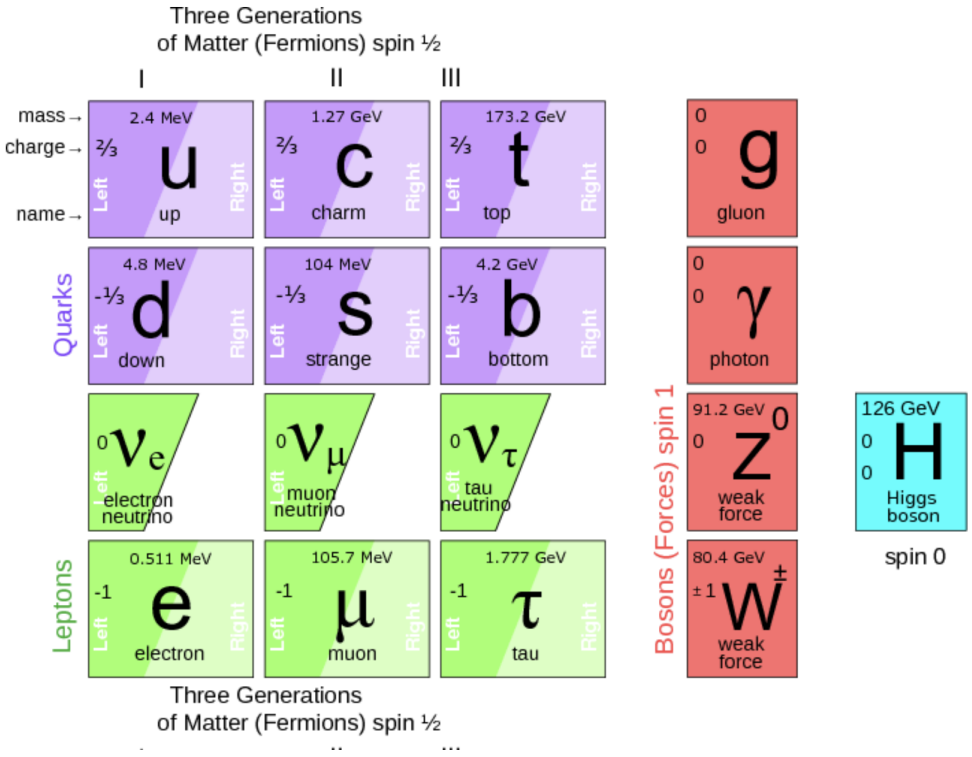

Figure 1.1: Fundemantal particles of the standard model and their caracteristics.

1.1.3 Dirac and Majorana Fermions

Helicity and chirality are two important properties of particles that describe their behavior in interactions with other particles. Helicity refers to the projection of a particle's spin into its direction of motion. It is a measure of how much a particle's spin is aligned or anti-aligned with its direction of motion, and can take on values of +1, 0, or -1. This quantity depends on the frame where you are measuring it.

Chirality, on the other hand, is intrinsec quantity of a particle . It describes whether a particle is left-handed or right-handed in its interactions, i.e. independently from the frame. This is determined by the way the particle's spin is aligned relative to its momentum, and is an important concept in the study of weak interactions. For massless or relativistic particles, helicity and chirality are equivalent.

The distinction between left- and right-handed particles is also important, as some fundamental interactions in the universe only affect one type of particle. The weak nuclear force, for example, only interacts with left-handed particles and right-handed antiparticles, which is known as chirality or parity violation, and has important implications for the behavior of particles in various physical processes.

In the Standard Model, all of the charged fermions are described as Dirac fermions, which means that they have distinct particles and antiparticles. For example, an electron and a positron are two distinct particles with opposite charges, and the same is true for other charged fermions like quarks and muons. However, neutrinos are electrically neutral, which means that they could be either Dirac or Majorana fermions.

A Majorana neutrino is a hypothetical particle that is its own antiparticle. In other words, if you swapped a particle and its antiparticle, a Majorana neutrino would look exactly the same before and after the swap. This property arises from the fact that Majorana fermions have no electric charge, which means that they can't be distinguished from their antiparticles based on their electric charge.

In QFT, the following Lagrangian describes in general a given free fermion particle with a

mass parameter m, whether it has Majorana or Dirac nature:

$$\mathcal{L} = \bar{\psi}(i\gamma^{\mu}\partial_{\mu} - m)\psi, \tag{1.1}$$

where ψ is a field particle and $\bar{\psi} = \psi^{\dagger}\gamma^{0}$ is its Hermitian conjugate. The first part of the equation is the Lagrangian kinetic term, and the second part is the Lagrangian mass term of a particle. For massless particles, it becomes simply

$$\mathcal{L} = \bar{\psi}i\gamma^{\mu}\partial_{\mu}\psi. \tag{1.2}$$

The mass term of the Lagrangian depends on the nature of the described particles. Given that ψ can be broken into left- and right-handed parts $\psi = \psi_L + \psi_R$, for a massive Dirac charged fermion such as a lepton or a quark, the Lagrangian mass term must be expressed as a superposition of left- and right-handed particle/antiparticle fields, as follows. Terms such as $\bar{\psi_L}\psi_L$ and $\bar{\psi_R}\psi_R$ vanish after applying the chiral projectors [60].

$$\mathcal{L}_{\text{Dirac mass}} = m(\bar{\psi_R}\psi_L + \bar{\psi_L}\psi_R) \tag{1.3}$$

As the nature of neutrinos is still not yet confirmed, they could be either Majorana or Dirac fermions, unlike all the other fermions in the SM which are confirmed to be Dirac fermions. If neutrinos are indeed Majorana fermions, their Lagrangian mass term is expressed differently as follows:

$$\mathcal{L}_{\text{Majorana mass}} = m(\bar{\psi_L}\psi_L^{c} + \bar{\psi_R^{c}}\psi_R) \tag{1.4}$$

If neutrinos are Majorana particles, it would result in a violation of the Lepton number by two units, denoted as $\Delta L = 2$. This quantity is typically conserved in the Standard Model. The information presented in this paragraph will be referenced in support of section 1.4.

1.2 The structure of the standard model

The standard model is a gauge theory based on a unified framework for the strong force that describes the interaction among quarks mediated by gluons and the electroweak force describing the interactions between quarks and leptons mediated by γ and $Z^0/W^{\pm}$ bosons as described in the following [16] [44]:

$$G_{SM} = SU(3)_C \otimes SU(2)_L \otimes U(1)_Y \tag{1.5}$$

where C, L, and Y represent the color charge, left-handedness, and hypercharge respectively. The standard model lagrangian can be written in the following form:

$$\mathcal{L}_{SM} = \mathcal{L}_{gauge} + \mathcal{L}_{fermion} + \mathcal{L}_{Higgs} + \mathcal{L}_{Yuk} \tag{1.6}$$

The gauge lagrangian term ($\mathcal{L}_{gauge}$) describes the free propagation of the gauge fields and their self-interactions and can be expressed as follows

$$\mathcal{L}_{gauge} = -\frac{1}{4}B_{\mu\nu}B^{\mu\nu} - \frac{1}{4}W^a_{\mu\nu}W^{\mu\nu}_a - \frac{1}{4}G^a_{\mu\nu}G^{\mu\nu}_a \tag{1.7}$$

The first term in the Lagrangian corresponds to the electromagnetic field and the second and third terms correspond to the weak and strong fields respectively where

$$W^i_{\mu\nu} = \partial_\mu W^i_\nu - \partial_\nu W^i_\mu + g\epsilon^{ijk}W^i_\mu W^k_\nu,\ i,j,k = 1,2,3$$

$$B_{\mu\nu} = \partial_\mu B_\nu - \partial_\nu B_\mu,$$

$$G^a_{\mu\nu} = \partial_\mu G^a_\nu + \partial_\nu G^a_\mu + g_s f^{abc}G^b_\mu G^c_\nu,\ a,b,c = 1,.....,8 \tag{1.8}$$

are the field strength tensors of W^i_μ, $B_{\mu\nu}$, and G^a_μ gauge fields respectively for the $SU(2)_L$, $U(1)_Y$, and $SU(3)_C$ gauge groups respectively. f^{abc} and ϵ^{abc} are the structure constants of the groups $SU(3)_C$ and $SU(2)_L$ respectively and g, $g^{'}$ and g_s are the gauge couplings.

The fermion lagrangian term ($\mathcal{L}_{fermion}$) represents the interaction of fermions of the three generations, both quarks, and leptons, with gauge fields, γ, Z^0 and $W^{\pm}$, and can be written in

the following form:

$$\mathcal{L}_{ferm} = \bar{\psi}_L i D_\mu \gamma^\mu \psi_L + \bar{\psi}_{l_R} i D_\mu \gamma^\mu \psi_{l_R} + \bar{\psi}_Q i D_\mu \gamma^\mu \psi_Q + \bar{\psi}_{u_R} i D_\mu \gamma^\mu \psi_{u_R} + \bar{\psi}_{d_R} i D_\mu \gamma^\mu \psi_{d_R} \quad (1.9)$$

note that ψ is a Dirac fermionic field i.e (matter field) and $\bar{\psi}$ is Dirac conjugate, D_μ is the covariant derivative and γ^μ are the Dirac matrices for relativistic fermions. The SU(2) group behaves differently on fermions with left/right-handed chiralities therefore the fermionic fields are written $\psi_{L/R} = (1 \pm \gamma^5)\psi$. $L = (\nu_{\ell_L}, \ell_L)^T$ are the left-handed doublets of the SU(2) group where ℓ = e, μ, τ, ν_ℓ and ℓ_R are their corresponding neutrinos and right-handed singlets respectively. Similar to the leptons sector, $Q = (u_L, d_L)^T$ are quarks, left-handed doublets of SU(2) where $u = u, c, t$ and $d = d, s, b$. u_R and d_R are their corresponding right-handed singlet. The covariant derivative serves to couple the fermionic field to the gauge fields

$$D_\mu = \partial_\mu + igI^i W^i_\mu + ig^{'} Y B_\mu + ig_s T^a_c G^a_\mu \quad (1.10)$$

I^i, Y and T^a_c are the generators of $SU(2)_L$, $U(1)_Y$, and $SU(3)_C$ respectively where $I^i = \sigma^i/2$ (σ^i are Pauli matrices) for the left-handed SU(2) doublets and $I^i = 0$ for the right-handed singlets. In addition, Y is the weak hypercharge and it is related to the electric charge Q of a particle as $Q = I^3 + Y$ where I^3 is the third component of the weak isospin. $T^a_c = \lambda^a/2$ (λ^a are the Grell-Mann matrices) for SU(3) quark triplets, $T^a_c = 0$ for the leptons. Therefore the covariant derivative acts differently on the left and right-handed ψ as follow

$$D_\mu \psi_L = (\partial_\mu + igW^i_\mu T^i + ig^{'} Y B_\mu)\psi_L$$

$$D_\mu \psi_R = (\partial_\mu + ig^{'} Y B_\mu)\psi_R \quad (1.11)$$

The described part of the lagrangian $\mathcal{L}_{gauge} + \mathcal{L}_{fermion}$ is invariant under gauge symmetries but does not include the mass term which means that all particles are kept massless. However, experiments have shown that weak gauge bosons and fermions are massive particles. Any additional mass term added by hand to the lagrangian will lead to the violation of SU(2)×U(1) local gauge invariance. To introduce the mass term to the lagrangian without violating the gauge

invariance of the dynamics of the model an extension to $\mathcal{L}_{gauge} + \mathcal{L}_{fermion}$ by the lagrangian of the Higgs sector $\mathcal{L}_{Higgs}$ is required where the breaking of the electroweak gauge symmetry occurs [51]. The $\mathcal{L}_{Higgs}$ is described as follow

$$\mathcal{L}_{Higgs} = (D^{\mu}\phi)^{\dagger}(D_{\mu}\phi) - V(\phi), \tag{1.12}$$

where ϕ is a complex scalar field and D_{μ} is the covariant derivative. Note that, for example, in the electroweak sector, mass generation is required only for the weak $W^{\pm}$ and Z^0 bosons while the γ needs to remain massless to satisfy nature observation. Hence, a complex scalar $SU(2)$ doublet ϕ with weak hypercharge 1/2 and 4 real degrees of freedom is introduced as described in equation 1.13.

$$\Phi = \begin{pmatrix} \phi^{+} \\ \phi^{0} \end{pmatrix} = \frac{1}{\sqrt{2}} \begin{pmatrix} \phi_1 + i\phi_2 \\ \phi_3 + i\phi_4 \end{pmatrix} \tag{1.13}$$

where ϕ_i are the 4 real scalar fields. The self-interaction of the field ϕ is described by the potential $V(\phi)$ where

$$V(\phi) = -\mu^2\phi^{\dagger}\phi + \lambda(\phi^{\dagger}\phi)^2 \tag{1.14}$$

where μ^2 and λ are real free parameters. μ^2 is a mass parameter and λ is a dimensionless self-coupling constant. When $\lambda > 0$ and $\mu^2 > 0$ the potential has one minima however when $\lambda > 0$ and $\mu^2 < 0$ the potential has a degenerated non-zero minima and is minimised for any ϕ satisfying

$$\phi^{\dagger}\phi = \frac{1}{2}(\phi_1^2 + \phi_2^2 + \phi_3^2 + \phi_4^2) = -\frac{\mu}{2\lambda} = \frac{\nu^2}{2} \tag{1.15}$$

where ν is the vacuum expectation value(VEV) of the Higgs field. The shape of the given field has the form of a Mexican hat as shown in figure 1.2 and the minimum can be chosen as

$$\phi_0 = -\frac{1}{\sqrt{2}} \begin{pmatrix} 0 \\ \nu \end{pmatrix} \tag{1.16}$$

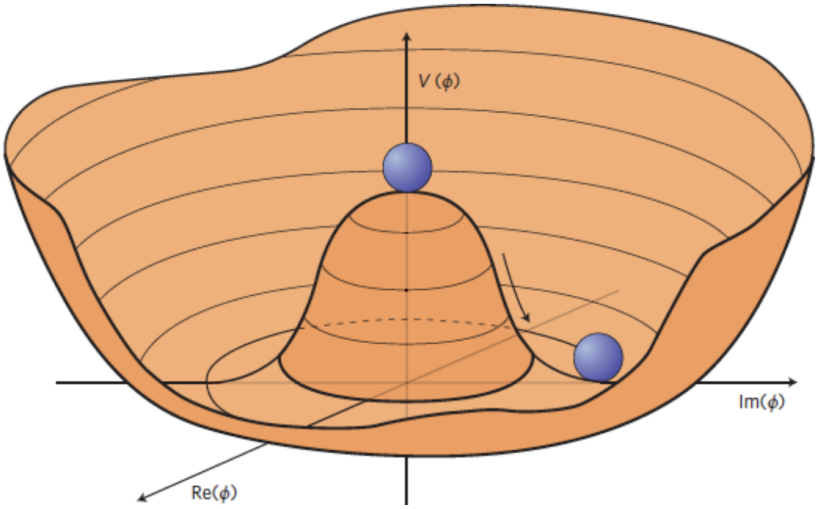

Figure 1.2: The Higgs potential V(ϕ) for $\lambda > 0$ and $\mu^2 < 0$ conditions.

The scalar field may be expanded as

$$-\frac{1}{\sqrt{2}}\begin{pmatrix} 0 \\ \nu + H \end{pmatrix} \tag{1.17}$$

where H is a scalar Higgs field. Given that the physical W, Z, γ (A) gauge bosons are the combination of the gauge fields defined previously

$$W^{\pm} = \frac{1}{\sqrt{2}}(W^1_\mu \mp iW^2_\mu) \tag{1.18}$$

$$\begin{pmatrix} Z_\mu \\ A_\mu \end{pmatrix} = \begin{pmatrix} cos(\theta_W) - sin(\theta_W) \\ sin(\theta_W) + cos(\theta_W) \end{pmatrix} \begin{pmatrix} W^3_\mu \\ B_\mu \end{pmatrix} \tag{1.19}$$

By injecting equation 1.17 and 1.15 in 1.12, the 2 masses of the weak gauge bosons are obtained as described in equation 1.20 while γ remains massless exactly reflecting experimental observations

$$M^{\pm}_W = \frac{1}{2}g\nu, M_Z = \frac{g\nu}{2cos\theta_W}, M_A = 0 \tag{1.20}$$

The last term in the SM lagrangian equation to the fermions mass generation through the interaction with the Higgs fields. The simplest way to express the $\mathcal{L}_{Yuk}$ lagrangian term is

following

$$\mathcal{L}_{Yuk} = -\frac{1}{(\sqrt{2})}(\nu + H)(f_{mn}\bar{e}_{Lm}e_{Rn} + h_{mn}\bar{L}\bar{m}d_{Rn} + k_{mn}\bar{u}_{Lm}u_{Rn}) + h.c \tag{1.21}$$

note f_{mn}, h_{mn} and k_{mn} are the coupling matrices of the Yukawa coupling between lepton generations. h.c denotes the hermitian conjugate terms of the equation. Only terms for electron, quarks u and d are presented here. The second and third generation of leptons and quarks are not shown but obey the same equation. No term describes the three active neutrinos interaction with the Higgs since they do not have a right handed counterpart. Therefore, neutrinos remains massless in the SM.

1.3 Successes and limitations of the standard model

The SM is a successful theory in describing the behavior of fundamental particles and their interactions. However, it is not a complete theory as it fails to include gravity at the quantum scale. Although the effects of gravity are negligible at the electroweak scale, it becomes significant at higher energies close to the Planck scale.

Apart from the theoretical shortcomings, several experimental observations remain unexplained or in contradiction with the SM. One of the most intriguing questions in particle physics is the nature of dark matter, which constitutes around 26.8% of the universe [58]. The first evidence of dark matter was based on the measurement of the flat galactic rotation curves by the astrophysicist F.Zwicky. Later, several other observations such as gravitational lensing around the bullet cluster [52] and the cosmic microwave background [68] have provided further evidence for the existence of dark matter.

Another open question is the baryon asymmetry of the universe (BAU), which refers to the observed imbalance between matter and antimatter. The process of baryogenesis that led to the creation of more matter than antimatter in the early universe is still a mystery. The conditions required for BAU include the violation of the baryon number and charge-parity violation (CPV) of the physical process. Although the SM includes CP violation, it is not strong enough to explain the observed quantity of BAU.

Neutrinos are another area of research beyond the SM. In the SM, neutrinos are considered massless. However, the observation of neutrino oscillation [47] since 1998 contradicts this assumption, suggesting that neutrinos must have mass

1.4 Heavy Neutral Leptons in the νMSM theory

1.4.1 Introduction

The ν minimal standard model νMSM is a possible theoretical extension to the SM that introduces three right-handed neutrinos, known as Heavy Neutral Leptons (HNLs), as shown in figure 1.3. These three right handed neutrinos are responsable on the neutrino mass generation instead of the SM Higgs mechanism. In addition, HNLs can also explain dark matter and the matter antimatter asymmetry. HNLs are singlet fermions under the three SM interactions, and only undergo a small fraction of the weak interaction through mixing with active neutrinos via the seesaw mechanism [55]. In this thesis, we will explore the properties and potential implications of HNLs within the framework of the ν minimal standard model (νMSM) [48] [61]. The νMSM lagrangian term can be written as

$$\mathcal{L}_{HNL} = \mathcal{L}_{\text{Kin term}} + \mathcal{L}_{\text{mass term}} \tag{1.22}$$

In the HNL Lagrangian, the kinematic term can be expressed as shown in Equation 1.23. The mass term in the HNL Lagrangian is shown in equation 1.24 and is composed of both the Dirac mass and Majorana mass terms. The Dirac mass term relies on the type-I seesaw mechanism, defined by the Yukawa couplings among active neutrinos, HNLs, and the Higgs field. These Yukawa couplings lead to the generation of mass terms for neutrinos. On the other hand, the Majorana mass term relies on the coupling between neutrinos and antineutrinos for the generation of neutrino mass.

$$\mathcal{L}_{\text{Kin term}} = i\overline{N_I}\gamma^{\mu}\partial\mu N_I \tag{1.23}$$

$$\mathcal{L}_{\text{mass term}} = -F_{\alpha I}\overline{L_\alpha}N_I\phi - \frac{1}{2}M_I\overline{N_I^c}N_I + \text{h.c.} \tag{1.24}$$

The lagrangian of νMSM model can finally be expressed as :

$$\mathcal{L} = \mathcal{L}_{\text{SM}} + \mathcal{L}_{HNL} \tag{1.25}$$

$$\mathcal{L} = \mathcal{L}_{\text{SM}} + i\overline{N_I}\gamma^\mu\partial\mu N_I - F_{\alpha I}\overline{L_\alpha}N_I\phi - \frac{1}{2}M_I\overline{N_I^c}N_I + \text{h.c.} \tag{1.26}$$

where $\mathcal{L}_{\text{SM}}$ is the Lagrangian of the Standard Model, N_I are the heavy neutral leptons, $L\alpha$ are the lepton doublets where (α =e,μ τ) , $M_D = F < \phi >$ and M_I are the Dirac and Majorana masses of the heavy neutrinos are introduced. Further details can be found in [14].

This Lagrangian describes the interactions between the active and heavy neutrinos and can be used to predict the production and decay of heavy neutral leptons in collider experiments.

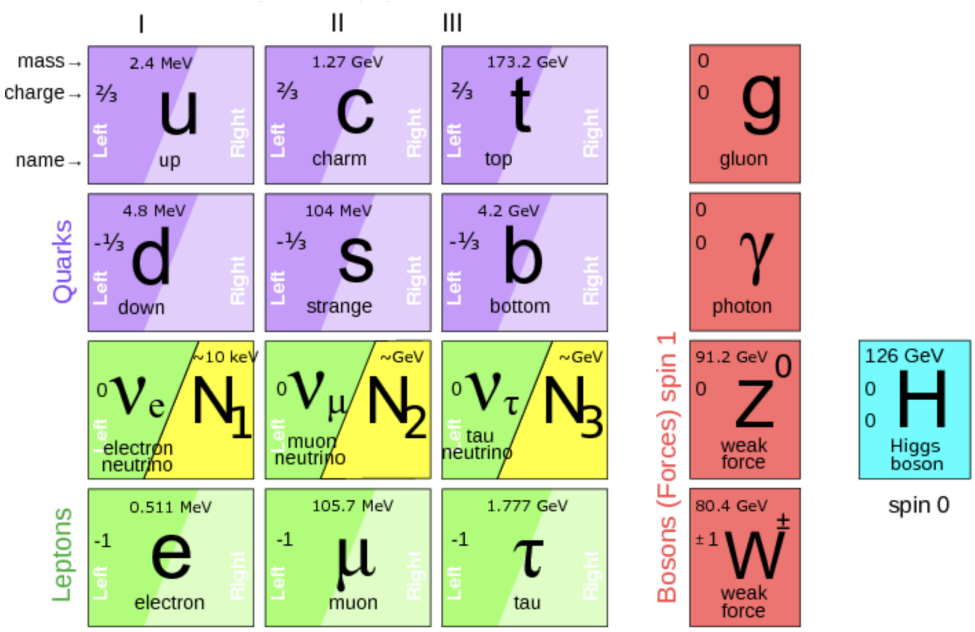

Figure 1.3: Fundemantal particles of the SM including its minimal extension by N_1, N_2 and N_3 in the neutrino sector and their caracteristics[21].

1.4.2 Heavy Neutral Leptons production and decay modes

One of the main ways to search for HNLs is through their production and subsequent decay through the weak interaction. In this dissertation, HNLs are searched for that and can be produced through the decay of W bosons, which are produced in proton-proton (p-p) collisions as shown in 1.27

$$pp \to \mathrm{W}^{\pm} \to \ell^{\pm} N \,. \tag{1.27}$$

The cross section of HNLs production through this process, which is in another words the probability per units of area, is given in the following

$$\sigma_N = \sigma(pp \to \mathrm{W}^{\pm}) \cdot B(\mathrm{W}^{\pm} \to \ell \mathrm{N}) \tag{1.28}$$

where $\sigma(pp \to \mathrm{W}^{\pm})$ is the inclusive cross section of the W boson production in p-p collision, $B(\mathrm{W}^{\pm} \to \ell^{\pm}\mathrm{N})$ is its branching ratio to a lepton and an HNL and is expressed as [45]

$$B(\mathrm{W}^{\pm} \to \ell^{\pm}\mathrm{N}) = B(\mathrm{W}^{\pm} \to \ell^{\pm}\nu) \cdot \sum_{\ell} |V_{\ell N}|^2 \left(1 - \frac{m_{\mathrm{N}}^2}{m_{\mathrm{W}}^2}\right)^2 \left(1 + \frac{m_{\mathrm{N}}^2}{2m_{\mathrm{W}}^2}\right) . \tag{1.29}$$

where $B(\mathrm{W}^{\pm} \to \ell^{\pm}\nu)$ is the standard branching ratio of $W^{\pm} -> \ell^{\pm}\ \nu_{\ell}$, $V_{\ell N}$ are the mixing angles between HNL and the three active neutrinos and m_N and m_W are the mass of HNL and $W^{\pm}$ boson respectively.

The HNL decays are all mediated by either charged or neutral current interactions. In this work, the focus is only on the 3 body semi-leptonic decay channel of HNLs .

$$N \to \ell_{\beta} \mathrm{W}^{*} \to \ell_{\beta} j j \tag{1.30}$$

The decay rate Γ_{N} to this specific channel is proportional to the mixing angle $V_{\ell N}$ and the HNL mass m_N

$$\Gamma_{\mathrm{N}} \propto G_{\mathrm{F}}^2 m_{\mathrm{N}}^5 \sum_{\ell=e,\mu,\tau} |V_{\ell N}|^2 \,. \tag{1.31}$$

The proper lifetime HNLs, denoted by τ_0 and measured in seconds, is inversely proportional to their total decay width, Γ_{tot}, as expressed in equation 1.32. Specifically, the lifetime is

proportional to $\frac{1}{m_{\mathrm{N}}^5 |V_{\ell N}|^2}$, where m_{N} is the HNL mass. This means that for a fixed coupling value $|V_{\ell N}|^2$, smaller masses correspond to longer lifetimes. In our search, we explore the mass and coupling parameter space of HNLs in the range $m_N = [1, 20]$ GeV and $|V_{\ell N}|^2$ as low as $|10^{-7}|$. As shown in figure 1.4, this allows for the possibility of long-lived HNLs. In our analysis, we use the proper decay length, expressed as $c\tau_0$ (where c is the speed of light), to describe the displacement of HNL decay. We exclude a shaded grey region in figure 1.4 that is disallowed by present experimental constraints.

$$\frac{1}{\tau_0} = \Gamma_{\mathrm{tot}}(m_{\mathrm{N}}, V_{\mathrm{e}}, V_\mu, V_\tau) = \Gamma_e + \Gamma_\mu + \Gamma_\tau \tag{1.32}$$

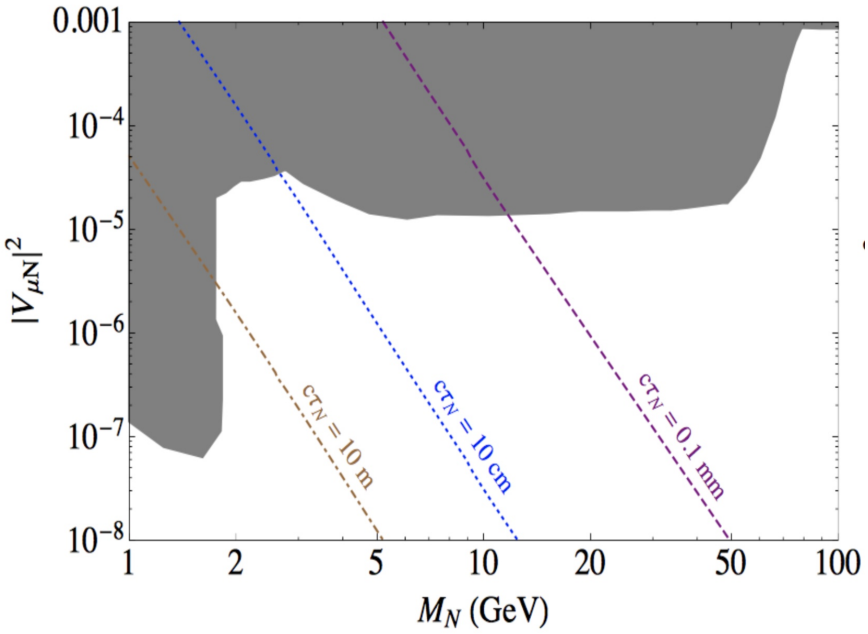

Figure 1.4: Contour lines for the HNL proper decay length $c\tau_0$. Shaded areas correspond to approximate current exclusion by different experiments.

In summary, the HNL search is conducted using proton-proton collision data, wherein a W boson is produced. This W boson then decays into a lepton and an HNL. The HNL subsequently decays into another lepton and an off-shell W boson, which in turn decays into hadrons. This described process results in the final state consisting of two leptons and hadrons.

1.4.3 Previous experimental results

In recent years, there has been growing interest in the study of Heavy Neutral Leptons (HNLs) predicted by certain extensions of the Standard Model of particle physics. Previous experimental results on HNLs have provided tantalizing hints of their existence, but definitive evidence has not yet been found. Summary plots of many HNL limit results are shown with colored filled contours in figure 1.5, unfilled ones are expected exlusion limits of future experiments performed using simulation only. As an example, the DELPHI experiment at CERN's Large Electron-Positron (LEP) collider searched for HNLs with masses from 3 GeV up to 50 GeV. The experiment analyzed the decays of Z bosons and placed stringent limits on the mixing between the HNL and the known neutrinos, as well as on the HNL mass. The results excluded a significant fraction of the parameter space for HNL masses below 50 GeV, for certain values of the mixing parameters. In addition, DELPHI also performed a measurement of the total width of the Z boson, which provided further constraints on the properties of HNLs [41].

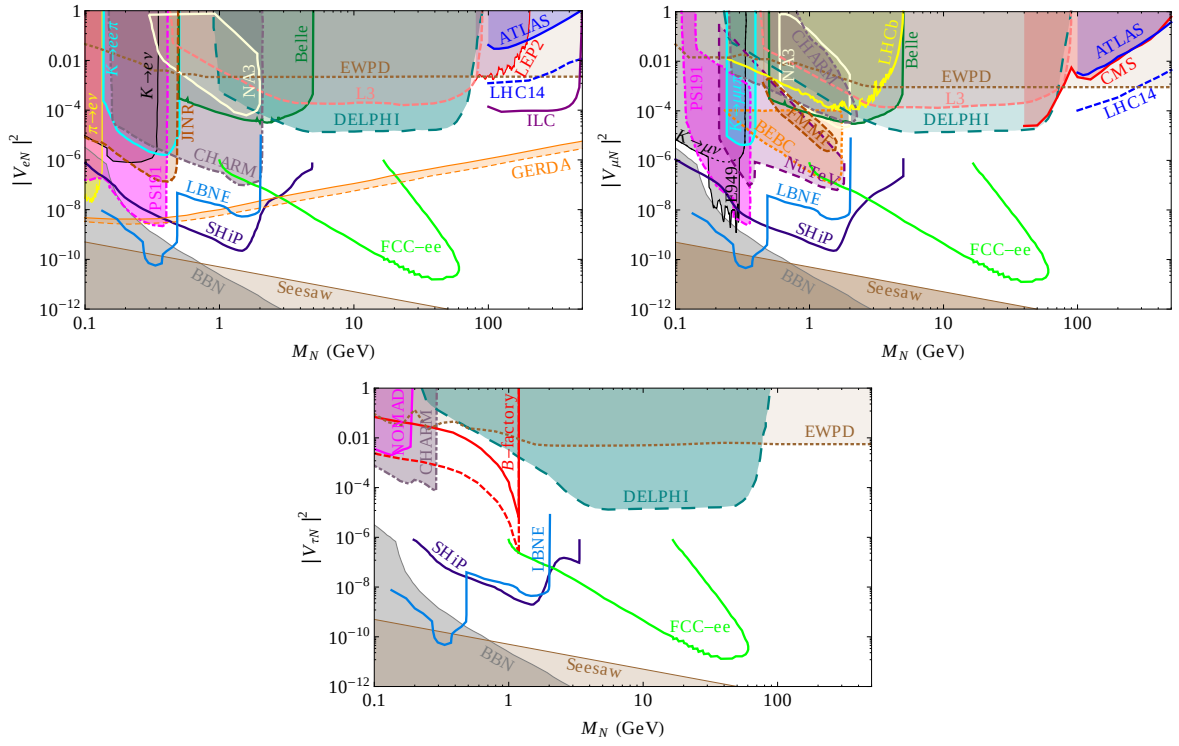

Figure 1.5: Existing limits on the mixing angle between HNLs and active neutrinos as a function of the HNL mass m_N in the mass range from 100 MeV to 500 GeV [41].

More recent results from CMS and ATLAS experiments at the Large Hadron Collider (LHC)

were published after the summary plot has been made. Both experiments have searched for HNL from the decay of W boson on or off shell produced in p-p collisions for different HNL mass and coupling scenarios. These results are summarised seperately in the following.

CMS collaboration has published HNL results in the mass range from 1 GeV to 1.2 TeV by looking at prompt HNLs decaying to a W^* and a lepton where the $W^* \to \ell + \nu_\ell$ with $\ell =$ (e, μ) [64]. These results are performed using data collected in 2016 and shown in figure1.6. Stringent constraints at low mass region were set and published later on by studying displaced HNL dacays (including searches for displaced vertices) using the collected data during 2016, 2017 and 2018 (full RunII dataset) as shown in figure 1.7.

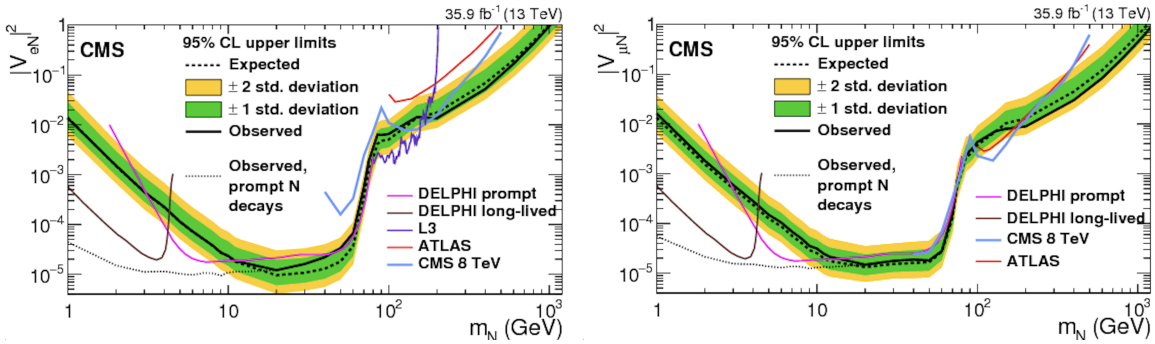

Figure 1.6: Limits at 95% CL in the $|V_{Ne}|^2$ as a function of m_N (left) and $|V_{N\mu}|^2$ as a function of m_N (right) planes. The dashed black curve is the expected upper limit, with one and two standard-deviation bands shown in dark green and light yellow, respectively. The solid black curve is the observed upper limit, while the dotted black curve is the observed limit in the approximation of prompt HNL decays. Also shown are the best upper limits at 95% CL from other collider searches in L3 [10], DELPHI [9], ATLAS [4], and CMS [49].

Contrary to CMS, the first results from ATLAS cover both prompt and displaced HNLs decay in the same mass range from 1 GeV to 1.2 TeV and they are shown in figure 1.8. Only Majorana HNLs decaying to a W^* and a lepton were studied, where the $W^* \to \ell + \nu_\ell$ given that $\ell =$ (e, μ). These results are also performed using 2016 data only [5]. Similarly, stringent results at the low mass region were recently published, studying both displaced Dirac and Majorana HNLs decay using the full RunII dataset. These results are shown in figure 1.9. A recent review of HNL searches was published in this reference [8].

Despite extensive efforts, no clear signal of HNLs has yet been observed, placing stringent constraints on the allowed parameter space for these particles. Nevertheless, ongoing research in this area continues to push the limits of experimental sensitivity and explore new ways of

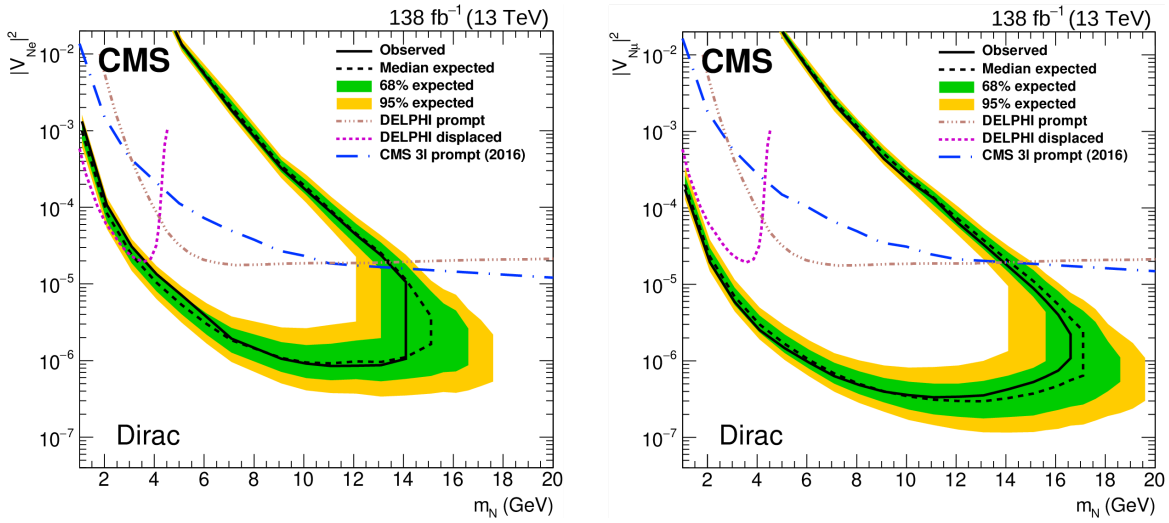

Figure 1.7: The 95% Confidence Level (CL) exclusion limits on the mixing angle of HNLs with active electron and muon neutrinos, $|V_{Ne}|^2$ (left) and $|V_{N\mu}|^2$ (right) respectively, as functions of m_N for a Dirac HNL. The area inside the solid (dashed) black curve indicates the observed (expected) exclusion region [67].

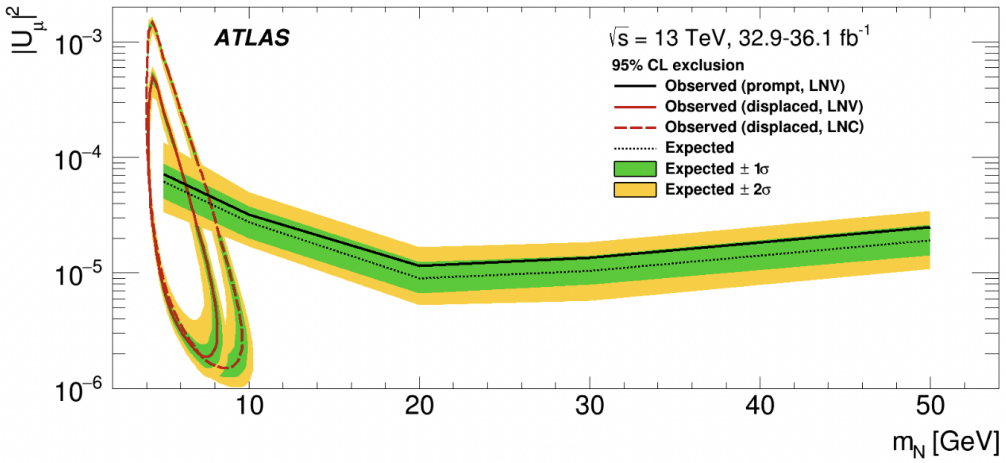

Figure 1.8: The 95 % confidence level (CL) exclusion limits on the mixing angle of HNL to ν_μ i.e $|U_\mu N|^2$ as a function of HNL mass m_N. for the prompt and displaced signatures, the region above the black line and the region enclosed by the red line are exluded respectively. Majorana HNL limits are shown with solid lines, where half of the events contain decays assuming Leptonic number violation (LNV) and the second half consides HNL decays with Leptonic number conservation (LNC). The Dirac limits are shown with long dashed line assuming only events with LNC. These results are taken from[5].

searching for HNLs in the GeV mass range which is the case of this dissertation topic.

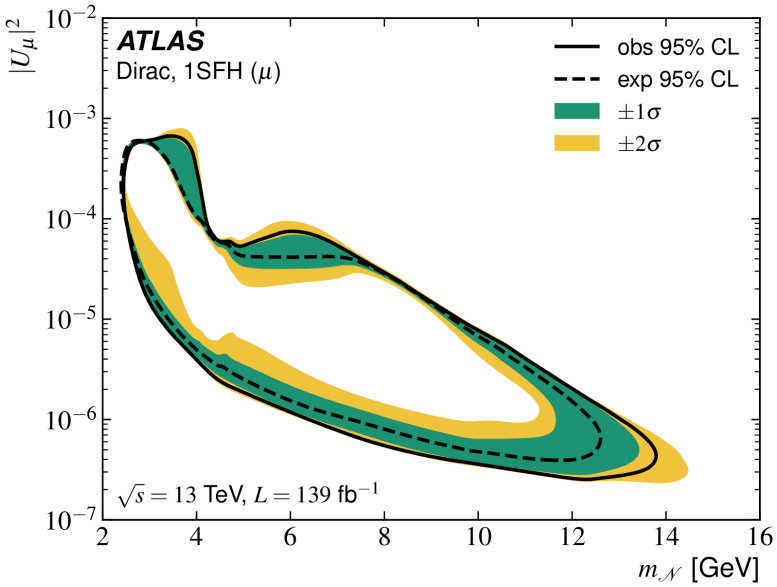

Figure 1.9: The 95% CL exclusion limits on $|U_{N\mu}|^2$ as a function m_N for HNL Majorana case. The green and yellow bands are ±1 and ±2 standard deviation (σ) spreads respectively for the expected limits. This figure is taken from [35]

Chapter 2

The CMS experiment at the large hadron collider

2.1 The Large Hadron Collider (LHC)

The world's giant machine, the Large Hadron Collider (LHC), was built by the European Organization for Nuclear Research (CERN) in Geneva, Switzerland. This two-ring synchrotron has a circumference of 26.7 kilometers and is installed underground in a stable environment between France and Switzerland in the LEP tunnel [1]. The LHC can accelerate proton or heavy ion beams in opposite directions and reach a center of mass energy (CME) of up to 13.6 TeV. The two rings merge in four interaction points where the two beams collide, and each of the four main experiments of the LHC is located at one interaction point. These experiments are ATLAS [3], CMS [29], LHCb [12], and ALICE [6]. ATLAS and CMS are general-purpose detectors designed to search for the Higgs boson, study physics beyond the Standard Model, and perform many Standard Model measurements. ATLAS is the most voluminous detector, while CMS is more compact but heavier. LHCb is primarily dedicated to studying B and D mesons physics, while ALICE is designed to study quark-gluon plasma physics, an extreme phase of matter, by colliding heavy ions. The first proton-proton collision was recorded in March 2010 at a CME of $\sqrt{s} = 7$ TeV, and the LHC has been operating since the end of 2009.

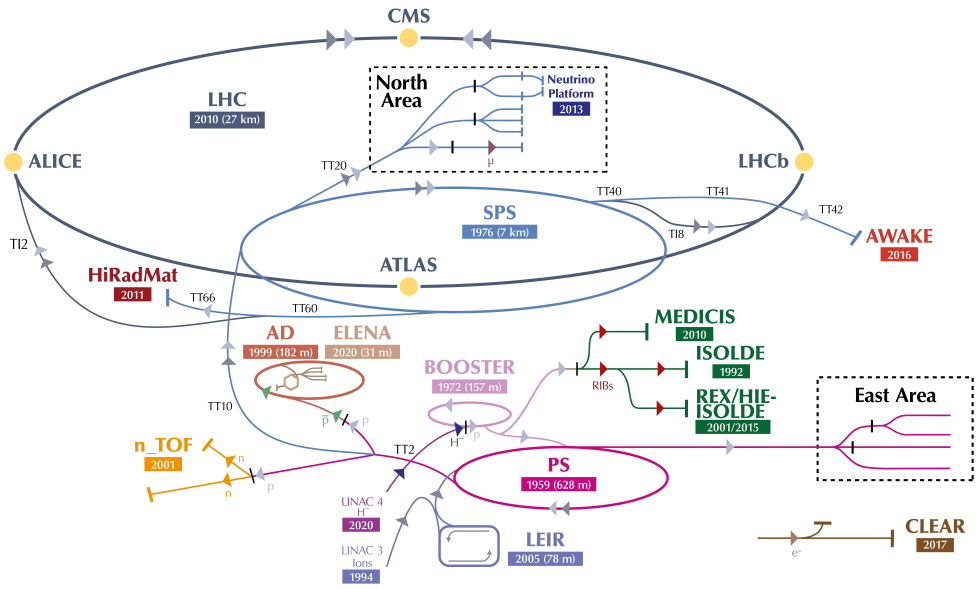

Figure 2.1: The structure of the CERN accelerator complex.The protons are accelerated through the following chain LINAC4 → BOOSTER → Proton Synchrotron (PS). The protons are then injected in the LHC. [54]

2.1.1 Accelerator Complex

The CERN complex comprises a proton source, LINAC4, and several synchrotrons. The first step in the process is the production of the proton beam using a duoplasmatron device. This device ionizes hydrogen gas to produce protons with an initial kinetic energy of 100 keV. The proton beam is then injected into the LINAC4, Proton Synchrotron Booster (PSB), Proton Synchrotron (PS), and Super Proton Synchrotron (SPS) to reach 1.4, 25, and 450 GeV proton energy, respectively. Finally, the protons are injected into the LHC ring for the final acceleration. Figure 2.1 shows the structure of the CERN accelerator complex. The duoplasmatron device is an essential component of the CERN accelerator complex and is a testament to the ingenuity of the scientists and engineers who developed it.

2.1.2 Accelerator parameters

The accelerator has a large number of parameters, but only a few of them are relevant for physics analysis. The most important parameters are the instantaneous luminosity, the integrated luminosity, and the number of events for a given physics process. The instantaneous luminosity is defined as

$$L_{inst} = \frac{n_1 n_2 f}{4\pi\sigma_x\sigma_y} \times F$$

where n_1 and n_2 are the number of protons in each beam. σ_x, σ_y are are the root-mean-square of the horizontal and vertical bunch size respectively and f is the collision frequency. Finally, F is a geometrical correction to account for the nonzero crossing angle between the two proton beams. The integrated luminosity is then computed as the integral of the instantaneous luminosity over a given period (t). The LHC Run 1 took place from 2010 to 2012, operating at $\sqrt{s} = 7$ TeV in 2010-2011 and $\sqrt{s} = 8$ TeV in 2012, with a total of 74.4 fb^{-1} of collected data. The Run 2 took place from 2015 to 2018, operating at $\sqrt{s} = 13$ TeV, where 160 fb^{-1} of data was collected. Most of the Run 2 analyses do not include data recorded in 2015, since it is very little compared to the other years. The recorded full Run 2 dataset is almost a factor of two more compared to Run 1. The integrated luminosity per year for both Runs is shown in figure 2.2.

$$L = \int L_{inst} dt$$

Finally, the most important parameter is the number of events for a given process produced in the collisions is computed as a function of the luminosity and the cross-section of the process as follows

$$N = L \times \sigma_{process}$$

where σ is the cross-section of the process and L is the integrated luminosity of the LHC beam.

2.2 CMS experiment

The CMS detector concept relies on cylindrical detection layers surrounding the beam axis, each designed to identify and measure different types of particles. When particles from proton-proton collisions pass through the detector, the tracker sub-detector first identifies the particle's charge and reconstructs its trajectory and origin (vertex). The electromagnetic calorimeter (ECAL) serves as the second sub-detector, which stops electrons and photons and clusters their energy deposits into electromagnetic showers, thereby allowing for the measurement of their energy and direction. The third sub-detector, the hadronic calorimeter (HCAL), clusters energy deposits into hadronic showers to detect charged and neutral hadrons and measure their energy and

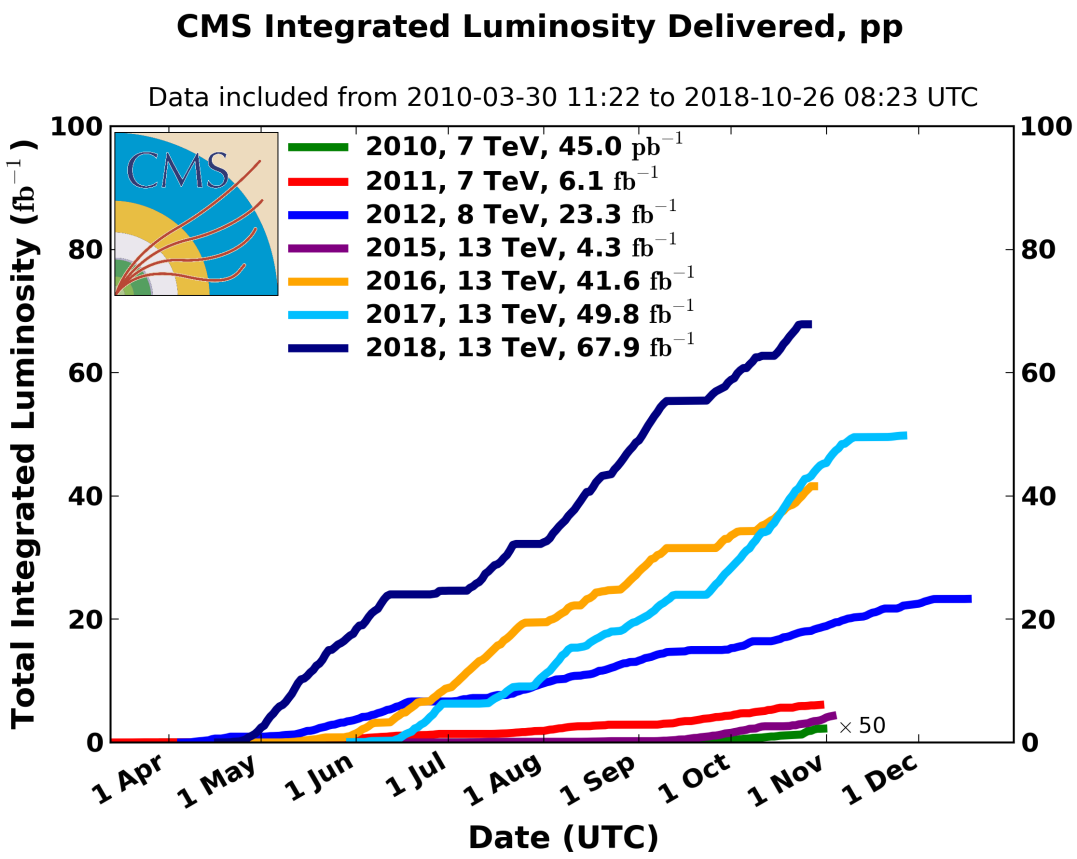

Figure 2.2: The integrated luminosity delivered to CMS experiment since 2010.

direction. The magnet that surrounds the calorimeters bends the trajectory of charged particles, enabling the measurement of their momentum and charge. Muons and neutrinos can pass through the calorimeters, with only muons producing hits in the final layer of the detector, the muon chambers. Neutrinos do not interact with the CMS detector, resulting in missing energy. Figure 2.3 provides a detailed illustration of the CMS detector.

2.2.1 Tracker

Figure 2.4 shows the tracker, which is the closest sub-detector to the interaction point and is used to track charged particles by measuring their trajectories. The tracker measures the charge and momentum of the particles by using the magnetic field (from the magnet) that bends their trajectories. It analyzes tracks and identifies the position of primary and secondary decays (vertices) inside the tracker region or in the beam pipe. The tracker comprises the silicon pixel and the silicon strip modules, both covering a pseudorapidity region of $|\eta| < 2.5$. The pixel

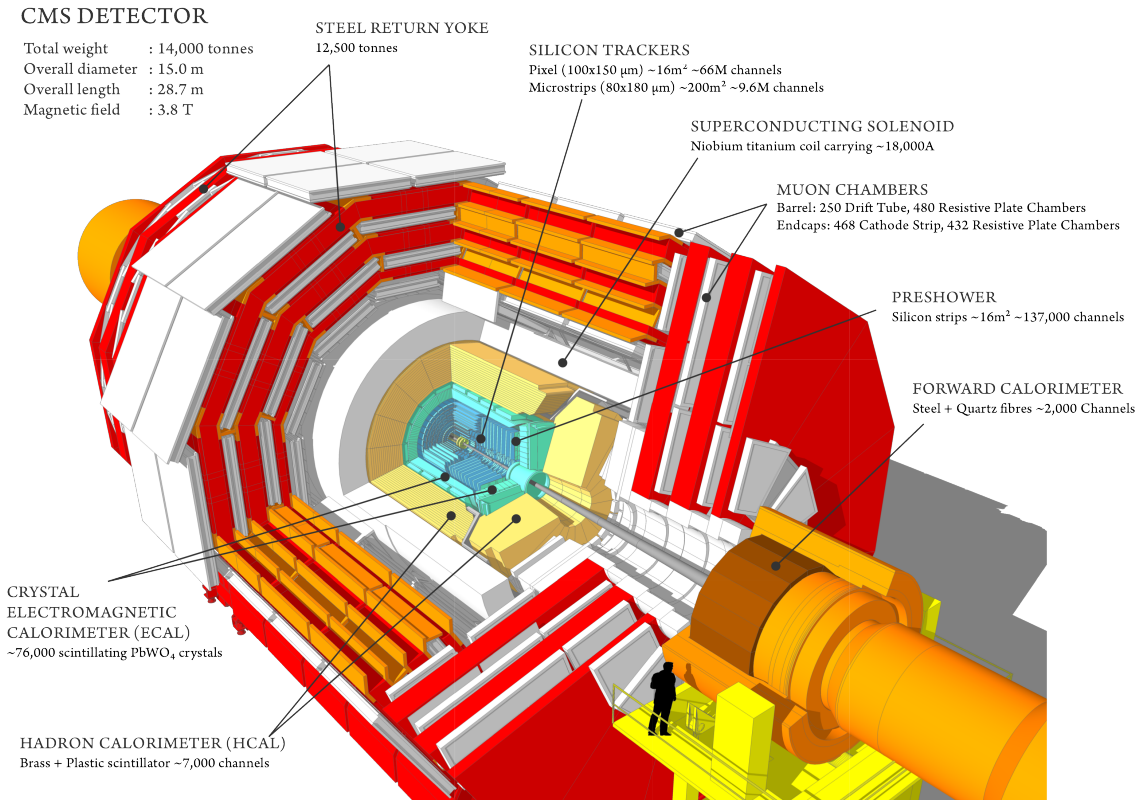

Figure 2.3: Overview of the full CMS detector compared with the size of a human.

modules are the closest sub-detector to the beam pipe. In 2016, at the beginning of Run 2, the pixel detector consisted of three cylindrical barrel layers located at a radius of 4.4 cm, 7.3 cm, and 10.2 cm and four endcap disks located at ±34.54 and ± 46.5 cm (two on each side along the z-axis). However, at the end of 2016, the pixel detector was upgraded by adding a fourth additional layer to increase the tracking performance efficiency and capability to reject pileup (see section 3.10) since its contribution rose substantially in 2017 and 2018 compared to 2016, where the average pileup was 23, 33, and 32 for 2016, 2017, and 2018 respectively. Figure 2.5 summarizes the pixel detector upgrade. The strip module is installed around the pixel detector, with a radius of $20 < r < 116$ cm, and it has four sub-detectors installed in the barrel and the endcap of the CMS experiment. In the barrel region, the strip module comprises two parts, the tracker inner Barrel (TIB) and the tracker outer barrel (TOB), both parallel to the beamline. The TIB has six cylindrical layers extended over a $20 < r < 55$ cm radius. However, the TOB has only four cylindrical layers spread over a $55 < r < 116$ cm radius. In the endcap region, the strip module is composed of two additional parts, the tracker inner disks (TID), which are

composed of three disks over a z region of $58 < |z| < 124$ cm, and the tracker endcap (TEC), which is made of nine disks and covers a z region of $24 < |z| < 282$ cm.

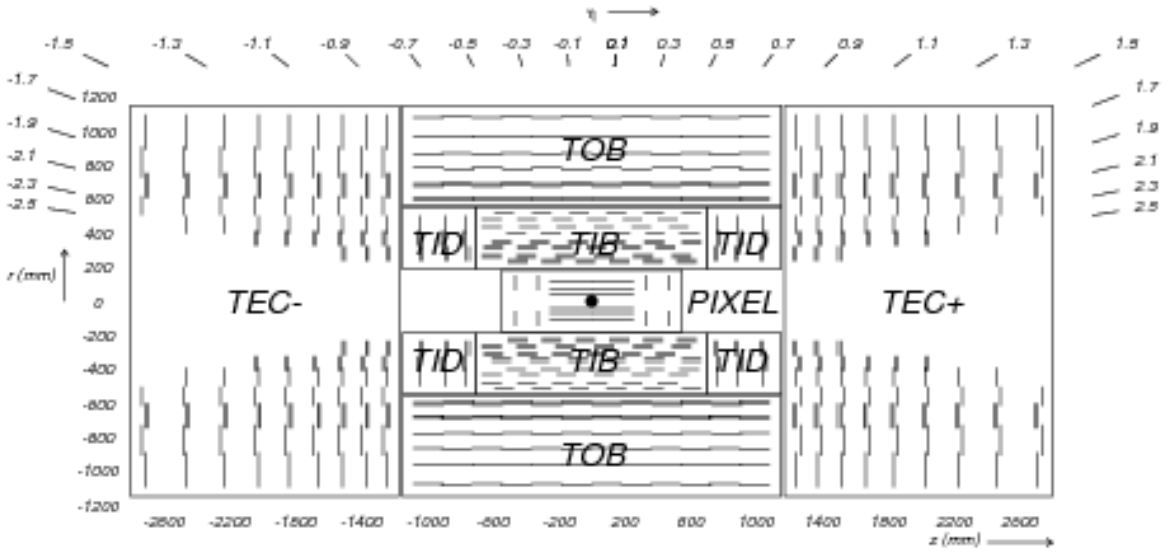

Figure 2.4: 2D view of the CMS tracker detector.

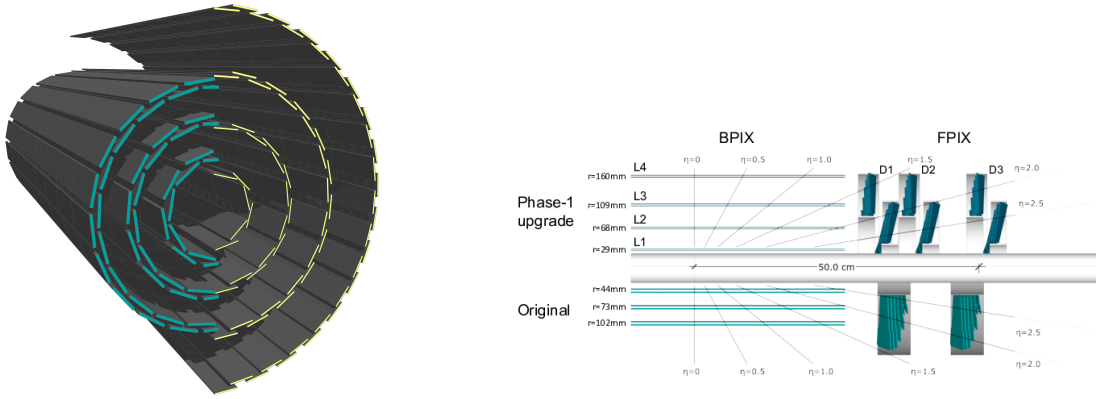

Figure 2.5: A comparison between the original and the phase-I upgrade version of the pixel detector.

2.2.2 Electromagnetic Calorimeter

The electromagnetic calorimeter (ECAL) is a homogeneous calorimeter made of 75848 crystals of lead tungstate ($PbWO_4$) in total for the barrel (61200 crystals) and endcap (7324 crystals) regions in each part. The ECAL's role is to detect energetic electrons and photons, and it is designed to be capable of detecting the decay to two photons of the Higgs boson. It is composed

of 3 main parts, the ECAL barrel (EB), ECAL endcap (EE), and the preshowering (ES) system, and it covers in total a pseudorapidity region $|\eta| < 3$. The EB system covers the region up $|\eta| < 1.479$, with a radius of 1.29 cm starting from the IP m and a length of 23 cm. The EE system covers $1.479 < |\eta| < 3.0$ and is located at 3.145 m in the longitudinal direction from the IP. The ES is a sampling calorimeter composed of lead absorbers and silicon strip detectors. It is installed in front of each ECAL endcap from both sides. Its total thickness is 20 cm. The preshowring system aims to identify photons originating from neutral pion decays. They also help to identify electrons and to determine their position resolution. The lead tungstate material was chosen due to its three important characteristics, which are the very high density (8.28 g/cm^3), the short radiation length (0.89 cm), and the small Molière radius (2.2 cm). All these characteristics help to have a compact ECAL with fine granularity. The energy resolution of the ECAL calorimeter is given in equation 2.1 and taken from [30].

$$\frac{\sigma}{E} = \frac{a}{\sqrt{E}} \oplus \frac{b}{E} \oplus c\%. \tag{2.1}$$

where a = 2.8 %, b = 12% and c = 0.3 % are constant parameters, where a for example representing the stochastic noise and it was determined using an electron test beam.

2.2.3 Hadronic Calorimeter

The hadron calorimeter system is vital in measuring the hadronic activity and missing energy in the events. It covers a region up to $|\eta| = 5.2$. The system has several components: the Hadron Barrel (HB), Hadron Endcap(HE), Hadron Outer (HO), and Hadron Forward (HF) calorimeters. The HB and HE calorimeters are installed between the tracker and the magnet system, as shown in figure 2.6. The HB spans a region of $|\eta| < 1.3$. It starts at a radius R = 1.77 m and ends at R = 2.95 m. Unlike the ECAL barrel, the HB is a sampling calorimeter. It comprises 15 plates of brass and 16 plates of plastic scintillator material (Kuraray SCSN81) placed alternately. An additional scintillator plate (layer 0) made of (Bicron BC408) was installed in front of HCAL. The main role of this layer is to detect hadronic activity started between the EB and HB.
Due to the radial space restriction on the HB and HE, the material used is insufficient to absorb

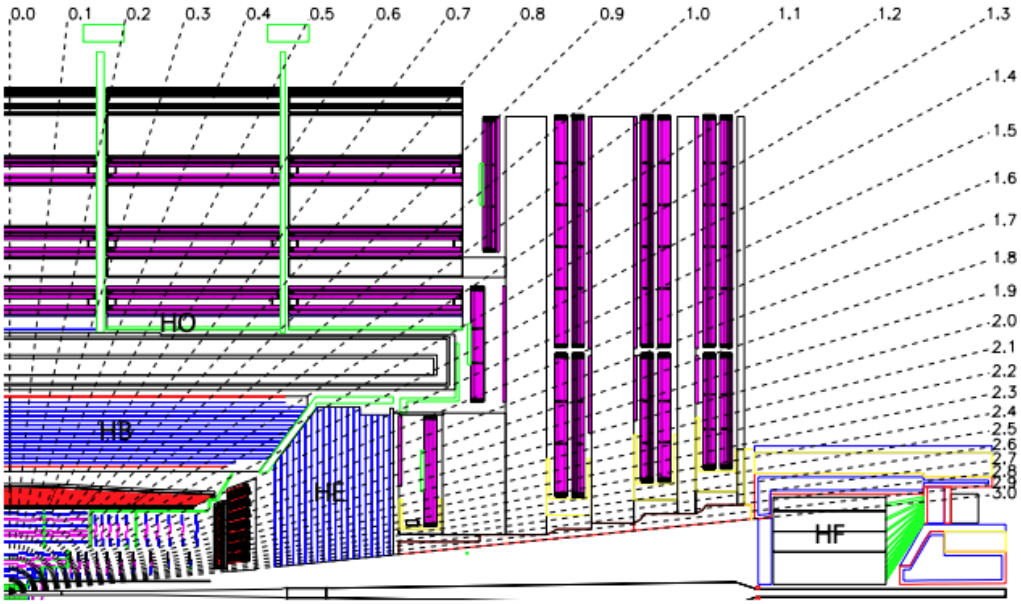

Figure 2.6: Overview of the CMS hadronic calorimeter system [30].

all the hadronic showers. To accommodate this, an additional hadron outer calorimeter is placed after the magnetic system to play the role of a tail catcher. This other hadronic part is the HOy. It is installed outside the solenoid magnet and covers the region $|\eta| < 1.26$. It increases the thickness of the hadronic system to a maximum of $10.6X_0$. The HE calorimeter spans a pseudorapidity region of $1.3 < |\eta| < 3.0$ and it covers a big solid angle (13.2%) it has an interaction length of about $\approx 10X_0$ where X_0 is the radiation length. The HF span $|\eta| > 3.0$ and at 11.2 m from IP. The HF part extends the pseudorapidity range of the HCAL system to $|\eta| = 5.2$. It has a cylindrical steel structure with a radius of 1.3 m. The energy resolution of HCAL has been measured in charged pion beams with energies of $20 < E < 300$ GeV [36] where

$$\frac{\sigma_H}{E} = \frac{94.3\%}{\sqrt{E}} \oplus 8.4\% \tag{2.2}$$

2.2.4 Solenoid Magnet

The CMS experiment magnetic system consists of the superconducting solenoidal magnet. It is 12.5 m long with a diameter of 5.9 m. Liquid helium is used to cool the magnet to its operating temperature which is around 4.5 K. It operates at a very high magnetic field value ≈ 3.8 T, needed to curve the trajectory of high energy charged particles, which allows a very precise measurement of their charge and momentum in the tracker as well as in the muon spectrometer.

2.2.5 Muon System

The muon spectrometer, see figure 2.7 consists mainly of two significant parts: the muon barrel (MB) and muon endcap (ME) systems. It covers a pseudorapidity region down to $|\eta| < 2.5$ and is located outside the magnet, and it is the most outside transverse layer of the CMS experiment. The muon detector is very rich. It has several sub-detectors. The DT, CSC, GEM, and RPC chambers refer respectively to drift tubes, cathode strip chambers, gas electron multiplier chambers, and resistive plate chambers. Some of these stations are installed in the muon barrel, some of them in the endcaps, and some of them in both. This sophisticated design of the muon system aims to identify muons' momentum (up to several TeV) and charge with high efficiency.

The muon barrel contains four layers of stations, and each of the two muon endcaps has four disks, as shown in Figure 2.7. The MB is located at a distance of 4.0 m from the beam. It is composed from DTs and RPCs covering the pseudorapidity range $|\eta| < 1.2$. The resolution of a DT chamber is 100 µm in position and 1 mrad in direction. Each DT station has 1 or 2 RPC chambers installed with it. The DTs have better position resolution than RPCs. However, RPCs can measure the time with a better resolution due to their fast response to ensure no overlap between consecutive bunch crossings.

2.2.6 Trigger

The LHC delivers data to CMS at a rate of 40 MHz. However, due to several limitations, CMS can not save all the delivered data. First, the electronics buffer would fill and halt the data

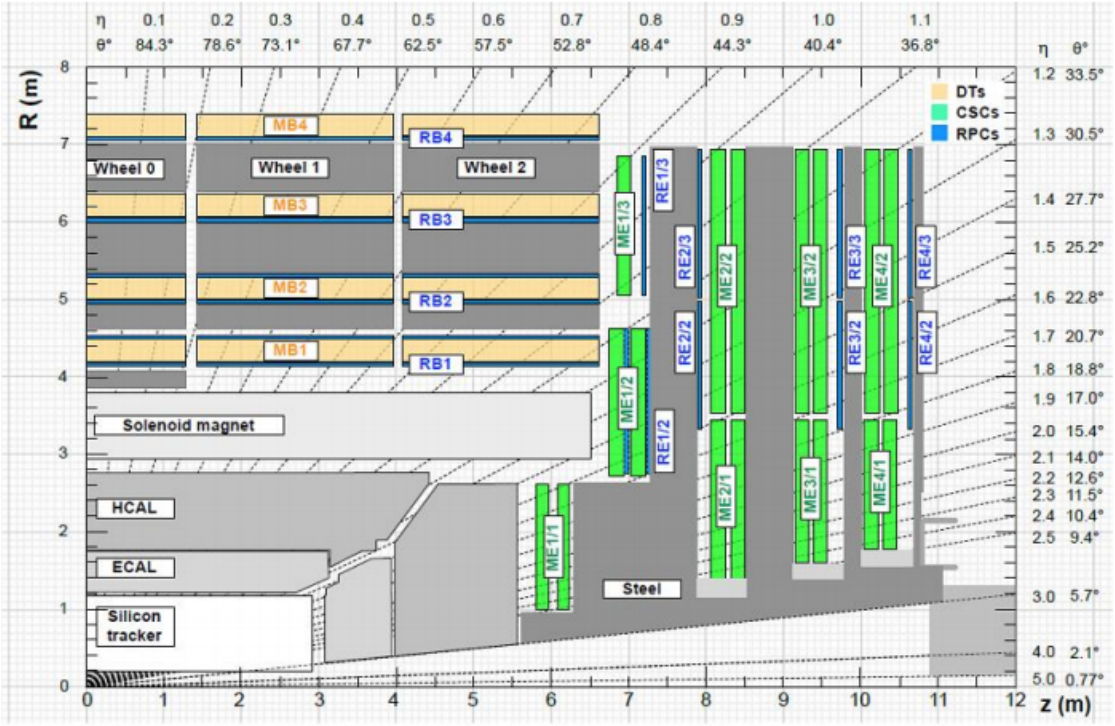

Figure 2.7: Overview of the CMS muon system by the end of LHC Run 2 taken fro [63]

from the next collision, and second, it would require an enormous offline storage space which is not available in the experiment.

To reduce the amount of data to be saved, CMS has adopted a triggering technique based on two subsystems. The L1 trigger subsystem comes first and pre-selects only physics events of interest at the hardware level based on a few subdetectors such as the muons chambers, HCAL and ECAL. This reduces the event rate from 40 MHz to 100 kHz maximum. The L1 trigger has a latency of $\approx 4\ \mu s$, which is imposed as the maximum time limit to decide whether to keep the event for further processing. This would prevent the flow of incoming data from being halted and eventual loss of events for the CMS experiment.

The second subsystem is the High-Level Trigger (HLT) which processes the remaining 100 kHz of events to keep only 1 kHz as the final event rate to be saved and transferred to the permanent storage system. Unlike the L1 trigger, the HLT uses all subdetector's information for fast event reconstruction, allowing an excellent reconstruction efficiency comparable to the offline one.

Chapter 3

Event Reconstruction

3.1 Introduction

The CMS detector, as described in the previous section, is capable of reconstructing and identifying all standard model (SM) particles. The tracker detects the trajectory and origin of charged particles (tracks), while the magnetic field generated by the superconducting solenoidal magnet bends these trajectories to determine their charge and momentum. Electrons and photons are absorbed in the ECAL sub-detector, which creates an electromagnetic shower that allows for measurements of their direction and energy deposition. Similarly, charged and neutral hadrons are mostly stopped in the HCAL sub-detector, where a hadronic shower is created, allowing for determination of their direction and energy deposition. Muons, unlike other particles, leave additional hits in the muon system, allowing for their identification, while other particles are typically stopped before reaching this system. Finally, neutrinos escape the detector, and their presence is inferred from the missing energy they carry.

The combination of all local information from different sub-detectors by using the particle flow algorithm (PF) leads to the identification of particles and detector objects as detailed below and shown in figure 3.1. The particle flow algorithm detailed in section 3.4 is then an essential output for particles and detector object reconstruction.

In this chapter, the reconstruction of the key physics objects for the HNL analysis is discussed. These objects are used as input to the displaced jet tagger, for event selection and categorization,

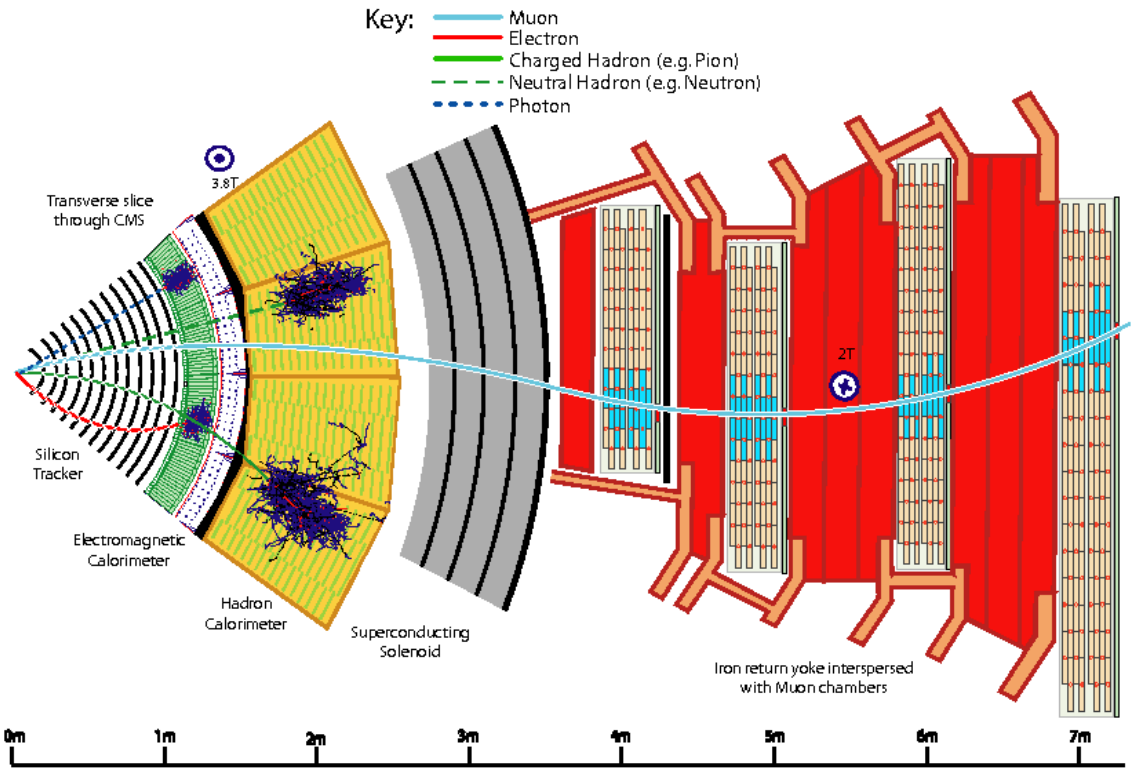

Figure 3.1: Transverse view of the CMS detector. Figure taken from **??**.

and to define the control regions.

3.2 Charged Particles Track finding

Tracks are the trajectories of charged particles in the tracker(pixel and strips) sub-detector. They are reconstructed from hits using the CMS Combinatorial Track Finder (CTF) algorithm [20]. To obtain the final collection of reconstructed tracks using the CTF algorithm, six iterations are performed to find tracks based on their p_T , number of pixel hits, and location. The first iteration consists of finding tracks with three pixel hits and the largest p_T that are produced in the central region. A minimum requirement on p_T threshold is applied ($p_T > 0.8$ GeV). The second iteration looks for tracks with two pixel hits. The third one consists of finding low p_T tracks that have three or two pixel hits. The last two iterations are configured to find tracks that are not selected in previous iterations e.g. tracks located away from the beam spot region. After each iteration, the hits associated with the reconstructed tracks are removed to reduce the complexity for the next iterations. Further details can be found in [31].

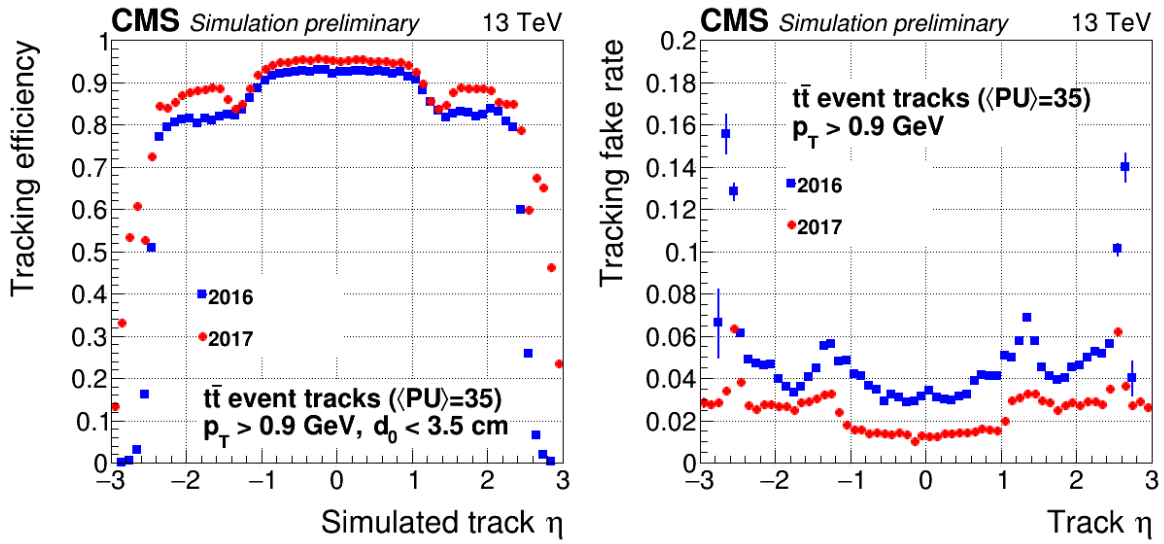

Figure 3.2: Tracking reconstruction efficiency as a function of track η using simulated $t\bar{t}$ events and 2017 conditions.

Since the pixel detector was upgraded in 2017 as mentioned in section 2.2.1, the CTF algorithm was updated to accommodate the new pixel geometry. Figure 3.2 shows the comparison of tracking performance between 2016 and 2017 detector conditions using $t\bar{t}$ simulated events with an average of pileup equal to 35: on the left is the tracking efficiency as a function of the track η and on the right is the tracking fake rate as a function of the track η. An overall improvement in the performance can be seen. The tracking efficiency increases and the tracking fake rate decreases. The tracking efficiency is found to be greater than 90 % and 80 % for $|\eta| < 1$ and $|\ \eta|\ | > 1$ respectively.

3.3 Vertex finding

Due to the high number of proton-proton interactions produced per bunch crossing each 25 ns at the CMS detector, the reconstruction of all proton-proton interaction origins (vertices) in CMS is crucial to distinguish signal from pileup vertices.

The first step of the reconstruction is to select tracks using a number of quality criteria to ensure tracks come from the primary vertices e.g. prompt tracks.

The second step is the clustering of the tracks using a specialized algorithm called deterministic annealing (DA) which is a technique based on the points of the closest approach of

the track to the beam spot. This step serves to determine possible candidate vertices. Each candidate vertex needs to have at least two tracks that are compatible exclusively with that vertex.

Finally, the third step consists of fitting all candidate vertices using an adaptive vertex fitter (AVF) [46]. The fit computes several parameters to determine the quality of each vertex such as 3D space coordinates (x,y,z) and the number of degrees of freedom (NDOF) which is proportional to the sum of the likelihood of each track belonging to the vertex. The reconstruction efficiency resulting from the procedure is higher than 98% for interaction with two to four tracks and it reaches 100% for events with five tracks or more. Only vertices passing specific criteria on the fitting parameters, NDOF, z, and transverse impact parameter with respect to the beam axis $\mid d_{xy} \mid$, are retained for most of the physics analysis that requires primary vertices. These criteria are:

- ndof > 4
- $|z| < 24$ cm
- $|d_{xy}| < 2$ cm

These primary vertices are ordered as a function of the sum of p_T^2 of their tracks. The leading vertex is then considered as the primary vertex of interest while the other vertices are considered as pileup.

3.4 Particle flow algorithm

The particle flow algorithm [29] is crucial to the identification of particles within the CMS experiment. It correlates reconstructed local objects from all subdetectors and combines their measurements to identify particles while avoiding double counting. The algorithm proceeds through several steps:

- The link algorithm checks for correlation between objects in different sub-detectors. The first step is to check the link between tracks in the tracker and a calorimeter energy deposit

(cluster) by extrapolating the last hit in the tracker to different calorimeter sub-detectors. The link is established only if the extrapolated position is within the calorimeter cluster edges.

- Photons emitted by electrons through the bremsstrahlung process are identified, and their energy is measured by extrapolating the tangents of the electron track (GSF) from the intersection point of the tracker layers with the track. A link between the extrapolated tangent and the cluster is established only if their position matches within an uncertainty of $|\eta| < 0.05$.

- The link between clusters in different calorimeters, ECAL and HCAL or ECAL and ES, is set if the cluster in the more granular calorimeter is within the cluster of the coarser one.

- The link between a tracker track and a track in the muon system is established if the resulting χ^2/ndof fit value from the global muon reconstruction is less than 10.

Once all possible links are established, PF blocks are created, and the identification of particles proceeds in the following order:

- Global muons are classified as PF muons if the measured tracker track momentum is compatible with the combined global measured momentum from both the tracker and muon system within the uncertainty. The corresponding PF elements are then removed from the PF block.

- PF electrons are identified by combining information from electron tracks fitted by the GSF with ECAL clusters, from electron and potential bremsstrahlung photons emitted by the electron. Once the PF electrons are defined, the corresponding PF elements are excluded from further action.

- All the remaining tracker tracks in the PF block that are linked to the HCAL energy cluster are classified as PF charged hadrons.

- Neutral hadrons are identified by measuring the energy fraction of neutral hadrons. This is done by subtracting the energy fraction of the charged particles from the calibrated energy of the linked calorimeter clusters.

3.5 Jets

A jet of particles is formed when quarks and gluons undergo hadronization process. At the reconstruction level in the CMS experiment, the most common jets are formed by clustering particle flow candidates using the anti-k_{T} algorithm with a distance parameter of 0.4 (AK4) [26], which combines information from the tracker and calorimeter subsystems. To remove the effects of pileup, charged contributions are removed using the charged hadron subtraction algorithm (CHS) [26], while neutral contributions are removed using the jet area method. The jet's momentum is calculated as the vectorial sum of all PF particles' momenta within the jet. In this search, the identification criteria mentioned in table 3.1 are applied to the jet objects per year of data-taking. This selection reduces substantially the fake jets rate, originating from detector noise while keeping the efficiency of the jets from strong interaction higher than 99%.

Table 3.1: Jet identification criteria for 2016 and 2017/2018 data-taking scenarios.

Variable	2016	2017/2018
Neutral hadron fraction	< 0.90	< 0.90
Neutral EM fraction	< 0.90	< 0.90
Number of constituents	> 1	> 1
Charged hadron fraction	> 0	> 0
Number of charged constituents	> 0	> 0
Charged EM fraction	< 0.99	-

3.6 Isolation

The isolation describes the hadronic and electromagnetic activities around a particle within a cone of size ΔR where $\Delta R = \sqrt{\Delta\eta^2 + \Delta\phi^2}$. In this analysis isolation plays an important role in the lepton identification. The isolation is defined as follows.

$$I^{l}_{\mathrm{rel.}} = \frac{I_{\mathrm{ch.had.}} + \max\Big(0,\ I_{\mathrm{neut.had.}} + I_{\gamma} - I^{\mathrm{neut}}_{\mathrm{PU}}\Big)}{p^{l}_{T}}, \tag{3.1}$$

where, p^{l}_{T}, $I_{\mathrm{ch.had.}}$, $I_{\mathrm{neut.had.}}$, I_{γ} and $I^{\mathrm{neut}}_{\mathrm{PU}}$ are the transverse momenta of the lepton, charged hadrons, neutral hadrons, photons, and neutral pileup. Only charged particles associated to the primary vertex are used in the calculation. The subtraction of the neutral pileup treatment

is done in two different ways, based on the $\Delta\beta$ and effective area (EA) methods, dedicated respectively to muons and electron candidates [27] [25]. The $\Delta\beta$ method calculates from simulation the neutral hadron energy based on the charged hadrons one as follow

$$\sum_{PU} p_T^{Neutral} = \frac{1}{2} \sum_{PF_{PU}} p_T^{CH} \tag{3.2}$$

The EA method is more complicated than $\Delta\beta$, it corrects the measured p_T of a given jet j by subtracting the following quantity

$$p_{T\,tj}^{sub} = p_{Ttj} - A_j \rho \tag{3.3}$$

where ρ is the level of diffuse noise which is the amount of p_T added to the event per unit area and A_j is the jet's area. More details about the EA correction can be found in this reference [25].

3.7 Muon Identification

Muon track reconstruction starts primarily in the muon chambers. Three main types of muons can be identified. The first is standalone muon when only hits from the muon chambers are used for the muon pattern recognition and track fitting. This reconstruction requires a muon to cross and leave hits in at least two muon detector planes. The second type is tracker muon. Each reconstructed inner track is extrapolated to the muon spectrometer. If at least one muon segment matches the extrapolated track, the inner track is classified as the tracker muon track. This type of muon increases the reconstruction and identification efficiency for low p_T muons. As those fail more often to cross more than one muon detector plane due to the large multiple scattering in the steel of the return yoke in the muon system and energy loss. Finally, the third type of muon is the global muon, where the extrapolated standalone muon track matches a tracker track with compatible parameters. The standalone muon is then qualified as a global muon. This type of muon is dominant by high p_T muons that succeed to cross at least two muon detector layers. In addition to the muon reconstruction requirements, identification (ID) criteria are used to define the quality of muons. A description of the two main muon IDs used

in this analysis is given in the following

Tight muon ID is optimized to select prompt muons, e.g originating from the primary vertex, with good p_T measurement while suppressing cosmic muons and muons from hadron decays in flight. To qualify as tight, the muon has to be a global muon with χ^2/ndof < 10, the inner track needs to have at least one pixel hit, at least 6 strip hits, an impact parameter $d_{xy} < 0.02$ cm w.r.t the primary interaction and a longitudinal distance w.r.t the primary interaction $d_z < 0.05$ cm. In addition the track fit of the global muon has to contain a minimum of one muon chamber hit and two muon segments in at least two muon stations.

Loose muon ID requires that muon is at least a tracker muon or better i.e global muon. This is to avoid selecting standalone muons. No additional requirements are applied.

Note that the muon IDs do not have requirement on the isolation. Additional requirement on the muon isolation will be applied later on during the analysis.

3.8 Electron Identification

The method used to reconstruct electrons in this analysis is called the "tracker-based approach", which is an alternative to the "ECAL-based approach" used for high-energy isolated electrons. Electrons can emit high-energy photons via bremsstrahlung or radiate low p_T electrons via ionization losses. The ECAL-based approach relies mainly on the ECAL measurement to reconstruct the electron. It uses the electron cluster energy and position to deduce the expected track position in the tracker, which is then seeded and fitted using the KF algorithm. However, this approach is limited by the ability to collect all the energy clusters of radiated photons, leading to inefficiency for low p_T electrons, which is highly pronounced due to the strong magnetic field causing the radiated photons to spread over a wide region.

The tracker-based approach was developed to recover the efficiency loss from the ECAL-based approach for electrons emitting high-energy photons or radiating low p_T electrons. The standard KF fitting algorithm is incapable of accommodating the significant change in momentum of

high radiating electron tracks, so a second fitting is applied using the Gaussian-sum filter (GSF) algorithm, which allows for important energy losses over the tracker trajectory. The GSF and KF track information is fed to a boosted decision tree (BDT) together with the distance between the extrapolated track and its ECAL closest cluster, and a requirement is applied to the BDT score for the electron candidate to be qualified.

In addition to the electron reconstruction, the quality of the electron (Electron IDs) is determined using cut-based and MVA-based approaches. In this analysis the electron IDs used are tight ID MVA-based approach and loose ID cut-based approach.

Tight electron ID is optimized to select prompt well-identified electrons originating from the primary vertex. The electron has to pass the iso_WP90 MVA-based ID working point.

Loose electron ID is defined using cut-based ID using information from the ECAL and HCAL energy clusters. The used parameters are detailed in table 3.2. In this analysis, a modified version of the electron loose ID has been used to increase the signal efficiency at high displacement. The modified version contains no requirements on the electron isolation and the number of missing track hits.

Table 3.2: The applied modified loose cut-based electron identification (94X-V2) criteria.

Quantity	ECAL barrel	ECAL endcap
$\sigma_{i\eta i\eta}^{5\times5}$	0.0112	< 0.0425
$\lvert\eta_{\text{seed}} - \eta_{\text{track}}\rvert$	< 0.00377	< 0.00674
$\lvert\phi_{\text{seed}} - \phi_{\text{track}}\rvert$	0.0884	< 0.169
$E_{\text{had.}}/E_{\text{EM}}$	$< 0.05 + 1.16/E_{\text{SC}} + 0.0324\rho/E_{\text{SC}}$	$< 0.0441 + 2.54/E_{\text{SC}} + 0.183\rho/E_{\text{SC}}$
$\lvert 1/E - 1/p\rvert$	0.193	< 0.111

3.9 Missing Transverse Momentum

Assuming the HNLs do not couple to the third-generation active neutrinos, missing transverse momentum (p_T^{miss}) also referred as MET is expected to be minor in the event, which can be used to reject background events. The expected amount of p_T^{miss} from the neutrinos present in the final state in the HNL events is around the average of p_T^{miss} resolution (~ 30 GeV).

The p_T^{miss} is obtained as the negative vectorial sum of the transverse momenta of all reconstructed PF candidates and is further tuned by accounting for the jet energy corrections of the event [2].

$$\vec{p_T^{\text{miss}}} = -\vec{p_T}, \quad p_T^{\text{miss}} = |\vec{p_T^{\text{miss}}}| \tag{3.4}$$

In this analysis, p_T^{miss} is exploited in the event selection, where $p_T^{\text{miss}} < 50$ GeV is required to remove background events containing neutrino in the final state originating from a leptonic W decay. A set of MET filters, summarised in table 3.3 are applied to both data and MC for the three years of data taken to reject events containing spurious missing transverse energy originating from various detector effects including dead ECAL channels and large HCAL noise.

Table 3.3: MET filters applied to data and MC for 2016, 2017 and 2018 data taken periods.

MET filters
Good primary vertex
Beam halo
HBHE noise
HBHEiso noise
ECAL dead cell trigger primitive
Bad PF muon
EE bad supercluster

3.10 Pileup

CMS detector records a high number of simultaneous collisions per bunch crossing each 25 ns. The resulting interactions lead to reconstructed primary vertices as explained in section 3.3. Only one primary vertex will be considered as the event of interest. The remaining vertices are considered as pileup (PU). The PU contribution in the event is an important source of low energy multijet background processes in many CMS analyses and in particular the HNL analysis. In principle, the PF algorithm is capable to identify charged hadrons that originate from a PU vertex. This is not true for neutral particles originating from PU interaction. To measure the neutral energy fraction contribution in the event produced by PU, the energy ratio of the charged and neutral particles is measured in simulation to determine the correction factors to

be applied. The average pileup distribution per year of data taken is shown in figure 3.3. Pileup has an important impact on the background contribution in this search, discussed in details in section 8.4.

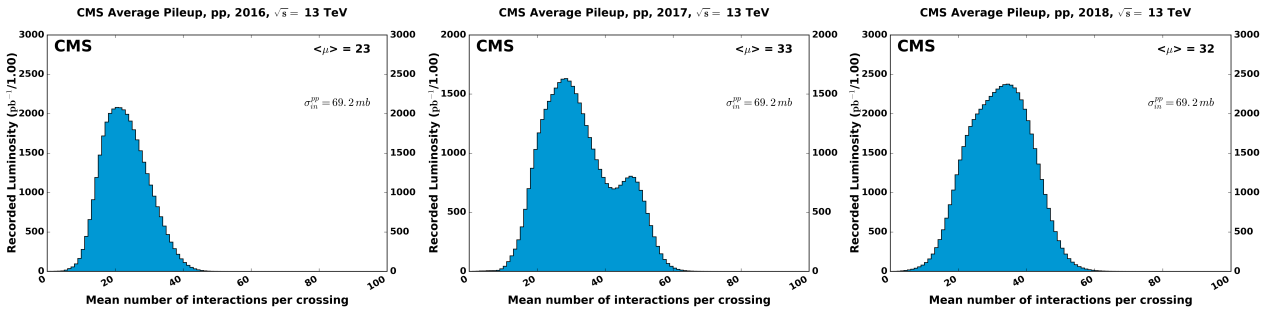

Figure 3.3: CMS average Pileup distribution for 2016, 2017 and 2018.

Chapter 4

The HNL search in the CMS experiment

In this chapter, the overview of the HNL analysis is presented, and the data, signal and background simulated samples are discussed.

4.1 HNLs Analysis overview

The current study investigates both Majorana and Dirac HNL scenarios with couplings to the three generations using the full Run 2 dataset. The analysis focuses on events with two leptons and at least one jet in the final state. The closest jet to the ℓ_2 is selected as the HNL jet, and denoted as j*, produced through W boson decays. The hypothesis of the HNL Dirac (Majorana) particle is studied with events exhibiting lepton number conservation (LNC) or lepton number violation (LNV), which is indicated by the charge of the two final state leptons being either opposite or same sign, respectively.

Moreover, this study also considers cases of lepton flavor conservation (LFC) and lepton flavor violation (LFV), allowing for the two final state leptons to have either the same or different flavors ($\mu\mu, ee, \mu e, e\mu$). The Feynman diagrams for the HNL production and decay scenarios under consideration are shown in figure 4.1. Additional information on the production and decay of HNLs can be found in Chapter1.4.

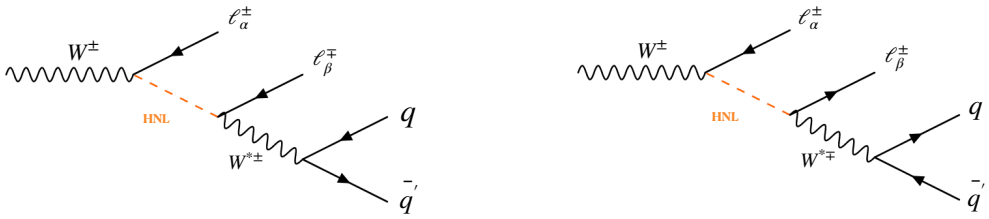

Figure 4.1: Left (Right): Feynman diagrams of the production and decay processes of Dirac(Majorana) HNL considered in this search.

It should be noted that events with two tau leptons in the final state are not explicitely considered in this study, but the analysis is still sensitive to events where both taus decay leptonically.

The HNL mass and coupling are free parameters, allowing for a wide range of parameter space exploration. Prior searches by CMS have focused on regions where HNLs have high masses of $m_{\mathrm{N}} > 20$ GeV, which correspond to prompt HNLs given the delivered luminosity. This analysis, however, focuses on displaced HNLs with $m_{\mathrm{N}} < 20$ GeV and specifically for $m_{\mathrm{N}} < 12$ GeV, where the HNL $c\tau_0$ ranges from a few millimeters to 1000 millimeters.

Given that the search for long-lived particles is not standard in the CMS experiment, displaced vertex reconstruction of exotic particles is not optimized for such searches. The existing secondary vertex reconstruction technique is not ideal for HNL searches as it has been optimized to find decays from B mesons with shorter proper lifetimes compared to HNLs. To address this, a dedicated displaced jet tagger based on deep learning techniques has been developed to identify such displaced decays. The tagger utilizes all particle and secondary vertex information as input to identify the displaced decay of HNLs, making it an inclusive displaced decay finder. Further details on the tagger mechanism and performance are provided in section 7.

The HNL analysis involves an extensive search encompassing various particle final states and topologies. To maximize the signal efficiency and reject background events, optimized objects and event selections are discussed in section 6.2. A broad events categorization is used to cover all signal scenarios and enhance the analysis sensitivity; and defined in section 6.6.

An extensive background study, detailed in section 8, has been done to suppress maximally prompt background originating from QCD, Z/γ^*+jets, and W+jets processes (reducible), and a data-driven technique i.e an ABCD factorization method is then used to estimate the residual background(irreducible) contribution in the signal region resulting mainly from misreconstructed processes identified as nonprompt or real displaced mesons decay such as B mesons. Finally the statistical analysis of the results is discussed in section 10.

4.2 Data samples

This HNLs search was performed using 136 fb^{-1} of proton-proton collision collected by the CMS experiment at the LHC between 2016 and 2018. Only events of interest in this data samples are selected using a standard single lepton trigger developed by the CMS trigger POG which requires at least one isolated lepton denoted ℓ_1 above a certain p_T threshold. The name and the ℓ_1 p_T threshold of the triggers used for the three years of data taken are shown in Table 4.1.

In the HNL search selected events contain two leptons in the final state. For the analysis strategy, also standard dilepton triggers could be used instead. However, due to the displacement of the second lepton denoted as ℓ_2 in HNL signal events, these triggers are found to be highly inefficient and are therefore not considered in this search to avoid unnecessary complexity.

Table 4.1: Trigger names and the corresponding ℓ_1 p_T threshold for the three years.

trigger name	ℓ_1 p_T [GeV]		
	2016	2017	2018
Single muon	24	27	24
Single electron	27	32	-
Single electron or photon	-	-	32

4.3 HNL samples production

To cover a wide range of possible HNL scenarios, we simulated a large number of Dirac and Majorana HNL events with leading-order (LO) accuracy using the MadGraph(v2.6.5) event generator [13]. The production and decay of HNL events, as well as the calculation of the

proper lifetime τ_0, were performed using this generator. After production and decay, the HNL events underwent hadronization using the Pythia8.2 [66] event generator. By using these state-of-the-art event generators, we were able to produce accurate simulations that closely matched the expected properties of HNLs. To simulate the production and decay of HNLs in the CMS detector, we used the Geant4 simulation toolkit [11].

In this context, over 200 million signal events for more than 76 different mass and mixing angle points were generated. The HNL mass ranged from 1 to 20 GeV, while the mixing parameters spanned from 10^{-5} to 10^{3}. These points are depicted in figure 4.2, which shows the mass and mixing angle points for both Dirac and Majorana samples. For each sample, 67 mixing weights, i.e. neutrino-HNL mixing parameters, were saved in barycentric coordinates which are a mathematical concept used to specify a point's position within a triangle by expressing its location in terms of three weights or ratios. These ratios indicate the relative distances between the point and the triangle's three vertices. In essence, barycentric coordinates provide a way to break down a point's position into its "share" of influence from each vertex of the triangle. These barycentric coordinates denoted f_e, f_μ and f_τ where $(f_e + f_\mu + f_\tau) = 1$ to probe couplings to all three standard model neutrino generations with equal strength ($\mid V_e \mid = \mid V_\mu \mid = \mid V_\tau \mid$). The triangle plot in figure 4.3 illustrates the distribution of these weights across the three generations. To simulate specific coupling scenarios, the associated weight was applied on an event-by-event basis. High statistics samples were also produced with coupling weights in the vicinity of our expected limits to increase the statistical precision of signal events. An event filter was implemented to keep only generated events with at least one lepton with $p_T > 20$ GeV, satisfying the online trigger conditions defined in section 4.2.

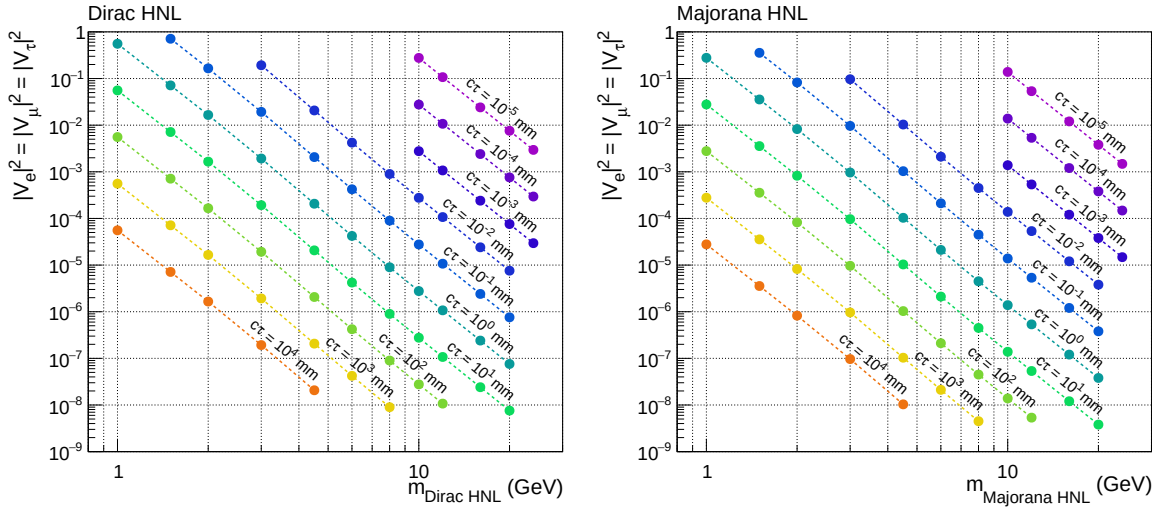

Figure 4.2: The produced signal scenarios with $|\ V_e\ | = |\ V_\mu\ | = |\ V_\tau\ |$ in the mass-coupling plane for Majorana. Scenarios with the same proper lifetime, $c\tau_0$, as calculated by MadGraph, are colour-coded and connected by dashed lines.

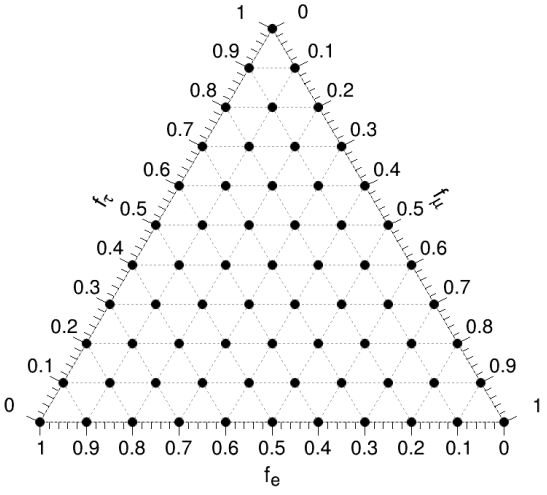

Figure 4.3: The 67 relative coupling points considered in the analysis for reweighting each signal sample generated with equal couplings to all three generations of standard model neutrinos. The relative coupling points are plotted in barycentric coordinates, where $(f_e + f_\mu + f_\tau) = 1$.

4.3.1 Signal kinematic

The kinematics of signal events play a key role in determining the object selection requirements, defining the signal region, and discriminating between signal and background processes. Therefore, it is crucial to have a good understanding of different observables. In this section, we study the kinematics of signal events at the generator level. Figure 4.4(a) shows the ℓ_1 p_T distribution originating from the W "on-shell" decays, which peaks at around 35 GeV. As mentioned before, ℓ_1 is used to trigger events. Similarly, Figure 4.4(b) shows the p_T distribution of ℓ_2, which peaks at lower values compared to ℓ_1. The jet p_T distribution is shown in Figure 4.4(c). Signal events with $m_{\mathrm{N}} = 4.5$ GeV peak at higher values compared to events with $m_{\mathrm{N}} = 10$ GeV due to the different event topology for low and high HNL mass values, which will be further discussed in the next section.

4.3.2 Event observables

Event selections are set based on several event observables. The event observables are defined, using the kinematics of the selected objects defined in section 6.2 as

$\Delta R(\ell_2, \mathrm{j}^\star)$:The opening angle in the lab frame between the ℓ_2 and the HNL jet $\mathrm{j}^\star$ used for event categorisation.

$$\Delta R(\ell_2, \mathrm{j}^\star) = \sqrt{(\phi(\ell_2) - \phi(\mathrm{j}^\star))^2 + (\eta(\ell_2) - \eta(\mathrm{j}^\star))^2} \tag{4.1}$$

$m(\ell_1, \ell_2)$: The invariant mass of the dilepton system, used to reject events from Z/γ^*+jets.

$$m(\ell_1, \ell_2) = (p(\ell_1)^2 + p(\ell_2)^2)^{1/2}. \tag{4.2}$$

where $p(\ell_1)$ and $p(\ell_2)$ are the 4-vectors momentum of ℓ_1 and ℓ_2 respectively.

$m(\ell_1, \ell_2, \mathrm{j}^\star)$: The invariant mass of the dilepton and $\mathrm{j}^\star$ candidate system is used for the ABCD background estimation and defined as

$$m(\ell_1, \ell_2, \mathrm{j}^\star) = (p(\ell_1)^2 + p(\mathrm{j}^\star)^2)^{1/2} \quad \text{if } \Delta R(\ell_2, \mathrm{j}^\star) \leq 0.4. \tag{4.3}$$

$$m(\ell_1, \ell_2, \mathrm{j}^\star) = (p(\ell_1)^2 + p(\ell_2)^2 + p(\mathrm{j}^\star)^2)^{1/2} \quad \text{if } \Delta R(\ell_2, \mathrm{j}^\star) > 0.4. \tag{4.4}$$

where p is the four-momentum of the particles. The $m(\ell_1, \ell_2, \mathrm{j}^\star)$ definition ensures that there is no double-counting of the ℓ_2 energy in the case of boosted events where the $\mathrm{j}^\star$ overlaps with ℓ_2. Figure 4.4(e) shows the $\Delta R(\ell_2, \mathrm{j}^\star)$ distribution where two main signal topologies can be distinguished.

- Boosted: $\Delta R(\ell_2, \mathrm{j}^\star) < 0.4$
- Resolved: $\Delta R(\ell_2, \mathrm{j}^\star) > 0.4$

For events with low m_N, the HNL decay product is highly boosted, resulting in ℓ_2 being clustered within the jet cone of $\Delta R = 0.4$. Conversely, for events with higher m_N, the HNL decay products are less boosted and ℓ_2 may be outside the jet cone. This difference affects the $\mathrm{j}^\star$ p_T distribution, as discussed earlier. The distinct event topologies have important implications for object selection and event categorization, which will be further discussed in the following.

The $m_{\ell_1\ell_2}$ distribution is illustrated in figure 4.4(f). Because the jet mass is not taken into account during mass reconstruction, the distribution drops before reaching the on-shell W mass. The aforementioned signal kinematic distributions are fundamental to object and event selection at the reconstruction level.

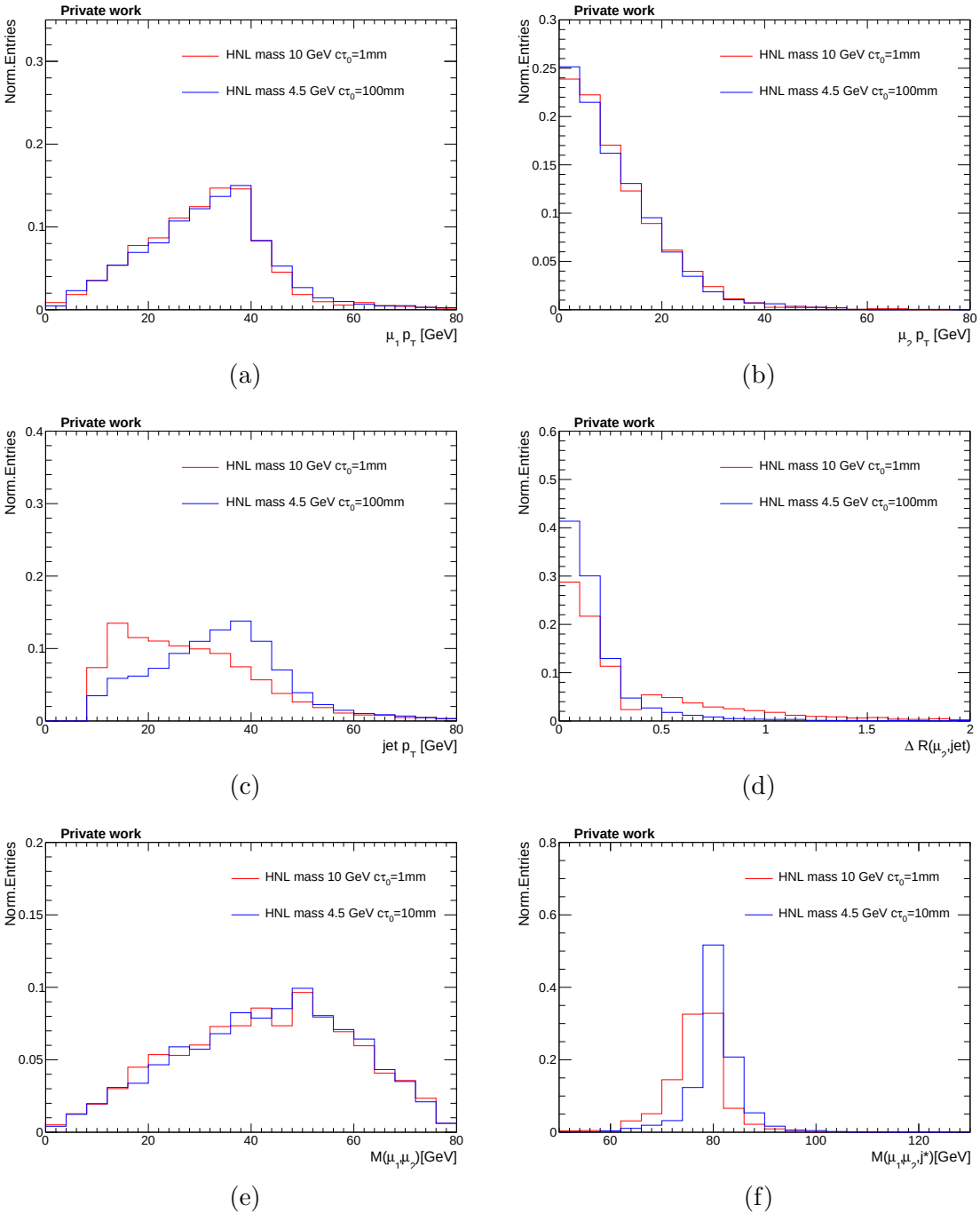

Figure 4.4: Kinematic distribution of signal events at the generator level.

4.4 Background simulation samples

To accurately search for HNLs, it is crucial to identify and mitigate the various standard model (SM) background processes that can mimic HNL signals. These include Z/γ^*+jets, W+jets, Vγ^*+jets, QCD, and $t\bar{t}$ processes, which were simulated using the MadGraph (v2.6.5) software, except for the QCD background samples, which were generated using Pythia8.2. In all cases, the hadronisation of gluons and quarks was performed using Pythia8.2, and the detector response was simulated using GEANT4.

The simulated background samples were used to define the event selections and validate the modelling of several observables in simulation compared to data. Additionally, they were used to train the displaced jet tagger in chapter 7, which plays a critical role in distinguishing HNL signals from background events. However, it is important to note that the final background estimation in the signal region is purely data-driven, and the simulated background samples are not used in the final results.

It is expected that some events from the following background processes described below will pass our event selection criteria defined in section 6.2. A detailed definition is given in the following

Z/γ^*+jets contains Z/γ^* events decay to two leptons final state, in addition to the jets originating from ISR/FSR or pileup where one of the jets could overlap with the second lepton.

W+jets contains only W $\rightarrow \ell\ \nu$ plus jets from pileup and ISR/FSR where one of the jets containing a displaced or misreconstructed lepton resulting from heavy flavour quark decay accured during the hadronization process.

Vγ^*+jets contains an inclusive production of Z/γ^* events in addition to prompt photons that can wrongly be reconstructed as a jet.

QCD contains multijet events where several lepton could be produced during the hadronization process, one of the leptons could be isolated and produced outside the jet cone and the second one contained in a jet.

$t\bar{t}$/**single-t** contains $t\bar{t}$ events that decay leptonically or semi-leptonically. Both processes contain additional jets from pileup or ISR/FSR similar to the previously mentioned backgrounds.

Chapter 5

QCD Dynamics, and Pythia Tuning in HNL Analysis

5.1 Introduction

In the realm of Quantum Chromodynamics (QCD), the transition between perturbative and non-perturbative regimes [43] serves as a pivotal cornerstone, influencing the intricate dynamics of strong interactions across a spectrum of energy scales. At energies significantly exceeding the QCD scale, quarks and gluons engage in interactions of weak strength, resembling nearly independent entities amenable to perturbative treatment. This high-energy domain characterizes the perturbative QCD regime. In stark contrast, as energy levels diminish, the strong force intensifies, compelling quarks and gluons to congregate within hadrons through a phenomenon termed color confinement. This confinement instigates the non-perturbative QCD regime, where quarks and gluons are indiscernible as individual entities due to the strong force's overwhelming potency. The delineation between these distinct regimes is embodied by the QCD scale, denoted $_{QCD}$, albeit its value—commonly residing within the realm of several hundred MeV—is subject to theoretical intricacies and renormalization schemes. This transition acquires paramount significance, influencing processes encompassing perturbative and non-perturbative facets of QCD, including the intricate interplay of color interactions, parton showers [56], fragmentation [18], and the formation of jets. Pertinently, in the ambit of our pursuit—the

quest for HNLs—the unique mass ranges of both HNLs and W bosons endow the study with intricacies characterized by this transition, particularly given the distinct QCD physics at play in low and high mass regimes.

An essential tool in this journey is the Pythia event generator version 8.2. Pythia, often employed to simulate particle collisions and decays, is founded on the string model of QCD. This model envisions the strong force between quarks as a kind of 'string' that stretches and breaks, producing the particles observed in detectors. This representation captures aspects of the confinement phenomenon, leading to the formation of color-neutral hadrons from energetic quarks. However, Pythia's string model approximation is most suitable for energy scales that are not extremely high (where perturbative QCD dominates) or extremely low (where non-perturbative QCD and confinement effects dominate), but instead fall in between these two extremes—what we refer to as intermediate energy ranges.

To ensure the accuracy of its predictions, Pythia employs a set of parameters, often referred to as 'tuning parameters,' which control various aspects of the simulation. These parameters influence how particles are produced, decay, and interact within the simulation. The process of tuning involves adjusting these parameters to align the simulation's outputs with experimental data, enhancing the agreement between the two. Given that our focus lies on the HNL search and understanding processes at energies both within and beyond Pythia's standard range, the choice of these parameters and their effects on the simulation's fidelity becomes of paramount importance.

The application of Pythia to our analysis warrants careful consideration and tuning, especially when dealing with energy scales outside its usual range. This accentuates the significance of meticulous appraisal of simulation tools, such as Pythia, to confer faithful representation to the complexities governing hadronization processes.

It is important to note that Pythia8.2's tuning, performed in the energy range from 14 GeV up to 200 GeV, warrants careful consideration when applying it to the specific mass ranges relevant to our analysis. Therefore, this section aims to evaluate the performance of Pythia8.2 event generator in hadronising jets produced at low center of mass (CM) energies. Specifically, the study focuses on the energy range of 1 GeV $< \sqrt{s} <$ 14 GeV to ensure an

accurate simulation of such processes in this energy regime. To achieve this, a comparison is made between the hadronisation properties observed in data from previous experiments and those predicted by the Pythia8.2 event generator. This comparison is crucial as previous CMS studies have not covered the hadronisation process at low CM energies and since the HNL mass range considered in this search is $m_N \in [1, 20]$ GeV. The choice of Pythia8.2 for the study is justified as it is the tool used for hadronising HNL decays in this analysis.

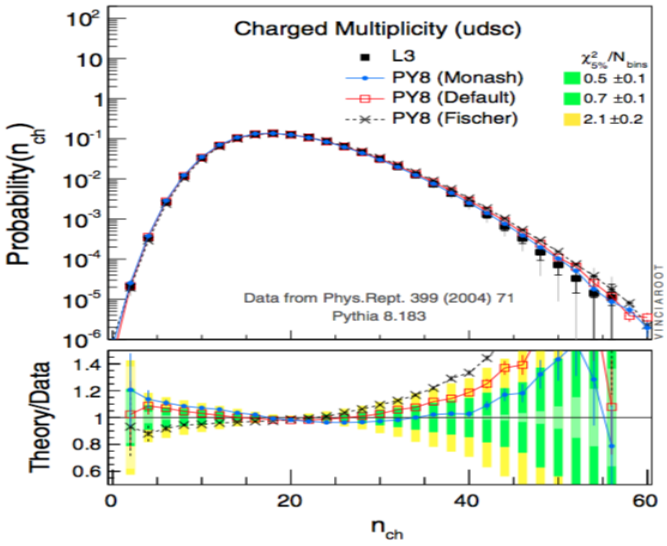

Figure 5.1: Charged particle multiplicity (n_{cp}) distribution for data and simulation with different hadronisation tunes at $\sqrt(s) = 91.2$ GeV [59].

The hadronization tune used in Pythia 8.2 is called the Monash tune [59]. The tuning was performed with data collected at the Z pole ($\sqrt{s} \approx 90$ GeV) from the L3 experiment. The charged particle multiplicity is shown in figure 5.1. To describe the hadronization at different CM energies, an energy scaling was performed with $\sqrt{s} \in [14, 200]$ GeV, where the data was mainly collected from TASSO [22], HRS [42], and TOPAZ [57] measurements. The results are shown in figure 5.2, where a good description of the average charged particle multiplicity $< n_{cp} >$ for the full energy range is observed. No energy scaling is performed below 14 GeV, as discussed previously, and therefore the following study will focus on that region. Note, in the following study n_{cp} and n_{ch} refer to the same quantity.

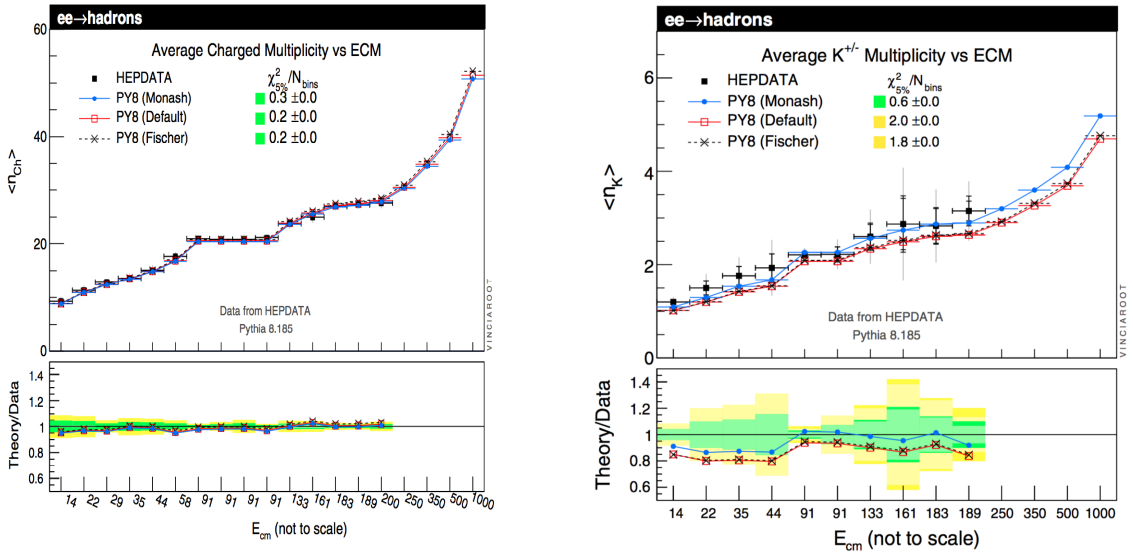

Figure 5.2: Average charged particles multiplicity (n_{cp}) as a function of CM energy for data and several tunes including "Monash" on the (left). Average $K^{\pm}$ multiplicity as a function of CM energy (right) [59].

5.2 Pythia8.2 Monash Tune at Low CM Energies

In this section the hadronisation properties such as $< n_{cp} >$ and particle composition are studied in the low CM energies. A comparison between the properties measured in data and predicted in simulation is performed to assess the validity of the Monash tune in this specific energy region.

5.2.1 Measurements of $< n_{cp} >$ in data

Several experiments, such as ADONE [15] at Frascati, SPEAR at SLAC-LBL, and TASSO [22] and JADE [19] at DESY, have conducted studies on the charged particle multiplicity from e^+e^- annihilation data at various center of mass (CM) energies lower than 14 GeV. The CM energy range below 10 GeV is primarily covered by the SPEAR and ADONE results, where they explored the energy ranges of $[1.5, 3]$ GeV and $[3.67, 7.4]$ GeV, respectively. The results of these studies, after applying all corrections including unfolding, are summarized in figure 5.3. The measured values are fitted using an exponential function [53] to extract essential information about the charged particle multiplicity distribution. The fit function is given in the following

$$< N_{ch} >= a + b \times \exp(c \times \sqrt{(\ln(\frac{S}{\Lambda^2}))})$$

where the parameter values are:

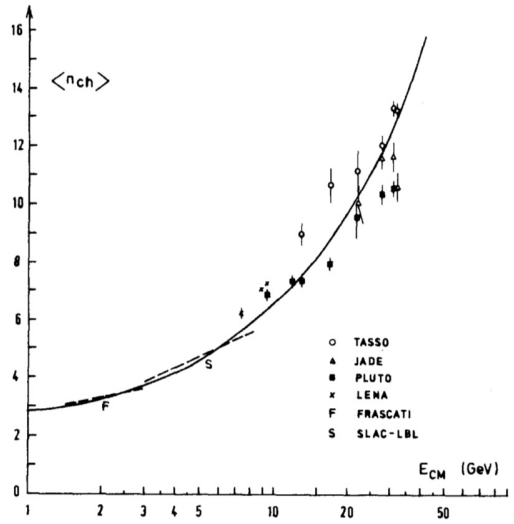

Figure 5.3: The fitted average charged particle multiplicity distribution from past experiments covering CM energy range from 1 to 50 GeV [53].

$$\text{a} = 2.5 \text{ , b} = 0.007 \text{ , c} = 2.4 \text{ , } \Lambda = 0.3 \text{ GeV}$$

5.2.2 Measurements of $< n_{cp} >$ in simulation

To simulate the hadronisation of quarks and gluons, e^+e^- annihilation events were generated using Pythia8.235 for the center of mass (CM) energy values listed in Table 5.1. The CM energies were chosen based on two criteria: first, the CM energy needed to be less than 14 GeV, and second, the values needed to have the smallest systematic and statistical uncertainties. The resulting n_{cp} distributions for the already mentioned CM energies are shown in figure 5.4 where the mean values are considered as $< n_{cp} >$. On the same figure, the $< n_{cp} >$ from CM energy i.e. $\sqrt{s} = 22$ GeV is already covered by the monash tune but we include it in this study to validate the production process. And indeed comparing the resulting $< n_{cp} > = 10.96$ from figure 5.4 to the value from monash tune in figure 5.2 we found a perfect agreement.

Furthermore, HNL events decaying to W^* or Z^* in the hadronic final state where also simulated. The resulting n_{cp} distributions are shown in figure 5.5 where the mean values are used as $< n_{cp} >$ for this study.

Table 5.1: $< n_{cp} >$ from past experiments, their corresponding CM energies and uncertainties.

Experiment	$\sqrt{s}$	$< n_{ch} >$	stat uncert	syst uncert
SLAC-LBL	2.60	3.75	± 0.42	25%
SLAC-LBL	5.10	4.43	± 0.23	25%
LENA	9.3	7.28	± 0.11	10%
TASSO	14	9.08	± 0.05	± 0.25
TASSO	22	11.22	± 0.007	$[\pm 0.25, \pm 0.45]$
JADE	22	10.1	± 0.7	± 0.6

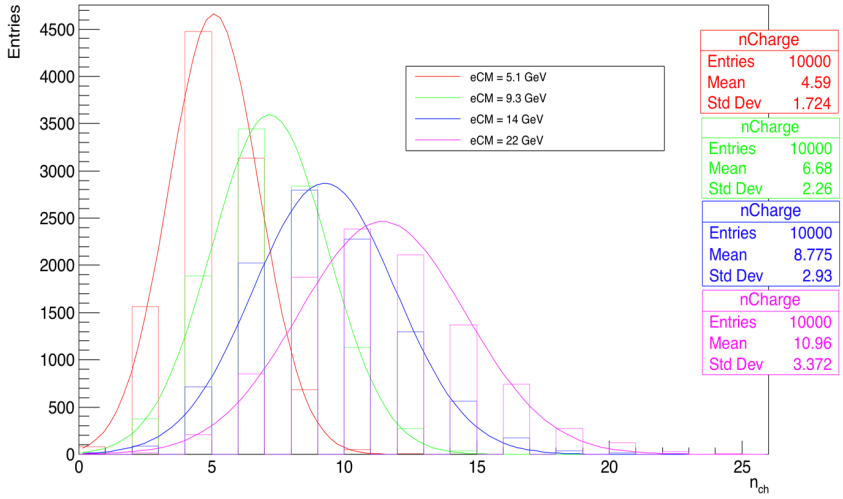

Figure 5.4: Charged particle multiplicity from e^+e^- annihilation events using pythia8 for different CEM values.

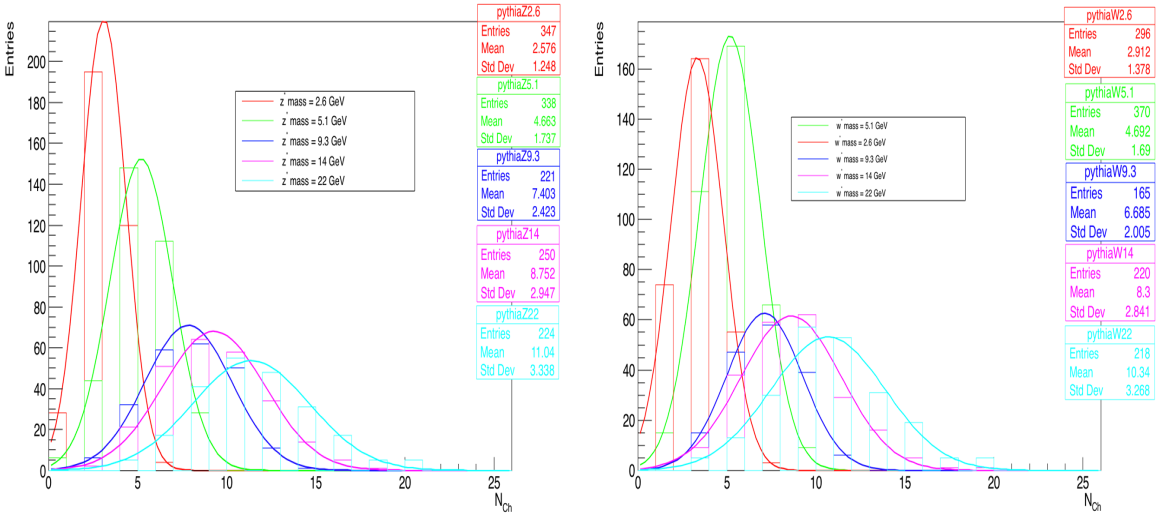

Figure 5.5: Charged particle multiplicity from HNL decaying to W^* or Z^* events using pythia8 for different CM energies.

5.2.3 Comparison of $< n_{cp} >$ measurements from pythia 8.2 and data

The comparison between $< n_{cp} >$ in simulated e^+e^- annhilation events and in data has been performed. The fit function used in figure 5.2 is reproduced. Results are presented in figure 5.6 where it shows a good agreement between data and simulation. To ensure that the average

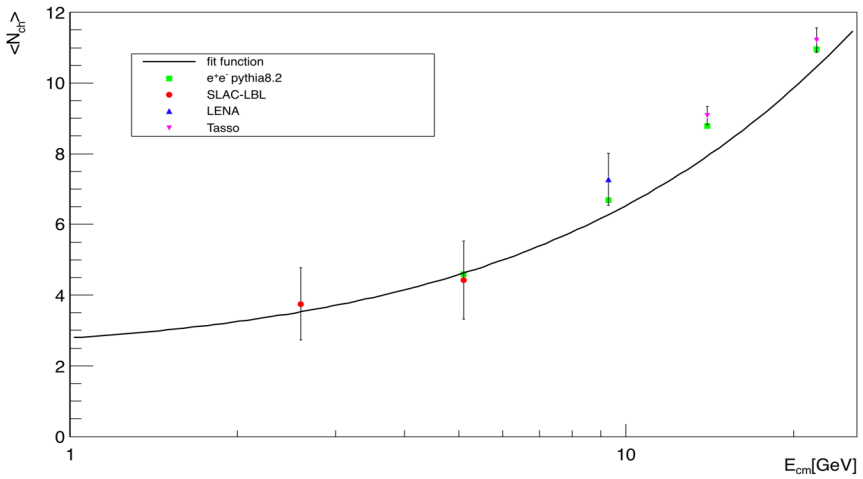

Figure 5.6: Comparison between $n_{cp} >$ measurements in e^+e^- annhilation events in simulation and in data.

number of charged particles produced ($< n_{cp} >$) in HNL signal decays matches experimental data, a comparison was made between $< n_{cp} >$ from e^+e^- annihilation in data and HNL decays producing Z^* and W^* in simulation. While it's not possible to directly compare the $< n_{cp} >$ of e^+e^- to that of W decays due to the different initial charges, the comparison was made to understand the behavior of $< n_{cp} >$ in W decays. Figure 5.7 displays the discussed comparison. Overall the the measured property $< n_{cp} >$ in data and its prediction in simulation has a good agreement.

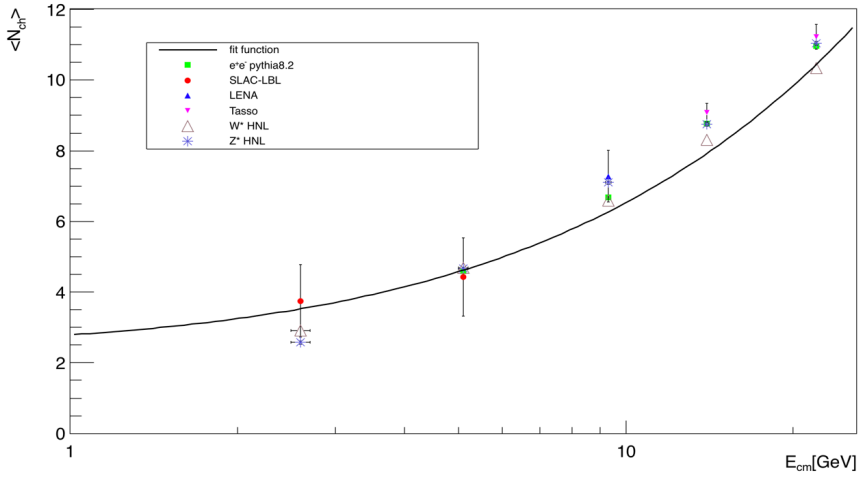

Figure 5.7: Comparison between $< n_{cp} >$ measured in e^+e^- annhilation events in data and HNL decays producing Z^* and W^* in simulation.

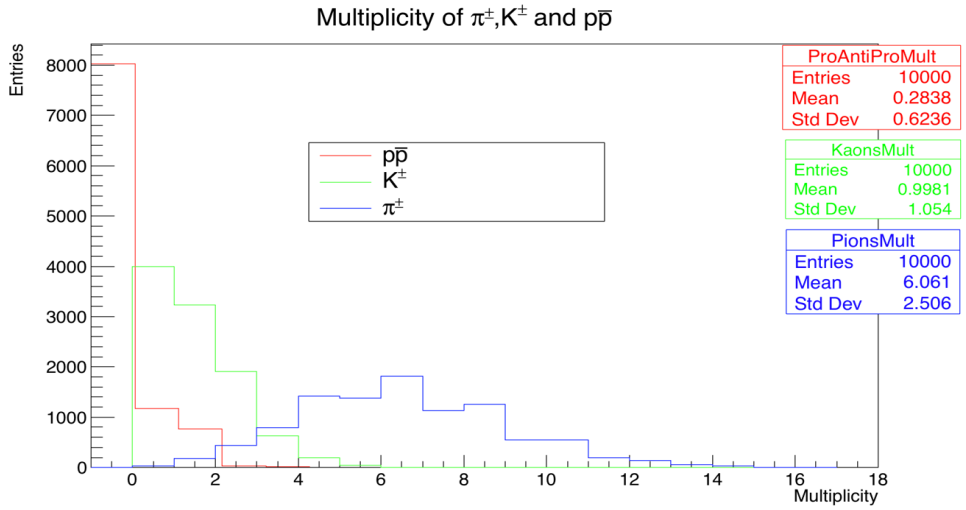

Figure 5.8: Particles composition in e^+e^- annihilation simulated events with Pythia8.2

Table 5.2: e^+e^- event composition from past experiments and two event generators pythia8.2 and HERWIG++.

Particle	Pythia8.2	BABAR	CLEO	ARGUS	HERWIG
$\pi^{\pm}$	6.061	$6.87 \pm 0.11 \pm 0.16$	8.3 ± 0.4	6.38 ± 0.12	6.31
$K^{\pm}$	0.9981	$0.972 \pm 0.012 \pm 0.016.$	1.3 ± 0.2	0.888 ± 0.030	1.01
$p\bar{p}$	0.2838	$0.265 \pm 0.008 \pm 0.002$	0.40 ± 0.06	0.271 ± 0.018	0.46

5.2.4 Particles composition in e^+e^- annihilation events

The aim of this study is to investigate the particle composition in e^+e^- annihilation events at CM energy of $\sqrt{s} = 10.54$ GeV. Figure 5.8 displays the multiplicity of $\pi^{\pm}, k^{\pm}$, and $p\bar{p}$ in the jet, where pions contribute the most, as they are the lightest mesons and thus easier to produce. To compare and summarize the multiplicity of each hadron in the jet, data collected from three experiments (BABAR, CLEO, and ARGUS) and two simulation softwares, Pythia8.2 and Herwig++, are presented in table5.2.

The results of the hadron multiplicity analysis are reasonably accurate. Comparing to the most recent experiment, BABAR, we find a 9% underestimation of $\pi^{\pm}$ and a small overestimation of $p\bar{p}$ by 3%, while the description of $K^{\pm}$ is good.

5.3 Summary

In conclusion, the thorough examination of Pythia's performance in simulating hadronization processes at low center-of-mass energies yields satisfactory results. The small disagreement observed, amounting to less than 10%, reaffirms the reliability of Pythia as a valid tool for event generation in this search. Given this level of agreement, no additional uncertainty considerations are warranted. The successful validation of Pythia's performance underscores its suitability for accurately representing the intricate dynamics of our analysis, contributing to the robustness of our results

Chapter 6

Analysis strategy

6.1 Introduction

In the analysis, events with two leptons ($\mu\mu$, ee , μe , eμ) and at least one jet in the final state are analysed. The closest jet to the ℓ_2 is selected as the HNL jet and denoted as j*. The ℓ_2 and j* can have two topologies: boosted or resolved for $\Delta R(\ell_2, j^\star) < 0.4$ and $0.4 < \Delta R(\ell_2, j^\star) < 1.3$ respectively. In this chapter the strategy of the analysis is presented: the object selections, the definition of signal and control regions, the applied corrections to simulation and the events categorisation.

6.2 Objects selection for HNL search

In this search HNL events contain two leptons and a jet in the final state denoted ℓ_1, ℓ_2 and j* respectively where ℓ_1 and ℓ_2 can be an electron or a muon. The object selection given in the following is optimised to find HNL objects. First, the primary vertex has to satisfy standard requirements detailed in section 3.3. The first lepton produced from the W boson on-shell decays can be either a muon or electron and must be originating from the primary vertex. A muon candidate has to be trigger matched and must pass tight ID and tight isolation ($I^{\mu}_{\text{rel.}} < 15\%$) requirements. Due to the trigger threshold, the p_T of the tight muon candidate has to be greater than 26, 29,26 GeV for the years 2016, 2017, and 2018 respectively.

An electron candidate has to be also trigger matched and must satisfy tight ID and tight isolation ($I^{e}_{\text{rel.}} < 15\%$). For a similar reason, the p_T has to be greater than 29(34) GeV for the years 2016, (2017, and 2018).
These tight criterias are applied to the first lepton ℓ_1 to suppress the background mainly from multijet QCD events while keeping the signal efficiency rather high. Furthermore, muons and electrons are required to be in the tracker acceptance $|\eta| < 2.4$ to ensure the track is reconstructed.
The second lepton ℓ_2, produced from the HNL decays, can also be either muon or electron. The ID and isolation requirements on the ℓ_2 are relaxed compared to ℓ_1. This is because ℓ_2 has lower p_T and looser isolation than ℓ_1.

The ℓ_2 muon candidates are required to pass loose muon ID cut and have $p_T > 3$ GeV for all the three years of data taken. This is the minimum p_T threshold for muon to be reconstructed as global muon. No special requirement for the isolation are required.
Similar to muons, electron candidates have to satisfy a modified loose cut based ID where the isolation requirement and the reconstruction minimum number of missed hits are removed, as discussed in section 3.8. The electron has to satisfy $p_T > 5$ GeV and $|\eta| < 2.4$.
The ℓ_2 reconstruction and identification efficiencies are shown in figure 6.1. For muons, the main efficiency loss is due to the reconstruction efficiency at high displacement values while the ID requirement does not affect the signal efficiency much. For electrons, the reconstruction and identification efficiencies both drop for a high displacement.

The HNL jet candidate j* is chosen to be the closest to the ℓ_2 in ΔR. For low mass HNLs, the decay products are boosted and the ℓ_2 is mostly found inside the jet cone of $\Delta R < 0.4$ (boosted scenario). For high HNL mass, the decay products are less boosted and the fraction of resolved events becomes more important. In this case, the ℓ_2 is found inside of the jet cone of $0.4 < R < 1.3$ (resolved scenario). The j* p_T is found to be higher in boosted events compared to resolved ones because of the presence of the ℓ_2 inside the jet as discussed in section 4.3.2. Jets j* are then required to have $p_T > 30(20)$ GeV for boosted(resolved) events.

Lepton with $p_T > 15$ GeV can be reconstructed by mistake as standalone jet by the PF

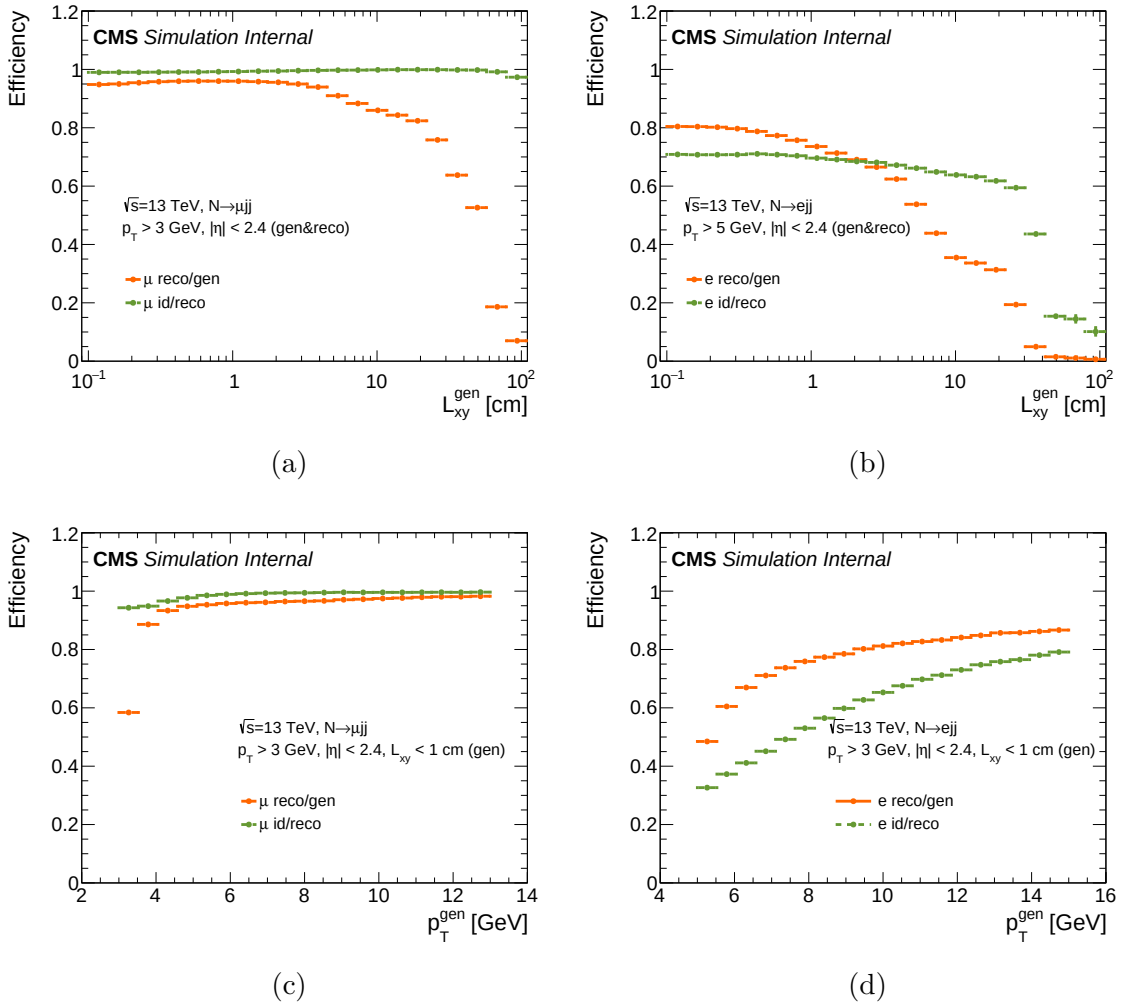

Figure 6.1: Muon (left) and electron (right) ($\ell_2 = \mu, e$) reconstruction and identification efficiency as a function of generator-level lab frame displacement (top) and generator-level p_T (bottom) [28].

algorithm. To avoid having events with ℓ_2 double counted as lepton and a jet the following requirements are applied. If ΔR < 0.4, ℓ_2 has to be non isolated e.g ($I^{\mu}_{\text{rel.}} > 15\%$) and the jet has to satisfy $p_T > 30$ GeV (boosted scenario). If one of the requirement is not satisfied, the closest jet in ΔR is not selected and the second closest jet to the ℓ_2 in ΔR is selected instead if it satisfies $p_T > 20$ GeV (resolved scenario) and no requirement on the ℓ_2 isolation is applied in this case since it reduces strongly the signal efficiency. The ΔR distributions before(left) and after(right) applying the jet overlap removal for signal boosted jets are shown in figure 6.2. Finally, the selected j* must be in the tracker acceptance within $|\eta| < 2.4$. Jet p_T distribution for signal events can have lower values than 30 GeV. At the beginning of this analysis, a lower threshold on the jet p_T (> 10 GeV) was considered to maximise signal efficiency. A significance

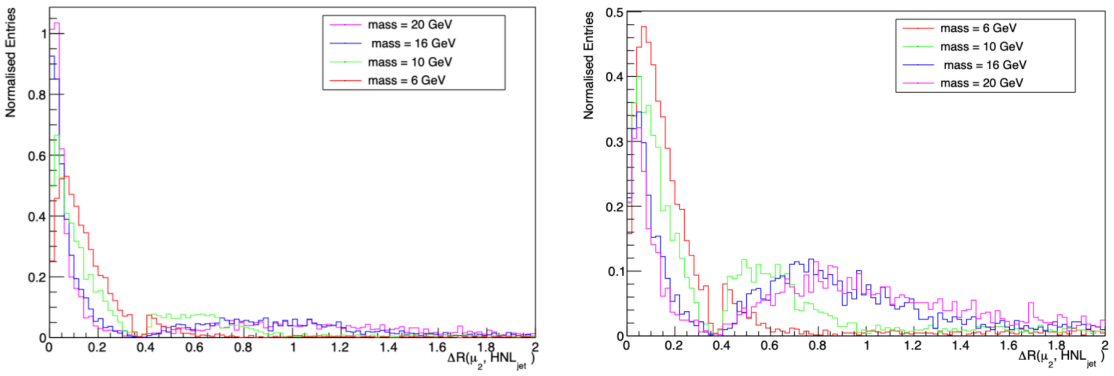

(a) (b)

Figure 6.2: $\Delta R(\ell_2, \mathrm{j}^\star)$ distributions for signal events (a) before and (b) after applying the jet overlap removal.

scan as a function of p_T shows no gain using a lower p_T threshold than 30 GeV due to the high background from pileup low p_T processes such as multijet QCD. Furthermore, to avoid unnecessary problems from pile-up contamination and miscalibrated jets the p_T threshold was chosen to be 30 (20) GeV for boosted(resolved) jet instead.

The non isolation requirement is only applied to ℓ_2 for events with boosted decay products. Figure 6.3 shows the fraction of non isolated ℓ_2 in resolved categories ≈60(30) % of the $\mu_2(e_2)$ are non isolated.

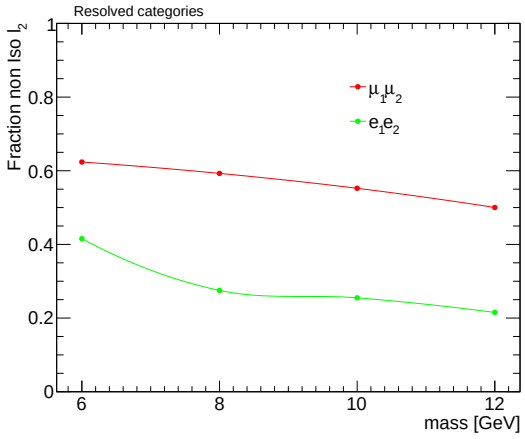

(a)

Figure 6.3: Fraction of non isolated ℓ_2 in resolved event.

6.3 Signal Region (SR)

Only signal events with two leptons and at least one jet are analysed. Therefore, events with exactly 2 leptons (ℓ_1, ℓ_2) are selected where ℓ_1 p_T must be larger than ℓ_2 p_T. The two leptons must satisfy requirements mentioned in section 6.2. Distributions of reconstructed kinematic variables for background simulation and two benchmark signal samples are shown in figure 6.4 and 6.5.

The number of jets in the events can be more than one, due to the hadronization of underlying events and pileup. Therefore the number of jets is required to be at least one but less than 5 to avoid unnecessary loss of signal efficiency while rejecting background from $t\bar{t}$ and multijet QCD events. An additional cut to the $\Delta R(\ell_2, \mathrm{j}^\star) < 1.3$ is imposed to reduce background for the resolved events scenario, see figures 6.4(b) and 6.5(b).

All objects in signal events are required to be reconstructed. Therefore no p_T^{miss} is expected for signal events. However due to the poor p_T^{miss} resolution a loose cut on $p_T^{\mathrm{miss}} < 60$ GeV is applied see figure 6.4(a). This cut reduces significantly the contamination from W+jets and $t\bar{t}$ backgrounds. In addition all events must pass the p_T^{miss} filter discussed in section 3.9.

To reject Z/γ^*+jets background events mainly for same lepton flavor signal events $m(\ell_1$, $\ell_2)$ is required to be less than 80 GeV. This cut removes the Z pole events that peak at 90 GeV while keeping the signal efficiency unchanged. A cut on the m(ℓ_1 , ℓ_2) to be greater than 20 GeV is applied. This additional cut has also no effect on signal efficiency while rejecting substantially multijet QCD background and low mass resonances see figure 6.4(e).

An additional cut, in principle, on $m(\ell_1, \ell_2, \mathrm{j}^\star)$ can be applied to significantly reduce background from different SM processes as it is a good observable to descriminate signal from background. However, the $m(\ell_1, \ell_2, \mathrm{j}^\star)$ variable is only for the background estimation study using an ABCD method, see section 8 therefore no initial cut has been applied to it here. All preselections are summarized in table 6.1

The above selections have been studied to keep signal events with high efficiency while rejecting an important fraction of the background. Inverted SR selections are also used to define control regions as discussed in the next paragraph.

Table 6.1: Overview of selection requirements in signal and control regions for the dilepton categories. The tight lepton requirements are shown per year of data-taking.

	Signal region	high $M(\ell_1, \ell_2)$ CR (ie. DY CR)	Resolved CR
Lepton selection			
Tight, isolated lepton (ℓ_1) Muon: $p_T > 26,\ 29,\ 26, \lvert\eta\rvert < 2.4$ Electron: $p_T > 29,\ 34,\ 34, \lvert\eta\rvert < 2.4$	✓	✓	✓
Loose lepton (ℓ_2) Muon: $p_T > 3, \lvert\eta\rvert < 2.4$ Electron: $p_T > 5, \lvert\eta\rvert < 2.4$	✓	✓	✓
$p_T(\ell_1) > p_T(\ell_2)$	✓	✓	✓
Third lepton veto	✓	✓	✓
Jet selection			
Jets w/leptons ($p_T > 30, I^{\ell_2}_{\text{rel}} > 0.15, \lvert\eta\rvert < 2.4$)	✓	✓	✓
Resolved jets ($p_T > 20, \lvert\eta\rvert < 2.4$)	✓	✓	✓
$N_{\text{jet}} < 5$	✓	✓	✓
Event observables			
< 60	✓	✓	✓
filter	✓	✓	✓
$\min \Delta R(\ell_2, \text{jets}) < 1.3$	✓	✓	inverted
$m(\ell\ell) > 20$	✓	✓	✓
$m(\ell\ell) < 80$	✓	inverted	✓

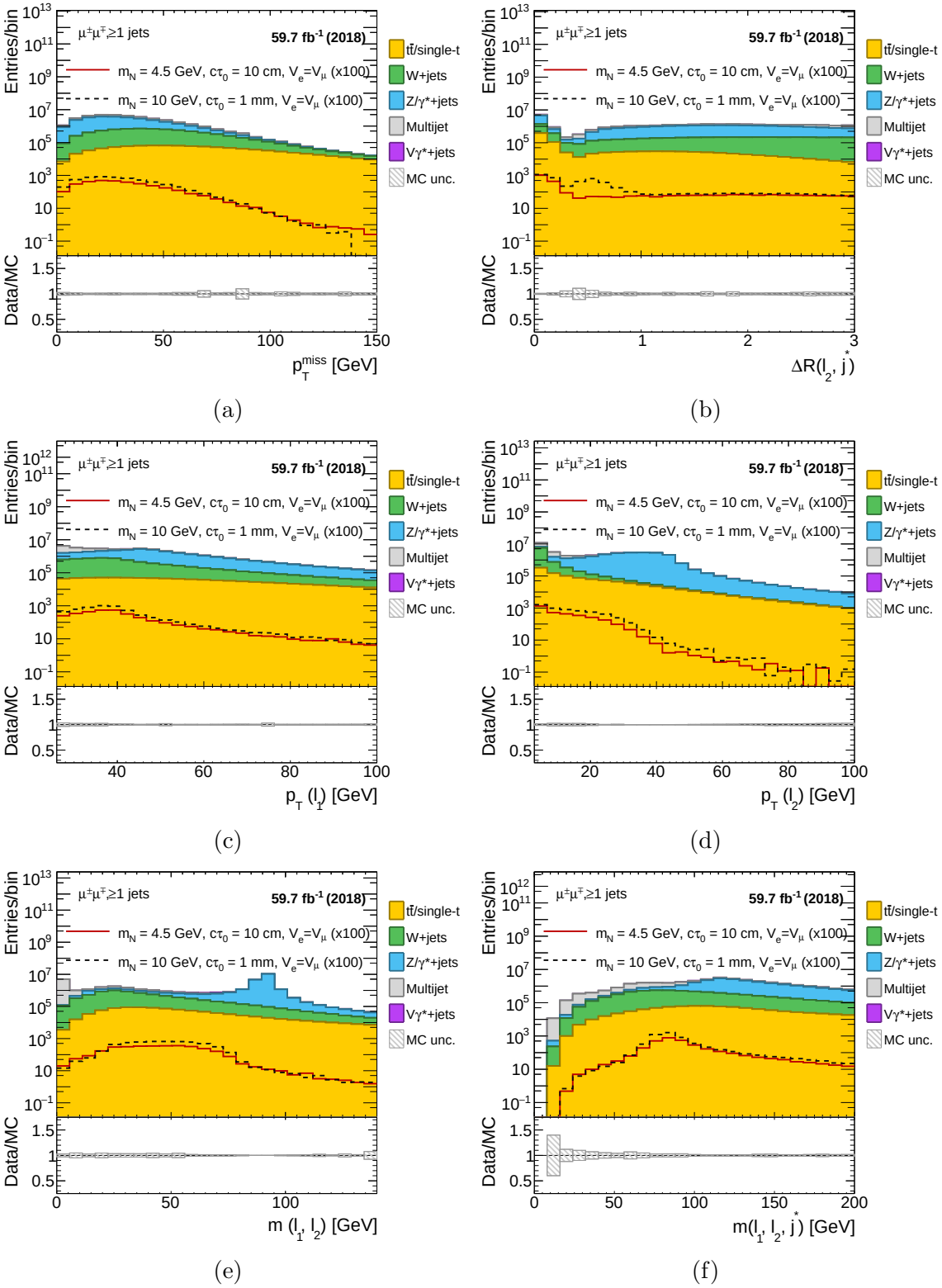

Figure 6.4: Distributions of reconstructed quantities for OS $\mu\mu$ final state background and signal events ($m_{\mathrm{N}} = 4.5$, $c\tau_0 = 100$, $V_e = V_\mu$) and ($m_{\mathrm{N}} = 10$, $c\tau_0 = 10$, $V_e = V_\mu$). The distributions are shown for p_T^{miss}, $\min \Delta R(\ell_2, \mathrm{jets})$, ℓ_1 p_T, ℓ_2 p_T, $m(\ell_1, \ell_2)$ and $m(\ell_1, \ell_2, \mathrm{j}^\star)$(simulation only).

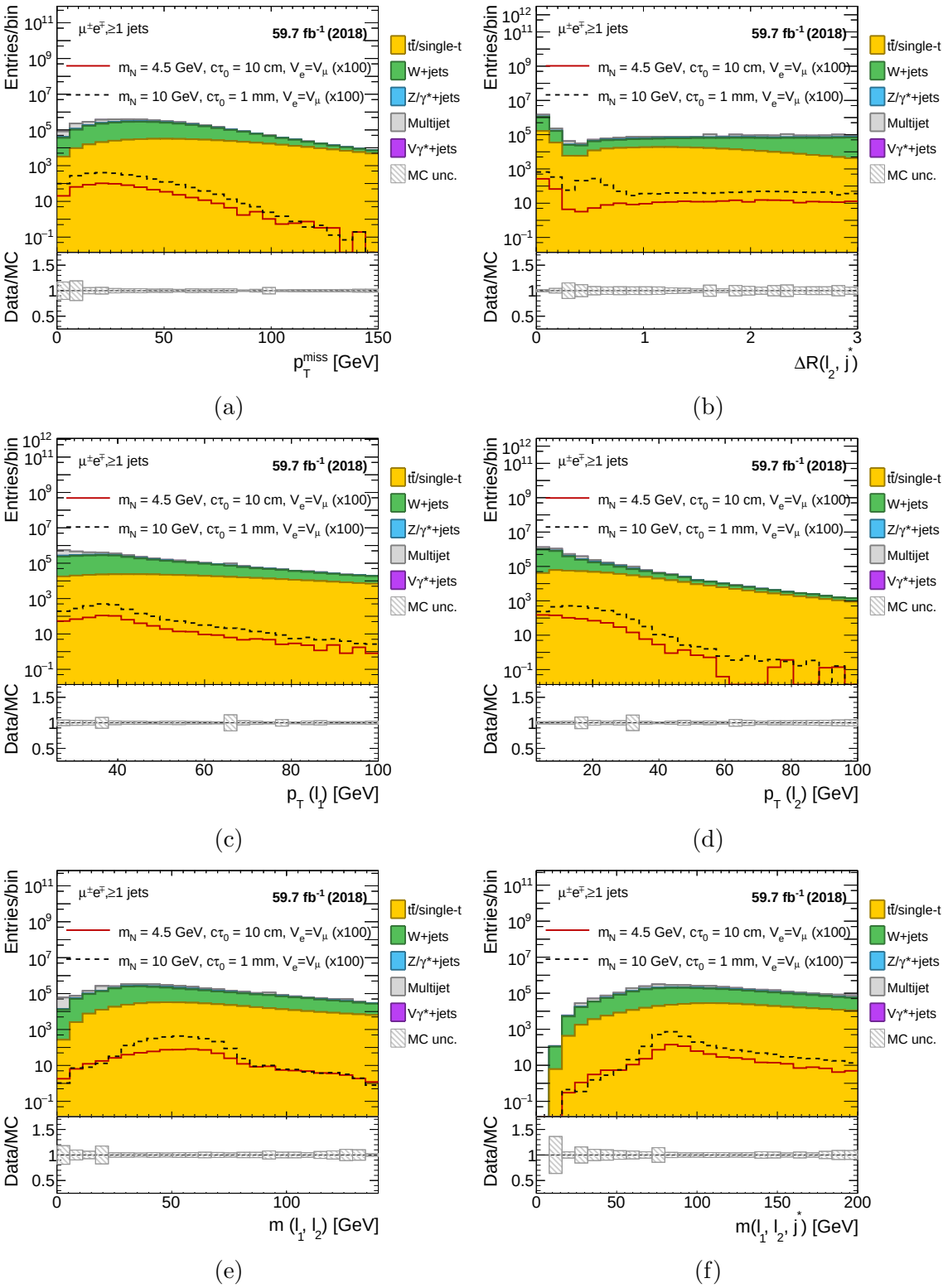

Figure 6.5: Distributions of reconstructed quantities for OS μe final state background and signal events ($m_{\mathrm{N}} = 4.5$, $c\tau_0 = 100$, $V_e = V_\mu$) and ($m_{\mathrm{N}} = 10$, $c\tau_0 = 10$, $V_e = V_\mu$). The distributions are shown for p_T^{miss}, $\min \Delta R(\ell_2, \mathrm{jets})$, ℓ_1 p_T, ℓ_2 p_T, $m(\ell_1, \ell_2)$ and $m(\ell_1, \ell_2, \mathrm{j}^\star)$(simulation only).

6.4 Control Regions (CRs)

The control regions are mainly used to inspect the modeling of the objects kinematics used for this search. CRs are made to be orthogonal to the SR by inverting at least one of the selections. The main background contribution in the signal region is estimated from data rather than MC but it is still necessary to have a good agreement between data and simulation as this ensures the good modeling of the objects in signal events. Corrections to the used objects in MC are derived using these CRs to cover any observed disagreement between data and MC. These corrections are finally applied to the signal events. Various control regions have been defined for different purposes as follows:

High dilepton mass region is defined by requiring the m(ℓ_1 , ℓ_2) to be greater than 80 GeV. This region is dominated by Z/γ^*+jets process in case of same flavor dilepton events and by QCD process in case of different flavor dilepton events. This region is used to inspect the agreement between data and MC for the main kinematic distributions for the Z/γ^*+jets background in boosted and resolved event scenario as shown in figures 6.6, 6.7, 6.8 and 6.9.

$t\bar{t}$**/single-t region** is defined by requiring ℓ_1 to be reconstructed and passing all criteria mentioned in section 6.2. No requirement on ℓ_2 to be reconstructed and identified, (total number of leptons >= 1), in addition to $p_T^{\text{miss}} > 100$ GeV and $H_T > 150$ GeV, number of jets >= 3 and at least one secondary vertex in the jet. This CR is used to derive displaced track and displaced tagger efficiencies SFs detailed in section 6.5

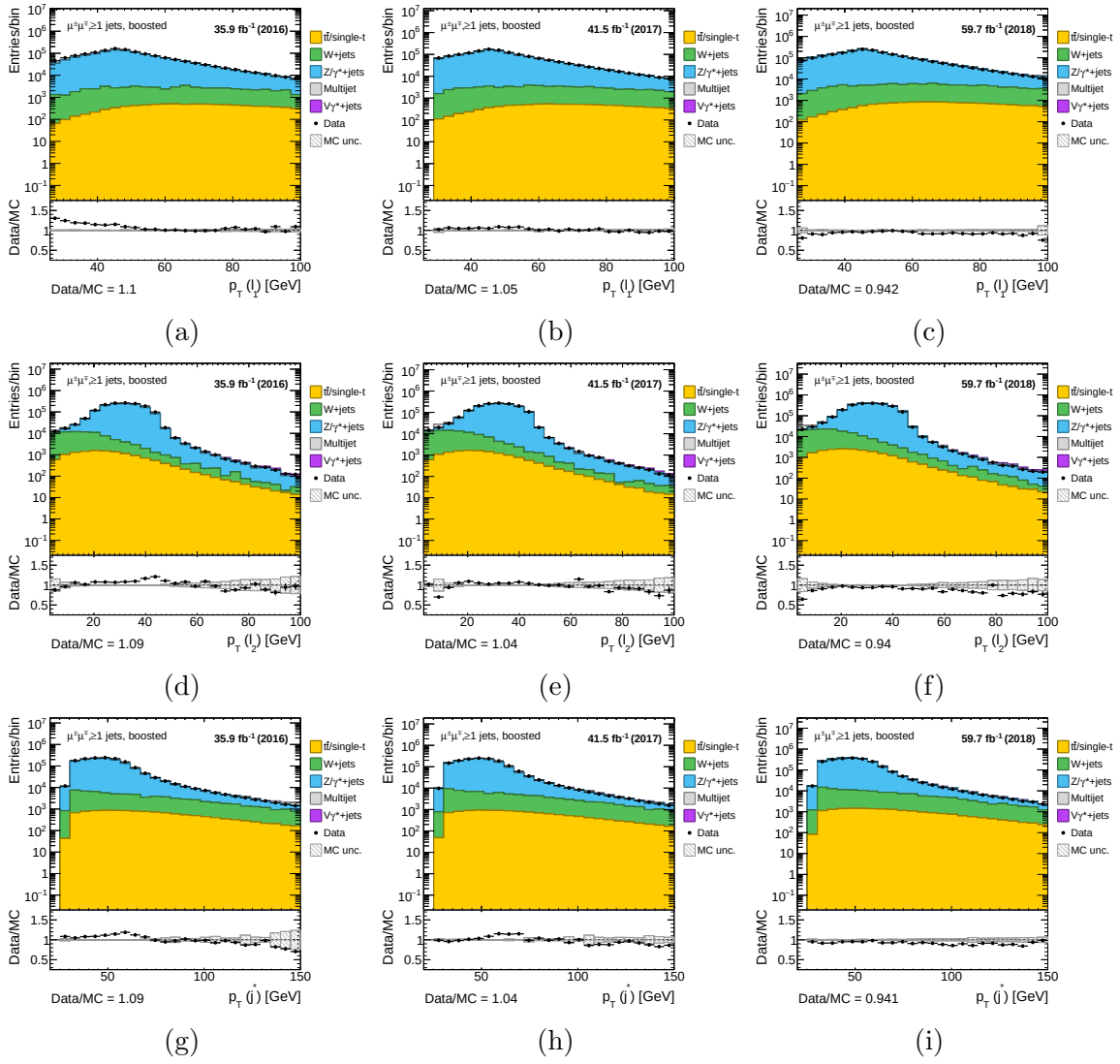

Figure 6.6: Modelling of reconstructed quantities for OS $\mu\mu$ boosted final state events in high dilepton mass CR for 2016, 2017 and 2018 on the left, middle and right respectively. The distributions are shown for ℓ_1 p_T, ℓ_2 p_T and $p_T(\mathrm{j}^\star)$(data and simulation).

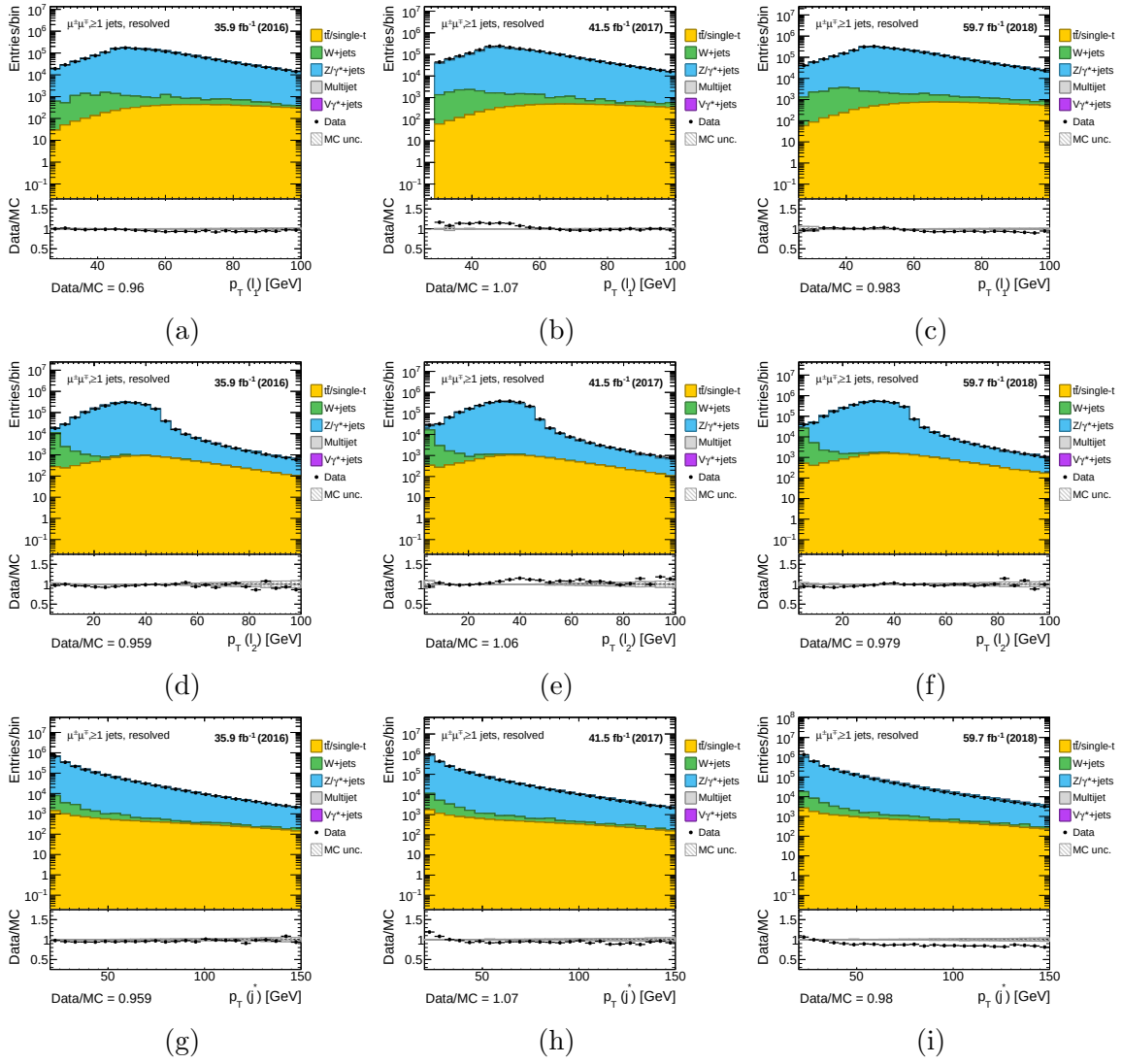

Figure 6.7: Modelling of reconstructed quantities for OS $\mu\mu$ resolved final state events in high dilepton mass CR for 2016, 2017 and 2018 on the left, middle and right respectively. The distributions are shown for ℓ_1 p_T, ℓ_2 p_T and p_T(j*)(data and simulation).

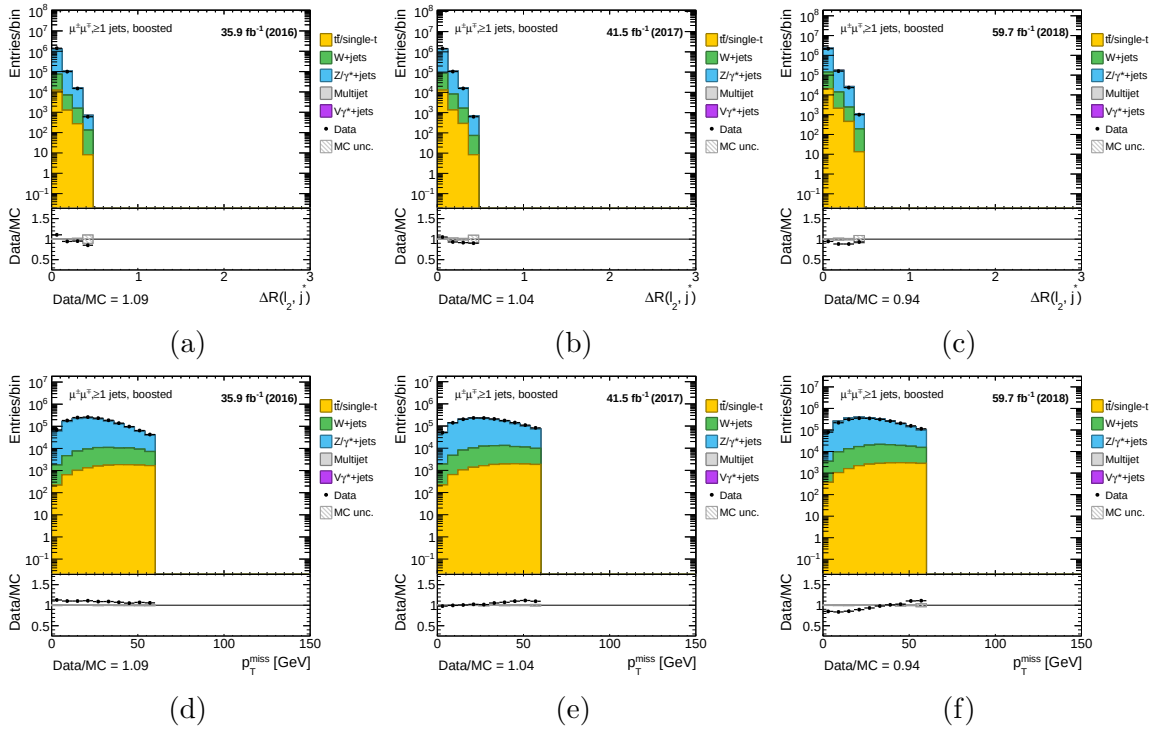

Figure 6.8: Modelling of reconstructed quantities for OS $\mu\mu$ boosted final state events in high dilepton mass CR for 2016, 2017 and 2018 on the left, middle and right respectively. The distributions are shown p_T^{miss} and $\min \Delta R(\ell_2, \text{jets})$(data and simulation).

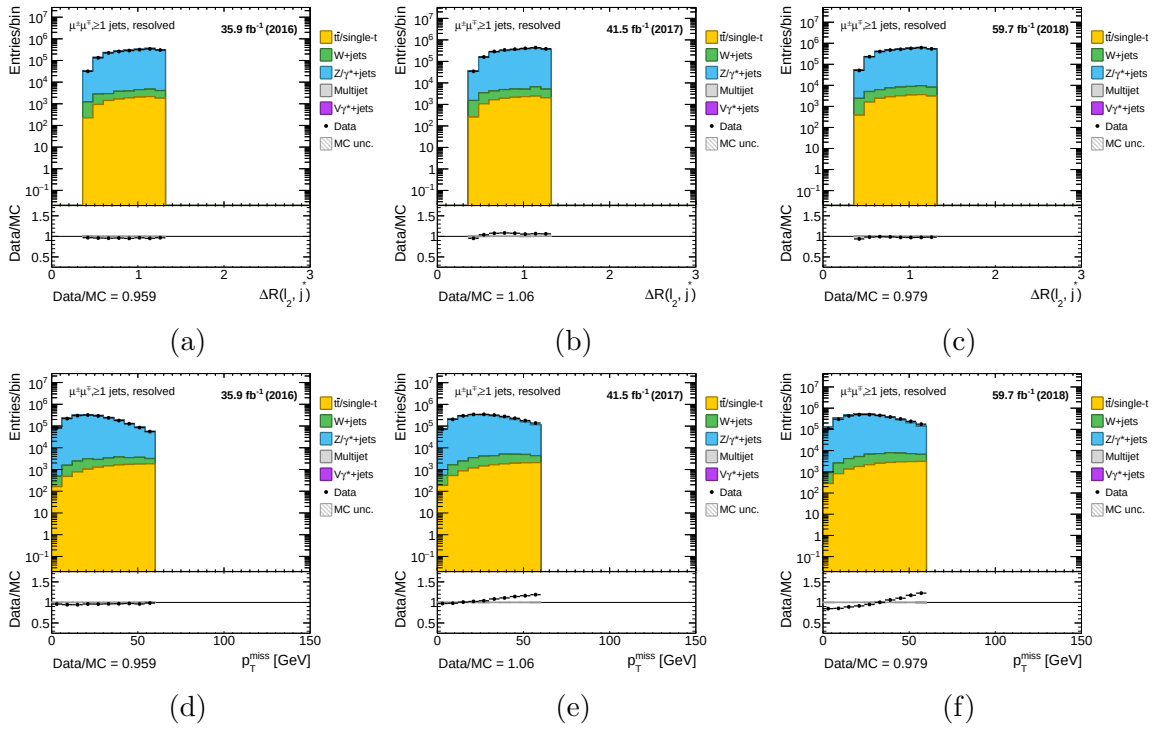

Figure 6.9: Modelling of reconstructed quantities for OS $\mu\mu$ resolved final state events in high dilepton mass CR for 2016, 2017 and 2018 on the left, middle and right respectively. The distributions are shown for p_T^{miss} and $\min \Delta R(\ell_2, \text{jets})$(data and simulation).

6.5 Corrections to simulation

Differences between data and MC in the modeling of event objects can arise from a variety of sources, including inaccuracies in the detector response and the simulation of physics processes such as the p_T spectrum of top quarks. For this analysis, the detector response is particularly relevant since the background will be estimated purely from data. To mitigate the impact of these differences, we applied several corrections to the simulated signal events.

Some of these corrections are common to many physics analyses, such as pile-up reweighting, jet energy corrections, and prompt lepton scale factors (SFs). These corrections are provided centrally by CMS physics object groups (POGs). However, additional corrections were necessary for our analysis, which made use of specific objects such as displaced leptons. The determination of these corrections was the responsibility of the analysis team.

The corrections were applied to the simulated signal events to ensure that they closely resembled data in terms of relevant observables. This allowed us to improve the accuracy of our final results. The specific corrections used in this analysis are discussed in detail below.

6.5.1 Pileup reweighting

The distribution of pileup interactions in simulation for both signal and background events are reweighted to match the one in data following the instantaneous luminosity of the data taken where it is determined by multiplying the measured instantaneous luminosity per bunch crossing by the p-p interaction's inelastic cross section. Pileup reweighting scale factors (SFs) are computed by dividing the distribution number of interactions in simulation by the one in data. These SFs are then applied to the simulated events as corrections.

6.5.2 Jet energy corrections

Jet energy corrections are applied to the reconstructed jets to account for detector effects and to ensure that the energy measurements of the jets are as accurate as possible. The corrections are applied in several steps, beginning with a set of "L1 corrections" that correct for effects due to the detector geometry and readout electronics. These corrections are followed by "L2

corrections," which correct for the differences in the energy response of jets as a function of their direction, and "L3 corrections," which correct for the differences in the energy response of jets as a function of their transverse momentum [26] [50].The distribution of jet energy resolution is further corrected in simulation to match the one in data.

6.5.3 Prompt leptons trigger, identification and isolation efficiency

The efficiency for prompt leptons, muons or electrons, to pass the trigger, isolation or identification requirements is different when measured in data and simulated in monte carlo. This difference is corrected by the use of scale factors p_T and η dependent determined using tag and probe method, a data driven technique to measure the efficiency of specific process [40], provided centrally.

6.5.4 Displaced Track reconstruction efficiency

The track reconstruction efficiency in data and simulation are centrally provided by the tracking POG for prompt tracks that are typically associated with the primary vertex. For displaced tracks, originating from displaced decays, the reconstruction efficiencies are instead not available and have to be determined for this analysis. Therefore the displaced track efficiency is calculated as a function of the two dimentional displacement from the primary vertex i.e. d_{xy} [cm] and scale factors are then derived and applied as correction to simulation. A $t\bar{t}$ enriched control region is defined to derive these SFs. The $t\bar{t}$ CR is populated by real displaced tracks originating from B mesons decay where the contamination from misreconstructed events originating from QCD and W+jets is minor. The $t\bar{t}$ CR is defined below. The correction is derived only by selecting charged PF jet constituents that are matched to a secondary vertex to further ensure that tracks are genuinely displaced and do not originate from misreconstruction effects.

The $t\bar{t}$/single-t region is defined by requiring the prompt ℓ_1 matched to the trigger. There is no requirement on the presence of a ℓ_2 i.e. total number of leptons ≥ 1), in addition to $p_T^{\text{miss}} > 100$, $H_T > 150$ and number of jets ≥ 3.

The agreement between data and simulation as a function of the d_{xy}, is shown in Fig. 6.10

for the three years of data taking in the electron and muon channels separately. The final correction is derived from this difference by combining the two channels which helps to increase the statistical precision in the displaced bins. To remove any mismodeling due to an incorrect

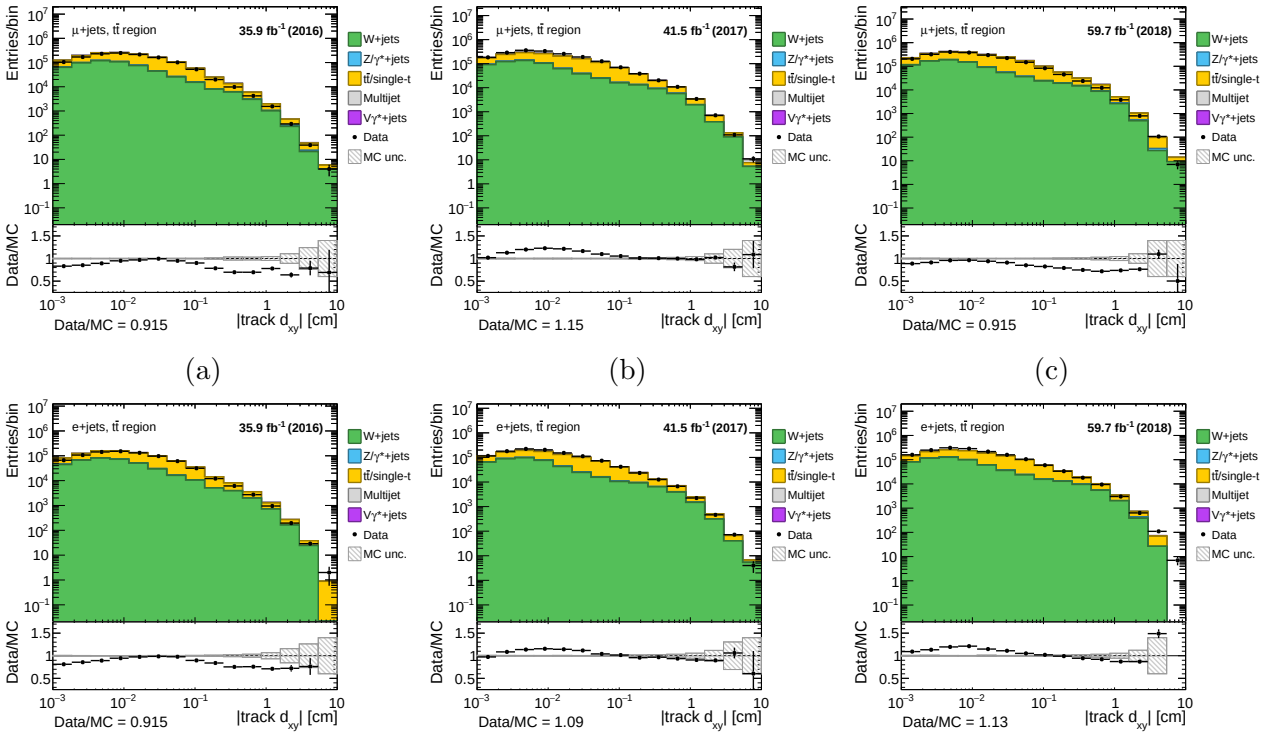

(a) (b) (c)

(d) (e) (f)

Figure 6.10: data monte carlo agreement for track d_{xy} for the three years of data taking

normalization of the simulated samples, a binned maximum likelihood fit to data using templates of $t\bar{t}$ and W+jets from simulation has been performed based on the leading track d_{xy} distribution. The fitted fractions per process with respect to data are shown in Table 6.2. The dominant contribution is $t\bar{t}$ while the fraction of W+jets contribution increases in 2017 and 2018 compared to 2016. This is caused by the higher pileup contribution in these years.

Table 6.2: The fitted fractions of $t\bar{t}$ and W+jets events with respect to data for muon and electron events per year of data taking.

	2016(%)	2017(%)	2018(%)
$t\bar{t}$ (muon region)	67.09 ± 0.39	57.17 ± 0.28	52.77 ± 0.25
W+jets (muon region)	32.90 ± 0.37	42.82 ± 0.28	47.22 ± 0.25
$t\bar{t}$ (electron region)	69.01 ± 0.33	59.56± 0.23	56.23 ± 0.21
W+jets (electron region)	30.98 ± 0.34	40.43± 0.22	43.76 ± 0.19

The displaced track reconstruction SFs are derived per year from the ratio between data and

simulation after the $t\bar{t}$ and W+jets templates are normalized to the fit result. The resulting SFs are shown in Fig. 6.11 where the SFs after normalization correction (distribution in red) are used for the final results of the analysis. In general, the corrections are found to be less than 10% for prompt like tracks below $d_{xy} = 0.1$ and between 10–20% for larger displacements. More details are given in the next paragraphs.

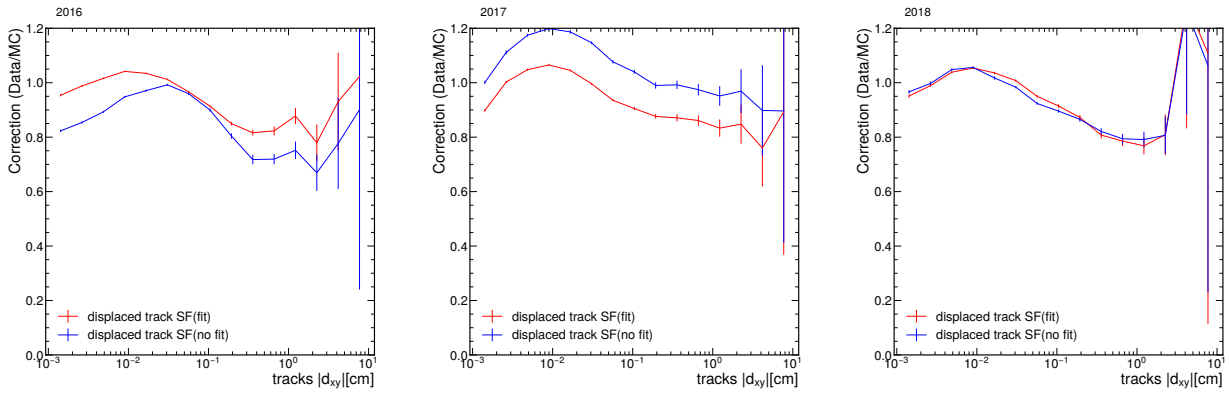

(a) (b) (c)

Figure 6.11: Displaced Track reconstruction scale factors for the year 2016, 2017 and 2018 before and after the fit.

During the 2016 data-taking period, due to high energy deposition in the strip sensors, a saturation of the APV25 front-end chip (the readout sensors of the tracker) happened occasionally and lead to a significant dead-time in the detector readout system. One of the reasons leading to the high energy deposition in the silicon sensors is the inelastic interactions between Highly Ionizing Particles(HIP) i.e hadrons and the nuclei of the sensors. Therefore, when a HIP crosses the strip tracker, the associated APVs can be saturated and no data is read out for a period of 700 ns. The data-taking period during 2016 is devided into periods B,C , D, E, F and G. The affected data period by HIP promblems is from Run B to Run F corresponds to 19.8 fb^{-1} of integrated luminosity. The issue was resolved for the Run G and H.

To check the impact of HIPs on the displaced track reconstruction SFs a dedicated study has been performed. Figure 6.12 shows the SFs values as a function of $|d_{xy}|$ for 2016 for the HIP and post-HIP period. The corrections are significantly different between the two periods namely is 60%(10%) at higher displacement for HIP(post-HIP) periods. The average values at high displacement for the overall 2016 period are $\approx 20\%$.

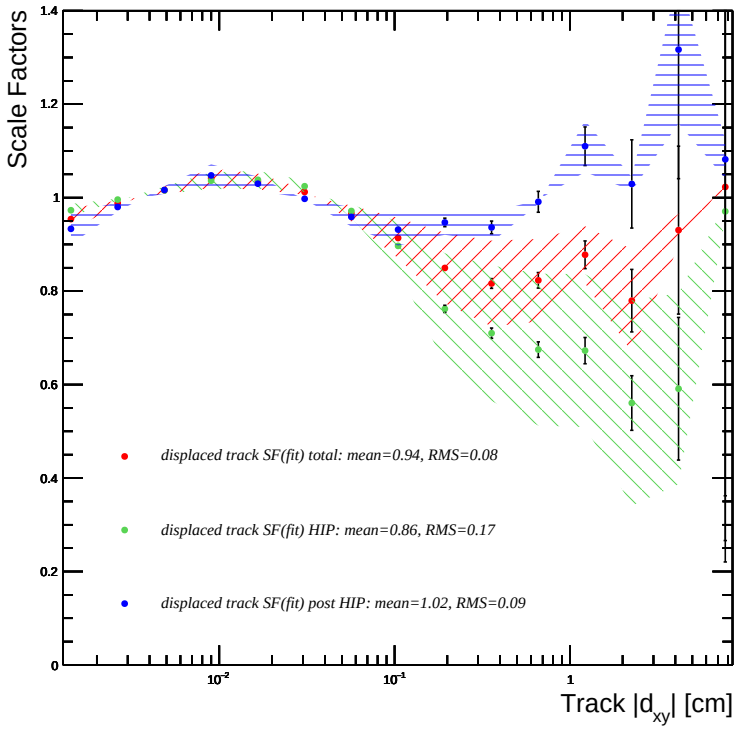

(a)

Figure 6.12: Displaced track reconstruction scale factors for the year 2016 during the HIP, post-HIP and combined periods.

Figure 6.13(a), shows the comparison of the SFs for the 2016 post HIP, 2017, and 2018 data-taking period. It demonstrates that the SFs degrade as a function of the purity of the $t\bar{t}$ CR, see Table 6.2. Figure 6.13(b) shows the comparison of the SFs for the total 2016, 2017, and 2018 data-taking periods where the Final SFs values are found to be similar despite the HIP effect in 2016.

The derived displaced track reconstruction SFs are applied as a correction for resolved events and parametrized as a function of the ℓ_2 displacement. Additionally, the displaced jet tagging efficiency is corrected for resolved events by deriving a corresponding correction from the displaced track SFs as a function of the three most displaced tracks within the HNL jet. In the case of boosted events, no correction is applied explicitly to ℓ_2 and only the displaced jet tagging efficiency is corrected as described in Section 6.5.5 to avoid applying this correction twice. From the corrected distribution we consider half the difference with respect to no correction as a systematic uncertainty, discussed later.

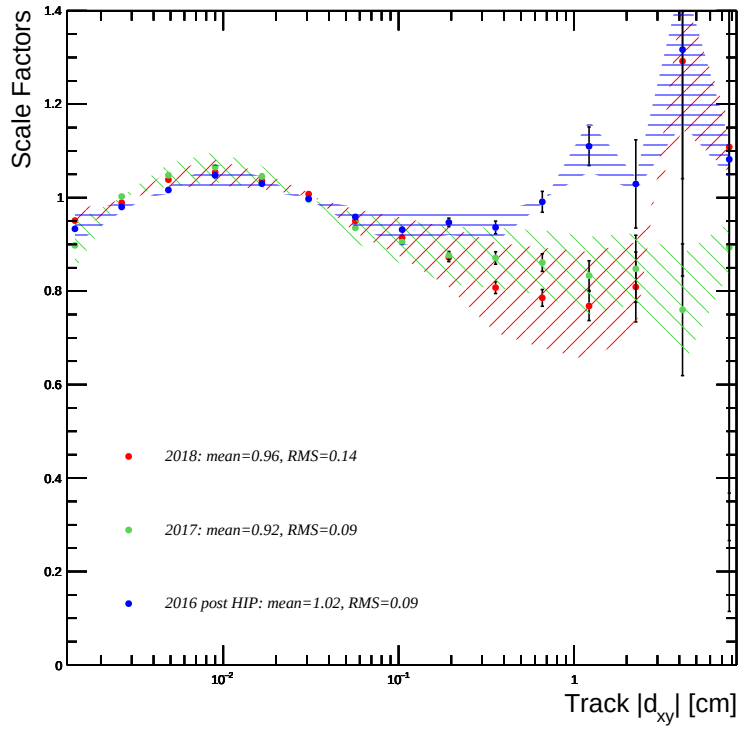

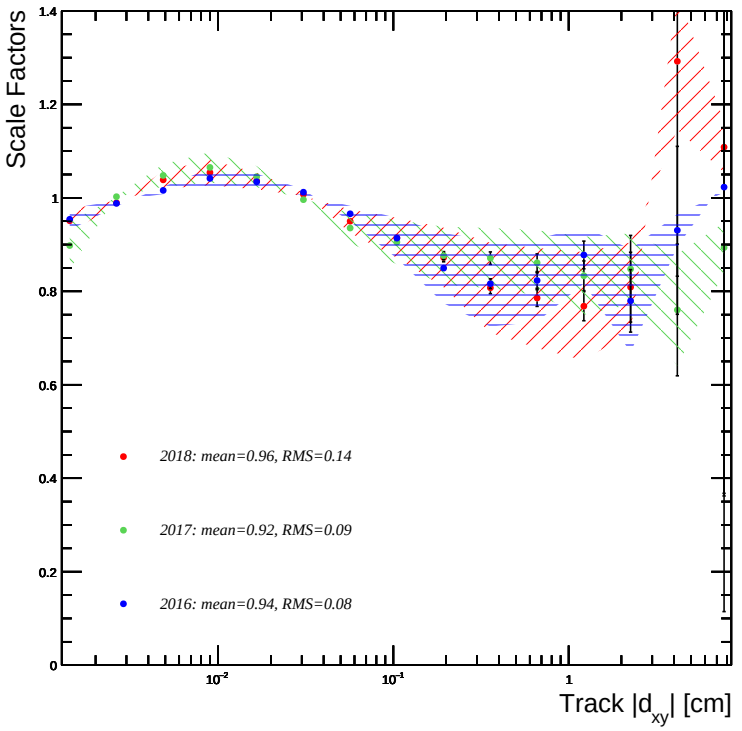

Figure 6.13: The comparison of the displaced track reconstruction scale factors for the year 2016 post-HIP, 2017 and 2018 on the left and for the year 2016 total , 2017 and 2018 on the right.

6.5.5 Displaced jet tagger efficiency

The displaced track correction is propagated to the jet level by calculating a per-track correction scale factor for the three tracks with the highest d_{xy} values in the HNL jet candidate. These individual corrections are then combined using a p_T -weighted average as

$$\mathrm{SF}_{\text{HNL jet}} = \prod_{i=1}^{\min(3,All_{\text{tracks}})} \mathrm{SF}_{\text{track}}(d^i_{xy}) \cdot p^{\text{rel}}_{i,\text{T}} \,, \qquad \sum_{i=1}^{\min(3,\text{All}_{\text{tracks}})} p^{\text{rel}}_{i,\text{T}} = 1. \tag{6.1}$$

We motivate this procedure as follows. First, the d_{xy}-significances of tracks within a jet are important inputs to the tagger and hence serves as a good proxy of the tagger performance. Secondly, at first order one can assume that the displaced jet tagging efficiency can be factorized into several per track efficiency. Lastly, we have observed that choosing the three most displaced tracks was empirically found to give the best data to simulation agreement as smaller values lead to overcorrection in case of a fake track, while choosing all tracks in the jet places too much weight on prompt tracks instead.

6.5.6 Displaced leptons reconstruction and identification efficiency

Similar to tracks the efficiency for displaced leptons to be reconstruced or identified is different than the prompt ones. Therefore a dedicated identification efficiency study was performed for both muons and electrons denoted as displaced muon ID SFs and displaced electron ID SFs respectively.

Displaced muon ID SFs

To derive the displaced muon ID SFs, J/ψ events produced from B meson decays described in equation 6.2 were selected.

$$B^{\pm} \to J/\psi K^{\pm} \to \mu^{-}\mu^{+}K^{\pm} \tag{6.2}$$

The tag and probe method was used. This method involves selecting a "tag" muon that satisfies strict identification criteria, i.e. used for the analysis, and then searching for a second "probe" muon in the same event. The probe muon is required to pass a looser set of identification

criteria, which allows for a larger sample size. The efficiency of the identification criteria for the probe muon is then determined by comparing the number of events where both the tag and probe muons pass the identification criteria to the number of events where only the tag muon passes. In this analysis, the efficiency of probe muon identifaction is computed as in equation 6.3. The final SFs are derived as a function of p_T and d_{xy}^{sig} as shown in equation 6.4. The final measured muon ID SFs are within 2 to 3 % variation from unity, see figure 6.14.

$$\epsilon = \frac{N_{probe(\text{ID and Reco})}}{N_{probe}(\text{Reco})} \tag{6.3}$$

$$SF(p_T, d_{xy}^{sig}) = \frac{\epsilon_{data}(p_T, d_{xy}^{sig})}{\epsilon_{MC}(p_T, d_{xy}^{sig})} \tag{6.4}$$

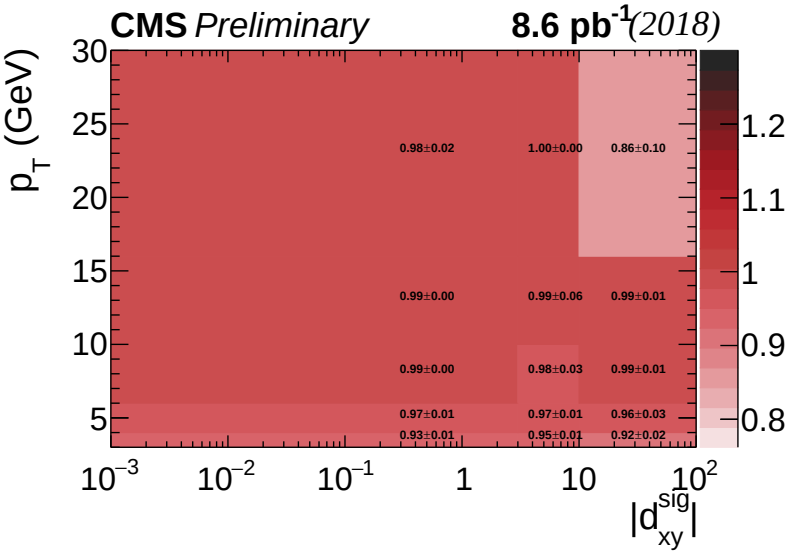

Figure 6.14: Example of the loose muon identification SFs binned as a function of its p_T and d_{xy}^{sig} for the year 2018

Displaced electron ID SFs

The displaced electron ID SFs were evaluated using tag and probe method in Z/γ^*+jets events with asymmetric photon conversion where both Z boson events with Initial State Radiation (ISR) photons or Final State Radiation ones are considered as mentioned in equation 6.5 and 6.6 respectively. The low p_T electron ($e^{\pm}$) is the probe electron candidate.

$$Z\gamma \rightarrow \mu\mu\gamma \rightarrow \mu\mu ee \tag{6.5}$$

$$Z \rightarrow \mu\mu\gamma \rightarrow \mu\mu ee \tag{6.6}$$

The final SFs are derived as a function of p_T and d_{xy}^{sig} as in equation 6.7 and their variation is within 20% from unity, , see figure 6.15.

$$SF(p_T, d_{xy}^{sig}) = \sqrt{SF(p_T) \times SF(d_{xy}^{sig})} \tag{6.7}$$

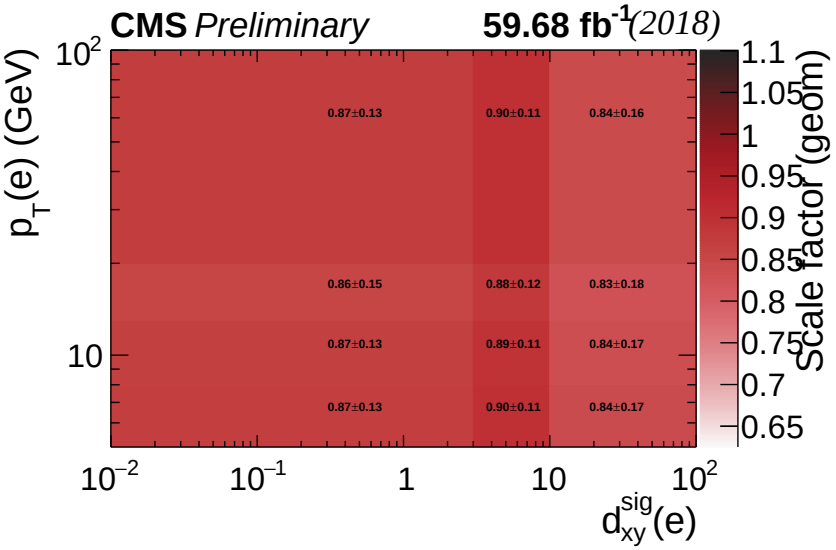

Figure 6.15: Example of the customised electron identification SFs binned as a function of its p_T and d_{xy}^{sig} for the year 2018

All discussed corrections are applied to background simulation in data to MC comparison plots. For the final results, corrections are only applied to simulated signal events since contributions from background processes in the SR are estimated from data instead.

6.6 Event categorisation

In this section, the categorization of signal events is described. Only events that pass the preselection requirements, as summarised in section 6.2, are considered. This analysis constitutes an inclusive search for HNLs, where LNC, LNV, LFC, and LFV scenarios are considered. Therefore, the events are categorized based on their leptons flavour, topology, dilepton charge, and displacement of the decay product to maximise the sensitivity to various HNL mass and mixing scenarios.

6.6.1 Event topologies

Signal events are classified as boosted' if ℓ_2 is clustered inside the HNL jet (ie $\Delta R(\ell_2, \mathrm{j}^\star) < 0.4$) or "resolved" otherwise. An additional cut on $\Delta R(\ell_2, \mathrm{j}^\star) < 1.3$ is applied to define the signal region.

Figure 6.16(a) shows the fraction of signal events classified as resolved for different HNL mass points for $\mu\mu$ and ee events final state events. The difference between electron and muon channels comes from the ℓ_2 p_T thresholds. The fraction is $\approx$ 5(10)% for $\mu\mu$ (ee) channels at low mass value 6 GeV, the other 95(90)% events are classified as boosted instead. The fraction of resolved events become more important ($\approx$ 50%) at higher mass ($>$ 10 GeV).

The figure 6.16(b) shows the truth matched fraction of resolved signal events in resolved $\mu\mu$ and ee categories using the ΔR approach(i.e. the reconstructed jet is matched to the generator level jet). The true fraction is very small for low mass events. This is due to the minimum threshold requirement on the HNL jet $p_T > 30$ GeV for boosted events scenario, when the signal event does not pass this requirement another random jet from parton showring is selected instead and results on classifying the event as resolved.

The true resolved fraction is instead important (80 %) for higher mass scenarios ($>$ 10 GeV) where signal events are classified $\approx$ 50% as resolved.

Based on the above discussion, in the low HNL mass regime, HNL decay products are mostly boosed and in the high HNL mass regime starting from 8 GeV the fraction of resolved decay products becomes important. Thus the choise of two categories based on the $\Delta R(\ell_2 \mathrm{j}^\star)$ to

maximise sensitivity for both scenarios.

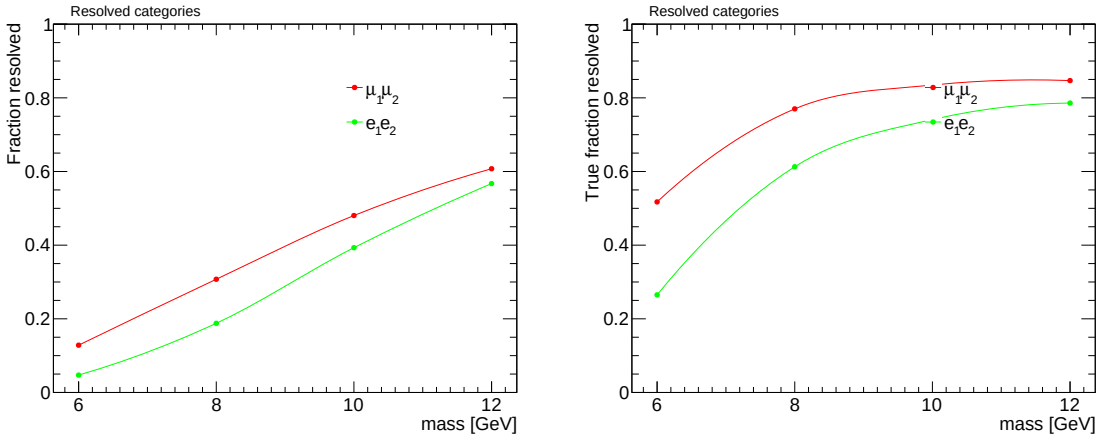

(a) (b)

Figure 6.16: Fraction of signal events classified as resolved for different HNL mass points using the ΔR approach.

6.6.2 Event displacement

The HNLs decay products are found to be mostly displaced for the considered mass and coupling parameter space. The decay products from SM processes are, in general, prompt, except for

eg B, D meson decays and dilepton SM processes, where one of the leptons is misreconstructed; ie. "fake". Hence, the lepton displacement is a powerful discriminant to separate signal from SM background events. To incorporate the displacement information into the categorization, the following three displacement variables have been studied:

- d_{xy}: transverse impact parameter of ℓ_2;
- d_{xy}^{sig}: $d_{xy}/\sigma(d_{xy})$, ℓ_2 transverse impact parameter significance;
- L_{xy}: profiled transverse displacement parameter (discussed in section 7).

The signal versus background distributions of these three variables is shown in Fig. 6.17.

For events with boosted topology, the ℓ_2 is clustered inside the jet and hence the corresponding displacement variables $d_{xy}(\ell_2)$ and $d_{xy}^{sig}(\ell_2)$ are among the tagger inputs. This is not the case for resolved events when the ℓ_2 is outside the jet cone. Consequently, the displacement information

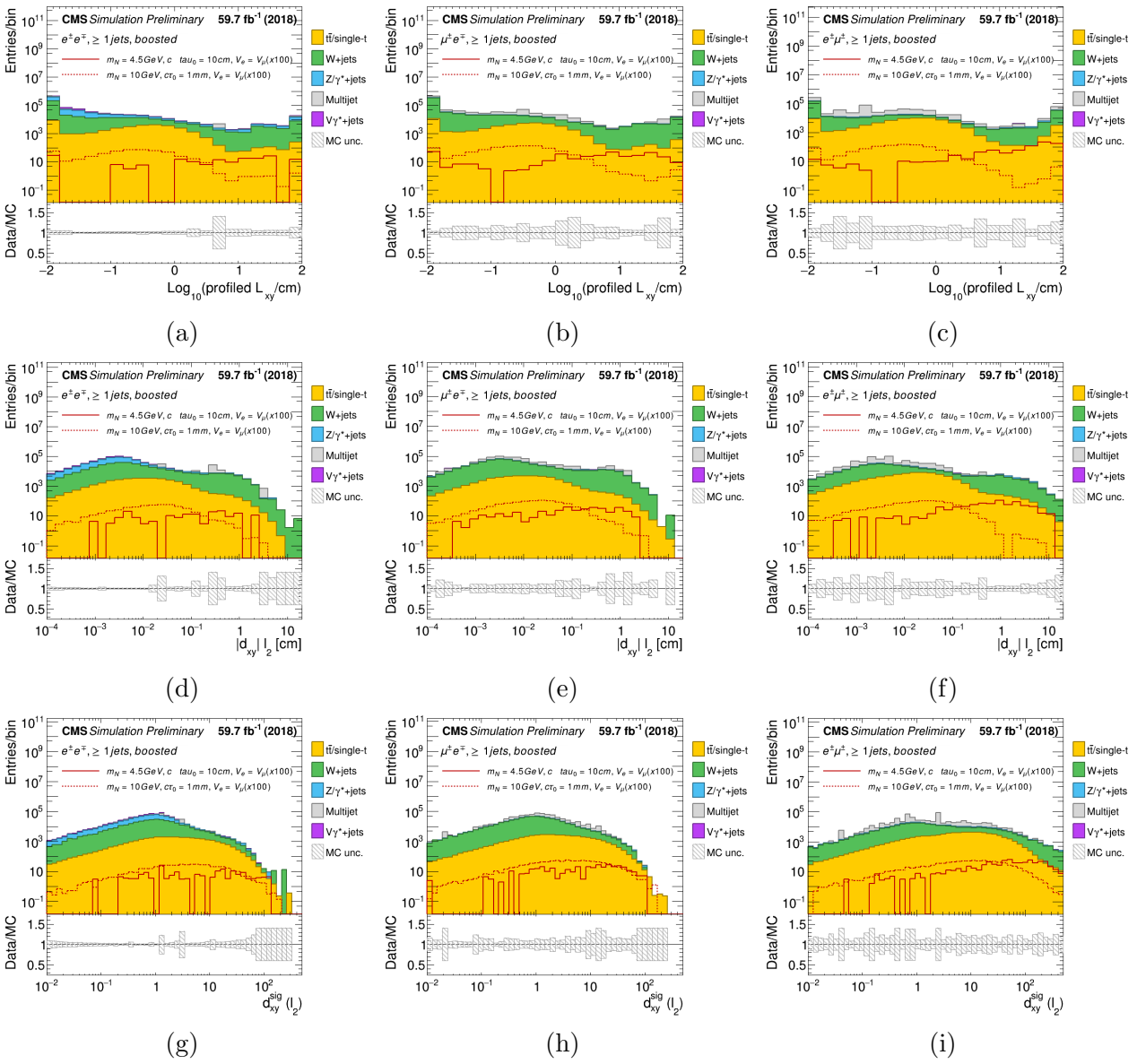

Figure 6.17: Distributions of the three displacement variables L_{xy}(top), $|d_{xy}|l_2$(middle) and $|d_{xy}^{sig}|(l_2)$(bottom) for background and signal processes ($m_{\mathrm{N}} = 8, c\tau_0 = 0.1, 1$ and 10)

carried by these three variables is expected to be largely correlated in boosted events. For resolved events, they are still expected to be correlated since the ℓ_2 and the jet come from the same HNL decay position. Due to this correlation, no clear choice can be made and further criteria have been considered to decide which variable would work best for the categorization as follows.

Data/MC agreement: The best agreement was observed for $d_{xy}^{sig}(\ell_2)$ in the 3 years, while the worst agreement was observed for the $d_{xy}(\ell_2)$. To further understand why $d_{xy}^{sig}(\ell_2)$ has a better data/MC agreement than $d_{xy}(\ell_2)$ an additional study has been performed. Fig-

ure 6.18 shows the distribution of $d_{xy}(\ell_2)$, $\sigma_{d_{xy}}(\ell_2)$ and their ratio $d_{xy}^{sig}(\ell_2)$. A mismodelling can be seen in both $d_{xy}(\ell_2)$, $\sigma_{d_{xy}}(\ell_2)$ however it cancels out when considering the ratio distribution $d_{xy}^{sig}(\ell_2)$. This can be attributed to miscalibrations of the tracker detector. Hence, the $d_{xy}(\ell_2)$ option is disfavoured.

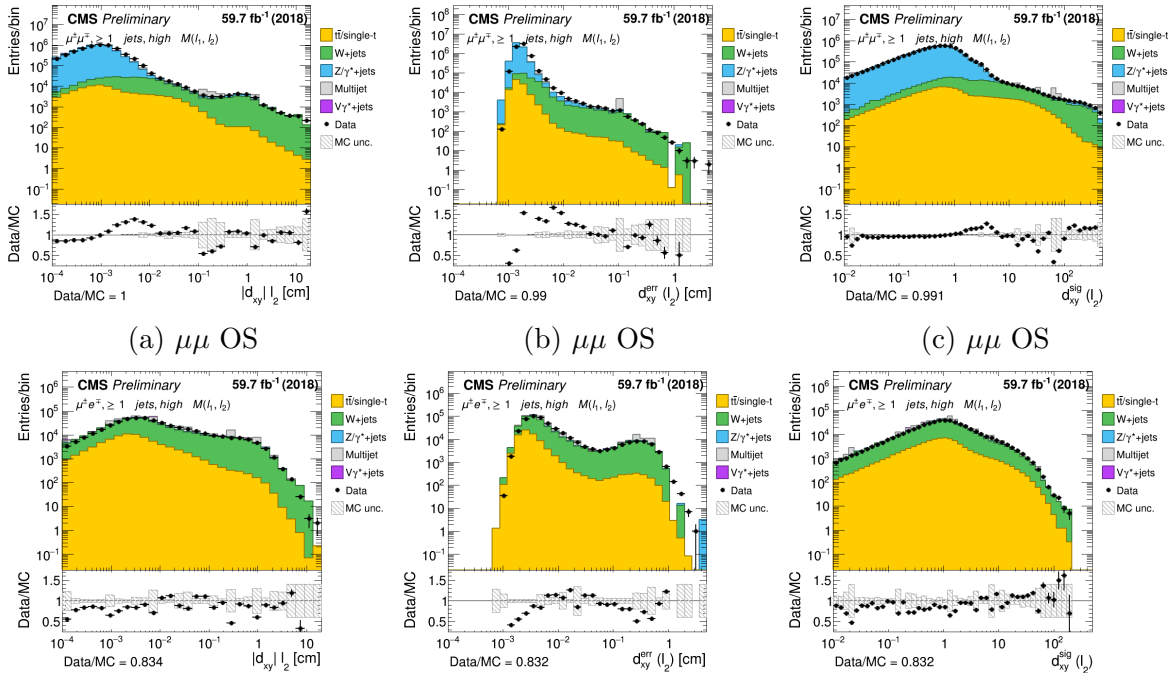

(a) $\mu\mu$ OS (b) $\mu\mu$ OS (c) $\mu\mu$ OS

(d) μe OS (e) μe OS (f) μe OS

Figure 6.18: Distribution of $d_{xy}(\ell_2)$, $d_{xy}^{sig}(\ell_2)$ and $\sigma_{d_{xy}}(\ell_2)$ in high $M(\ell_1, \ell_2)$ control region. the distribution are shown in two different lepton categories for 2018 datasets.

Significance scan: After rejecting the $d_{xy}(\ell_2)$ variable, the $d_{xy}^{sig}(\ell_2)$ and L_{xy} variables remain good candidates for the categorisation study. To make a final decision on which variable to keep, two displaced bins have been defined depending on the leptons category. For a fair comparison between the two variables, the L_{xy} threshold was tuned to ensure the same number of signal events in the two bins.

- $d_{xy}^{sig}(\ell_2) > 3$ for $\mu\mu$ and ee channels.
- $Log_{10}(L_{xy}) > -1$ for $\mu\mu$ channels.
- $Log_{10}(L_{xy}) > 0$ for ee channels.

The figure of merit used in the optimisation is the discovery sensitivity [37]. The significance has been computed in the defined displaced bins for signal, $m_{\mathrm{N}} > 4.5, 6, 8$ and 10 GeV,

and background events passing the preselections and a tagger score 7 cut of 0.4(0.2) for boosted(resolved) respectively as shown in figure 6.19 where it shows that $d_{xy}^{sig}(\ell_2)$ in the displaced bin has a better significance value comparing to L_{xy} with and without the tagger selections. The difference in the performance between the two variables is highly pronounced at high mass values. Therefore, the $d_{xy}^{sig}(\ell_2)$ variable is kept for the categorization study and the following bins have been defined:

- prompt: $d_{xy}^{sig}(\ell_2) < 3$.
- medium: $3 < d_{xy}^{sig}(\ell_2) < 10$.
- displaced: $d_{xy}^{sig}(\ell_2) > 10$.

The choice of the prompt bins threshold was motivated by the background composition at low $d_{xy}^{sig}(\ell_2)$ values. Figure 6.17 shows that Drell-Yan is a dominant background up to $d_{xy}^{sig}(\ell_2) = 3$ for OSSF categories. This choice helps improving the performance of the background estimation in the prompt category bins see section 8.

A significance scan as a function of $d_{xy}^{sig}(\ell_2)$ has been done to decide on the displaced bins threshold. A factor of ≈10 less background events was observed for $d_{xy}^{sig}(\ell_2) > 10$ comparing to $d_{xy}^{sig}(\ell_2) < 3$, where most of the standard model background is classified. Therefore $d_{xy}^{sig}(\ell_2) = 10$ has been chosen as the displaced bins threshold.

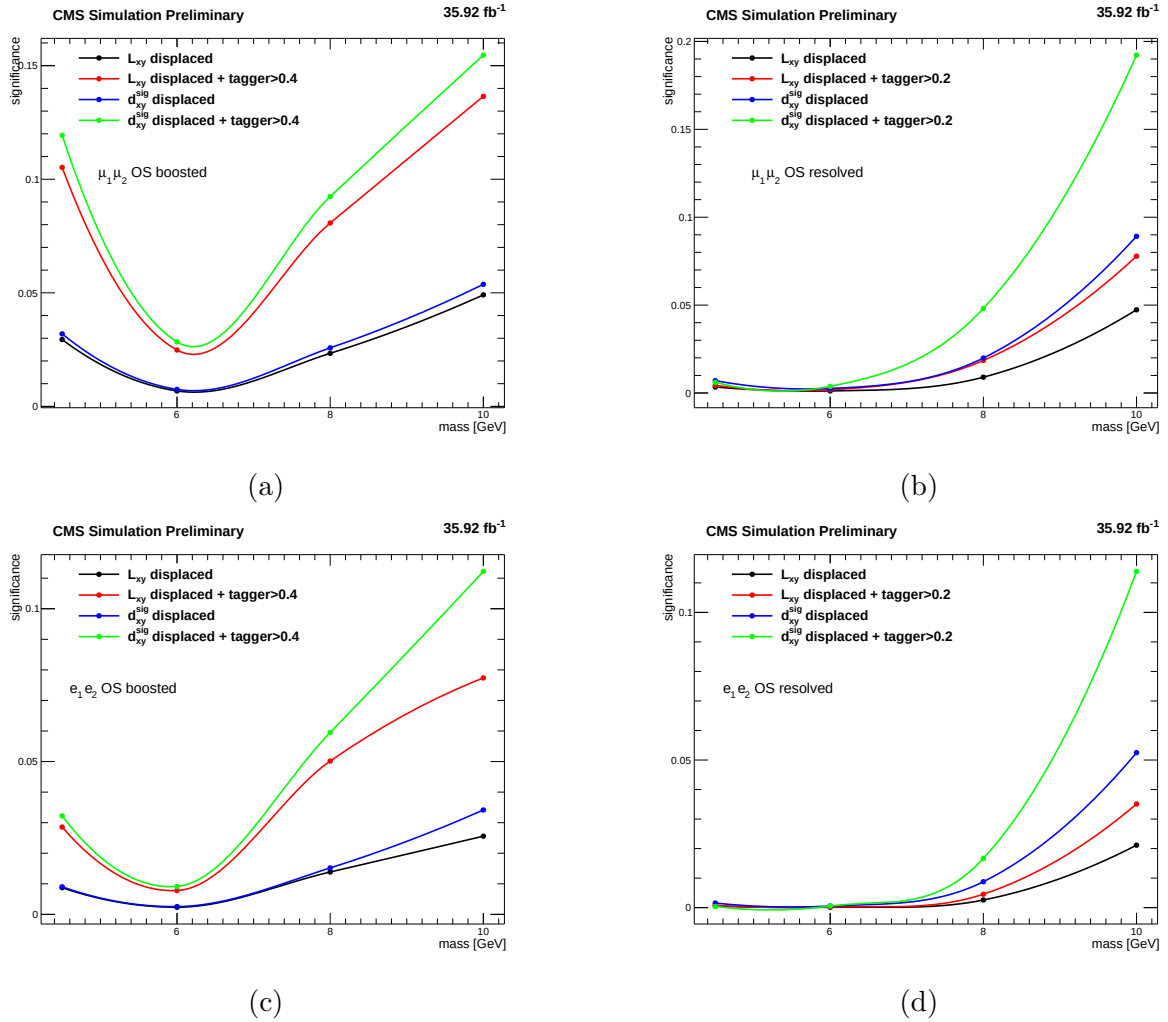

Figure 6.19: Significance scan for benchmark signal processes ($m_{\mathrm{N}} = 4.5, 6, 8$ and $10, c\tau_0 = 10, 10, 1$ and 1 respectively, for OS $\mu\mu$ (left) and OS ee (right) final states.

6.6.3 Summary

Overall, the events are categorised as follows:

- Event topology: $\min \Delta R(\ell_2, \text{jets}) < 0.4$ and $0.4 < \min \Delta R(\ell_2, \text{jets}) < 1.3$, to identify boosted or resolved topologies;
- Lepton flavour combination: $\mu\mu$, μe, $e\mu$, ee, allowing to probe different HNL-active neutrino mixing scenarios;
- Lepton charge combination: OS and SS final states, to be individually sensitive to Dirac and Majorana HNLs;
- ℓ_2 transverse impact parameter significance: 3 intervals to allow for further optimisation for prompt, displaced and very displaced HNL scenarios.
  - prompt: $d_{xy}^{sig}(\ell_2) < 3$
  - medium: $3 < d_{xy}^{sig}(\ell_2) < 10$
  - displaced: $d_{xy}^{sig}(\ell_2) > 10$

The categorisation results in $2 \times 4 \times 2 \times 3 = 48$ independent signal region categories as shown in figure 6.20.

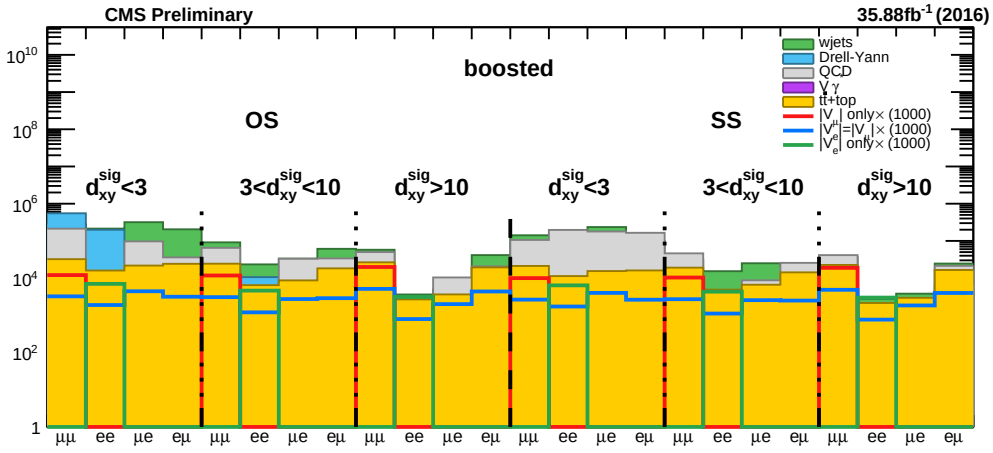

(a)

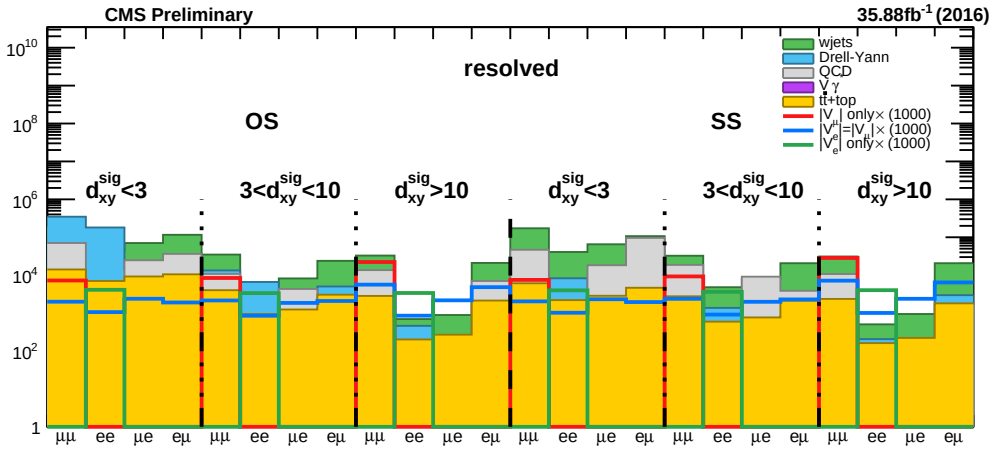

(b)

Figure 6.20: Categorisation of background and benchmark signal processes ($m_{\mathrm{N}} = 10, c\tau_0 = 1$ for $V_e = V_\mu$, pure muon and pure electron couplings.)

Chapter 7

Neural-network-based displaced jet tagger

7.1 Introduction

This search considers HNL events with two leptons and a jet in the final state. HNLs decay into a displaced lepton and a jet, denoted as ℓ_2 and $j^\star$, respectively. To identify the displaced HNL jet, a specialized machine learning algorithm based on neural network (NN) techniques called the displaced jet tagger was used. The tagger was first developed in [65], where only fully hadronic jets were considered. However, since the current study involves cases where ℓ_2 can overlap with $j^\star$, an extension of the tagger inputs to include lepton information was necessary. Detailed information about the tagger's architecture, inputs, performance and outputs is provided in the following sections.

7.2 Neural Network architecture

The displaced jet tagger is a neural network that utilizes a supervised learning technique for solving a multi-classification problem. The architecture of the network is illustrated in figure 7.1. The jet input features are first processed through a series of one-dimensional convolutional layers (CNN) with different filter sizes. These CNNs serve the purpose of reducing the number

of features used as input to the tagger and retaining only the most discriminant ones for the subsequent steps. The resulting information is then fed into two dense layers, each with 200 nodes. The tagger is then bifurcated into two branches. The first branch is responsible for predicting the output class of the input jet, which will be detailed below. The second branch is designed to predict the differences between the data and simulation i.e domain branch.

The NN parametrization refers to the use of parameters, such as particle proper lifetime or other physical properties, to describe a particle, which can then be used as input to a neural network. In this case, it is possible to use a single neural network with a parametrized input to model multiple related processes, rather than creating a separate neural network for each individual system. This approach can be particularly useful when the systems being modeled are related and share common features, such as particles with similar properties.

The neural network used in previous paper [65] was parametrized with the proper lifetime, $c\tau_0$. However, in the current analysis, a different parameter, the transverse displacement L_{xy} of HNL in the lab frame, is used instead. This is because the HNL can be highly boosted, particularly at low masses, and the transverse displacement better captures the various signatures that occur at different displacements in the detector compared to the proper lifetime. To optimize the performance of the analysis, the displacement parameter L_{xy} is profiled by selecting the value that results in the highest likelihood for a given jet class, within the range $10^{-1} < L_{xy} < 10^{3}$mm. The lower bound is set based on the primary vertex resolution, which is approximately $\sigma_{xy}^{\mathrm{PV}} \approx 50$ μm for primary vertices fitted from at least 10 charged tracks [32]. The upper bound is chosen to be close to the edge of the inner tracker (1.3 m), as beyond this point, no displaced tracks can be reconstructed.

7.2.1 Input features

The input features utilized in this tagger comprise global jet features, as well as constituent-specific features. The global jet features include several variables such as the uncorrected jet transverse momentum (p_T), mass, area, and energy fractions carried by the constituents within different angular distances from the jet axis. Additionally, the number of constituents carrying a certain percentage of the jet's energy, the energy fractions carried by charged,

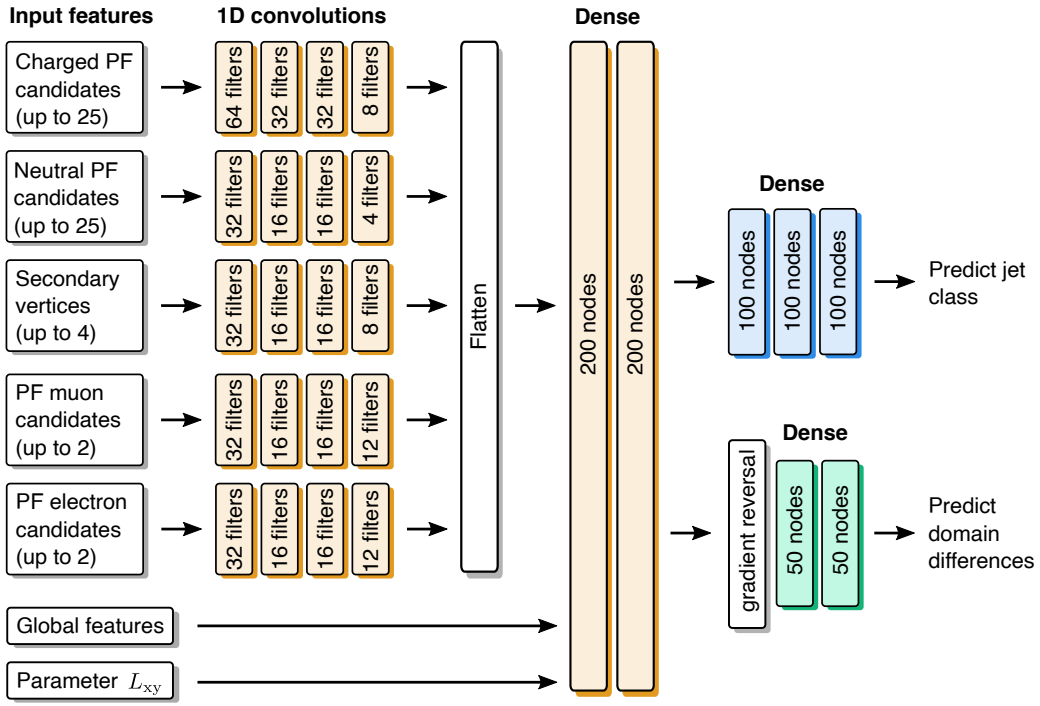

Figure 7.1: The default architecture of the neural network for identifying displaced jets from the HNL decay.

electromagnetic, muon, and electron constituents, and various event shapes (such as thrust, sphericity, circularity, isotropy, C, and D) are considered to explore the substructure of the jet. In total, 47 global jet features are used as documented in table 7.7. The constituent-specific features are grouped into different blocks based on their type, including charged and neutral PF candidates, PF muon and electron cadidates and secondary vertices. The input features for the neural network comprise information on both charged and neutral PF candidates, which form the constituents of jets. Charged PF candidates possess an associated track, providing details on the potential displacement of the jet within the tracking volume. The features for charged PF candidates encapsulate various properties of the track, including its displacement from the primary vertex and its association with a secondary vertex or a PF electron/muon. Up to 25 charged PF candidates are taken into consideration for each jet, sorted according to their significance of displacement in the transverse plane with respect to the primary vertex. Each charged PF candidate contributes 36 features summarised in table 7.1. The network considers up to 25 neutral constituents per jet, with features that encompass the probability of the constituent originating from pileup interactions as calculated by the pileup per particle i.e PUPPI algorithm [17]. These constituents are sorted based on their p_T. Each neutral PF

candidate provides a total of 9 features shown in table 7.2. Moreover, the neural network uses features specific to the reconstruction of PF muons or electrons if a charged PF candidate is linked to them. For muons, the features encompass details about the global track fit and the hit pattern in the muon chambers, while for electrons, the features encompass properties of the GSF track and matching clusters in the ECAL. The network considers up to 2 muons and electrons per jet, sorted based on their significance of displacement in the transverse plane with respect to the primary vertex. In total, the network utilizes 37 features for each muon candidate and 78 features for each electron candidate summarised in table 7.6 and 7.4 respectively. Finally, the neural network also incorporates features of up to 4 secondary vertices, reconstructed using the IVF algorithm, located within $\Delta R < 0.4$ of the jet and utilizing at least one jet constituent in their reconstruction. These features include the significance of their displacement in the transverse plane with respect to the primary vertex, and up to 14 features are used per secondary vertex and can be found in table 7.3.

Table 7.1: Features of charged PF features.

Internal name	Description
cpf_ptrel	Relative p_T
cpf_deta	$\Delta\eta$ to jet axis
cpf_dphi	$\Delta\phi$ to jet axis
cpf_deltaR	ΔR to jet axis
cpf_trackEtaRel	η relative to jet axis
cpf_trackPtRel	p_T relative to jet axis
cpf_trackPPar	Momentum parallel to jet axis
cpf_trackDeltaR	ΔR
cpf_trackPParRatio	Relative momentum parallel to jet axis
cpf_trackPtRatio	Relative p_T parallel to jet p_T
cpf_trackSip2dVal	Impact parameter d_{xy}
cpf_trackSip2dSig	σ_{xy}/d_{xy}
cpf_trackSip3dVal	Impact parameter d_{xyz}
cpf_trackSip3dSig	σ_{xyz}/d_{xyz}
cpf_trackJetDistVal	Distance between track and jet
cpf_trackJetDistSig	Significance of distance between track and jet
cpf_drminsv	Closest distance in ΔR to secondary vertex
cpf_vertex_association	Flag if track is used in PV fit
cpf_fromPV	Flag if track stems from PV
cpf_puppi_weight	PUPPI weight
cpf_track_chi2	χ^2 of track fit
cpf_track_ndof	NDOF of track fit
cpf_track_quality	Track quality flag
cpf_track_numberOfValidPixelHits	Number of pixel hits
cpf_track_pixelLayersWithMeasurement	Number of crossed pixel layers
cpf_track_numberOfValidStripHits	Number of strip hits
cpf_track_stripLayersWithMeasurement	Number of crossed strip layers
cpf_relmassdrop	Relative mass drop when removed from jet
cpf_trackSip2dValSV	Impact parameter d_{xy} wrt. SV
cpf_trackSip2dSigSV	σ_{xy}/d_{xy} wrt. SV
cpf_trackSip3dValSV	Impact parameter d_{xyz} wrt. SV
cpf_trackSip3dSigSV	σ_{xyz}/d_{xyz} wrt. SV
cpf_matchedMuon	Flag if candidate is matched to a PF muon
cpf_matchedElectron	Flag if candidate is matched to a PF muon
cpf_matchedSV	Flag if candidate is used in SV fit
cpf_dZmin	Minimum distance in z to another PV

Table 7.2: Features of neutral PF candidates.

Internal name	Description
npf_ptrel	Relative p_T
npf_deta	$\Delta\eta$ to jet axis
npf_dphi	$\Delta\phi$ to jet axis
npf_deltaR	ΔR to jet axis
npf_isGamma	Flag for passing loose photon ID
npf_hcal_fraction	Fraction of in HCAL
npf_drminsv	Closest distance in ΔR to secondary vertex
npf_puppi_weight	PUPPI weight
npf_relmassdrop	Relative mass drop when removed from jet

Table 7.3: Features of secondary vertices.

Internal name	Description
`sv_ptrel`	Relative p_T
`sv_deta`	$\Delta\eta$ to jet axis
`sv_dphi`	$\Delta\phi$ to jet axis
`sv_deltaR`	ΔR to jet axis
`sv_mass`	Secondary vertex mass
`sv_ntracks`	Number of tracks used in fit
`sv_chi2`	χ^2 of fit
`sv_ndof`	NDOF of fit
`sv_dxy`	Impact parameter d_{xy}
`sv_dxysig`	σ_{xy}/d_{xy}
`sv_d3d`	Impact parameter d_{xyz}
`sv_d3dsig`	σ_{xyz}/d_{xyz}
`sv_costhetasvpv`	$\cos\theta$ of SV wrt. PV
`sv_enratio`	Relative

Table 7.4: Features of PF electrons (part 1).

Internal name	Description
electron_ptrel	Relative p_T
electron_deta	$\Delta\eta$ to jet axis
electron_dphi	$\Delta\phi$ to jet axis
electron_deltaR	ΔR to jet axis
electron_energy	Relative energy
electron_EtFromCaloEn	Calorimeter energy
electron_isEB	Flag if electron is in ECAL barrel
electron_isEE	Flag if electron is in ECAL endcap
electron_ecalEnergy	ECAL energy
electron_isPassConversionVeto	Flag if electron passes photon conversion veto
electron_convDist	Conversion distance
electron_convFlags	Conversion flags
electron_convRadius	Conversion radius
electron_hadronicOverEm	HCAL over ECAL energy
electron_ecalDrivenSeed	Flag if electron is seed from ECAL
electron_IP2d	Impact parameter d_{xy}
electron_IP2dSig	σ_{xy}/d_{xy}
electron_IP3d	Impact parameter d_{xyz}
electron_IP3dSig	σ_{xyz}/d_{xyz}
electron_elecSC_energy	Relative energy in ECAL supercluster
electron_elecSC_deta	$\Delta\eta$ between ECAL supercluster and jet axis
electron_elecSC_dphi	$\Delta\phi$ between ECAL supercluster and jet axis
electron_elecSC_et	of ECAL supercluster
electron_elecSC_eSuperClusterOverP	ECAL supercluster ratio
electron_superClusterFbrem	Energy associated to bremsstrahlung
electron_eSeedClusterOverP	Electron energy ratio of GSF track over ECAL supercluster seed
electron_eSeedClusterOverPout	Electron energy ratio of GSF track over ECAL supercluster seed at exit
electron_eSuperClusterOverP	Electron energy ratio of GSF track over ECAL supercluster
electron_sigmaEtaEta	$\sigma_{\eta\eta}$ ECAL supercluster shape
electron_sigmaIetaIeta	$\sigma_{i\eta i\eta}$ ECAL supercluster shape
electron_sigmaIphiIphi	$\sigma_{i\phi i\phi}$ ECAL supercluster shape
electron_e5x5	Energy in 5x5 ECAL cells
electron_e5x5Rel	Relative energy in 5x5 ECAL cells
electron_e1x5Overe5x5	Energy ratio of 1x5 over 5x5 ECAL cells
electron_e2x5MaxOvere5x5	Maximum energy ratio of 2x5 over 5x5 ECAL cells
electron_r9	ECAL supercluster shape variable
electron_hcalOverEcal	Relative HCAL over ECAL energy
electron_hcalDepth1OverEcal	Relative HCAL at depth 1 over ECAL energy
electron_hcalDepth2OverEcal	Relative HCAL at depth 2 over ECAL energy
electron_deltaEtaEleClusterTrackAtCalo	$\Delta\eta$ between cluster and track at calorimeter
electron_deltaEtaSeedClusterTrackAtCalo	$\Delta\eta$ between cluster seed and track at calorimeter
electron_deltaPhiSeedClusterTrackAtCalo	$\Delta\phi$ between cluster seed and track at calorimeter
electron_deltaEtaSeedClusterTrackAtVtx	$\Delta\eta$ between cluster seed and track at PV
electron_deltaEtaSuperClusterTrackAtVtx	$\Delta\phi$ between cluster seed and track at PV
electron_deltaPhiEleClusterTrackAtCalo	$\Delta\phi$ between cluster and track at calorimeter
electron_deltaPhiSuperClusterTrackAtVtx	$\Delta\phi$ between cluster and track at PV

Table 7.5: Features of PF electrons (part 2).

Internal name	Description
`electron_sCseedEta`	Pseudorapidity of ECAL supercluster seed
`electron_EtaRel`	Relative η
`electron_dxy`	Impact parameter d_{xy} of track
`electron_dxyError`	σ_{xy} of track
`electron_dxySig`	σ_{xy}/d_{xy} of track
`electron_dz`	Impact parameter d_z of track
`electron_dzError`	σ_z of track
`electron_dzSig`	σ_z/d_z of track
`electron_nbOfMissingHits`	Number of missing hits
`electron_ndof`	NDOF of track
`electron_chi2`	χ^2 of track
`electron_numberOfBrems`	Number of photons from bremsstrahlung
`electron_fbrem`	Fraction of bremsstrahlung energy
`electron_neutralHadronIso`	Neutral hadron isolation within $\Delta R < 0.3$
`electron_particleIso`	Particle isolation within $\Delta R < 0.3$
`electron_photonIso`	Photon isolation within $\Delta R < 0.3$
`electron_puChargedHadronIso`	Pileup isolation from charged hadrons within $\Delta R < 0.3$
`electron_trackIso`	Track isolation within $\Delta R < 0.3$
`electron_ecalPFClusterIso`	ECAL cluster isolation within $\Delta R < 0.3$
`electron_hcalPFClusterIso`	HCAL cluster isolation within $\Delta R < 0.3$
`electron_pfSumPhotonEt`	Summed PF photon within $\Delta R < 0.3$
`electron_pfSumChargedHadronPt`	Summed PF charged hadron p_T within $\Delta R < 0.3$
`electron_pfSumNeutralHadronEt`	Summed PF neutral hadron within $\Delta R < 0.3$
`electron_pfSumPUPt`	Summed pileup p_T within $\Delta R < 0.3$
`electron_dr04TkSumPt`	Summed track p_T within $\Delta R < 0.4$
`electron_dr04EcalRecHitSumEt`	Summed ECAL within $\Delta R < 0.4$
`electron_dr04HcalDepth1TowerSumEt`	Summed HCAL from depth 1 within $\Delta R < 0.4$
`electron_dr04HcalDepth1TowerSumEtBc`	Summed HCAL from depth 1 behind ECAL cluster
`electron_dr04HcalDepth2TowerSumEt`	Summed HCAL from depth 2 within $\Delta R < 0.4$
`electron_dr04HcalDepth2TowerSumEtBc`	Summed HCAL from depth 2 behind ECAL cluster
`electron_dr04HcalTowerSumEt`	Summed HCAL within $\Delta R < 0.4$
`electron_dr04HcalTowerSumEtBc`	Summed HCAL behind ECAL cluster

Table 7.6: Features of PF muons.

Internal name	Description
muon_ptrel	Relative p_T
muon_deta	$\Delta\eta$ to jet axis
muon_dphi	$\Delta\phi$ to jet axis
muon_deltaR	ΔR to jet axis
muon_energy	Relative energy
muon_et	
muon_numberOfMatchedStations	Number of muon stations
muon_IP2d	Impact parameter d_{xy}
muon_IP2dSig	σ_{xy}/d_{xy}
muon_IP3d	Impact parameter d_{xyz}
muon_IP3dSig	σ_{xyz}/d_{xyz}
muon_EtaRel	Relative pseudorapidity
muon_dxy	Impact parameter d_{xy} of track
muon_dxyError	σ_{xy} of track
muon_dxySig	σ_{xy}/d_{xy} of track
muon_dz	Impact parameter d_z of track
muon_dzError	σ_z of track
muon_dzSig	σ_z/d_z of track
muon_numberOfValidPixelHits	Number of valid pixel hits
muon_numberOfpixelLayersWithMeasurement	Number of crossed pixel layers
muon_numberOfstripLayersWithMeasurement	Number of crossed strip layers
muon_chi2	χ^2 of track fit
muon_ndof	NDOF of track fit
muon_caloIso	Calorimeter isolation
muon_ecalIso	ECAL isolation
muon_hcalIso	HCAL isolation
muon_sumPfChHadronPt	Summed PF charged hadron p_T within $\Delta R < 0.4$
muon_sumPfNeuHadronEt	Summed PF neutral hadron within $\Delta R < 0.4$
muon_Pfpileup	Summed pileup p_T within $\Delta R < 0.4$
muon_sumPfPhotonEt	Summed PF photon within $\Delta R < 0.4$
muon_sumPfChHadronPt03	Summed PF charged hadron p_T within $\Delta R < 0.3$
muon_sumPfNeuHadronEt03	Summed PF neutral hadron within $\Delta R < 0.3$
muon_Pfpileup03	Summed pileup p_T within $\Delta R < 0.3$
muon_sumPfPhotonEt03	Summed PF photon within $\Delta R < 0.3$
muon_timeAtIpInOut	Timing at interaction point (in/out)
muon_timeAtIpInOutErr	Timing uncertainty at interaction point
muon_timeAtIpOutIn	Timing at interaction point (out/in)

Table 7.7: Global jet features.

Internal name	Description
`global_pt`	Uncorrected p_T
`global_eta`	Pseudorapidity
`global_mass`	Mass
`global_energy`	Energy
`global_area`	Area calculated by anti-algorithm
`global_beta`	Fraction of charged PF candidates from PV
`global_dR2Mean`	p_T -weighed ΔR average of charged PF candidates
`global_frac01`	Fraction of jet p_T within $\Delta R < 0.1$
`global_frac02`	Fraction of jet p_T within $\Delta R < 0.2$
`global_frac03`	Fraction of jet p_T within $\Delta R < 0.3$
`global_frac04`	Fraction of jet p_T within $\Delta R < 0.4$
`global_jetR`	Maximum relative p_T carried by one constituent
`global_jetRchg`	Maximum relative p_T carried by one charged constituent
`global_n60`	Number of constituents carrying 60% of total p_T
`global_n90`	Number of constituents carrying 90% of total p_T
`global_chargedEmEnergyFraction`	Charged electromagnetic energy fraction
`global_chargedHadronEnergyFraction`	Charged hadronic energy fraction
`global_chargedMuEnergyFraction`	Muon energy fraction
`global_electronEnergyFraction`	Electron energy fraction
`global_tau1`	1-subjettiness
`global_tau2`	2-subjettiness
`global_tau3`	3-subjettiness
`global_relMassDropMassAK`	Relative mass drop when clustering with anti-
`global_relMassDropMassCA`	Relative mass drop when clustering with Cambridge-Aachen
`global_relSoftDropMassAK`	Relative soft drop when clustering with anti-
`global_relSoftDropMassCA`	Relative soft drop when clustering with Cambridge-Aachen
`global_thrust`	Relative thrust of constituents in jet CM frame
`global_sphericity`	Sphericity of constituents in jet CM frame
`global_circularity`	Circularity of constituents in jet CM frame
`global_isotropy`	Isotropy of constituents in jet CM frame
`global_eventShapeC`	Event shape C of constituents in jet CM frame
`global_eventShapeD`	Event shape D of constituents in jet CM frame
`global_numberCpf`	Number of charged PF constituents
`global_numberNpf`	Number of neutral PF constituents
`global_numberSv`	Number of secondary vertices
`global_numberMuon`	Number of muons
`global_numberElectron`	Number of electron

7.2.2 NN training

To create the NN, the TENSORFLOWv1.6 [7] and KERASv2.1.6 packages [34] were utilized. A custom interface between ROOT and TENSORFLOW was employed to read the samples directly from TTrees that were saved in ROOTv6.18.04 files[23]. For training the jet class branch of the neural network, simulated samples of jets from multijet production, top quark pair production, V+jets events, Zγ^*+jets production, and Higgs production via gluon fusion are utilized. Specifically, light flavoured (`UDS`), gluon (`G`), and pileup (`PU`) jets are taken from multijet samples, while heavy-flavoured jets (`B` and `C`) are obtained from the top quark pair production sample. To increase the number of SM jets from prompt leptons (`E`, `MU`, `TAU`), samples of V+jets events are also utilized. Jets from prompt photons (`PH`) are obtained from the Zγ^*+jets production sample, and a sample of Higgs production via gluon fusion, where the Higgs decays to two tau leptons, is used to further top up the number of SM tau jets. To prevent any potential bias caused by overtraining, the samples used for the training are selected in a way that they are statistically independent from those used in the analysis.

The jets are adjusted in their p_T and η distribution using resampling method to match that of the average displaced jet resulting from HNL decay in the specific parameter space being analyzed. Furthermore, the L_{xy} distribution made identical across all HNL jet classes using resampling. For non-HNL jets, the L_{xy} value is randomly selected from the distribution of HNL jets. This procedure was considered to train the classifier on a balanced dataset and avoid any bias such that the NN would concentrate only on area where the background is low for these parameters.

7.2.3 Domain adaptation

Domain adaptation(DA) is a technique used to address differences between the data collected by CMS and the simulated samples used to train the NN through the domain branch. The goal of DA in this work is to improve the performance of the NN model on data by minimizing the gap between the distributions of the simulation and data using all input features.
Events with criteria defined in table 6.2 i.e high-mass CR are selected. In addition, the dilepton

system was required to have p_T above 40 GeV and consist of a pair of leptons with any flavor and charge combination (ee, eμ, μe, or $\mu\mu$). A sample of jets is selected from these events for the DA where the jets have to satisfy $p_T > 15$ GeV and $|\eta| < 2.4$. Jets from simulated events are taken from major backgrounds Z/γ^*+jets t$\bar{\text{t}}$ and W+jets.

7.2.4 NN outputs configuration

This section discusses the identification of the origin of the jet using truth information and the subsequent definition of tagger output classes.

7.2.5 Jet labelling: Truth level

The classification of jets according to their origin relies on the accurate representation of simulated events. In this work, various background and signal jet classes are defined, including those used in the CMS MVA-based b-tagging algorithm training [62]. The classification of displaced jets resulting from the decay of HNLs adopts the displaced jet definition introduced in [65]. A comprehensive description of the jet classes considered is provided below.

Displaced HNL jets

Jets that are displaced have to be matched with a corresponding jet at the generator level, with a requirement of $\Delta R < 0.4$, whose momentum is carried by a majority of particles originating from a displaced vertex. This is determined by calculating the fraction (f_v) of the jet momentum carried by particles from each vertex v where the vertex with the highest f_v value is selected as the corresponding displaced vertex. A detailed description on the procedure can be found in [65].

To conduct the analysis, it is necessary to link the displaced vertex with the HNL decay. We further investigate the jets that meet this requirement by examining their content, which includes whether they contain a lepton and if they can be associated with a parton-level quark from the HNL's subsequent W boson decay. To label these jets, we use the "ghost" labelling technique [24]. The NN training involves displaced quark jets (`LLP_Q`, `LLP_QQ`), displaced electron/muon jets with and without additional quarks (`LLP_E`, `LLP_QE`, `LLP_QQE`, `LLP_MU`, `LLP_QMU`, `LLP_QQMU`),

and displaced tau jets (`LLP_TAU`, `LLP_QTAU`, `LLP_QQTAU`). If the tau jet decays leptonically to an electron or muon, we label it as `LLP_E` or `LLP_MU`, respectively. As the HNL mass increases, displaced jets can also stem more frequently from final state radiation (`LLP_RAD`) of a displaced quark and are thus also included in the training. However, we do not use jets containing displaced b quarks for training, as these are kinematically highly suppressed and have small off-diagonal CKM matrix elements ($|V_{\mathrm{cb}}|^2 \approx 0.2\%$ and $|V_{\mathrm{ub}}|^2 \approx 8.0 \times 10^{-5}$ [69]), due to the probed HNL mass range being close to the b quark mass.

Gluon and light quark jets

Jets resulting from light quarks or gluons are defined by examining the hadronization history of the jet at the generator level within $\Delta R < 0.4$ of a reconstructed jet. It is important to note that jets from the decay of g $\rightarrow$ bb are classified as b jets instead.

Heavy flavour jets

Jets that result from the hadronization of b or c hadrons are identified in this study using the ghost-matching procedure. This method is commonly used to report particle-level results for heavy-flavored jets [24]. The procedure involves selecting b and c hadrons from the generator level and scaling their momenta to a small magnitude to create "ghosts". These "ghosts" are then added to the list of reconstructed PF candidates without affecting the jet kinematic since their momenta was scaled down. By reclustering anti-kT jets using the list of candidates, jets that contain one or more b or c hadron are labeled accordingly. The b hadron label takes priority since they can decay into c hadrons.

Prompt lepton and photon jets

Jets can consist solely of a prompt lepton (electron, muon, or tau) or photon located at its center, surrounded by some spurious soft activity, since jets are clustered from all reconstructed PF candidates. Prompt lepton/photon jets are defined when the majority of the jet momentum can be attributed to a corresponding prompt lepton/photon at the generator level. Prompt leptons/photons are classified as such if they do not originate from the hadronization of a quark

or gluon or from the subsequent decay of a hadron. Prompt lepton jets can be mistaken for jets formed by leptons (and quarks) resulting from HNL decay at short lifetimes, and are therefore included as background classes in the training. Photon jets are also considered as a background class, since they can be confused with very displaced, track-less jets that occur when the HNL decays beyond the inner tracking volume.

Pileup jets

Jets resulting from pileup interactions are identified in this study by particles that are not associated with the hard interaction. As a result, a reconstructed jet cannot be matched to a corresponding jet at the generator level within $\Delta R < 0.4$. Pileup jets typically have a very soft p_T spectrum ($p_T \leq 50$ GeV) and are not usually considered a background when training MVA-based b-tagging algorithms. However, since the presence of HNLs can lead to such soft jets, pileup jets are included as an additional jet class in the NN training. Given the low probability of simulating enough pileup jets with high p_T, this jet class is limited to jets with $p_T < 50$ GeV.

7.2.6 output classes

The categorization of the output classes used in neural network training and classification is based on the identification of the jets mentioned earlier. A total of 14 jet categories are employed, which encompass jets originating from prompt leptons/photons (E, MU, TAU, PH), heavy-flavored hadrons (C, B), light quarks (UDS), gluons (G), pileup (PU), as well as displaced jets originating from the HNL decay. The displaced jet subcategories are then grouped into larger macro classes: `LLP_Q`, `LLP_QQ`, and `LLP_RAD` are combined as `LLP_Q`, while `LLP_E`, `LLP_QE`, and `LLP_QQE` are grouped as `LLP_QE`. Additionally, `LLP_MU`, `LLP_QMU`, and `LLP_QQMU` are merged into `LLP_QMU`, and `LLP_TAU`, `LLP_QTAU`, and `LLP_QQTAU` are joined as `LLP_QTAU`.

7.2.7 NN performance and validation

The tagger output configuration is defined as the ratio of the discriminant of a given displaced jet class over the sum of the discriminant of all SM jet classes as follow

$$P(X/\mathrm{SM}|\,\mathrm{L_{xy}}) = \frac{P(X|\,L_{xy})}{\sum\limits_{c}^{\mathrm{SM}} P(c|\,L_{xy})} = \frac{P(X|\,L_{xy})}{1 - \sum\limits_{c}^{\mathrm{LLP}} P(c|\,L_{xy})} \tag{7.1}$$

$$\Rightarrow \hat{P}(X/\mathrm{SM}) = \max_{L_{xy}} [P(X/\mathrm{SM}|\,\mathrm{L_{xy}})] \tag{7.2}$$

where X is the displaced jet output classes (`LLP_QMU`, `LLP_QE`, `LLP_QTAU` and `LLP_Q`) defined above. The discriminant is transformed using a monotonic function defined in the following to modify the output configuration interval from $[0; \infty]$ to [0; 1] for clarity

$$P(X/\mathrm{SM}|\,L_{xy}) := \frac{1}{\log_{10}(1+10^4)} \times \log_{10}\left[1 + \frac{P(X|\,L_{xy})}{\max\left(10^{-4};\ \sum\limits_{c}^{\mathrm{SM}} P(c|\,L_{xy})\right)}\right], \tag{7.3}$$

The confusion matrix, a table that summarizes the performance of the classification model, is shown in figure 7.2. It illustrates the occurrence of predicted jet class c (x-axis) normalized with respect to each possible true jet class t (y-axis), denoted as $N(c|t)$. The matrix is normalized such that the sum of $N(c|t)$ over all predicted classes c equals 1 for every true jet class. The performance of the NN is in general good, with a high percentage of prompt E/MU/TAU/PH jets being correctly identified (77%/95%/69%/93%, respectively). The efficiency is a bit lower for displaced jet classes `LLP_QE`/`LLP_QMU` jets, with accuracies of about 66% and 89%, respectively. There is some confusion between the displaced `LLP_Q` and `LLP_QTAU*` classes identification, where about 20% of `LLP_Q` jets are incorrectly identified as `LLP_QTAU` jets. P(Q + TAU) discriminant has been defined as a combination of `LLP_Q` and `LLP_QTAU*` discriminant at the analysis level to maximise the NN performance whenever such a misidentification occures.

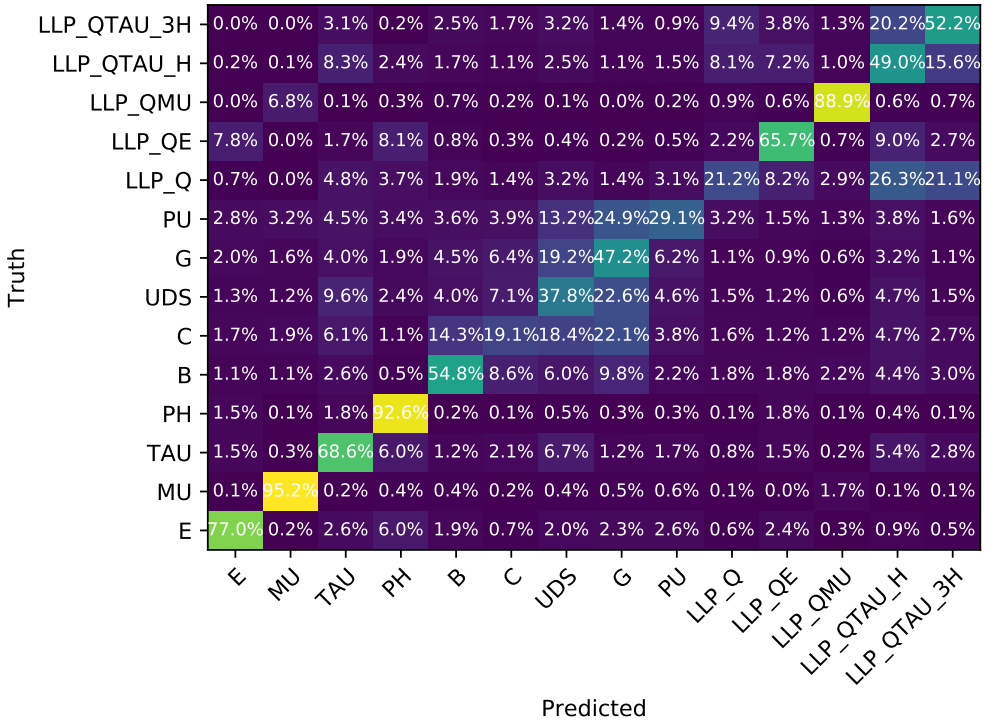

Figure 7.2: Confusion matrix quoting the normalized occurrence of how often a jet class is predicted (x axis) for each possible true jet class (y axis).

A ROC (Receiver Operating Characteristic) curve is a graphical representation that illustrates the performance of a binary classification model by plotting the trade-off between its true positive rate (sensitivity) and false positive rate (1-specificity) at various threshold settings. It helps to assess the model's ability to discriminate between classes. Figure 7.3 shows the ROC curves for several displaced HNL jet classes with a mass of $m_N = 4.5$ GeV and multiple proper decay length and SM jet classes. The ROC curves are shown for the 2016 data taking conditions. The tagger can accurately distinguish jets with lifetimes ranging from 10-100mm. It can reject 99.9% of UDS+G SM jets while retaining 20-30% of `LLP_Q` or `LLP_QTAU` jets. For `LLP_QMU`(`LLP_QE`) jets, it can keep around 80-90% (40-50%) of the jets and reject 99.9% of UDS+G SM jets, showcasing even higher discrimination power. Additionally, the performance of the tagger in overall displaced jet classes increases for higher displaced jets up to 10 mm. The `LLP_QMU` class shows the best performance compared to other displaced jet classes, with discrimination improving up to 100 mm. This is due to the additional information provided by the CMS muon chambers, which helps in the reconstruction of very displaced tracks.

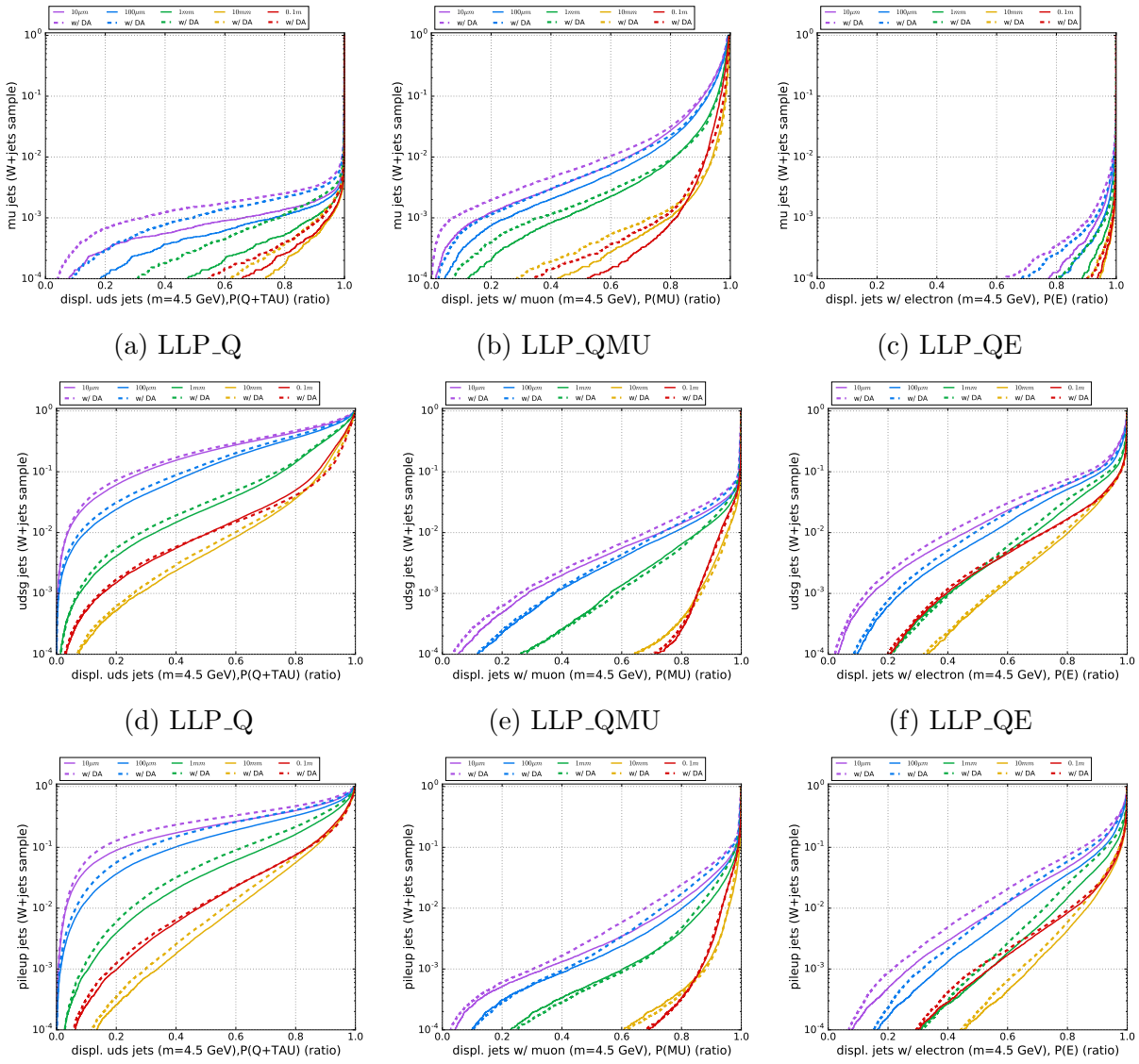

(a) LLP_Q (b) LLP_QMU (c) LLP_QE

(d) LLP_Q (e) LLP_QMU (f) LLP_QE

(g) LLP_Q (h) LLP_QMU (i) LLP_QE

Figure 7.3: An example of ROC curves of the trained tagger for displaced HNL jet classes(LLP_Q, LLP_QMU and LLP_QE)(columns), for HNL samples with mass $m_N = 4.5$ GeV and several lifetimes, against SM jets (mu, pileup and udsg) (rows), selected from an inclusive sample of W+jets production in 2016 conditions. An example Figure (h): For HNL with c$\tau = 0.1$ m, True LLP$_Q$ $Ejetareidentifiedwithefficiency$ 70%$whileTrueUDSjetsareselectedby10^{-4}$.

Extensive research has been conducted on the modeling of the tagger in the DY control region in both resolved and merged scenarios for all categories in the DY control region. To evaluate the modeling, Figure 7.4 displays distributions of NN discriminants for select categories. It was found that the simulation accurately represented the data for all displaced jet classes. This is a necessary step to validate the tagger performace on data. Therefore, the tagger performance in descriminating between signal and background on data is the same as on simulation and shown in ROC curves 7.3.

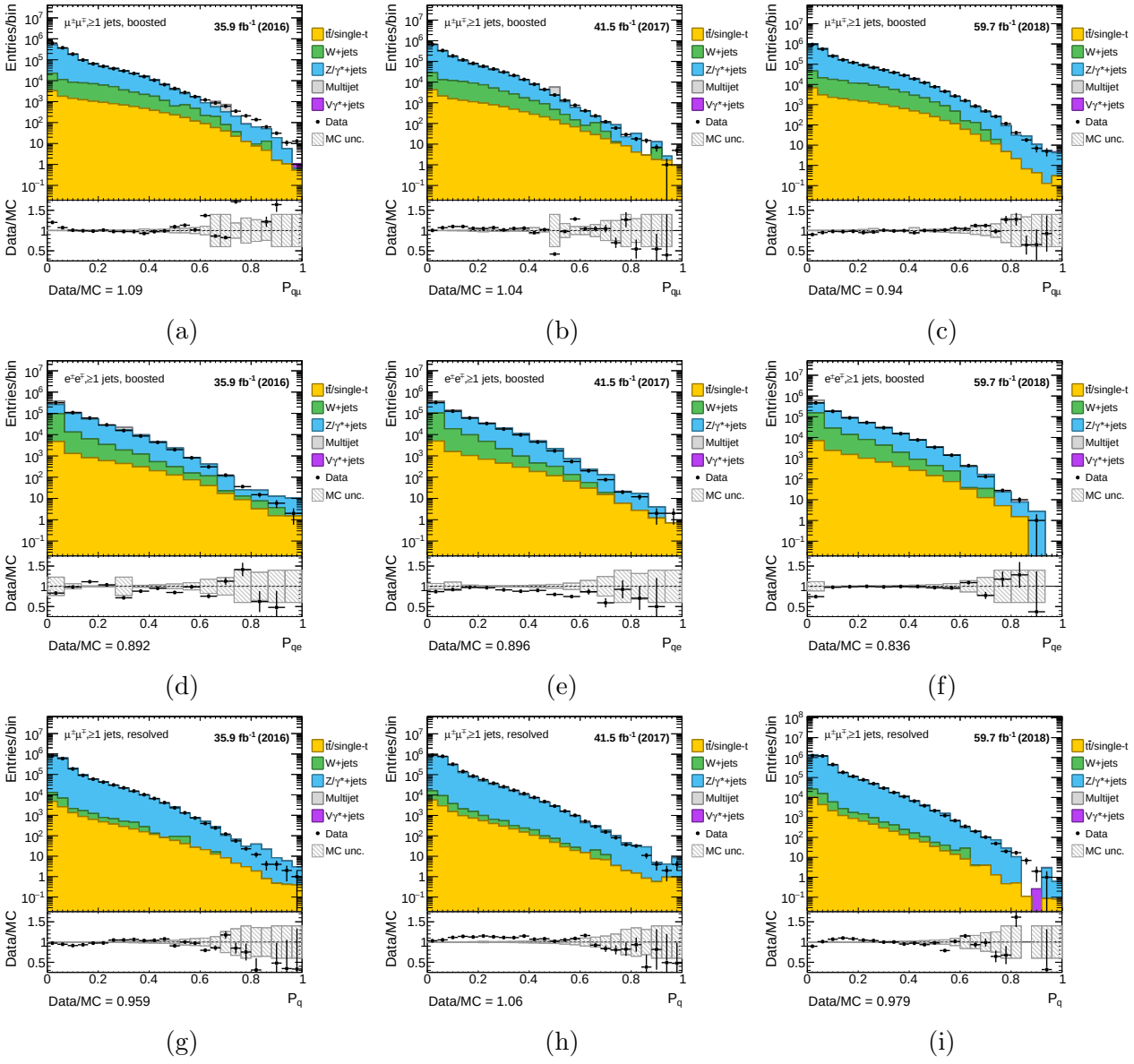

Figure 7.4: Data/MC agreement of the tagger score in the high dilepton mass control region, boosted muon class (LLP_QMU). The distributions are shown for the 2016, 2017, and 2018 scenarios in the left, middle and right columns, respectively. The distributions are shown for the OS dimuon category in the first row, and the SS electron-muon mixed flavor category in the bottom row. Only Statistical uncertainty is considered in these plots.

Chapter 8

Background estimation for the HNLs search

8.1 Introduction

This section describes a data-driven ABCD background estimation matrix method that uses the displaced jet tagger score, $P \in (P_{q\mu}, P_{qe}, P_q)$, and $m(\ell_1, \ell_2, \mathrm{j}^\star)$, which corresponds to the W boson mass in signal events. The procedure for choosing the optimal thresholds on these variables per SR category is explained. The background composition and the validity of the background estimation method are investigated. Tests that investigate the closure of the method, i.e. the agreement between the number of expected and observed background events, in different validation regions (VRs) are introduced. Finally, the procedure to cover for residual difference (i.e. non-closure) systematic uncertainty is described.

8.2 ABCD method

The basic idea of ABCD methods [33] is to choose two observables (X, Y), which are simultaneously statistically independent for the background processes and offer discrimination between the signal and background classes. The statement of independence of two variables implies that the probability density function factorizes:

Table 8.1: Boosted and resolved signal regions.

Boosted SR	Resolved SR
Preselections	Preselections
$70 < m(\ell_1, \ell_2, \mathrm{j}^\star) < 90$	$70 < m(\ell_1, \ell_2, \mathrm{j}^\star) < 90$
$P_{high} > 0.4$	$P_{high} > 0.2$

$$\rho(x, y) = p(x)q(y), \tag{8.1}$$

In other words, the normalized distribution of one variable is unaffected by any selection on the second one. By applying thresholds on these observables, events are partitioned into four regions. Three of these regions, called A, B, and C, are background-dominated control (sideband) regions, while the fourth, D, contains most of the signal events. If the observables are independent, then the background contribution in the SR can be predicted from the three sideband regions as

$$\hat{n}_{\mathrm{D}}^{\mathrm{bkg}} = n_{\mathrm{B}}^{\mathrm{bkg}} \times n_{\mathrm{C}}^{\mathrm{bkg}} / n_{\mathrm{A}}^{\mathrm{bkg}}, \tag{8.2}$$

where n_X^{bkg} is the number of background events per region.

The 2D distributions in figure 8.1 show the subdivision of the available phase space into the ABCD regions. The low tagger score $P_{low} < 0.2(0.1)$ for boosted (resolved) are not used for the reasons mentioned in section 8.4. The two signal regions (region D) for boosted and resolved are defined in Table 8.1 where P_{high} is the high tagger threshold used to define the signal region for the background studies on data. For the final results, the P_{high} are further optimised in section 8.3. For simplification, the $m(\ell_1, \ell_2, \mathrm{j}^\star)$ window is fixed to $[70; 90]$ GeV in this analysis. It was found from the study presented in section 8.3 that varying the mass window yields only negligible gain in sensitivity as compared to optimizing the tagger threshold (score).

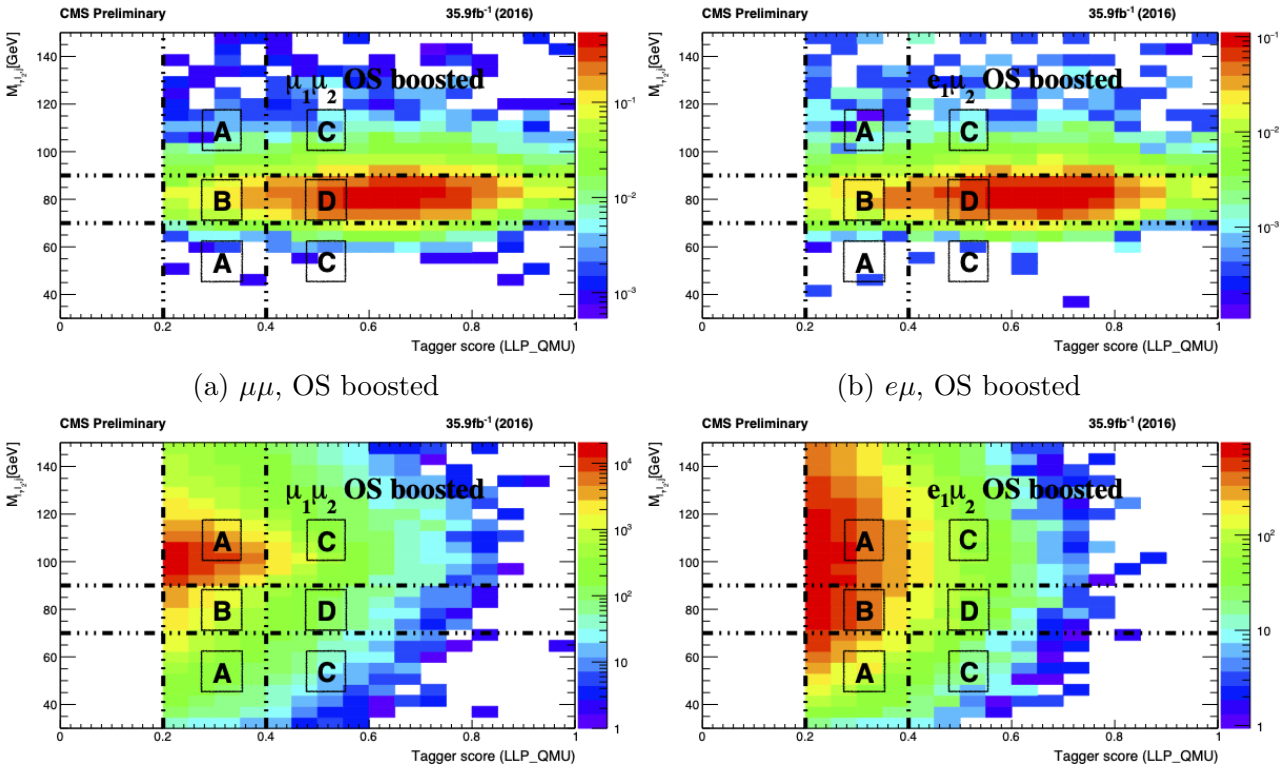

(a) $\mu\mu$, OS boosted

(b) $e\mu$, OS boosted

(c) $\mu\mu$, OS boosted

(d) $e\mu$, OS booseted

Figure 8.1: 2D plots of the three body mass as a function of the displaced jet tagger information for two different SR categories with inclusive displacement. Signal (top row) and background from simulation (bottom row).

8.3 Tagger threshold optimisation

In this section, the procedure of optimising the tagger threshold is described. The figure of merit used in the optimisation is the discovery sensitivity given in the following [38]

$$Z = \left[2\left((s+b)\ln\left[\frac{(s+b)\,(b+\sigma_b^2)}{b^2+(s+b)\sigma_b^2}\right] - \frac{b^2}{\sigma_b^2}\ln\left[1+\frac{\sigma_b^2 s}{b\,(b+\sigma_b^2)}\right]\right)\right]^{1/2} \tag{8.3}$$

where s, b are the expected signal and background yields, respectively, and σ_b is the uncertainty on the background prediction. In the case $s \ll b$ and $\sigma_b \sim 0$, the expression reduces to $Z \sim s/\sqrt{b}$.

To optimise the thresholds for each category and year without unblinding, a sideband is considered in the tagger score of $0.1(0.2) <$ tagger $< 0.2(0.4)$ for resolved (merged) categories and in Δm, defined as $|m(\ell_1, \ell_2, \mathrm{j}^\star) - m_\mathrm{W}|$, of 10 GeV. In the tagger sideband, the ratio of events above and below a Δm threshold is calculated in data as $N_{A'}/N_{B'}$. In the Δm sideband the ratio of events above and below the tagger threshold is calculated in data as $N_{C'}/N_{B''}$. The threshold in Δm is kept constant at 10 GeV as the performance is seen not to depend strongly on varying this parameter. Thresholds in tagger are scanned (in data) with the number of events in the signal region D calculated as N_B (observation in data inverting tagger and Δm cuts)$\times r_{A'/B'} \times r_{c'/B''}$. A cartoon showing this method is shown in figure 8.2. For each threshold value, the significance is calculated for a range of benchmark models shown in table 8.2. For each mass and lifetime, five couplings are considered: pure electron, pure muon, electron and muon, electron and tau, and muon and tau. The significance relative to the maximal significance over all categories and thresholds is then calculated for each benchmark (σ_{rel}). The σ_{rel} for each threshold is summed over all benchmark signal masses, lifetimes, and couplings, and the threshold with the highest value of $\sum \sigma_{rel}$ is chosen. The optimised thresholds are shown in figure 8.3.

Table 8.2: Signal samples used to optimise thresholds. For each mass and lifetime five couplings are considered: pure electron, pure muon, electron and muon, electron and tau, and muon and tau

mass (GeV)	$c\tau$ (mm)
2	1000
4.5	100
8	10
10	1
12	0.1
16	0.001

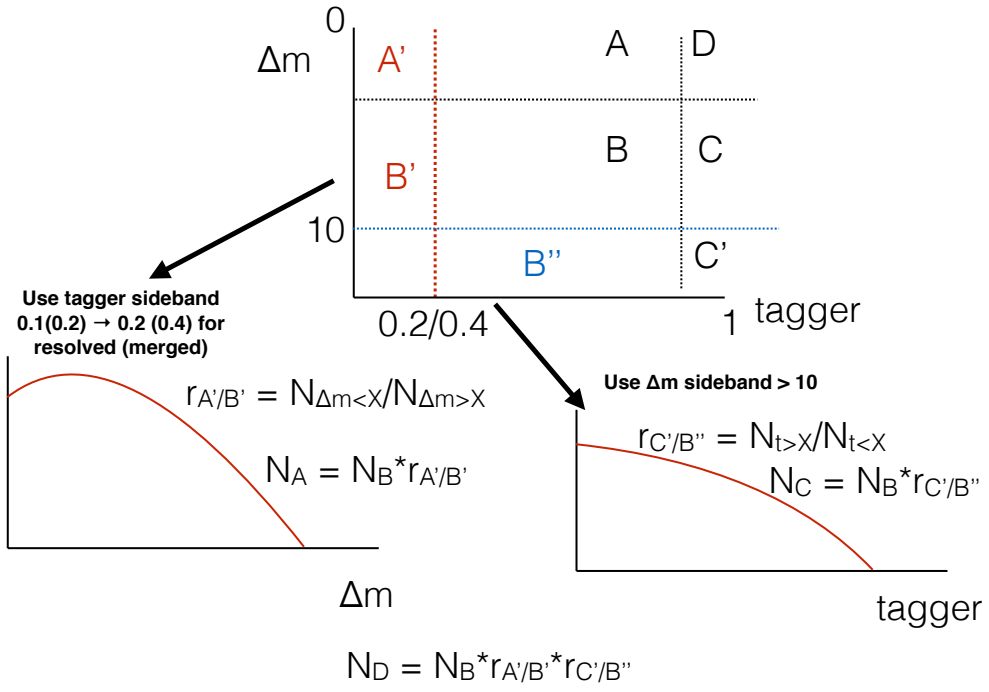

Figure 8.2: Cartoon showing sideband method for chosing thresholds without unblinding.

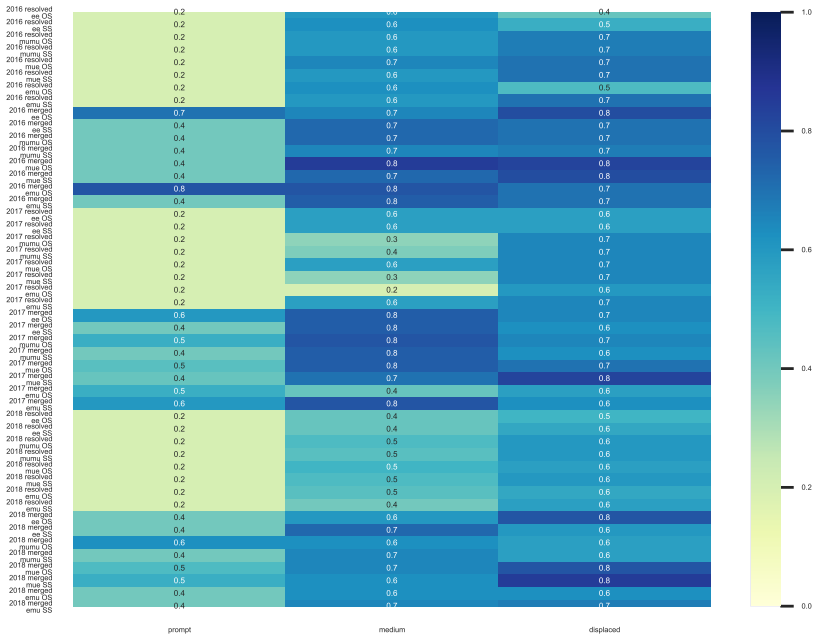

Figure 8.3: The optimised thresholds on the jet tagger. These thresholds are used as cuts on the tagger score per category.

8.4 Background studies in validation regions

In this analysis, only the sum of all backgrounds is estimated through the ABCD method. Even if the individual background processes separately satisfy the independence condition (Equation 8.1), it might not hold for the sum of background processes that have different distributions in one of the ABCD variables

$$\rho(x,y) = \rho_1(x,y) + \rho_2(x,y) = p_1(x)q_2(y) + p_2(x)q_2(y) \neq p(x)q(y). \tag{8.4}$$

For the ABCD assumption to hold for the sum of several background processes, the normalized distribution in at least one of the two ABCD variables has to be the same for all background processes, $p_1(x) = p_2(x) = p(x)$

$$\rho(x,y) = p(x)(q_1(x) + q_2(x)) \stackrel{!}{=} p(x)q(x). \tag{8.5}$$

To verify the validity of the method, the shape of the two variables, the tagger score, and the $m(\ell_1, \ell_2, \mathrm{j}^\star)$, were studied in the VRs in the data. Figure 8.4 shows the distribution of the three body mass for $\mu\mu$ OS prompt category in two regions of the tagger score validation region (VR) $[0, 0.2]$ and $[0.2, 0.4]$ while figure 8.5 shows the tagger distribution in the $m(\ell_1, \ell_2, \mathrm{j}^\star)$ signal sideband regions for the same category. For both variables, the two distributions have different shapes. Several other prompt categories are shown in Figs. 8.6 and 8.7 where a similar effect was observed. In summary, this issue is present in most of the prompt categories, in the 3 years of data taken and it is more pronounced in boosted than resolved categories. Thus, following Equation 8.4, the "vanilla" ABCD method does not work for the prompt categories. Studying this further, several investigations have been performed. Additional selections on the tagger score and hadronic energy fraction (fraction) were studied and deployed to improve the applicability of the method as described in the following sections.

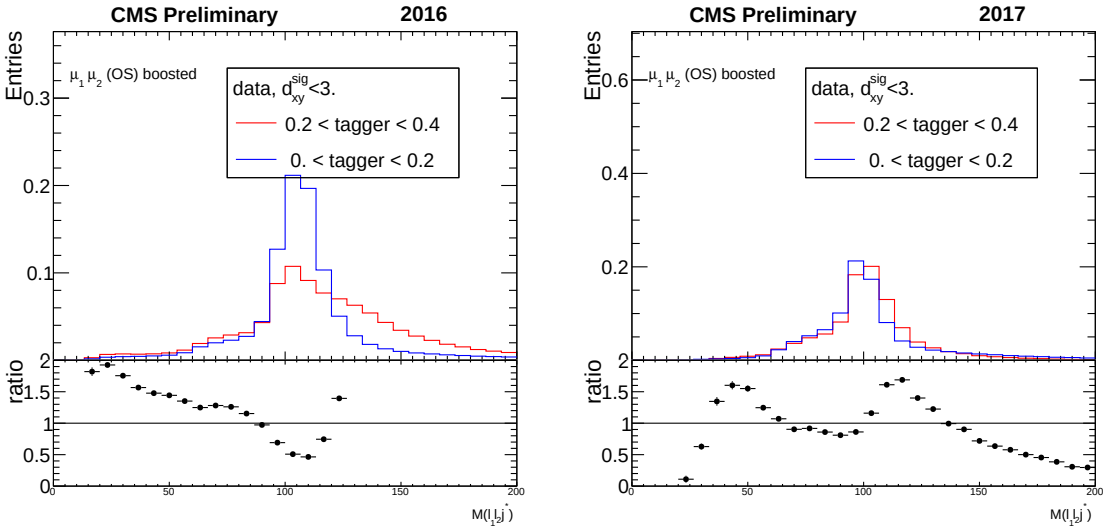

(a) 2016 $m(\ell_1, \ell_2, \mathrm{j}^\star)$

(b) 2017 $m(\ell_1, \ell_2, \mathrm{j}^\star)$

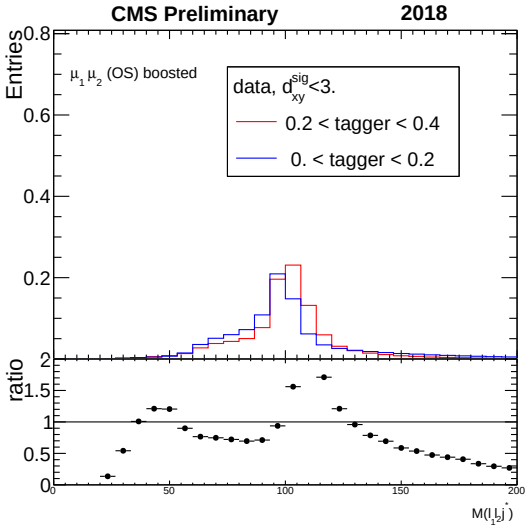

(c) 2018 $m(\ell_1, \ell_2, \mathrm{j}^\star)$

Figure 8.4: The $m(\ell_1, \ell_2, \mathrm{j}^\star)$distribution in data in low and high tagger score VR regions [0. , 0.2] and [0.2 , 0.4] respectively, for $\mu\mu$ OS boosted prompt category for 2016, 2017 and 2018.

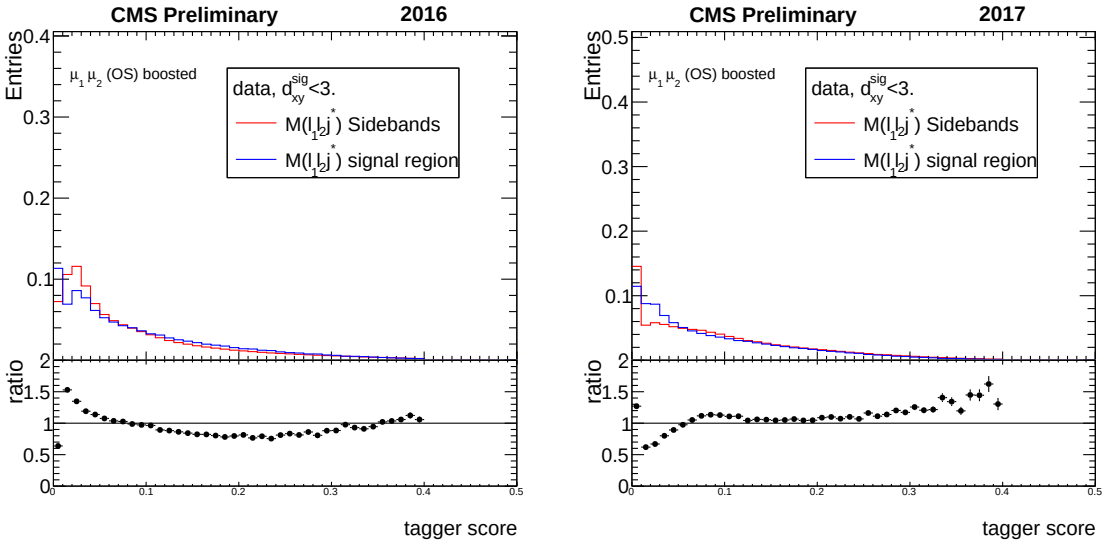

(a) 2016 tagger

(b) 2017 tagger

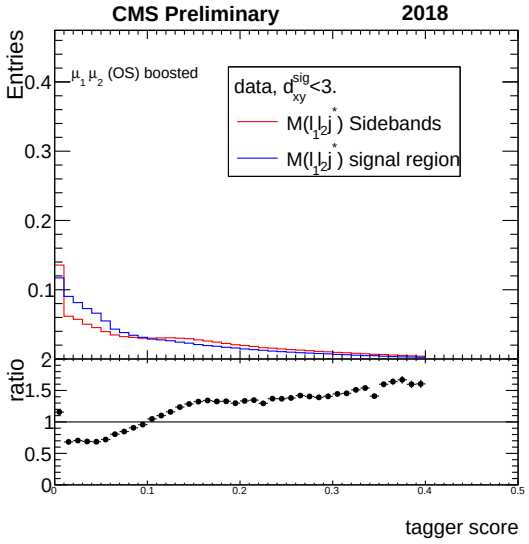

(c) 2018 tagger

Figure 8.5: The tagger score distribution in signal and sideband $m(\ell_1, \ell_2, \mathrm{j}^\star)$regions, for $\mu\mu$ OS boosted prompt category for 2016, 2017 and 2018.

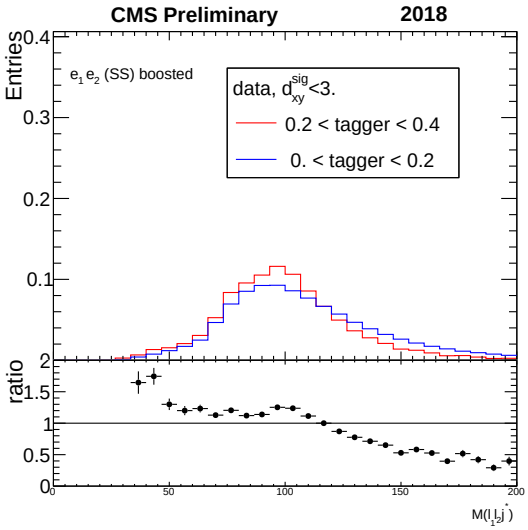

(a) ee, SS boosted

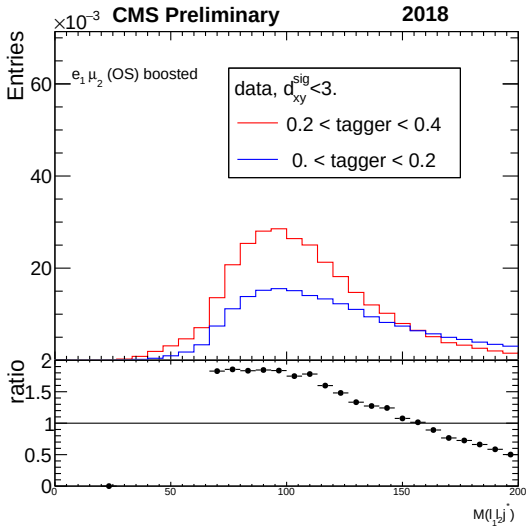

(b) $e\mu$, OS boosted

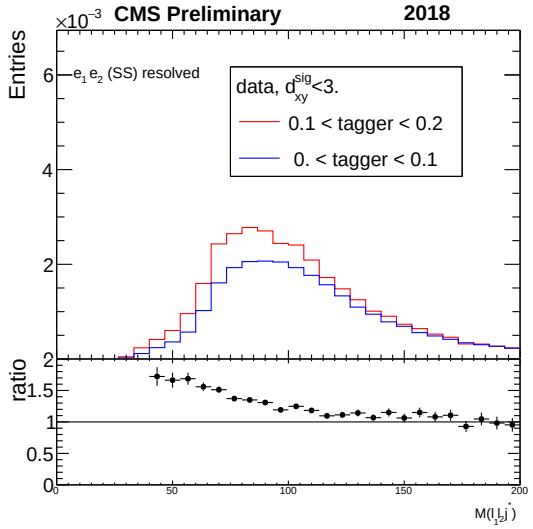

(c) ee, SS resolved

Figure 8.6: The $m(\ell_1, \ell_2, \mathrm{j}^\star)$distribution in data in low and high tagger score VR regions [0. , 0.2] and [0.2 , 0.4] respectively for 3 prompt categories for 2018.

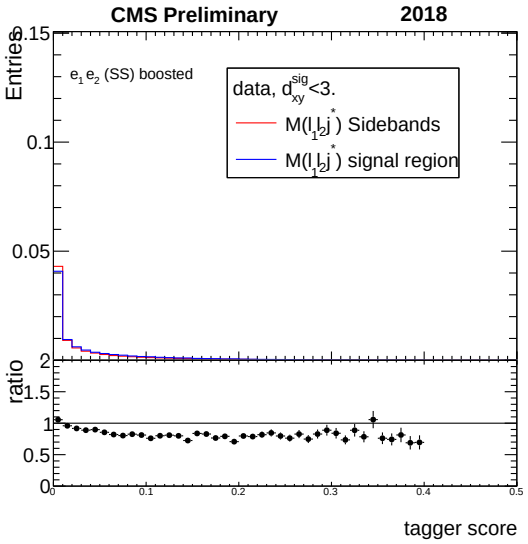

(a) ee, SS boosted

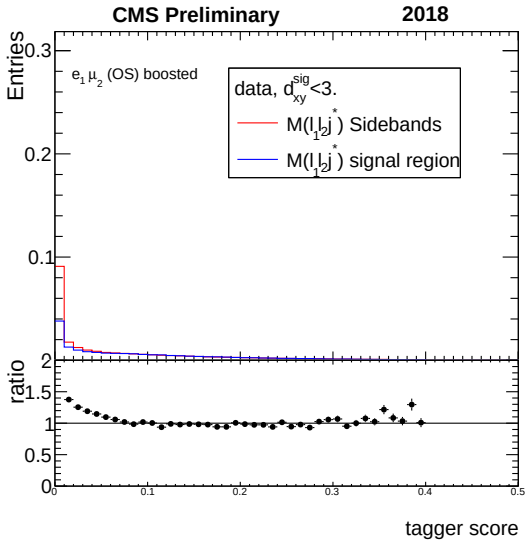

(b) $e\mu$, OS boosted

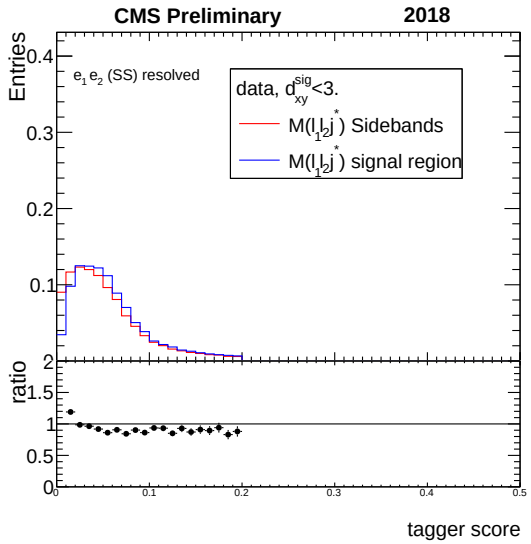

(c) ee, SS resolved

Figure 8.7: The tagger score distribution in signal and sideband $m(\ell_1, \ell_2, \mathrm{j}^\star)$regions for 3 prompt categories for 2018.

8.4.1 Standard model background suppression

Prompt categories

In order to understand the background composition at low and high tagger VRs two variables have been studied in the $\mu\mu$ OS and ee OS prompt categories where the issue was highly pronounced. The first variable is the (ℓ_2) p_T and the second is α defined as following

$$\alpha = \ell_2 p_T - \text{hadrons } p_T. \tag{8.6}$$

Figure 8.8 (left) shows the $\ell_2 p_T$ for the low and high tagger regions. For low tagger region the distribution has two peaks: the first at low and the second at high ℓ_2 p_T. For the high tagger region the distribution is smooth. Figure 8.8 (right) shows the distribution of α. The α variable describes the isolation of the ℓ_2. Similar to $\ell_2 p_T$, it has two peaks in low tagger region. The first peak occurs when $\ell_2 p_T$ is much higher than the hadrons p_T (ℓ_2 is nearly isolated) and the second peak when $\ell_2 p_T$ is smaller than the hadrons p_T (ℓ_2 is non isolated). For high tagger region, the distribution is smooth. Therefore, and based on figure 8.9, we distinguish two types of backgrounds in low tagger region and a third type of backgrounds in high tagger region.

Type-I Low tagger score: Low p_T non-isolated ℓ_2 corresponding to any SM backgrounds with a lepton originating from a heavy flavour jet hadronisation or a lepton overlapping with a pile up jet as explained in section 4.4. The latter is dominated by QCD background given its high cross section. This background is present in all categories.

Type-II Low tagger score: High p_T nearly isolated ℓ_2 corresponding to Z/γ^*+jets background. This background specific to $\mu\mu$/ee OS categories

Type-III High tagger score: No distinct features are present in the distributions of ℓ_2 p_T and α in high tagger region. This background is present in all categories.

To conclude, based on this study, the low tagger score region is dominated by SM processes with well-identified prompt jets (reducible background = Type-I and Type-II backgrounds) while the high tagger region is dominated by misidentified jets that look to be displaced (irreducible

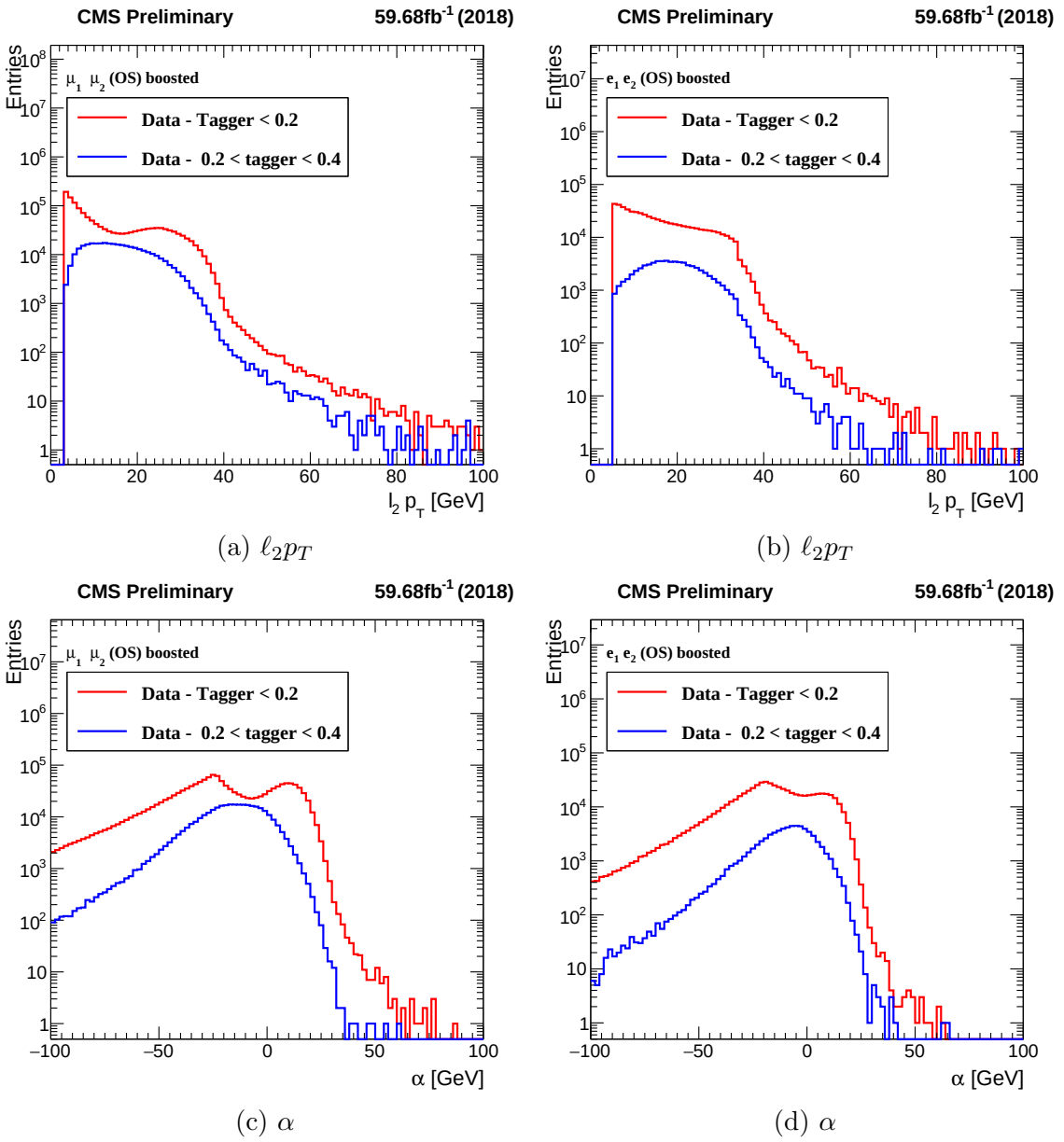

(a) $\ell_2 p_T$ (b) $\ell_2 p_T$

(c) α (d) α

Figure 8.8: Background distribution in low and high tagger score regions for $\mu\mu$ OS and ee OS prompt bins in data.

background = Type-III) which is the major background for this analysis to be considered. To reject undesired prompt background, which does not correspond to the background in the signal region, a lower cut on the tagger score of 0.2(0.1) for boosted(resolved) categories was applied during the background estimation. The distribution of the three-body mass in two high tagger VRs $[0.2, 0.3]$ and $[0.3, 0.4]$ has a much better agreement as can be seen Figs. 8.10 and 8.11. This selection does not affect the signal in the SR (tagger score $> 0.4(0.2)$ for boosted(resolved)). Residual Type-I and Type-II backgrounds suppression at high tagger score in the prompt

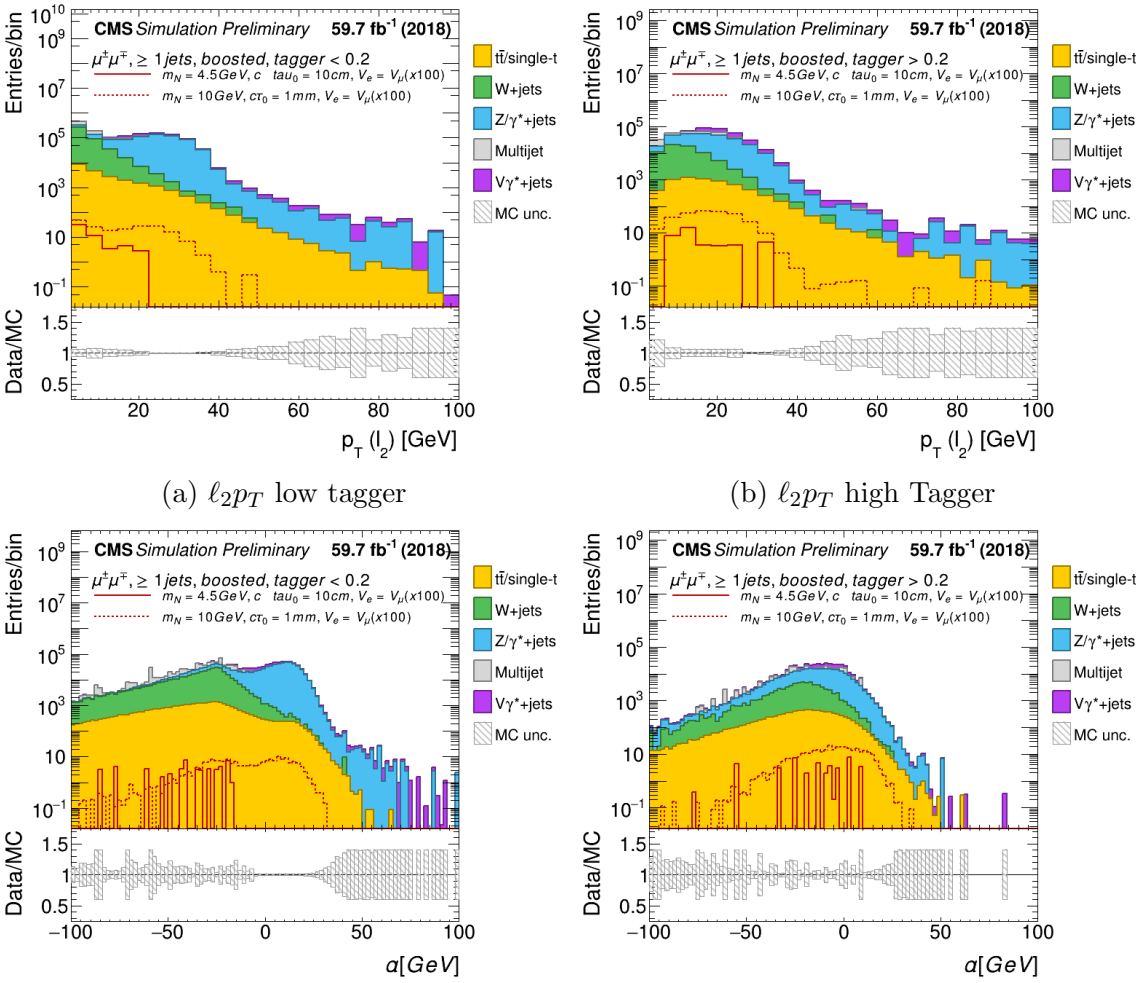

(a) $\ell_2 p_T$ low tagger

(b) $\ell_2 p_T$ high Tagger

(c) α low tagger

(d) α high Tagger

Figure 8.9: Background distribution in low and high tagger score regions for $\mu\mu$ OS prompt bin in simulation.

categories is discussed in section 8.4.2 and 8.4.3 to further improve the performance of the background prediction method.

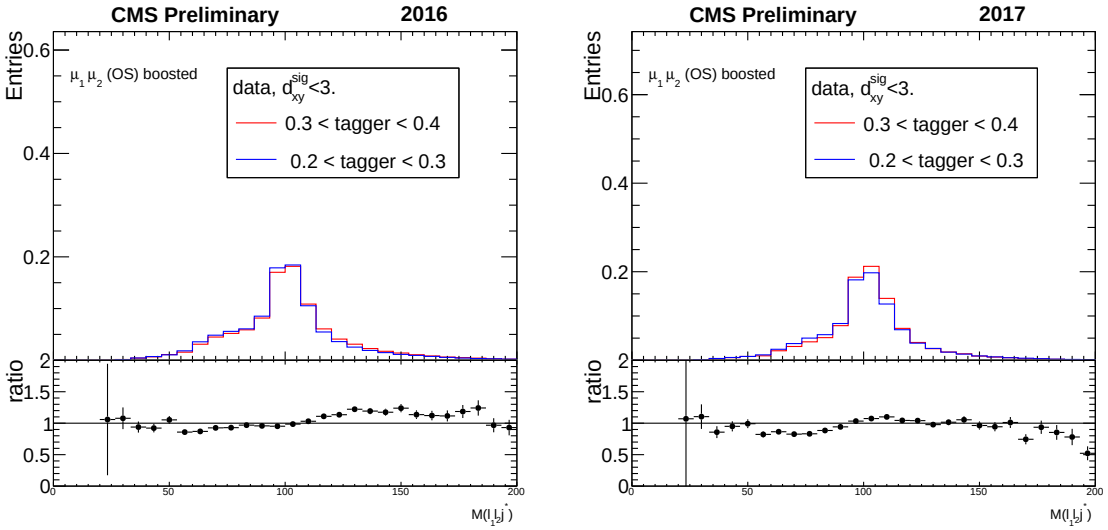

(a) 2016

(b) 2017

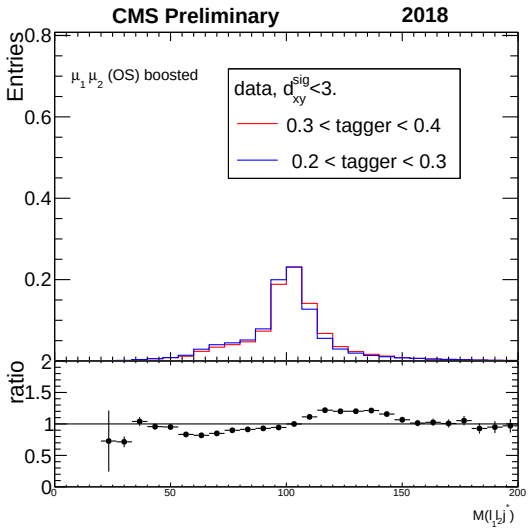

(c) 2018

Figure 8.10: The distribution in data of the 3 body mass in two high tagger score VR regions [0.2 , 0.3] and [0.3 , 0.4] for $\mu\mu$ OS boosted prompt category for 2016, 2017 and 2018.

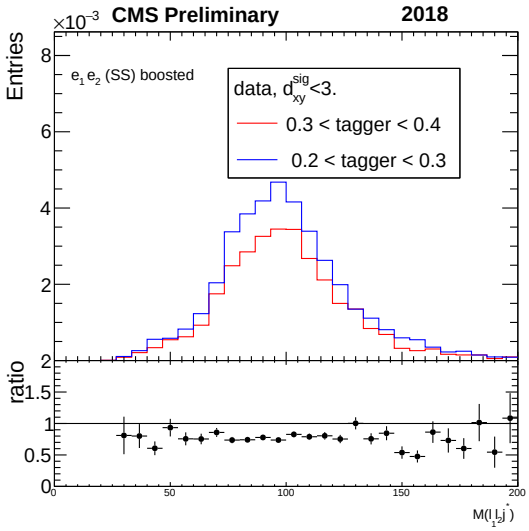

(a) ee, SS boosted

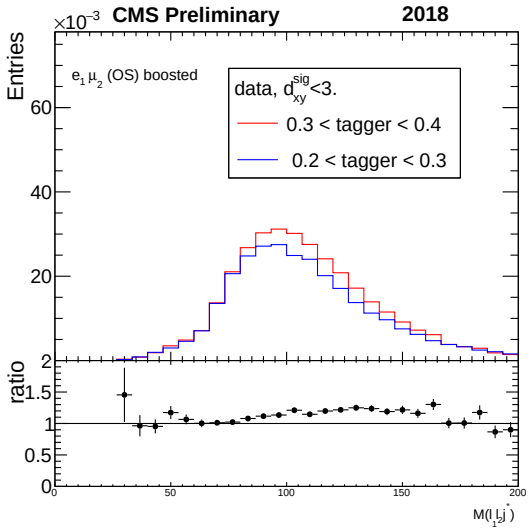

(b) $e\mu$, OS boosted

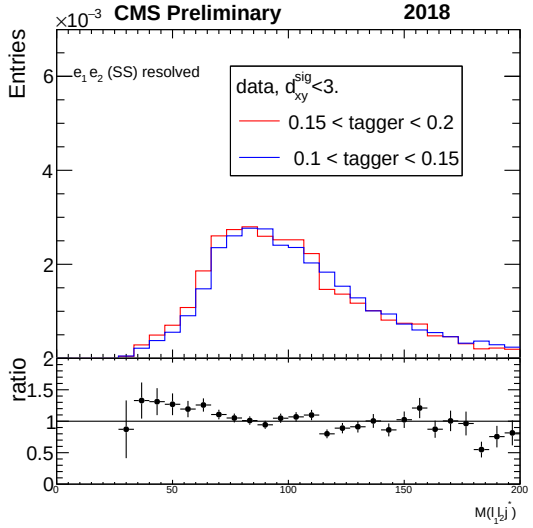

(c) ee, SS resolved

Figure 8.11: The distribution in data of the 3 body mass in two (low and high) tagger score VR regions $[0., 0.2]$ and $[0.2, 0.4]$ respectively, for 3 prompt categories for 2018.

Medium and displaced categories

For the medium and displaced categories, the contamination from prompt processes was lower as the background is expected to be mostly from misreconstructed events (i.e. tracking failure) and not from well-identified standard model processes. Nevertheless, increasing the tagger threshold for these categories improves the performance of the method (i.e. closure). A minimum threshold on the tagger is then also applied to reject prompt background in all categories. Residual Type-I and Type-II backgrounds at high tagger score were suppressed as discussed in section 8.4.2 and 8.4.3.

8.4.2 Residual type-I background suppression

An additional optimization was performed to further reduce Type-I background contamination, dominated by multijet QCD process, for events with a tagger score larger than 0.2 and to further improve the closure of the background estimation in the SR categories. The HNL jet hadronic fraction is defined as

$$\text{fraction} \ = p_T(\mathrm{j}^\star)/p_T(\ell_2)\,. \tag{8.7}$$

The fraction is sensitive to Type-I background as shown in figure 8.16, which is mostly found at high fraction values for both boosted and resolved categories. A customised cut on the fraction value is applied per category.

Prompt categories

For all prompt resolved categories, the fraction cut is required to be less than 4.0 to improve the significance. For boosted prompt categories, tighter cuts are applied per year to further reduce the Type-I background which leads to an improvement in the closure tests in VR1 and VR3 defined in section 8.5. The use of customized values per year is a result of the different data-taking conditions i.e. especially the differences in the pileup activity. The tighter value was applied to the 2017 and 2018 datasets which have the highest pileup contribution. Figure. 8.12 and 8.13 show the $m(\ell_1, \ell_2, \mathrm{j}^\star)$ in two high tagger score validation regions $[0.2, 0.3]$ and $[0.3, 0.4]$, for boosted and resolved categories, after applying the fraction cuts where a

significant improvement was observed in the shape comparison of these two regions.

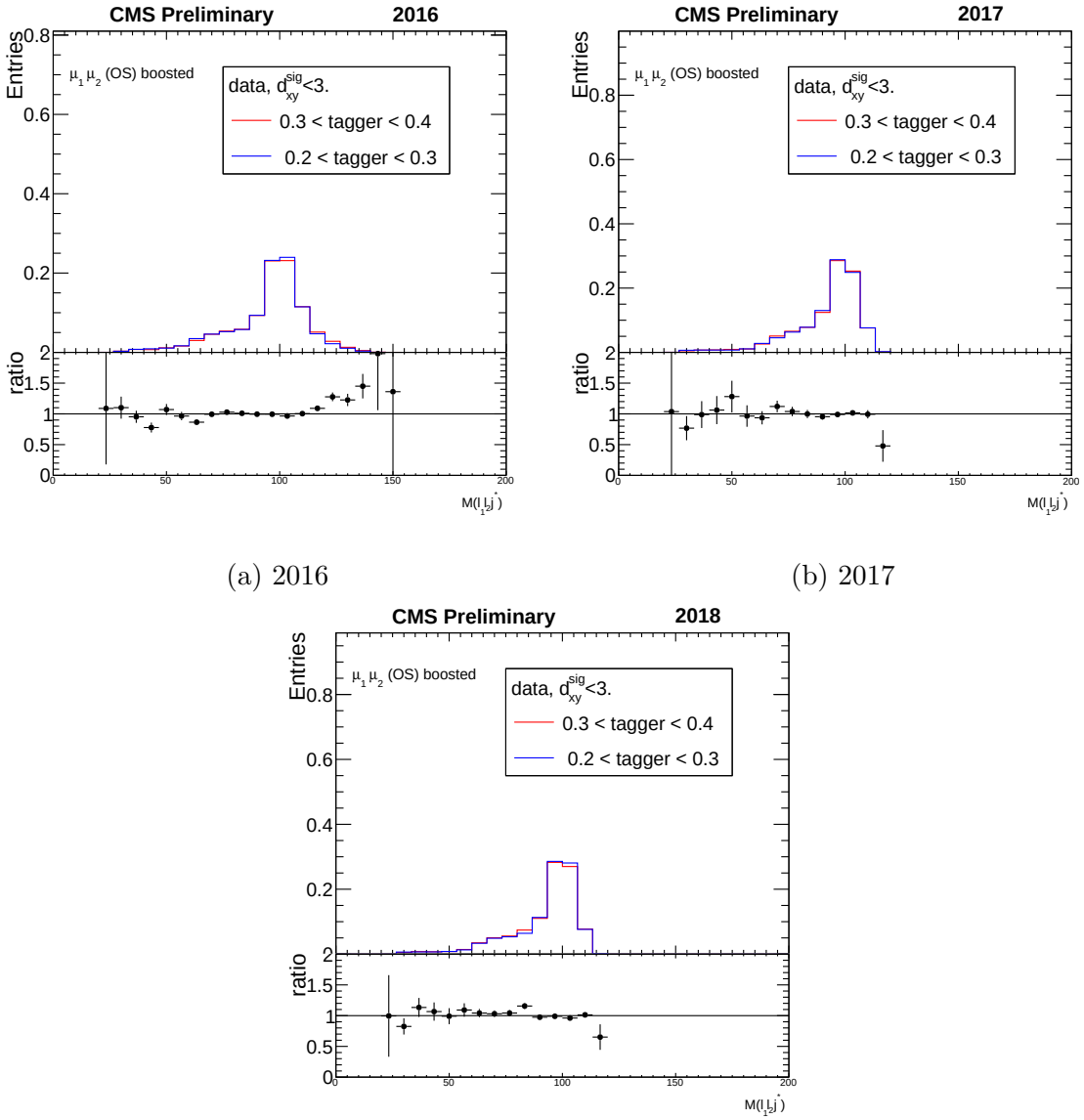

(a) 2016

(b) 2017

(c) 2018

Figure 8.12: The distribution of the 3 body mass in two high tagger score VR regions [0.2 , 0.3] and [0.3 , 0.4] including the fraction cuts for $\mu\mu$ OS boosted prompt category for 2016, 2017 and 2018.

Medium and displaced categories

For all resolved medium and displaced categories, similar to prompt ones, the fraction cut is required to be less than 4.0 to improve the sensitivity of the search. An example of the discrimination power of the fraction variable between the signal and data distributions in $m(\ell_1, \ell_2, \mathrm{j}^\star)$ SR and sidebands respectively is shown in figure 8.14 for displaced resolved categories

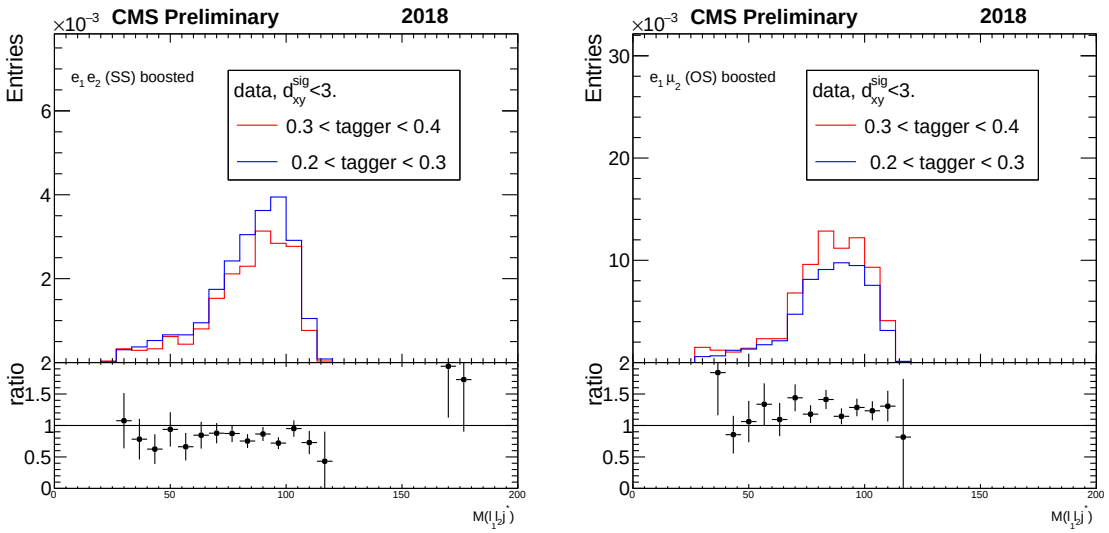

(a) ee, SS boosted (b) $e\mu$, OS boosted

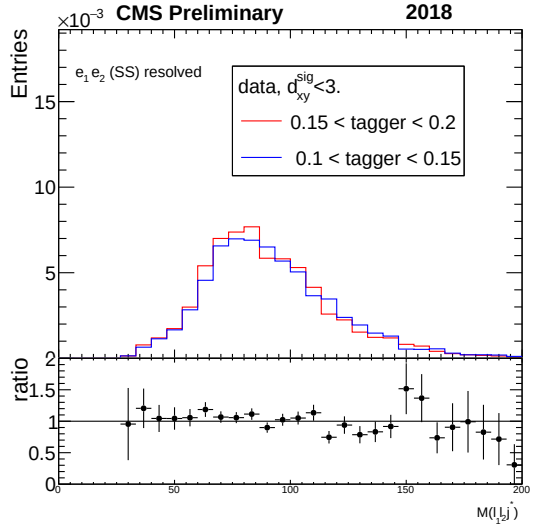

(c) ee, SS resolved

Figure 8.13: The distribution of the 3 body mass in two high tagger score VR regions [0.2 , 0.3] and [0.3 , 0.4] including the fraction cuts respectively, for 3 prompt categories for 2018.

after applying all preselections including the tagger.

For boosted medium and displaced categories, the fraction value is required to be less than 4.0 as well to improve the background prediction method in VR where a longer tail was found for the fraction distribution in data $m(\ell_1, \ell_2, \mathrm{j}^\star)$ sidebands compared to signal simulation in SR as shown in figure 8.15. Only for $\mu\mu$ OS categories a tighter cuts on the fraction are considered. This specific channel deserves a further more detailed study and it is discussed in section 8.4.3. The thresholds are tuned for two main reasons. To improve the background prediction method

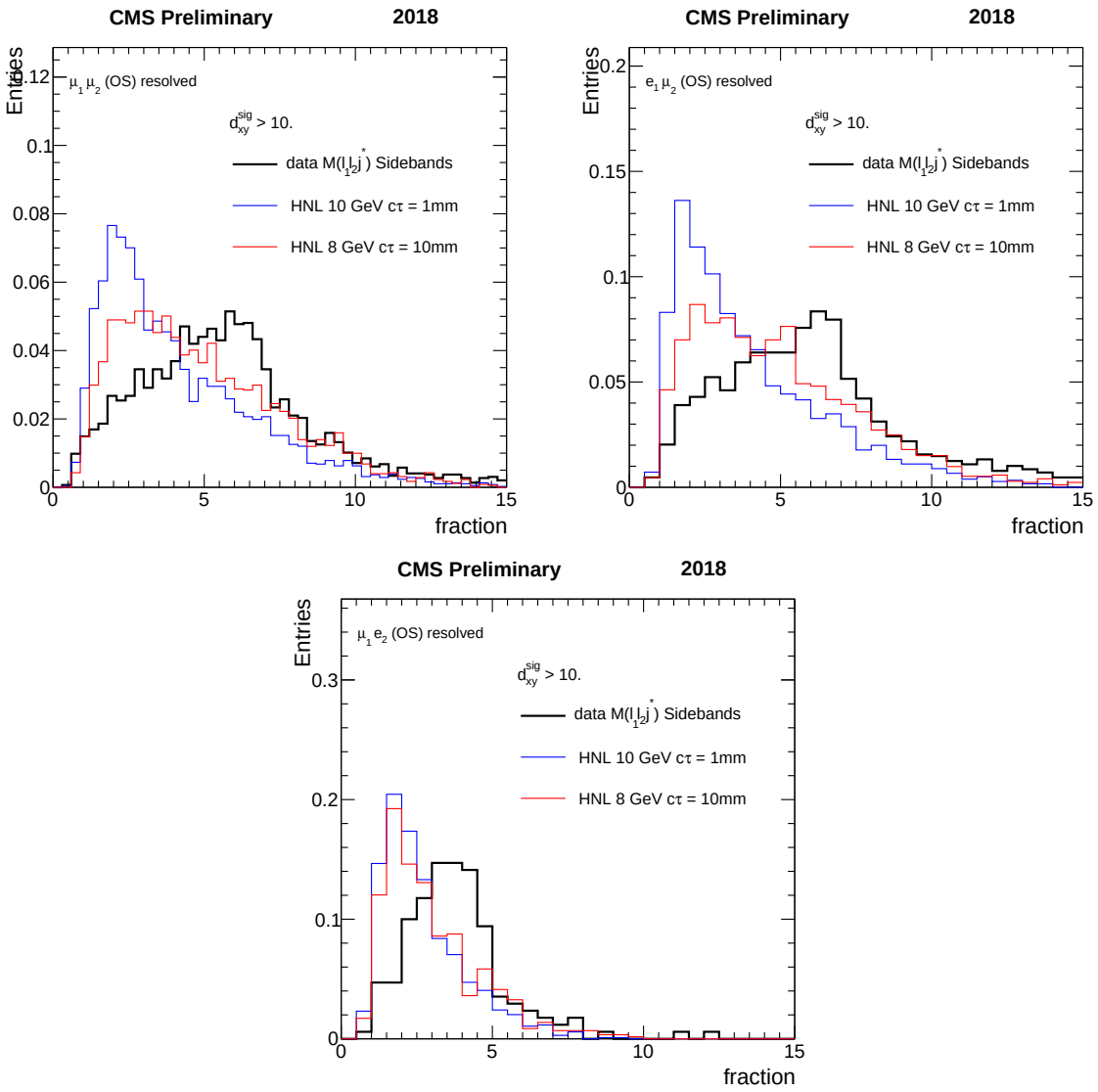

Figure 8.14: The fraction distribution for signal events in the signal region and data in the mass sideband regions for 3 displaced lepton flavor resolved for the year 2018.

and to increase the sensitivity for boosted and resolved categories respectively by rejecting Type-I background.

Signal efficiency of the fraction cuts

The signal efficiency of the fraction cuts as a function of HNL mass after applying the fraction cuts is shown in figure 8.17. The signal samples used are mentioned in table 8.3, which are the benchmark models that are in the vicinity of our expected sensitivity. Figure 8.17(a) shows the signal efficiency as a function of HNL mass after applying the fraction cuts in the prompt boosted categories. It demonstrates that these cuts have a negligible effect on the signal efficiency

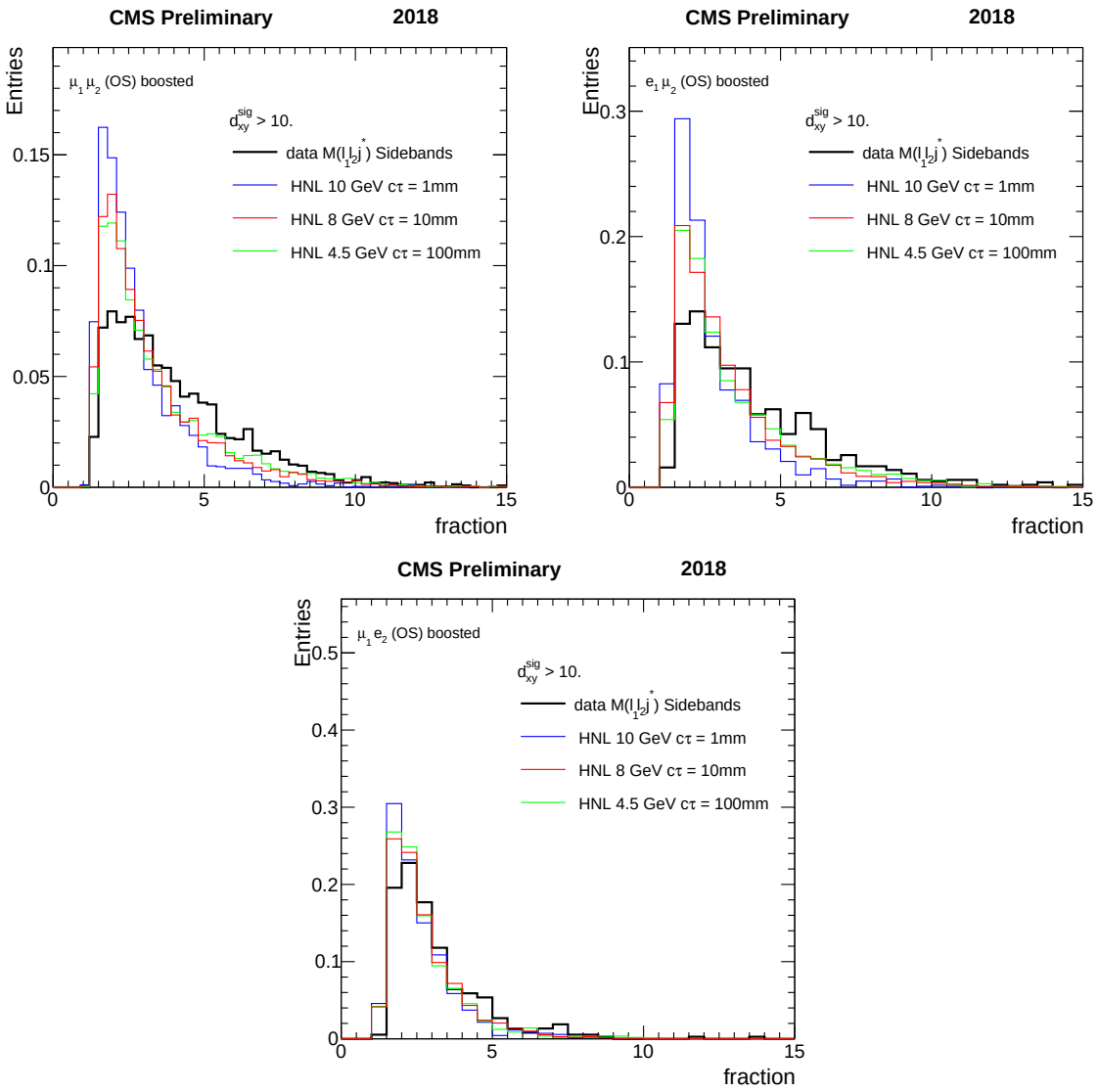

Figure 8.15: The fraction distribution for signal events in the signal region and data in the mass sideband regions for 3 displaced lepton flavor boosted categories for the year 2018.

where the signal efficiency is higher than 95% (90%) for events with muon(electron) in the final state for most of the HNL mass points. This is expected as the used signal samples are mostly categorised as displaced (section 6.6). Figure 8.17(b) shows the signal efficiency as a function of HNL mass after requiring the fraction value to be less than 4.0 in the medium and displaced categories in addition to the prompt cuts mentioned earlier. It shows that the cuts in the medium and displaced categories lead to a loss in signal events of approximately 30% (15%) for events with muon final state and electron final state respectively.

Despite the loss in signal efficiency, these cuts have a positive impact on the sensitivity. After applying these cuts, the expected limits improve in the intermediate-mass region between 6

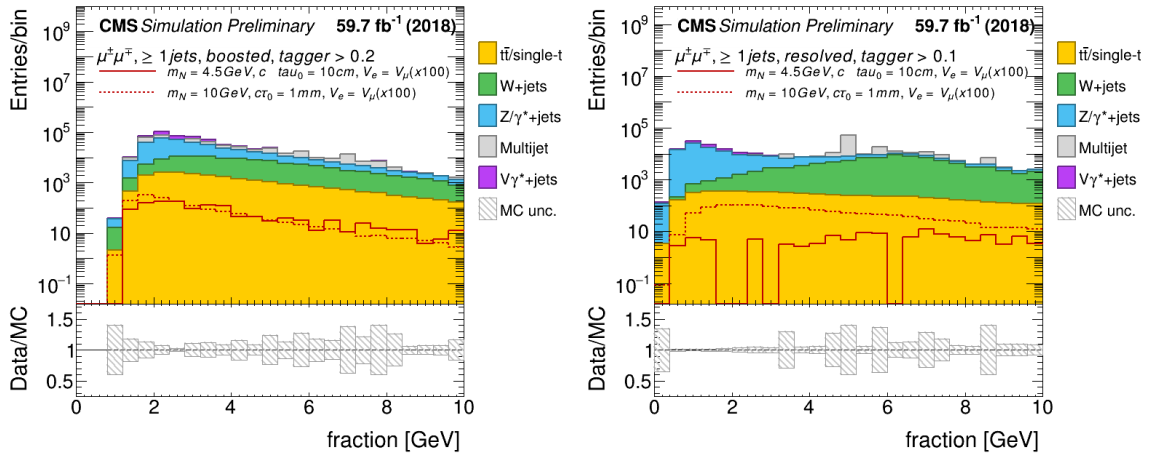

(a) Boosted (b) Resolved

Figure 8.16: The distribution of the fraction variable for $\mu\mu$ OS category for the year 2018.

GeV and 12 GeV due to the discrimination power of the fraction variable between signal and background in the resolved displaced categories as explained above. To further understand the situation, figure 8.18 shows the signal efficiency as a function of ℓ_2 p_T for HNL mass of 8 GeV and $c\tau = 10$ mm after applying all fraction cuts per category. It demonstrates that the main loss is in the events with ℓ_2 $p_T < 10$ GeV. The fraction cut is then an alternative way to reduce signal events with low ℓ_2 p_T that are indistinguishable from Type-I background.

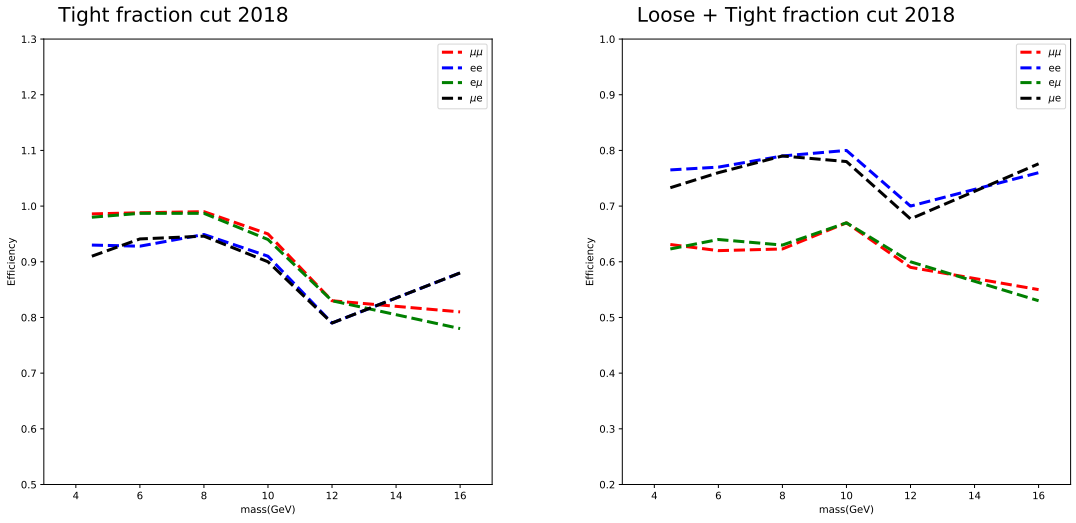

(a) (b)

Figure 8.17: Signal efficiency after applying the fraction cuts for HNL mass = 8 and $c\tau = 10$ for the year 2018.

Table 8.3: Signal samples used for the signal efficiency study.

mass (GeV)	$c\tau$ (mm)
4.5	100
6	100
8	10
10	1
12	0.1
16	0.001

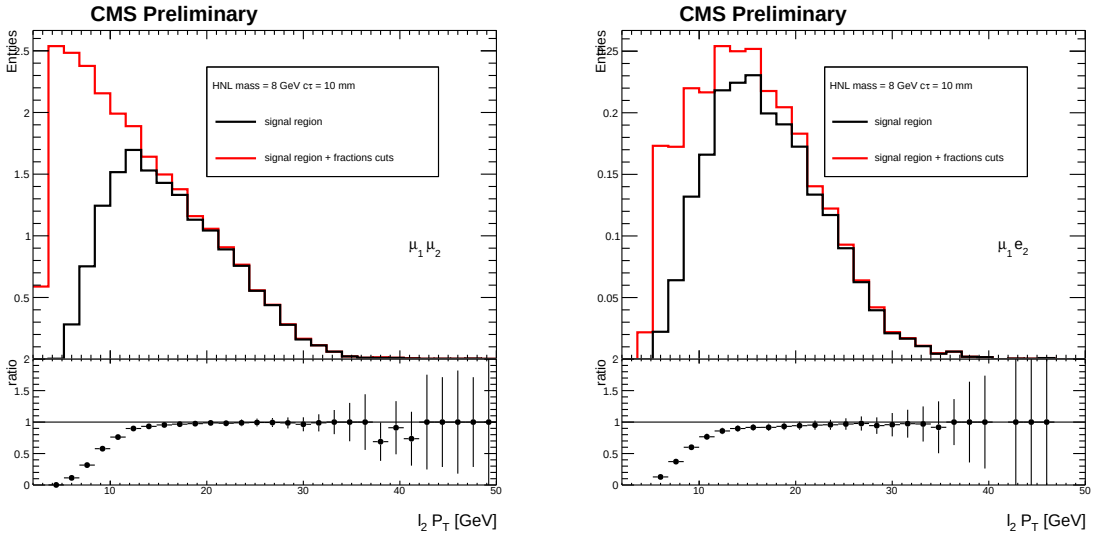

Figure 8.18: Signal efficiency as a function of the $l_2 p_T$ after applying the fraction cuts for HNL mass = 8 GeV and $c\tau = 10$ mm for the year 2018.

8.4.3 Residual Type-II background suppression

The study performed in mass and tagger validation regions VR1 and VR3 respectively show no clear evidence of a residual Type-II background at high tagger score. However, in the closure test (VR5) defined in section 8.5, an overestimation of the background was observed mainly in $\mu\mu$ OS boosted medium category in the year 2018 so we are looking closer into that.

The following studies based on MC simulation has been performed. Figure 8.19 shows the distributions of $m(\ell_1, \ell_2, \mathrm{j}^\star)$ in low and high tagger score regions for Z/γ^*+jets (left) and inclusive no Z/γ^*+jets (right) backgrounds. Two categories of displacement are shown: medium and displaced on top and bottom respectively. Figure 8.20 shows the distributions of the tagger score in $m(\ell_1, \ell_2, \mathrm{j}^\star)$ signal and sidebands regions. The shape comparison is good for inclusive no Z/γ^*+jets however, a bias is observed in Z/γ^*+jets events. For this we conclude that the deficit in VR5 is also present in the signal region and it is caused by Z/γ^*+jets background events.

To reduce the problematic Z/γ^*+jets background in $\mu\mu$ OS boosted categories at a high tagger score and based on the dilepton mass and the fraction distributions shown in figures 8.21 and 8.22, the following additional cuts are applied for these specific categories for the 3 years of data taking.

- Tightening the cut on m(ℓ_1,ℓ_2) from 80 to 70 GeV on the $\mu\mu$ OS categories.
- The fraction cut is required to be less than 3(2) for 2016(2017 and 2018) respectively for medium and displaced $\mu\mu$ OS categories.

Figure 8.23 shows the same shape distributions for the $m(\ell_1, \ell_2, \mathrm{j}^\star)$ and tagger score on simulation after applying the cuts. The Z/γ^*+jets events are mostly rejected in the high tagger score region. The closure test performed in the VR5 after applying the new additional cuts on the $\mu\mu$ OS categories and the background overstimation issue is now recovered. The results are shown in section 8.5 figures 8.30 and 8.33.

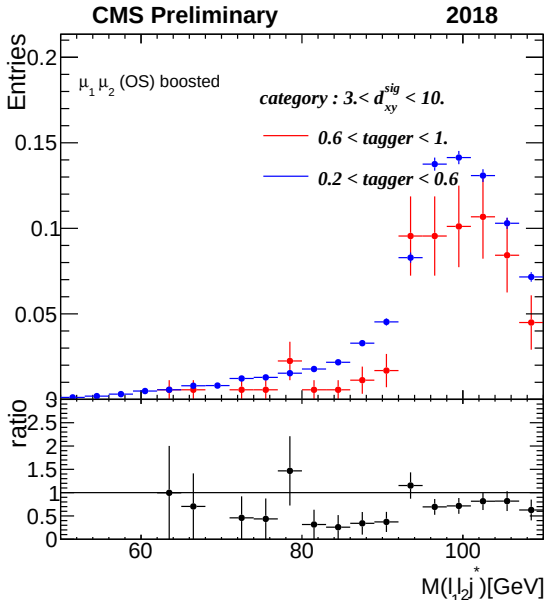

(a) Z/γ^*+jets

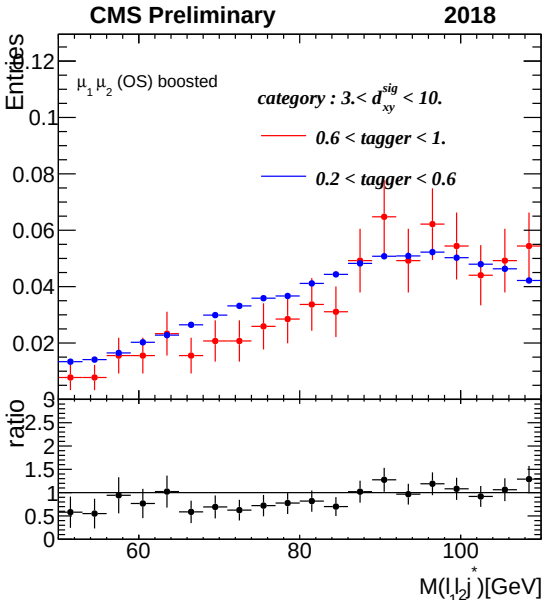

(b) inclu no Z/γ^*+jets

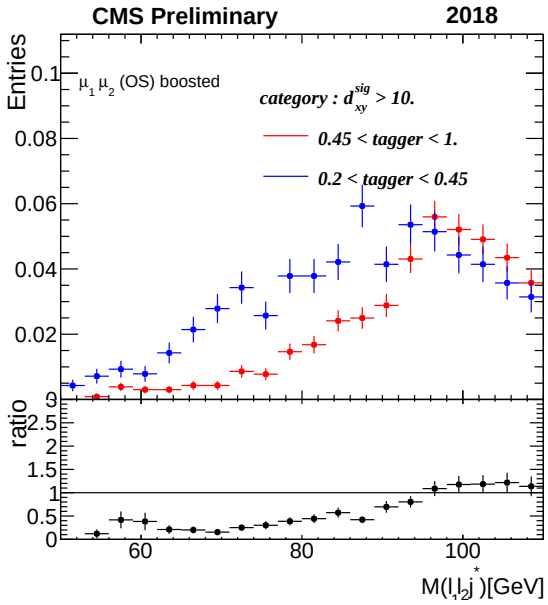

(c) Z/γ^*+jets

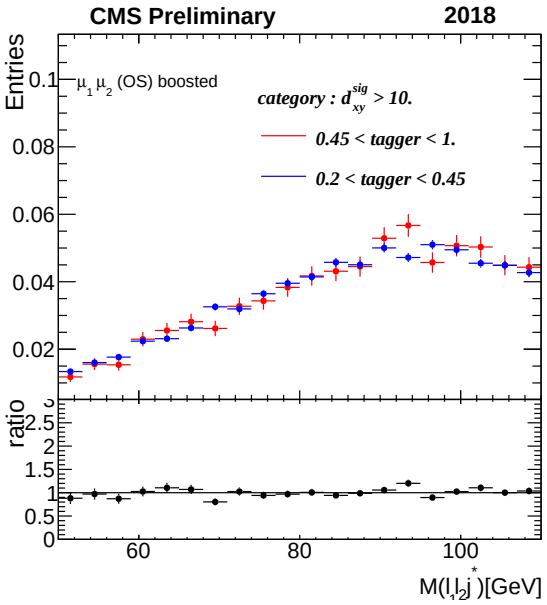

(d) inclu no Z/γ^*+jets

Figure 8.19: MC distributions for $m(\ell_1, \ell_2, \mathrm{j}^\star)$ in SR and sidebands for Z/γ^*+jets (left) and inclusive no Z/γ^*+jets (right) for the year 2018.

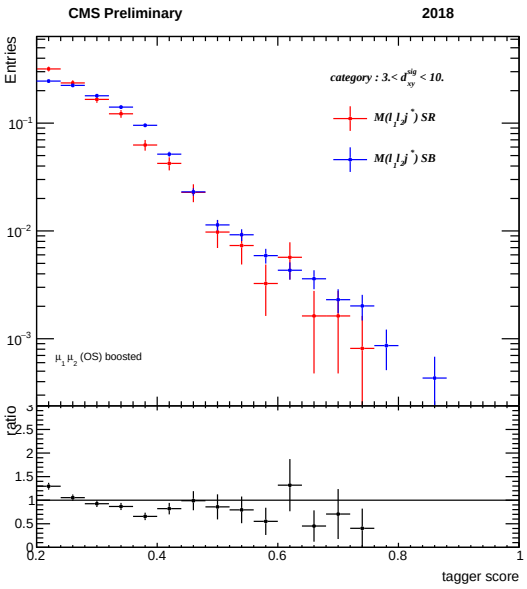

(a) Z/γ^*+jets

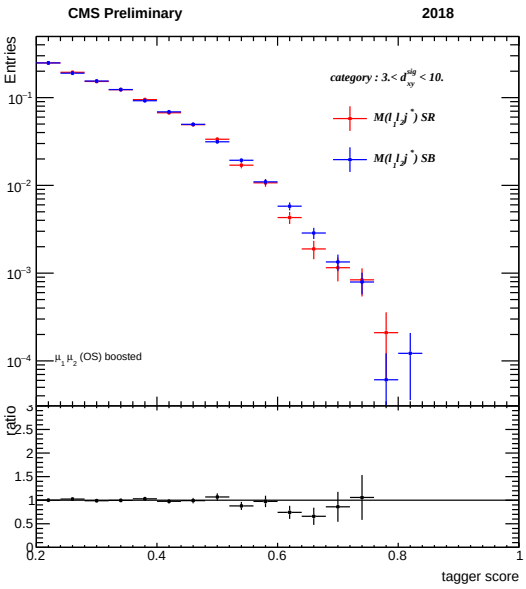

(b) inclu no Z/γ^*+jets

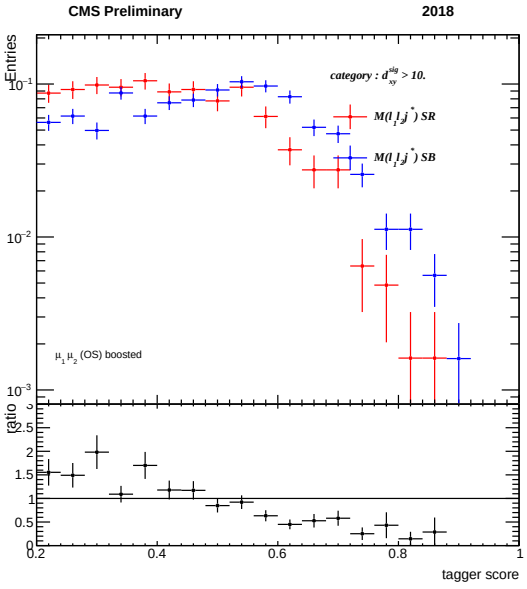

(c) Z/γ^*+jets

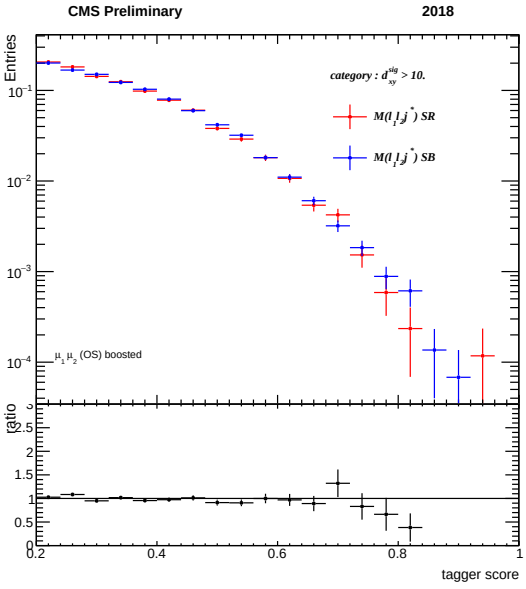

(d) inclu no Z/γ^*+jets

Figure 8.20: MC distributions for tagger score in $m(\ell_1, \ell_2, \mathrm{j}^\star)$ SR and sidebands for Z/γ^*+jets and inclusive no Z/γ^*+jets separately for the year 2018.

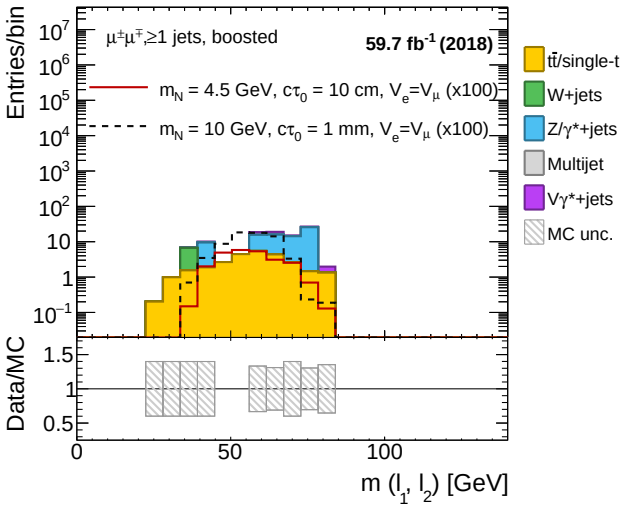

(a) high tagger

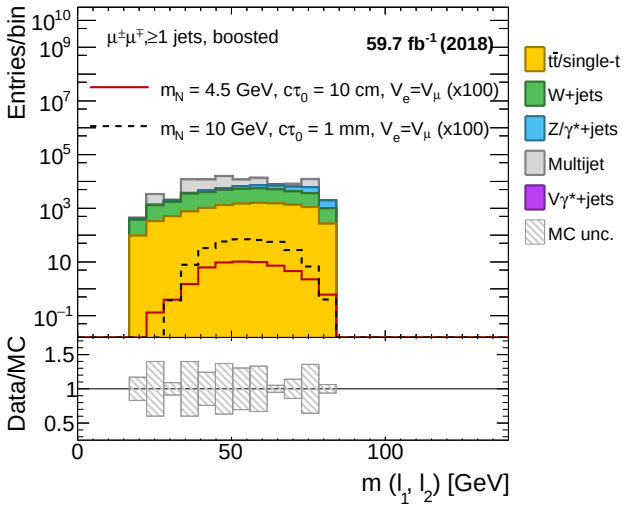

(b) low tagger

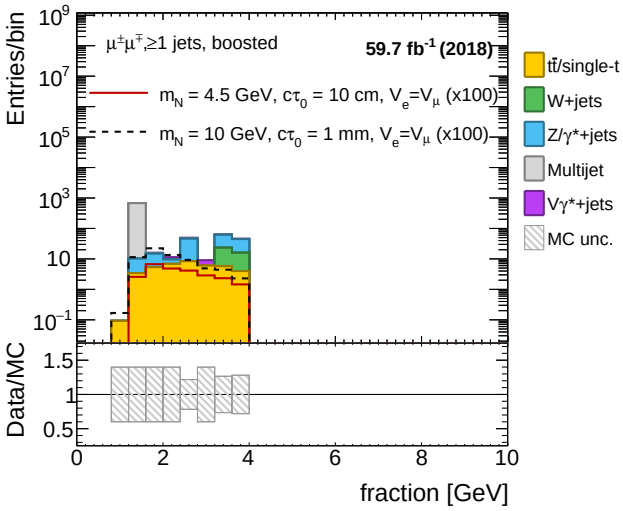

(c) high tagger

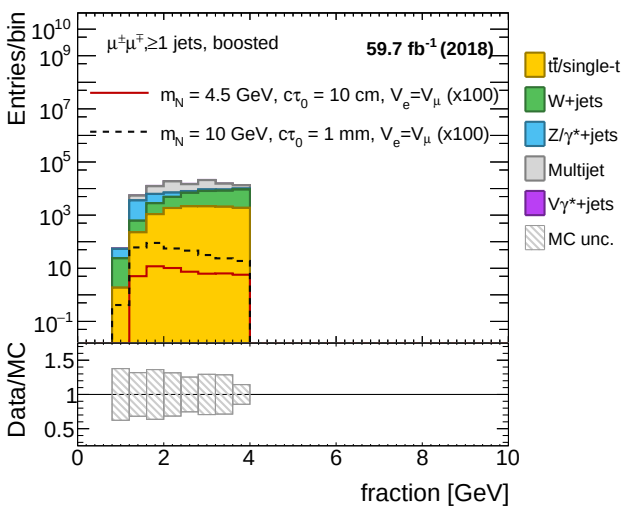

(d) low tagger

Figure 8.21: MC distribution for the dilepton mass and HNL jet hadronic fraction at high and low tagger score separately for boosted medium(top) and displaced (bottom) categories for the year 2018.

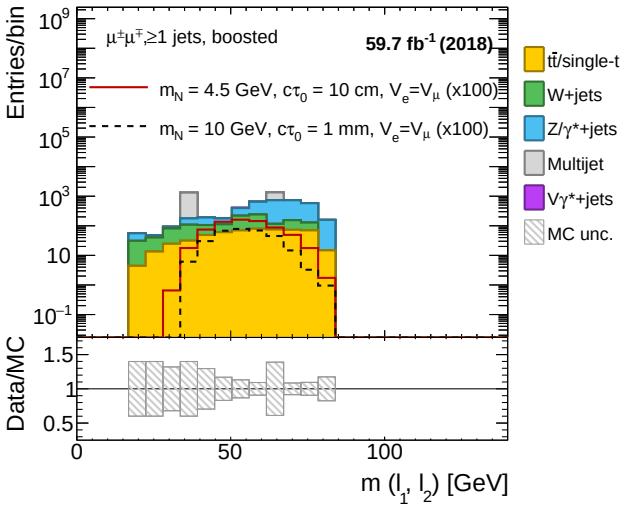

(a) high tagger

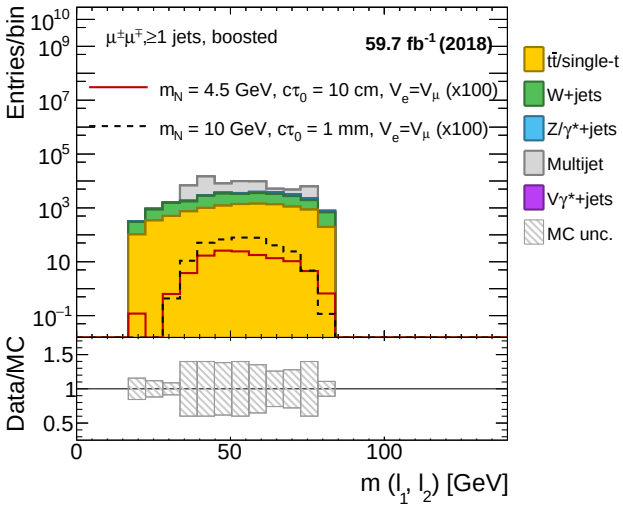

(b) low tagger

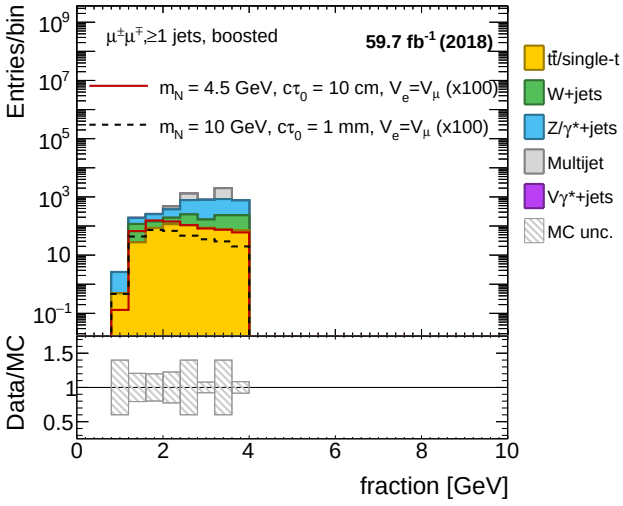

(c) high tagger

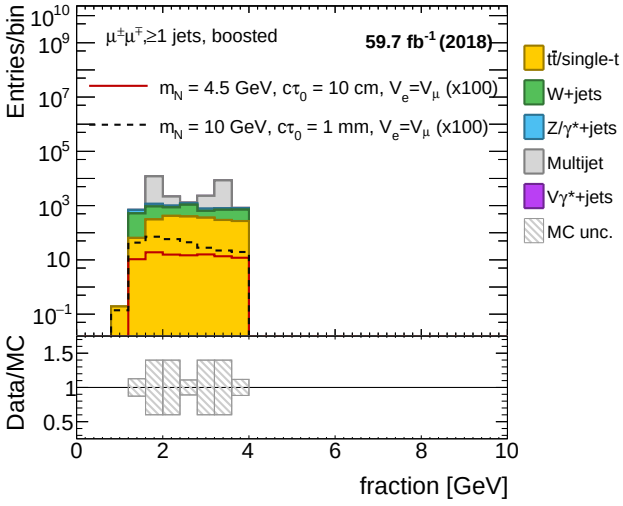

(d) low tagger

Figure 8.22: MC distribution for the dilepton mass and HNL jet hadronic fraction at high and low tagger score separately for boosted medium(top) and displaced (bottom) categories for the year 2018.

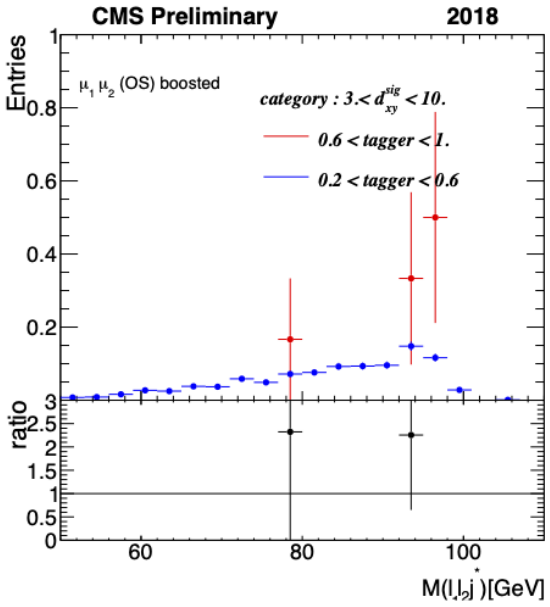

(a) Z/γ^*+jets

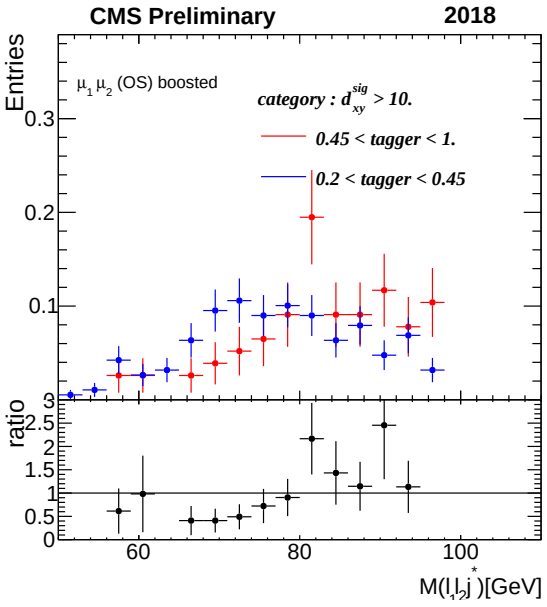

(b) Z/γ^*+jets

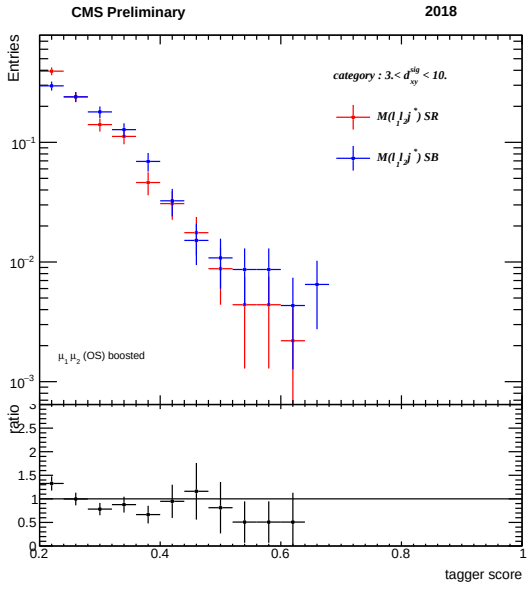

(c) Z/γ^*+jets

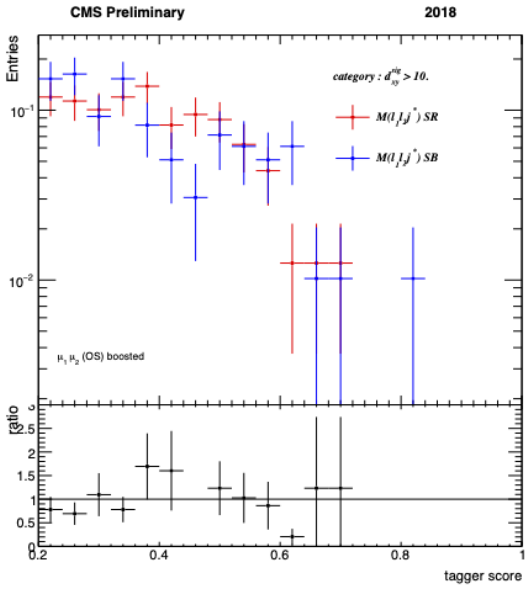

(d) Z/γ^*+jets

Figure 8.23: MC distribution for tagger score and $m(\ell_1, \ell_2, \mathrm{j}^\star)$ in SR and sidebands for Z/γ^*+jets for the year 2018 after applying the fraction and dilepton mass cuts.

8.4.4 Miscategorised displaced leptons

In the event categorisation, the significance of the transverse displacement of the second lepton d_{xy}^{sig}, which is d_{xy}/d_{xy}^{err} with respect to the primary vertex, is used (see Section 6.6). However, when a displaced lepton has also a high transverse uncertainty $\sigma_{d_{xy}}$ value due to a poor track fit it will be incorrectly categorized as prompt. Figure 8.24 shows the distribution of d_{xy} and $\sigma_{d_{xy}}$ with long tails despite the requirement $d_{xy}^{sig} < 3$. To reject such miscategorised events in the prompt categories an upper bound of $\sigma_{d_{xy}} < 0.05$ is applied in the prompt categories.

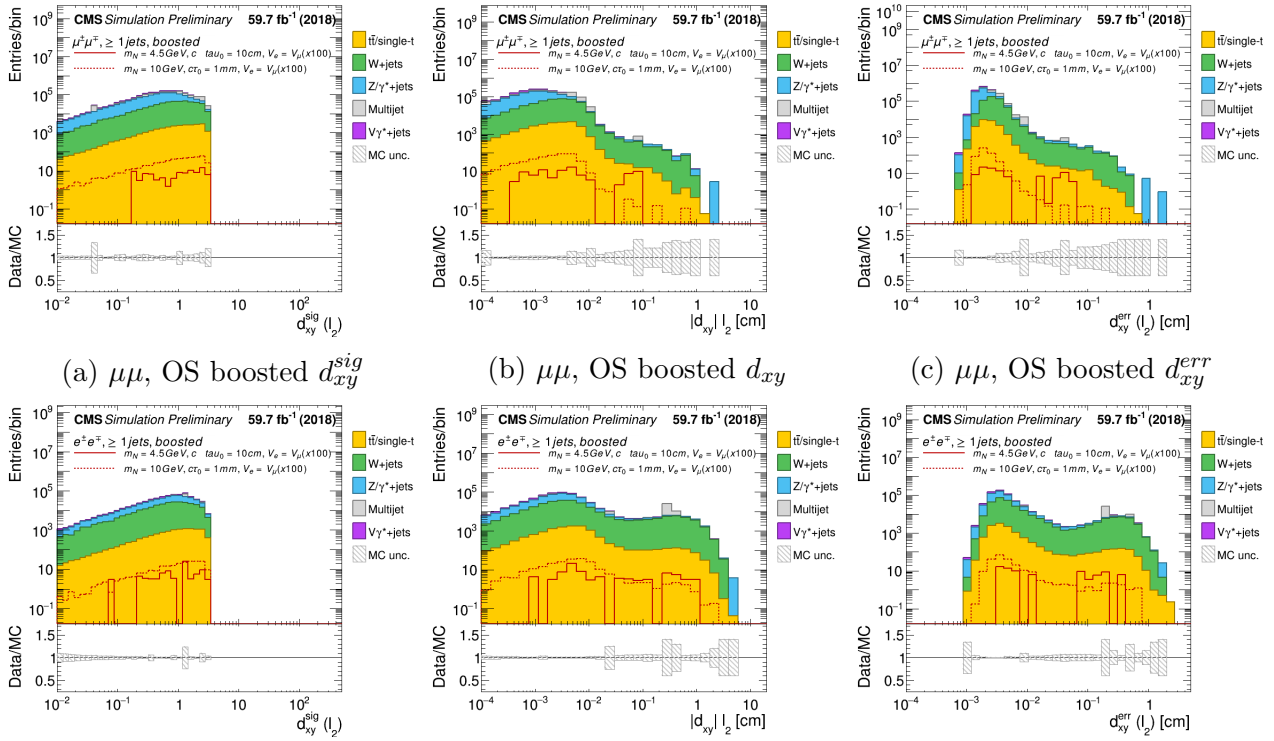

(a) $\mu\mu$, OS boosted d_{xy}^{sig} (b) $\mu\mu$, OS boosted d_{xy} (c) $\mu\mu$, OS boosted d_{xy}^{err}

(d) ee, OS boosted d_{xy}^{sig} (e) ee, OS boosted d_{xy} (f) ee, OS boosted d_{xy}^{err}

Figure 8.24: d_{xy}^{sig}, d_{xy} and d_{xy}^{err} MC distribution in $\mu\mu$ OS and ee OS prompt categories.

8.4.5 Summary

To suppress Residual type-I background the cuts per category except $\mu\mu$ OS on the fraction variable are summarized in table 8.4.

Table 8.4: Fraction thresholds for combined flavour categories except $\mu\mu$ OS per year of data taken.

		$p_T(\mathrm{j}^\star)/p_T(\ell_2)$ thresholds		
Topology	Displacement	2016	2017	2018
Boosted	Prompt	<3	<2	<2
	Medium	<4	<4	<4
	Displaced	<4	<4	<4
Resolved	Prompt	<4	<4	<4
	Medium	<4	<4	<4
	Displaced	<4	<4	<4

To suppress Residual Type-II background the following cuts are applied in $\mu\mu$ OS categories. A cut on $m(l_1, l_2) < 70$ GeV is applied on the $\mu\mu$ OS categories inclusive displacement.
The fraction cut is required to be less than 3(2) for 2016(2017 and 2018) respectively for both medium and displaced $\mu\mu$ OS categories. For the prompt $\mu\mu$ OS categories the used cuts are the same as in table 8.4

8.5 Closure tests

A closure test involves a meticulous comparison between the estimated background events and the actual number of background events observed in an orthogonal region, typically referred to as a validation region. This evaluation aims to assess the effectiveness of the background estimation technique within the signal region by ensuring that the estimation method accurately reproduces the background contributions.

Several closure tests of the estimated background are performed using data and/or simulation in various validation regions (VRs) to assess the validity and robustness of the ABCD method. All concluded cuts studied in section 8.4 are applied during the following study. More detailed description of the VRs are given in the following section.

8.5.1 Validation regions

The cartoon in figure 8.25(a) shows the definition of A, B, C and D regions where D is the signal region and is blinded, therefore not used for the closure tests performed on data. The cartoon in figure 8.25(b) shows a simplfied definition of the three VRs (VR1, VR2 and VR3) where the closure tests were performed using data. Another test, not included in the cartoon, was done on data in VR5 where a detailed definition of this region is given in the following. These VRs surround region D and the signal contamination in these VRs is expected to be negligeable. Finally a closure test is performed on simulation in signal region (VR4) for completeness.

VR1 (data high mass sideband) The closure test is performed in data in the $m(\ell_1, \ell_2, \mathrm{j}^\star)$ sideband (90 GeV $< m(\ell_1, \ell_2, \mathrm{j}^\star) <$ 110 GeV). Due to the difference in the background composition at $m(\ell_1, \ell_2, \mathrm{j}^\star) >$ 110 GeV region compared to the SR, an upper bound on the $m(\ell_1, \ell_2, \mathrm{j}^\star) <$ 110 GeV is used. Two tests are performed in this region by subdividing it in four other regions(A'B'C'D') with the same $m(\ell_1, \ell_2, \mathrm{j}^\star)$ intervals where A'C' = [100, 110] (GeV) and B'D' = [90, 100](GeV), more detailed description is shown in equation 8.8. The first test shown in figure 8.26 uses a relaxed tagger threshold $P_{\mathrm{i}} = P_{\mathrm{mid}} = 0.3$ and the second test in figure 8.31 uses the optimal tagger thresholds $P_{\mathrm{i}} = P_{\mathrm{opt}}$ from Section 8.3. The first test with high statistics is necessary to avoid a situation, where the statistical

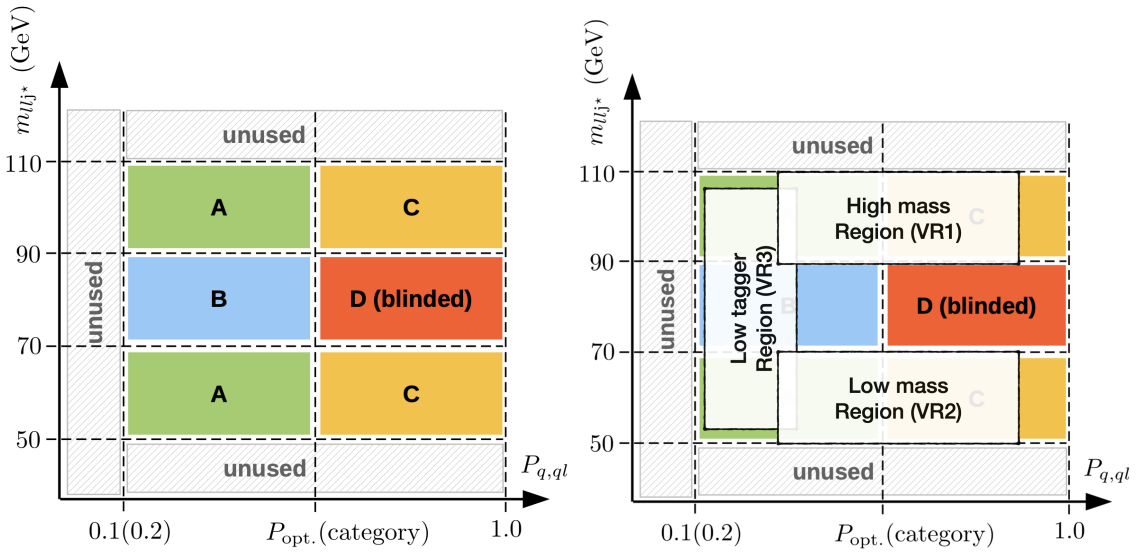

Figure 8.25: Cartoons of the SR on the left and of the three validation regions VR1, VR2 and VR3 on the right.

uncertainty is too high to draw meaningful conclusions about the level of closure. The second test then confirms that the resulting estimates agree also well independently from the chosen tagger interval.

$$\text{A' region: tagger} = [P_{min}, P_i], m(\ell_1, \ell_2, \text{j}^\star) \text{ region} = [100, 110](\text{GeV}) \tag{8.8}$$

$$\text{B' region: tagger} = [P_{min}, P_i], m(\ell_1, \ell_2, \text{j}^\star) \text{ region} = [90, 100](\text{GeV})$$

$$\text{C' region: tagger} = [P_i, 1], m(\ell_1, \ell_2, \text{j}^\star) \text{ region} = [100, 110](\text{GeV})$$

$$\text{D' region: tagger} = [P_i, 1], m(\ell_1, \ell_2, \text{j}^\star) \text{ region} = [90, 100](\text{GeV})$$

VR2 (data low mass sideband) The closure test is performed in data in the $m(\ell_1, \ell_2, \text{j}^\star)$ sideband (50 GeV $< m(\ell_1, \ell_2, \text{j}^\star) <$ 70 GeV). The $m(\ell_1, \ell_2, \text{j}^\star) <$ 50 GeV region is not used for the closure test given the difference in the background composition compared to the SR. Similar to the high mass region, two tests are performed by subdividing the low mass region to another four regions (A'B'C'D') with the same $m(\ell_1, \ell_2, \text{j}^\star)$ intervals where A'C' = [50, 65] (GeV) and B'D' = [65, 70](GeV), for more detailed description see equation

8.9. The first and second test are shown in figure 8.27 and 8.32 respectively where the former uses a relaxed tagger threshold $P_{\text{mid}} = 0.3$ and the latter uses the optimal tagger thresholds P_{opt} from Section 8.3. This sideband region has lower data statistics than the high mass one. The background distribution is less similar to the signal region, however, the closure is studied in this region for completeness as well.

$$\text{A' region: tagger} = [P_{min}, P_i], m(\ell_1, \ell_2, \text{j}^\star) \text{ region} = [50, 65](GeV) \tag{8.9}$$

$$\text{B' region: tagger} = [P_{min}, P_i], m(\ell_1, \ell_2, \text{j}^\star) \text{ region} = [65, 70](GeV)$$

$$\text{C' region: tagger} = [P_i, 1], m(\ell_1, \ell_2, \text{j}^\star) \text{ region} = [50, 65](GeV)$$

$$\text{D' region: tagger} = [P_i, 1], m(\ell_1, \ell_2, \text{j}^\star) \text{ region} = [65, 70](GeV)$$

VR3 (data low tagger sideband) The closure test in figure 8.28 is performed in data in the tagger score sideband where the AB region, $P \in [P_{min}, P_{SR}]$ where P_{SR} is 0.2(0.4) for boosted(resolved) categories respectively, is subdivided into four new regions, $AB \rightarrow A'B'C'D'$ as defined in equation 8.10. The $m(\ell_1, \ell_2, \text{j}^\star)$ region remains the same as for signal region where for A'C' region, 90 GeV $< m(\ell_1, \ell_2, \text{j}^\star) <$ 110 GeV or 50 GeV $< m(\ell_1, \ell_2, \text{j}^\star) <$ 70 GeV and for B'D' region 70 GeV $< m(\ell_1, \ell_2, \text{j}^\star) <$ 90 GeV.

$$\text{A' region: tagger} = [P_{min}, P_{mid}], m(\ell_1, \ell_2, \text{j}^\star) \text{ region} = [50, 70] \cup [90, 110](GeV) \tag{8.10}$$

$$\text{B' region: tagger} = [P_{min}, P_{mid}], m(\ell_1, \ell_2, \text{j}^\star) \text{ region} = [70, 90](GeV)$$

$$\text{C' region: tagger} = [P_{mid}, P_{SR}], m(\ell_1, \ell_2, \text{j}^\star) \text{ region} = [50, 70] \cup [90, 110](GeV)$$

$$\text{D' region: tagger} = [P_{mid}, P_{SR}], m(\ell_1, \ell_2, \text{j}^\star) \text{ region} = [70, 90](GeV)$$

VR4 (simulation signal region) The closure test in figure 8.29 is performed in the signal region D using only simulated samples, where the tagger threshold is however relaxed to $P_{\text{mid}} = 0.3$ to increase the available number of simulated events. Same sign categories are mostly populated by misreconstructed events which are not well modelled in the

simulation. These events have low statistics in the simulation but also high weight, leading to meaningless closure. Therefore, the weight of the events is only applied to $\mu\mu$ OS and ee OS channels which are dominated by well-defined Drell-Yan processes.

VR5 (data low + high mass sidebands) The closure test in figure 8.30 and 8.33 is performed in data in low and high $m(\ell_1, \ell_2, \mathrm{j}^\star)$ sidebands. Both regions are subdivided in four other regions simultaniously and the sum of each subregions are considered for the closure test. This region is the closest to the signal region in terms of background composition and it is further explained in the following equations 8.11 and 8.12.

$$A' = A_1 + A_2, \quad B' = B_1 + B_2, \quad C' = C_1 + C_2, \quad D' = D_1 + D_2 \tag{8.11}$$

where:

$$A_1 \text{ region: tagger} = [P_{min}, P_{opt}], m(\ell_1, \ell_2, \mathrm{j}^\star) \text{ region} = [50, 65](GeV) \tag{8.12}$$

$$A_2 \text{ region: tagger} = [P_{min}, P_{opt}], m(\ell_1, \ell_2, \mathrm{j}^\star) \text{ region} = [95, 110](GeV)$$

$$B_1 \text{ region: tagger} = [P_{opt}, 1], m(\ell_1, \ell_2, \mathrm{j}^\star) \text{ region} = [50, 65](GeV)$$

$$B_2 \text{ region: tagger} = [P_{opt}, 1], m(\ell_1, \ell_2, \mathrm{j}^\star) \text{ region} = [95, 110](GeV)$$

$$C_1 \text{ region: tagger} = [P_{min}, P_{opt}], m(\ell_1, \ell_2, \mathrm{j}^\star) \text{ region} = [65, 70](GeV)$$

$$C_2 \text{ region: tagger} = [P_{min}, P_{opt}], m(\ell_1, \ell_2, \mathrm{j}^\star) \text{ region} = [90, 95](GeV)$$

$$D_1 \text{ region: tagger} = [P_{opt}, 1], m(\ell_1, \ell_2, \mathrm{j}^\star) \text{ region} = [65, 70](GeV)$$

$$D_2 \text{ region: tagger} = [P_{opt}, 1], m(\ell_1, \ell_2, \mathrm{j}^\star) \text{ region} = [90, 95](GeV)$$

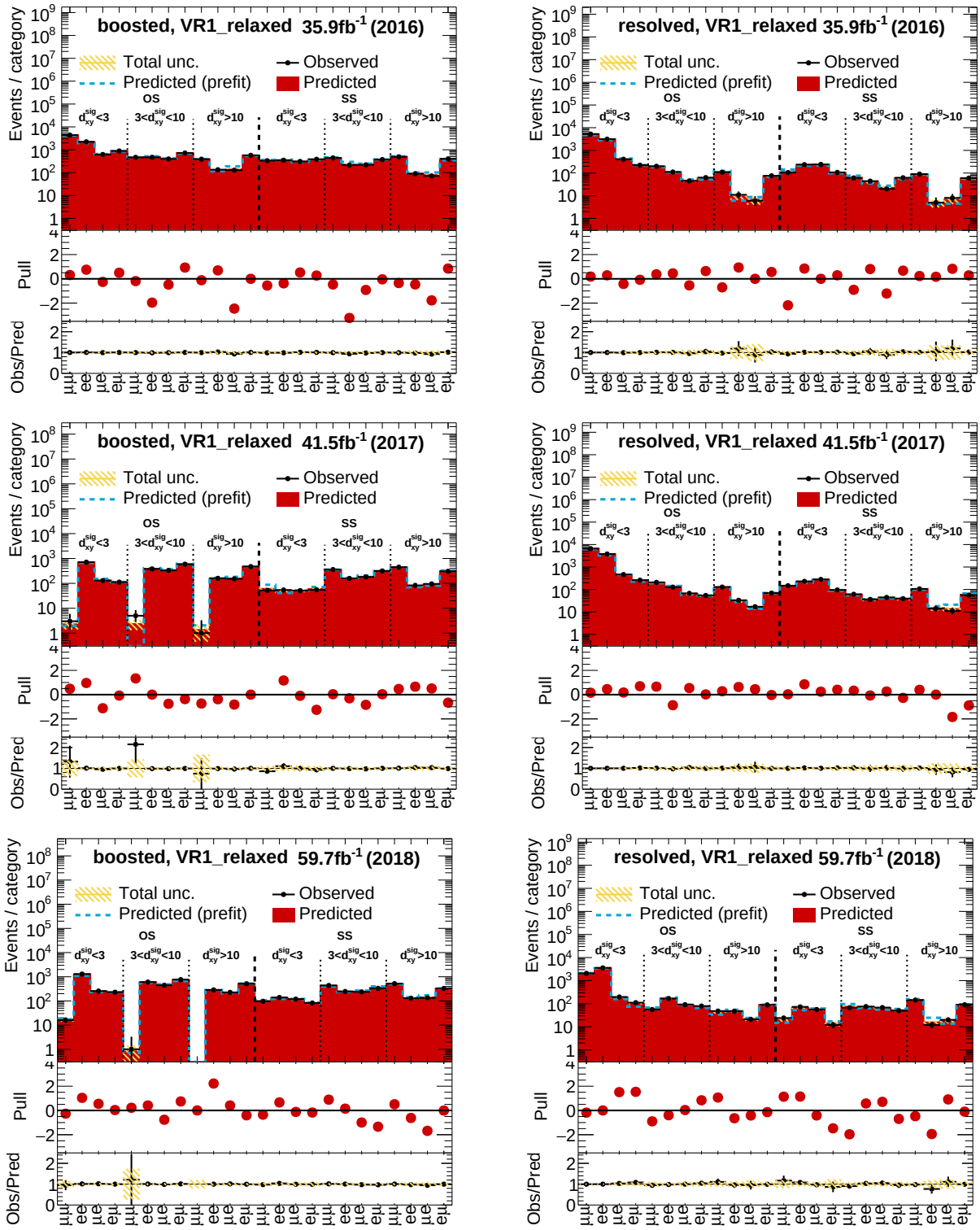

Figure 8.26: Closure test in VR1 data sideband $m(\ell_1, \ell_2, \mathrm{j}^\star) > 90$ with loose tagger thresholds for boosted (left) and resolved (right) categories.

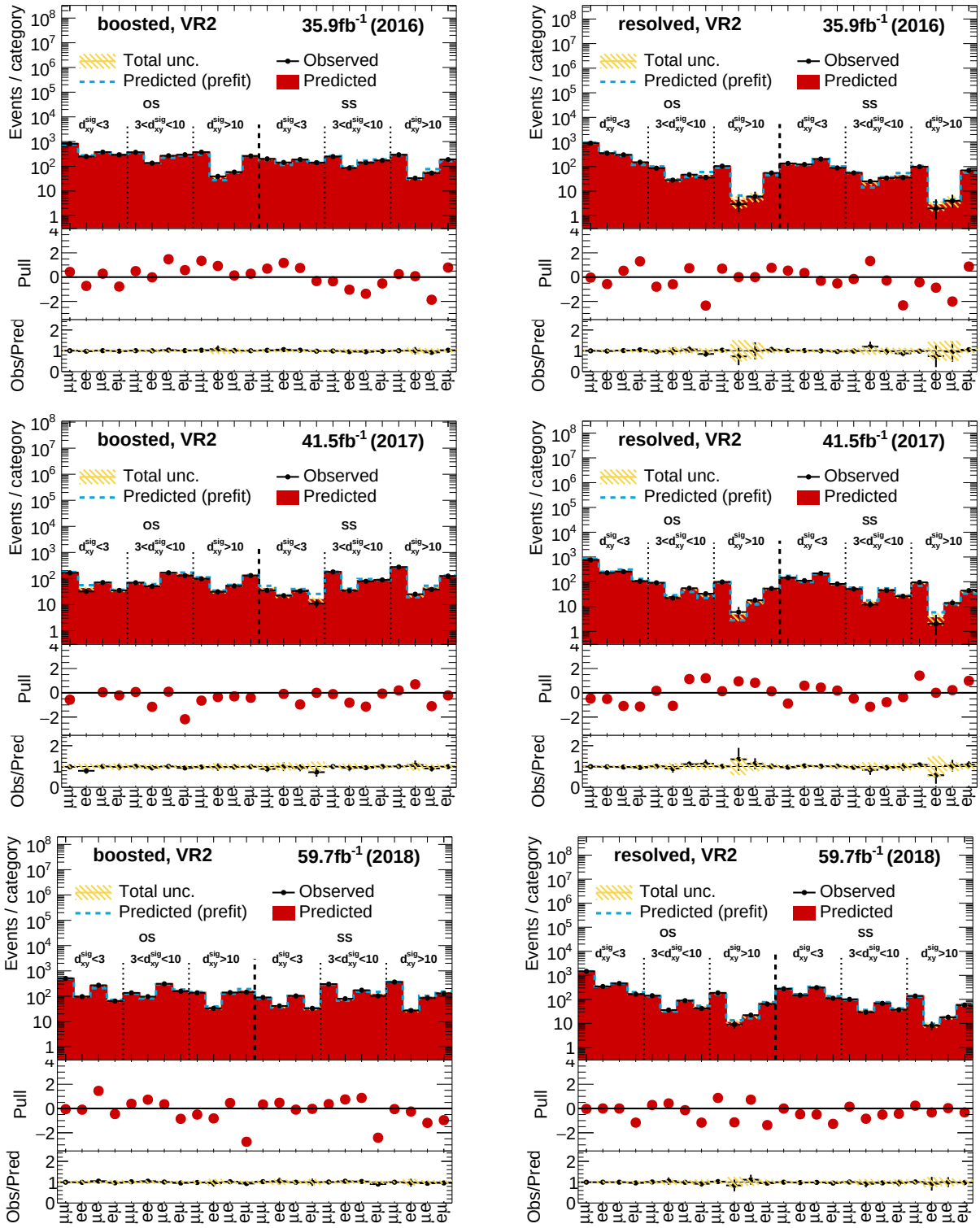

Figure 8.27: Closure test in VR2 data sideband $m(\ell_1, \ell_2, \mathrm{j}^\star) < 70$ with loose tagger thresholds for boosted (left) and resolved (right) categories.

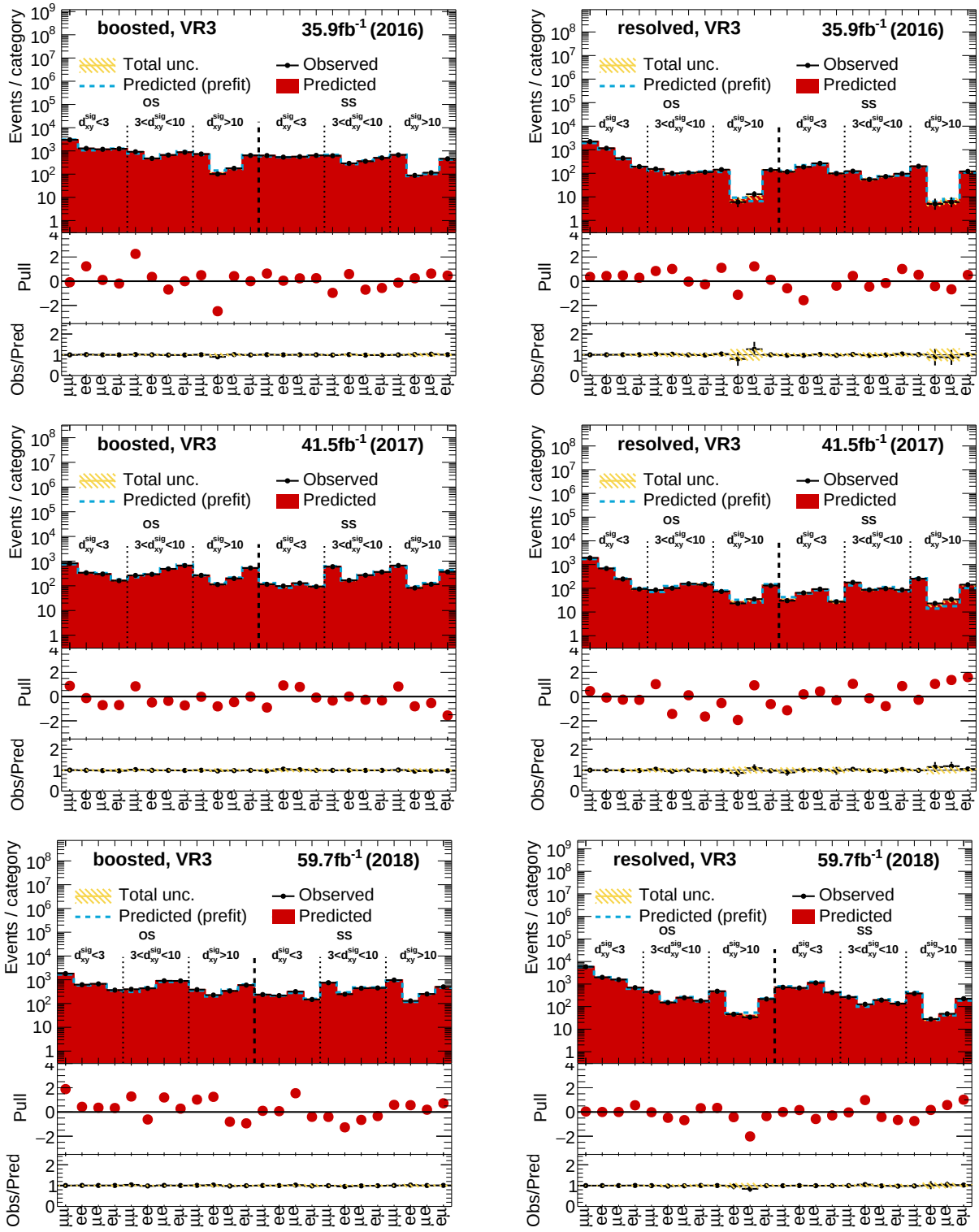

Figure 8.28: Closure test in VR3 data sideband for boosted (left) and resolved (right) categories.

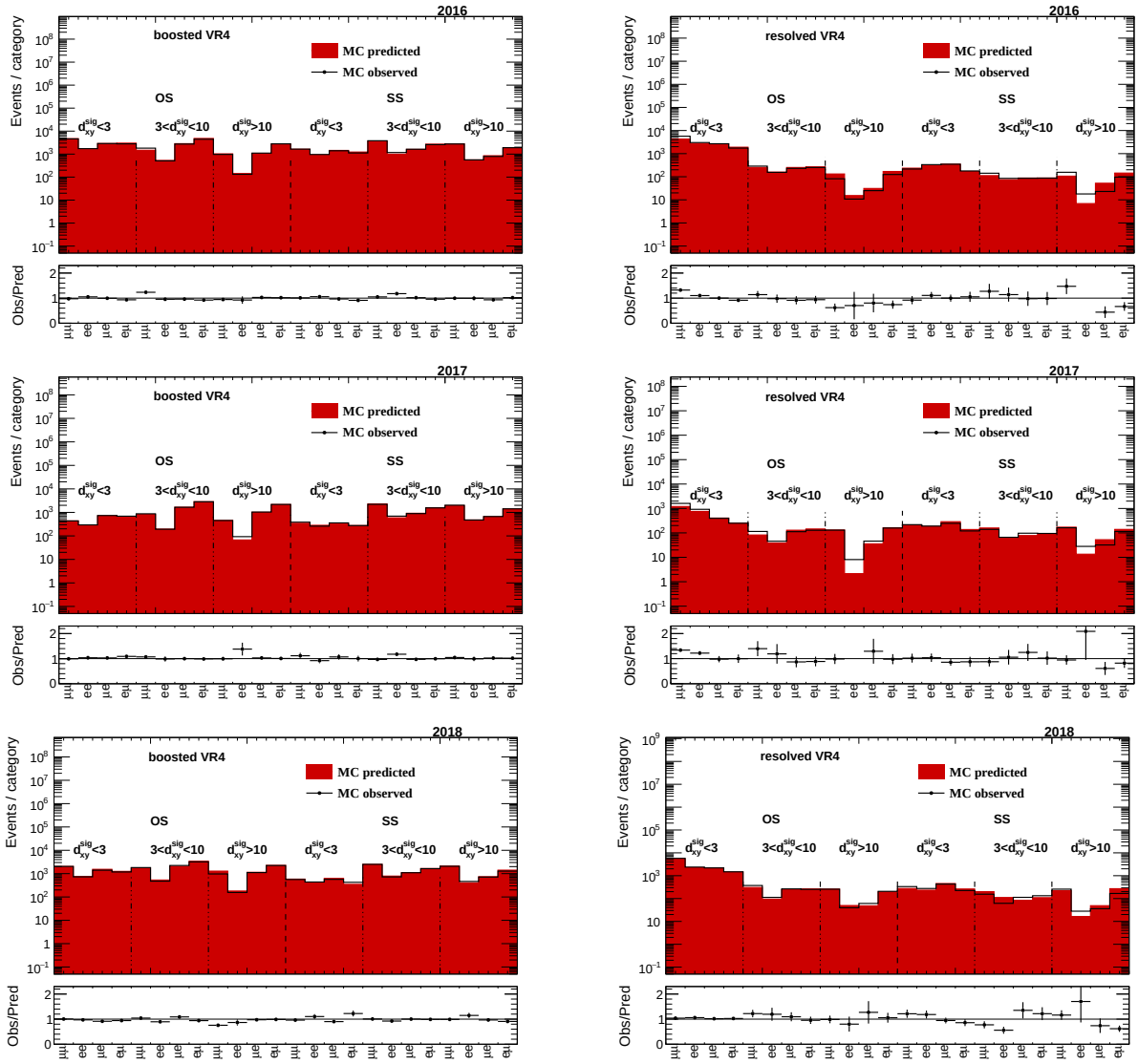

Figure 8.29: Closure test in VR4 simulation sideband for boosted (left) and resolved (right) categories.

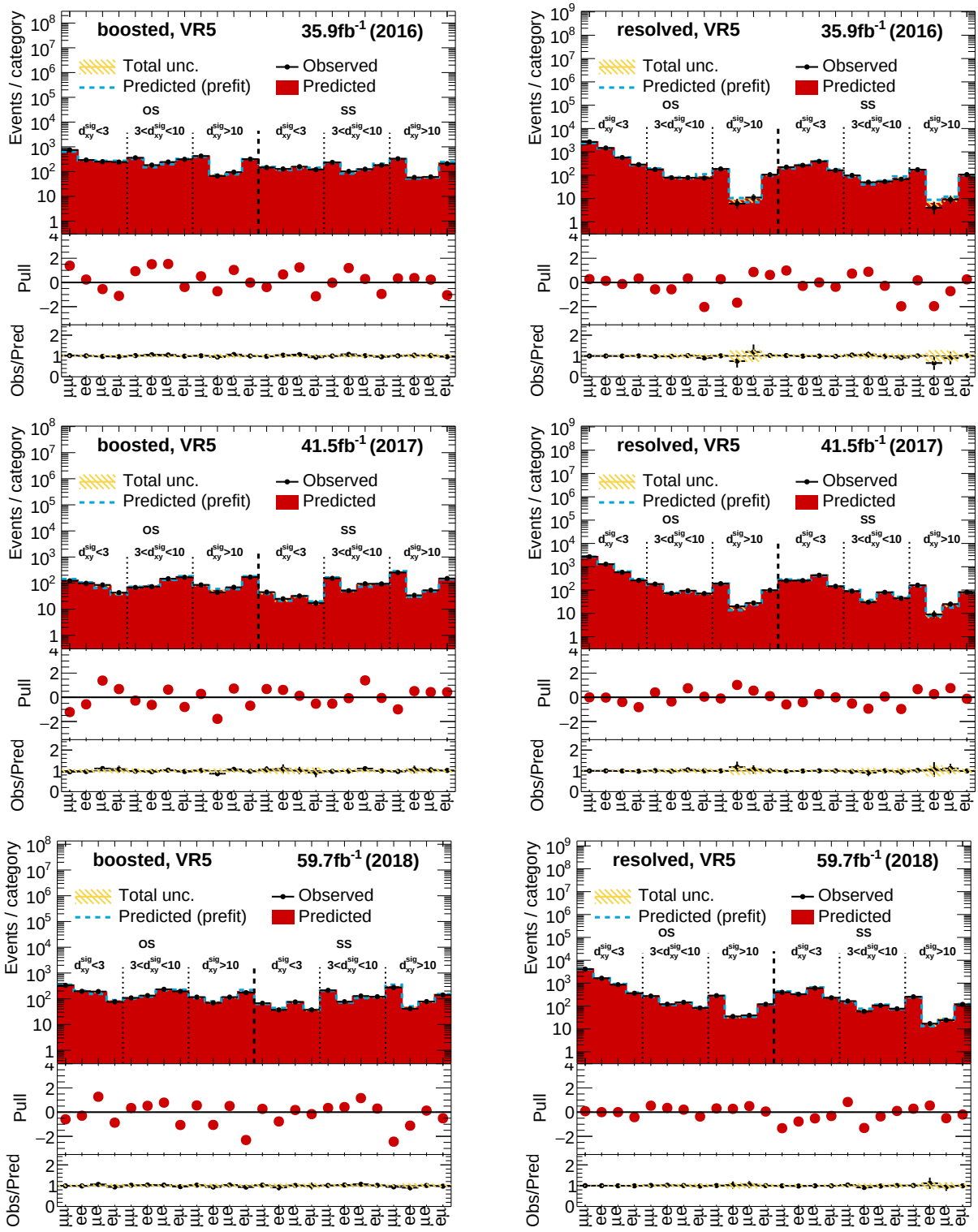

Figure 8.30: Closure test in VR5 data sideband for boosted (left) and resolved (right) categories.

The closure tests are also performed using the optimal tagger thresholds as computed in section 8.3. As expected, these regions have low statistics in the displaced bins. The closure tests are shown in figure 8.31 and 8.32 demonstrating excellent agreement within uncertainties. The GOF in figure 8.38 and 8.39 further confirms the validity of the closure where we observe high p-values for most of the categories with the lowest value being 23% in the VR1 boosted 2018 category. The blue arrows on the figures indicate the resulting p-values.

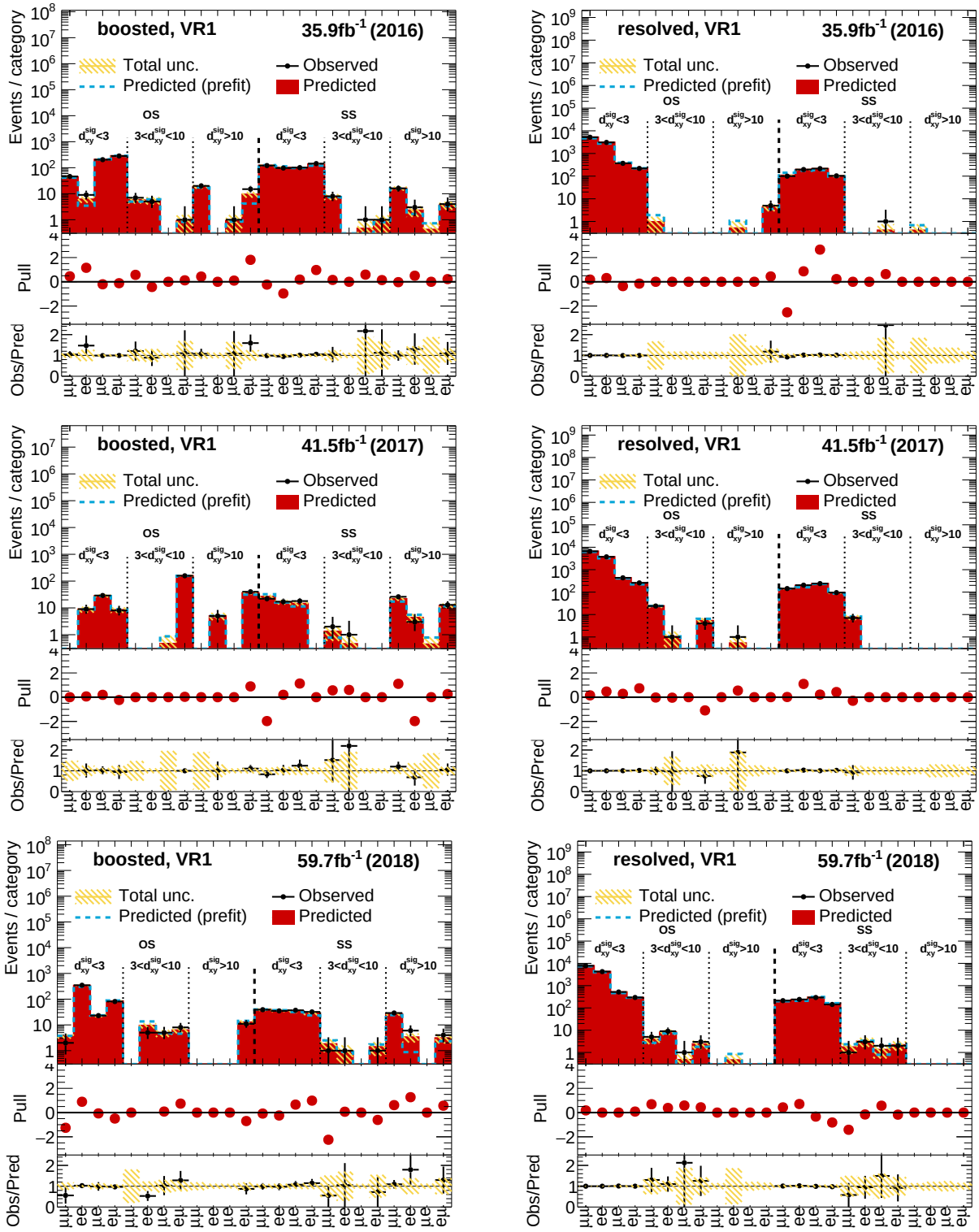

Figure 8.31: Closure test in VR1 data sideband $m(\ell_1, \ell_2, \mathrm{j}^\star) > 90$ with optimised tagger thresholds for boosted (left) and resolved (right) categories.

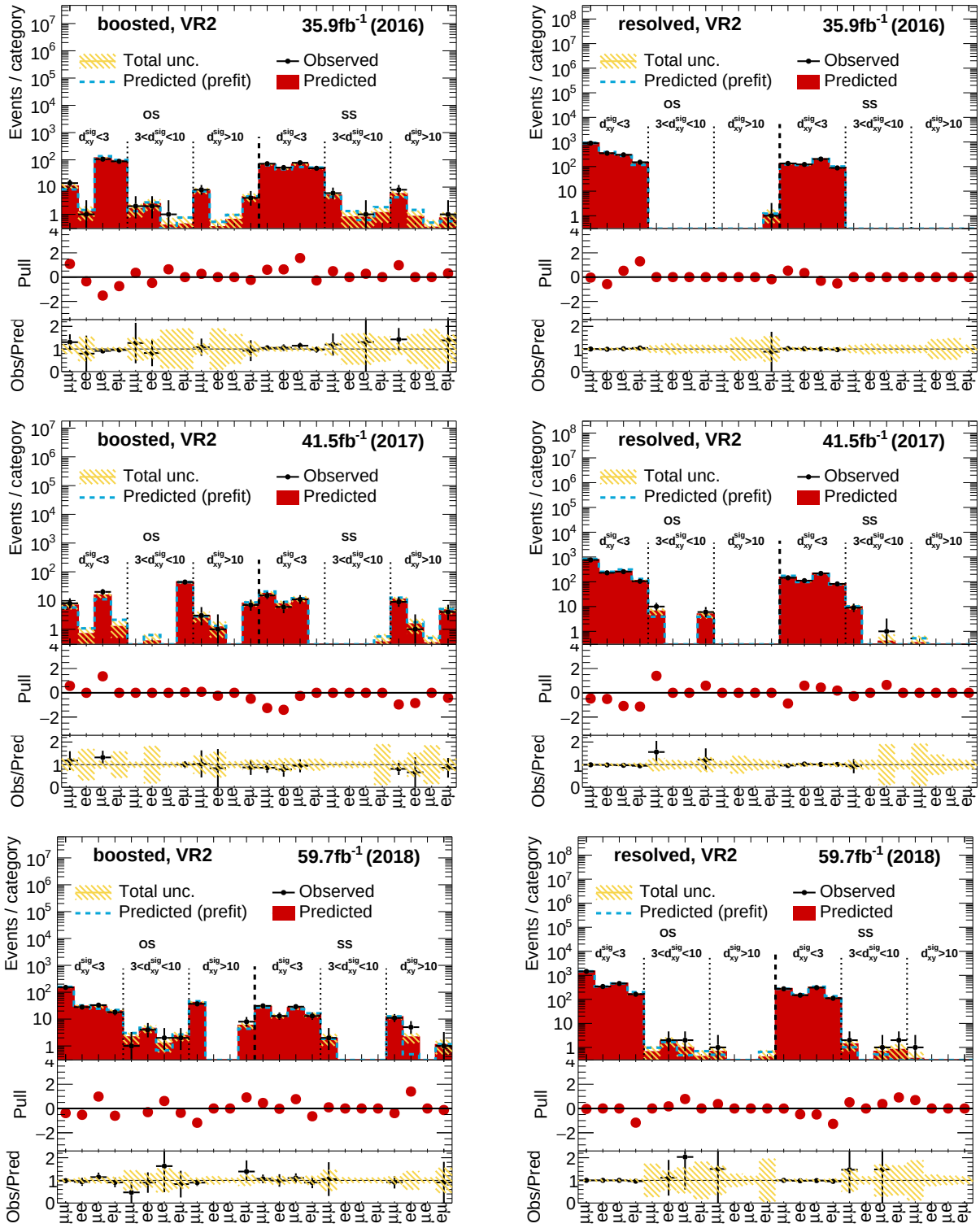

Figure 8.32: Closure test in VR2 data sideband $m(\ell_1, \ell_2, \mathrm{j}^\star) < 70$ with optimised tagger thresholds for boosted (left) and resolved (right) categories.

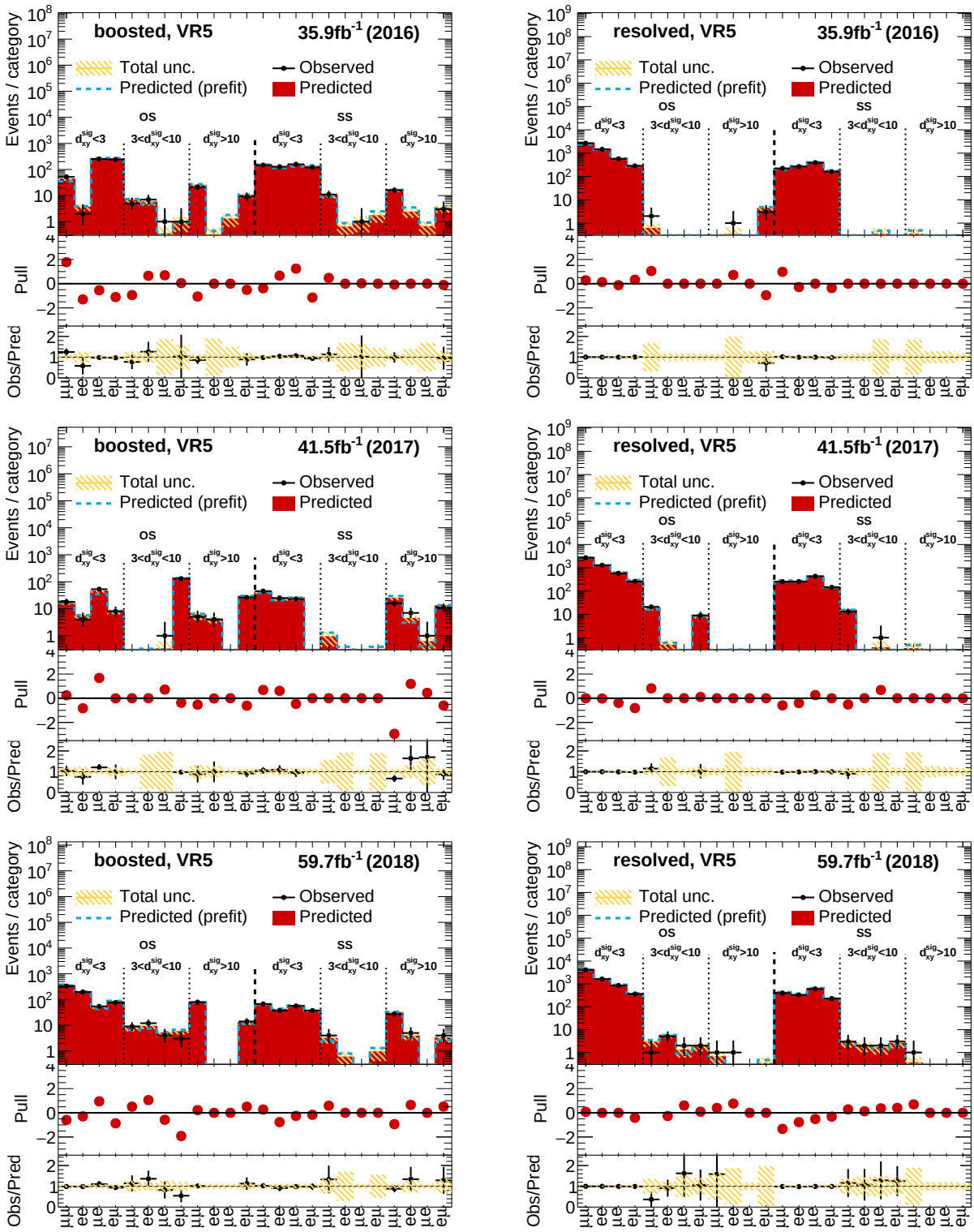

Figure 8.33: Closure test in VR5 data sideband $m(\ell_1, \ell_2, \mathrm{j}^\star) < 70$ with optimised tagger thresholds for boosted (left) and resolved (right) categories

8.5.2 Goodness of fit

A goodness-of-fit (GOF) test is a standard statistical tool used in experimental particle physics to check whether the observed number of events agrees with the expected values based on a probability distribution function (PDF) model. In this study, we perform a GOF test in the validation regions (VRs) using the saturated likelihood-ratio test statistic. This statistic, defined as the negative twice the natural logarithm of the ratio of the likelihood function to the saturated likelihood function, provides a measure of the agreement between the data and the PDF model. The saturated likelihood function is constructed by fixing all model parameters to their measured values, and acts as a normalization term. When the data sample is sufficiently large, the distribution of the test statistic follows a chi-squared distribution. The formula for the saturated likelihood-ratio test statistic is given by:

$$q_{\text{sat}} = -2 \ln \lambda_{\text{sat}}(\mu, \vec{\theta}) = -2 \ln \frac{\mathcal{L}(\mu, \vec{\theta})}{\mathcal{L}_{\text{sat}}}, \tag{8.13}$$

where $\mathcal{L}(\mu, \vec{\theta})$ is the likelihood function for the model parameters μ and $\vec{\theta}$, and $\mathcal{L}_{\text{sat}}$ is the saturated likelihood function. We generate toy datasets using Monte Carlo simulations and compare their test statistic distribution to the observed data. Our results, presented in figure 8.5.2, 8.35, and 8.36 for six macro categories with relaxed tagger thresholds, show that the p-value is greater than 5% for all categories, and in most cases exceeds 20% in each of the three VRs using real data. This validates the ABCD method and provides confidence in the accuracy of the PDF model.

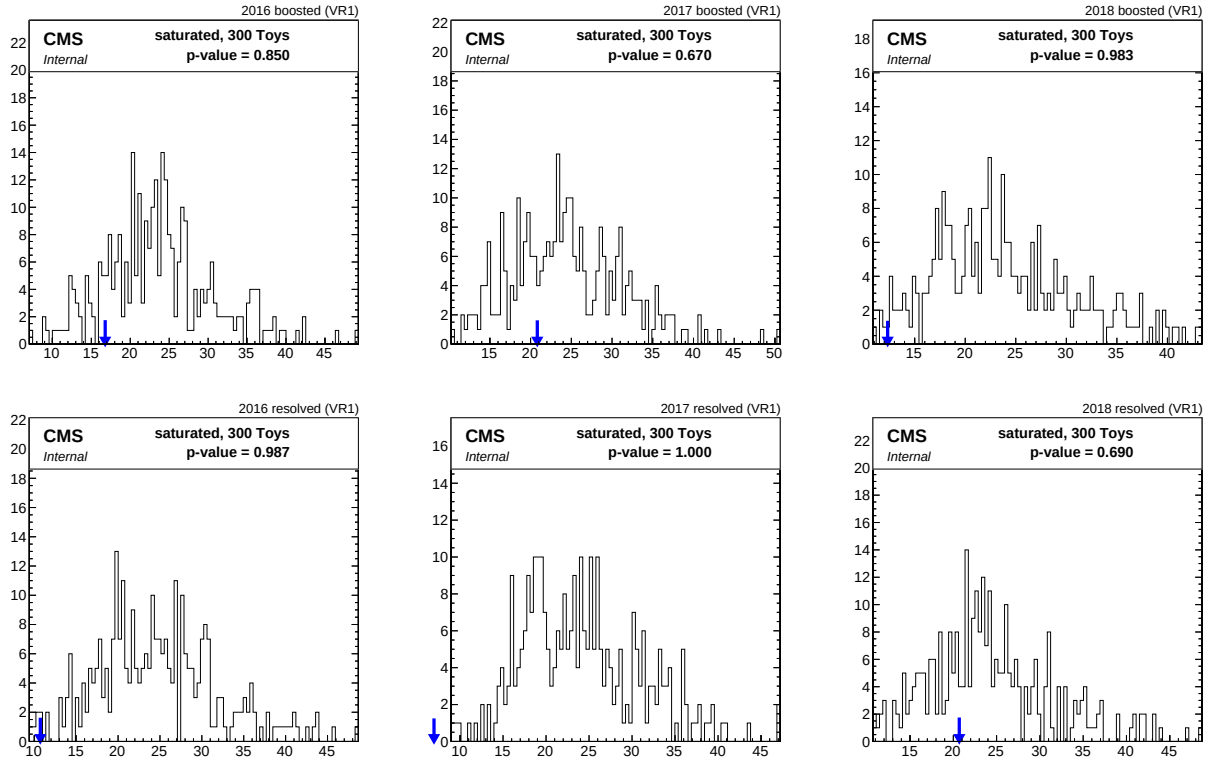

Goodness of fit in VR1 in data sideband for boosted (up) and resolved (bottom) categories.
Goodness of fit in VR1 in data sideband for boosted (up) and resolved (bottom) categories.

Figure 8.34:
Goodness of fit in VR1 in data sideband for boosted (up) and resolved (bottom) categories.

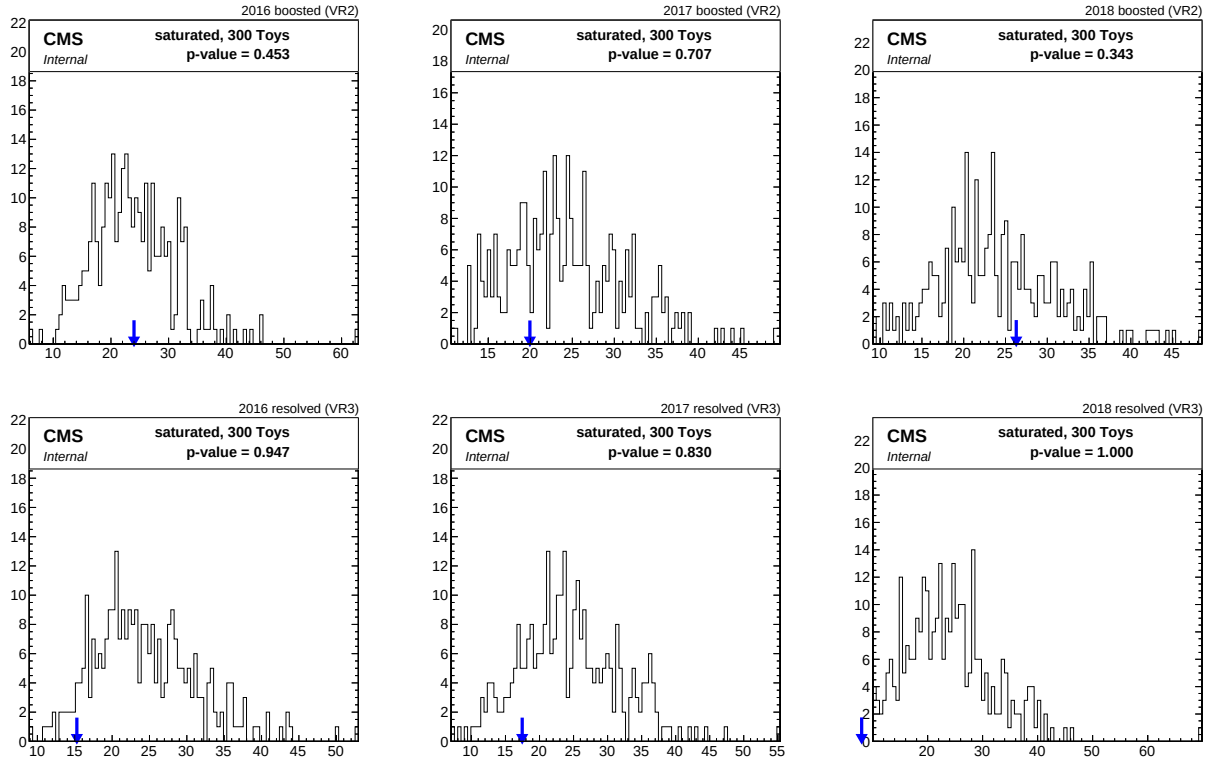

Figure 8.35: Goodness of fit in VR2 in data sideband for boosted (up) and resolved (bottom) categories.

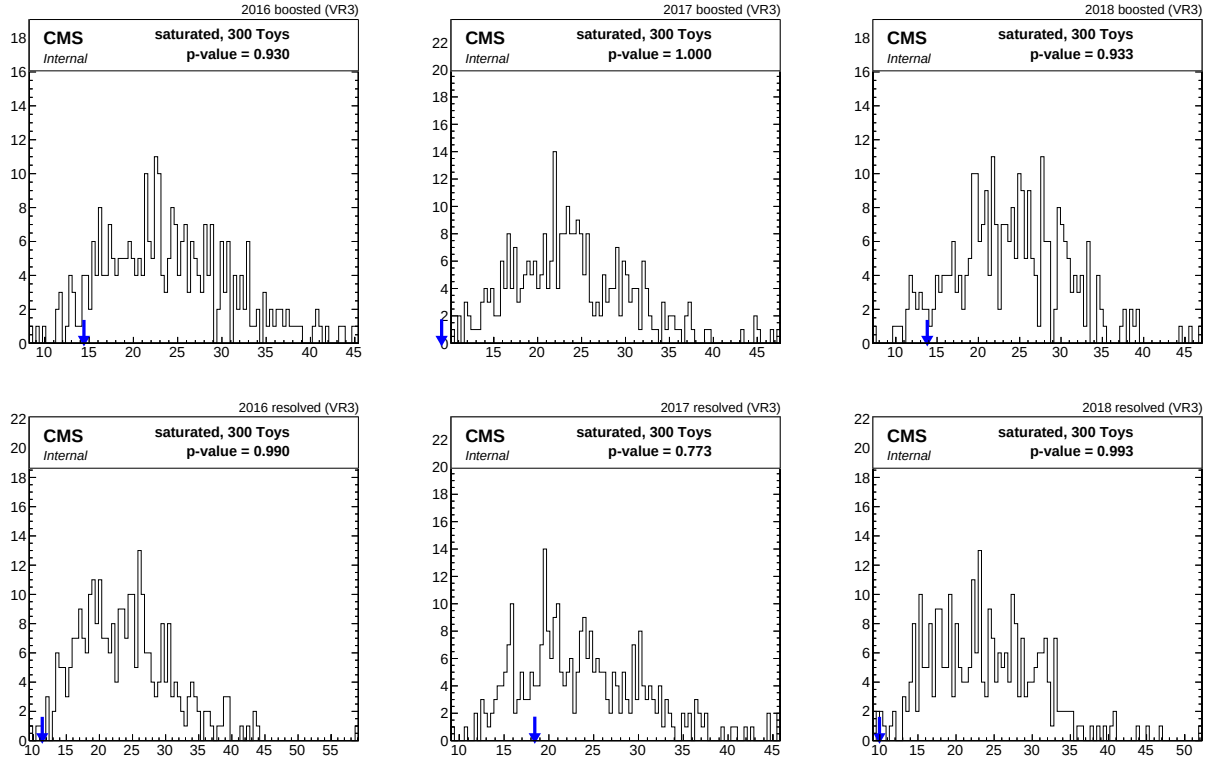

Figure 8.36: Goodness of fit in VR3 data sideband for boosted (up) and resolved (bottom) categories.

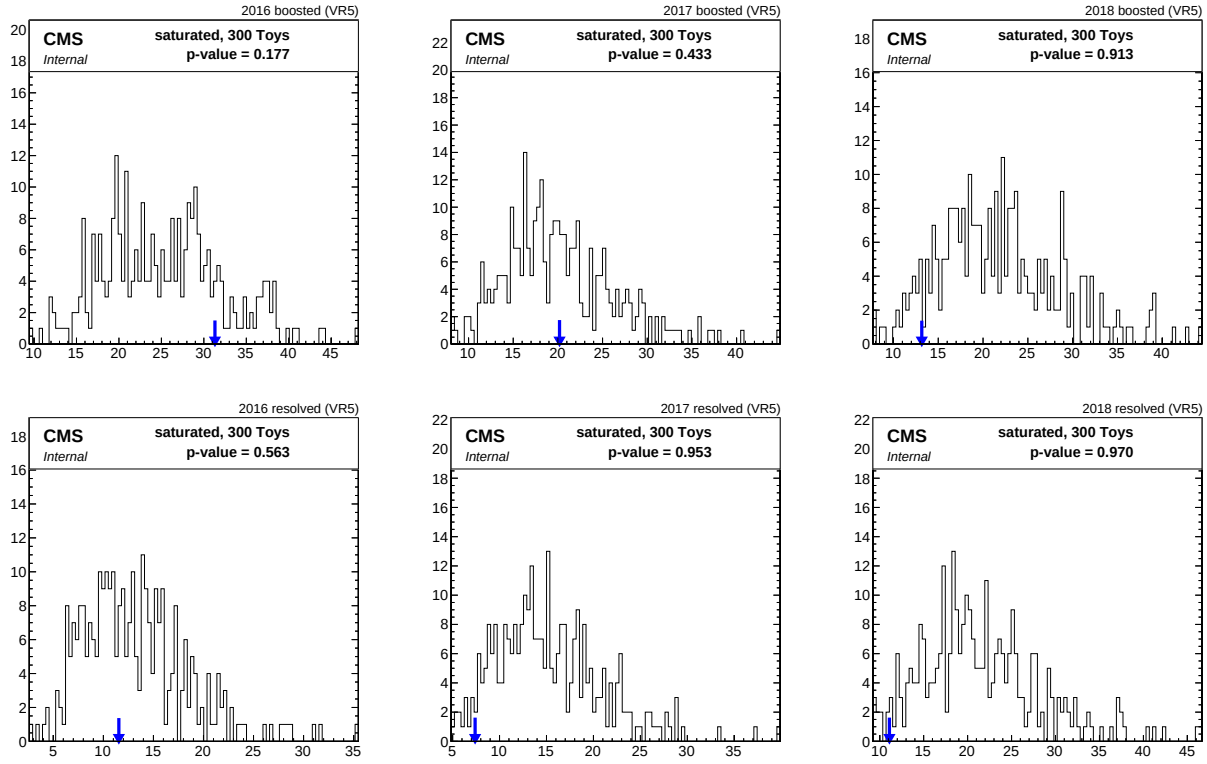

Figure 8.37: Goodness of fit in VR5 data sideband for boosted (up) and resolved (bottom) categories.

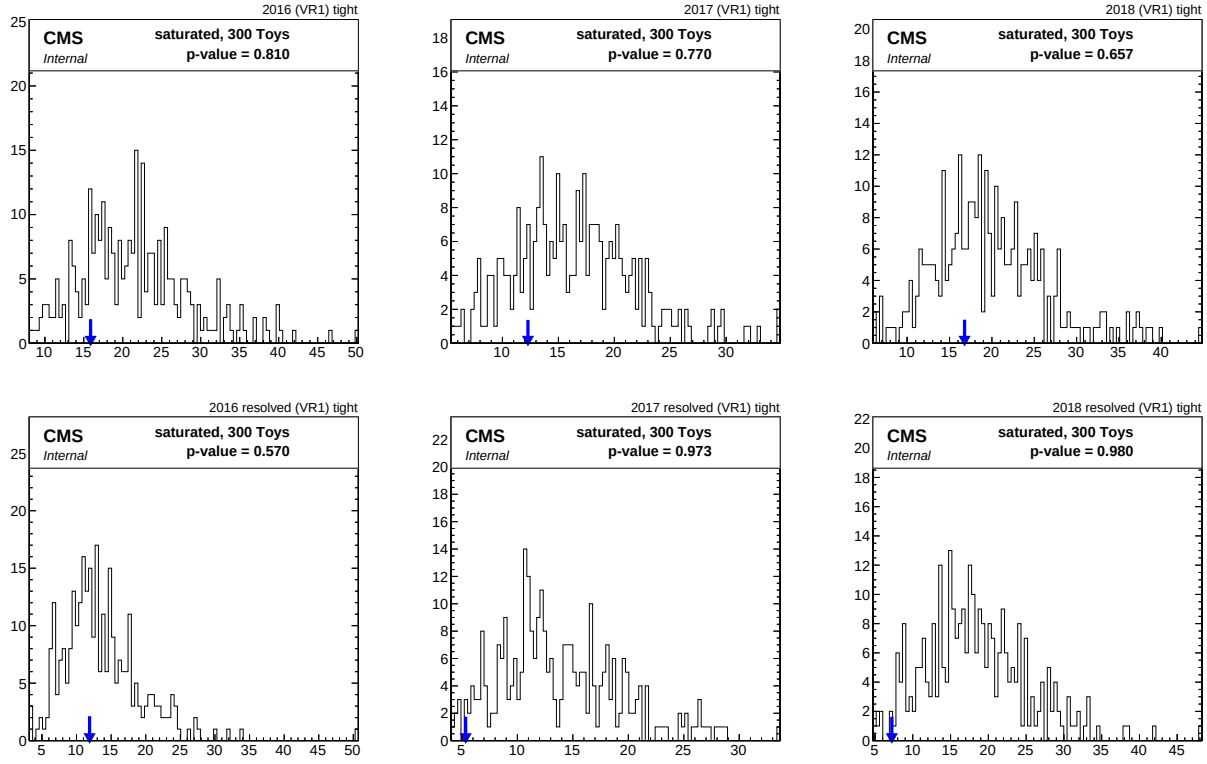

Figure 8.38: Goodness of fit in VR1 with tagger optimized thresholds data sideband for boosted (up) and resolved (bottom) categories.

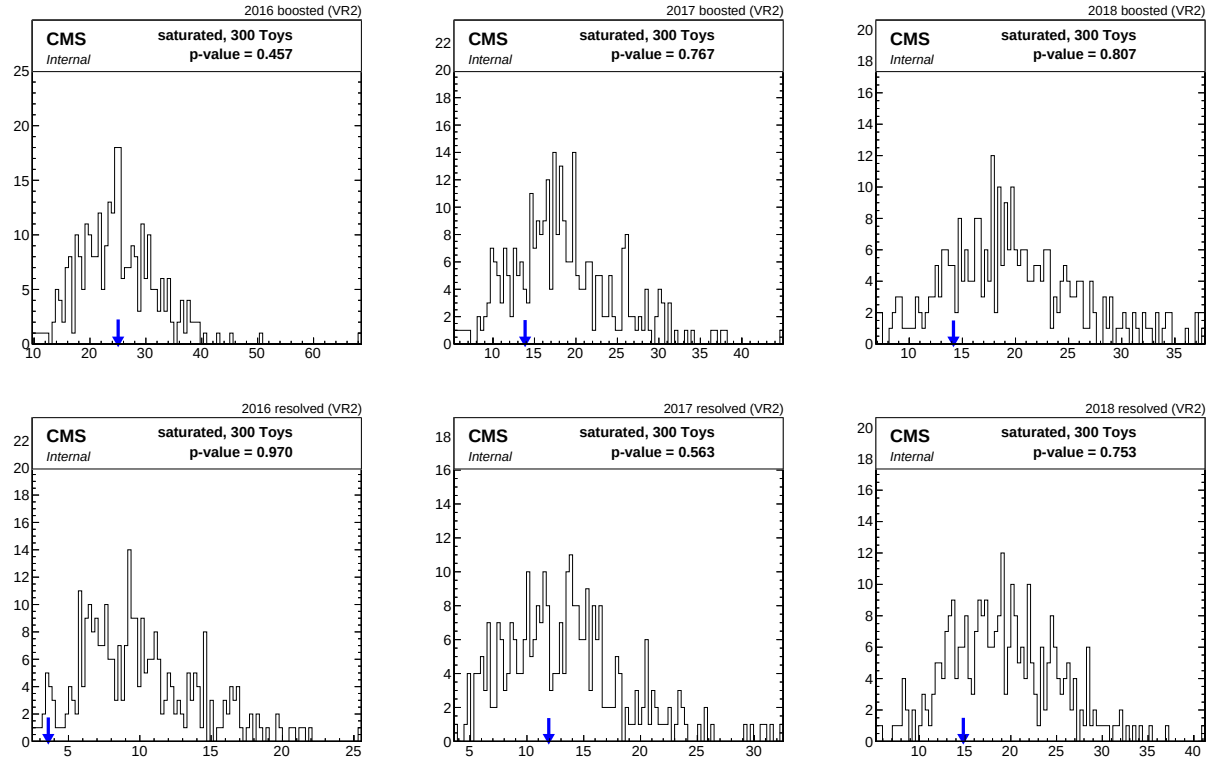

Figure 8.39: Goodness of fit in VR2 with tagger optimised thresholds data sideband for boosted (up) and resolved (bottom) categories.

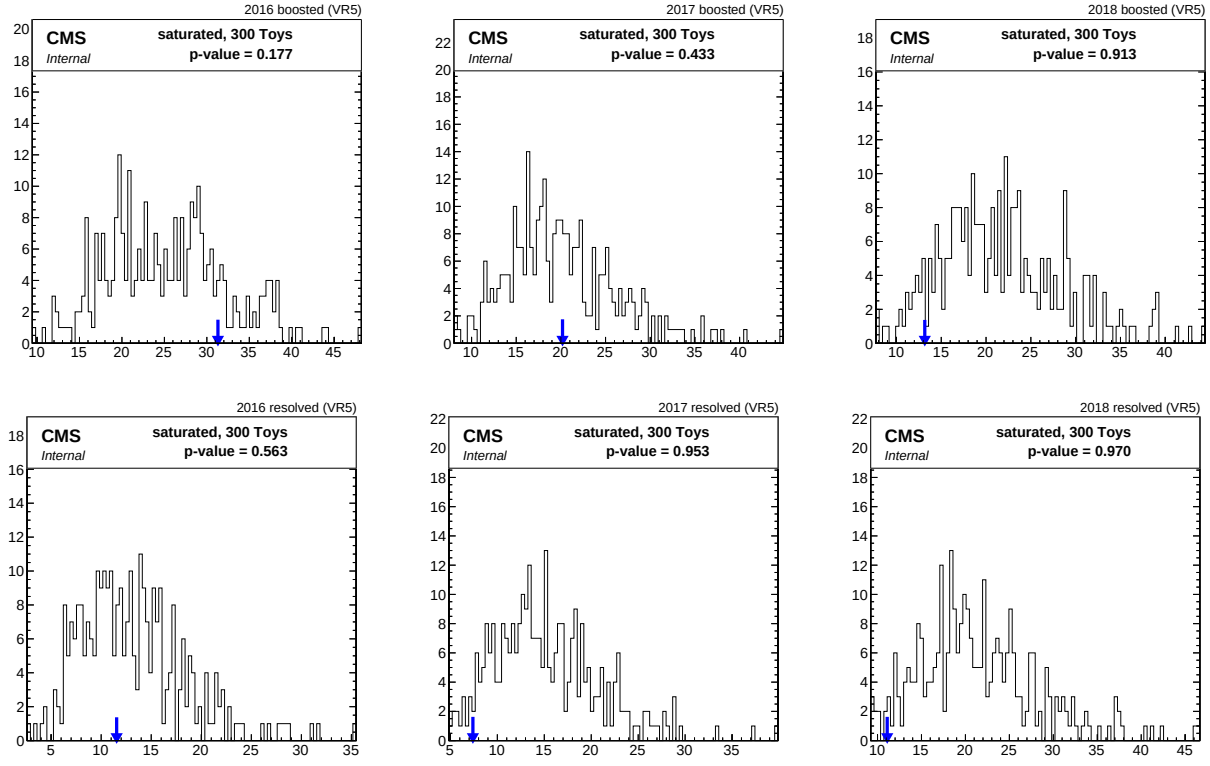

Figure 8.40: Goodness of fit in VR5 with tagger optimised thresholds data sideband for boosted (up) and resolved (bottom) categories.

Chapter 9

Systematic uncertainties

Systematic uncertainties are a type of uncertainty that arises from imperfections or limitations in the experimental setup, rather than from random fluctuations in the data (statistical uncertainty). These imperfections can include imperfect calibration of detectors, incomplete understanding of the physics processes being studied, or imperfect control of external factors that may affect the experiment.

In this chapter, all possible sources of systematic uncertainties are discussed. Most of them have an impact only on signal simulated events but not on the expected background since the former is produced in simulation, while the latter is computed from data using the ABCD method. However, additional non-closure uncertainties will be applied to the data arising from the background estimation.

9.1 systematic uncertainties on signal

The expected pileup distribution in data is affected by a 5% uncertainty in the minimum bias cross section. The jet energy scale and resolution in simulated events are adjusted using p_T and η-dependent scale factors, and the resulting differences are propagated to the missing transverse momentum. The unclustered energy, which is not corrected by the jet energy scale and resolution, is varied within its uncertainty. Uncertainties in the parton distribution function are evaluated by reweighting each event according to the prescribed variations of the corresponding PDF set. The factorisation and renormalisation scale is also varied in simulated samples

using precomputed weights by the event generators, with only residual changes after selection considered as uncertainty for signal samples. The theoretical uncertainty on the normalisation (approximately ±12%) is also taken into account. Higher order corrections to the Wboson p_T spectrum in signal events have been studied but the considered uncertainty is deemed sufficient to cover these potential corrections.

The measurement of prompt lepton SFs is a source of systematic uncertainty due to the imperfections in the reconstruction, identification, and trigger measurements. To account for these systematic uncertainties, p_T - and η-dependent scale factors provided centrally by the EGamma and Muon Physics Object Groups (POGs) are varied within their uncertainties.Similarly, Systematic uncertainties related to the identification efficiency of displaced lepton candidates are considered, the applied p_T - and $|d_{xy}^{sig}|$-dependent scale factors are varied within their uncertainties.
Uncertainties on the efficiency of both displaced track reconstruction and displaced jet tagging are taken into account and they are discussed in section 6.5.4 and 6.5.5 respectively.

The measured luminosity is also a source of systematic uncertainty and therefore un uncertainty of 1.2 % 2.3 % and 2.5 % are taken into account for 2016,2017 and 2018 respectively.

9.2 systematic uncertainties on background

Non-closure systematic uncertainty refers to the systematic uncertainty that arises from the use of background estimation methods that may not fully account for all sources of background events. This can result in a discrepancy between the estimated background and the true background, which is known as non-closure. To account for this discrepancy and ensure that the final result of the analysis is reliable, additional systematic uncertainties are considered.
To derive the non-closure systematic uncertainty, the high mass region VR1 is used. An additional factor, κ, is introduced to modify the yield in region D per SR category within the likelihood model from Equation 10.5 as:

$$\mathcal{L}^d = \prod_{i=1}^{24} \text{Poisson}\left(n_{i,\text{res.}} \mid \kappa^i_{\text{res.}} \frac{b^B_{i,\text{res.}} \cdot b^C_{i,\text{res.}}}{b^A_{i,\text{res.}}} \right) \times \prod_{i=1}^{24} \text{Poisson}\left(n_{i,\text{boost.}} \mid \kappa^i_{\text{boost.}} \frac{b^B_{i,\text{boost.}} \cdot b^C_{i,\text{boost.}}}{b^A_{i,\text{boost.}}} \right) \tag{9.1}$$

resulting in 48 additional nuisance parameters per year. The level of closure is determined first per SR macro category (i.e per bin of displacement per boosted/resolved and per year) by fitting this model with a priori unconstrained κ parameters. Any resulting deviation of κ parameters from unity will then indicate the level of non-closure per macro category.

Based on the measured κ factor per macro category summarized in table 9.1, the non-closure systematic uncertainty per macro category is concluded and summarised in table 9.2. Finally, due to the difference in the background composition between SF and OF categories in addition to the difference in the tagger performance between $\mu\mu$ OS and ee OS categories, the systematic uncertainty is applied per SR category to avoid any correlation between categories.

Additonal 25% systematic uncertainty is considered related to Type-II background discussed in section 8.4.3 to cover the remaining non-closure observed in VR5 only in $\mu\mu$ OS categories. The 25 % is concluded based on the measured κ parameter values per $\mu\mu$ OS category derived from fits to the VR5 similar procedure to the one discussed above. These κ values are summarized in table 9.3.

Table 9.1: Measured κ parameter per category derived from fits to the VR1.

Macro category	Boosted			resolved		
	2016	2017	2018	2016	2017	2018
prompt	1.0±0.03%	0.87±0.06%	0.92±0.06%	1.09 ±0.01	1.10±0.33	1.09 ±0.29
medium	0.95±0.08%	0.94±0.07%	1.02±0.07%	1.09 ±0.01	1.20 ±0.17	1.17 ±0.34
displaced	1.0±0.02%	0.97±0.05%	1.09±0.06%	1.04 ±0.01	1.15 ±0.14	0.85 ±0.22

Table 9.2: Systematic uncertainty applied per category based on the measured κ parameters.

Macro category	Boosted			resolved		
	2016	2017	2018	2016	2017	2018
prompt	10 %	10 %	10%	10%	10%	10%
medium	10%	10%	10%	10%	10%	10%
displaced	10%	10%	10%	15%	15%	15%

Table 9.3: Measured κ parameter per $\mu\mu$ OS category derived from fits to the VR5.

Macro category	Boosted		
	2016	2017	2018
prompt	1.44±0.17%	1.07±0.43%	0.94±0.08%
medium	1.02±0.18%	1.12±0.31%	0.98±0.24%
displaced	0.88±0.16%	0.71±0.18%	1.04±0.18%

9.3 summary

All considered systematic uncertainties are mentioned in table 9.4. Two main type of systematic uncertainties are considered either shape or rate uncertainty. shape uncertainty pertains to variations in the entire distribution's form, while rate uncertainty concerns the uncertainty in the event yields or overall normalization of the distribution. In the table we indicate all sources of systematic uncertainties, their types as well as their correlation among the three years of data taking.

Table 9.4: Sources of systematic uncertainties considered in the HNL search.

systematic uncertainty	type	correlation
PDF	shape	uncorrelated
Factorisation and renormalisation scale	shape	uncorrelated
JES	shape	uncorrelated
JER	shape	uncorrelated
Unclustered energy	shape	uncorrelated
pileup	shape	uncorrelated
Luminosity	rate	uncorrelated
Prompt lepton efficiencies	shape	uncorrelated
Displaced lepton efficiencies	shape	uncorrelated
Displaced track efficiency	shape	uncorrelated
Displaced jet tagger efficiency	shape	uncorrelated
background estimation	rate	uncorrelated

Chapter 10

Results and interpretation

This chapter presents the statistical results and their interpretation. Section 10.1 describes the likelihood model used in the interpretation of the HNL search. The results of the fit to the data are presented in section 10.2. As there is no significant deviation of the observed data from the expected values, hence no signal of HNL particles, upper limits at a 95% confidence level (CL) are placed on the production cross section of HNLs in the mass and coupling parameters plane, $\sigma(m_N, \mid V_{\ell N} \mid^2)$. The details of these results are provided in section 10.4. The limits as a function of the relative coupling are also discussed in section 10.6. Finally, the impact plots are displayed and analyzed in section 10.5.

10.1 Likelihood model

In theory the likelihood model represents the level of agreement between the parameter of interest (POI), which is the signal strength denoted r in the HNLs search, with the observed datasets. A Poisson likelihood model is constructed for a given POI and observed dataset n as follow

$$\mathcal{L}(r, \theta \mid n) = \text{Poisson}(n \mid E_n) \cdot p(\theta), \tag{10.1}$$

The variables E_n stand for the expected number of events, encompassing both background and signal contributions. These are represented by the parameters b and s respectively, as

defined in equation 10.3. Furthermore, the Poisson likelihood model, outlined in equation 10.4, is employed to describe the statistical properties of the observed data in relation to the expected event yields.

$$p(\theta_k) = \frac{1}{\sqrt{2\pi}} e^{-\frac{1}{2}\theta_k^2} \tag{10.2}$$

$$E_n = b(\theta) + r \cdot s(\theta) \tag{10.3}$$

$$\text{Poisson}(n \mid \lambda) = e^{-\lambda} \frac{\lambda^n}{n!} \tag{10.4}$$

In this HNLs search, the expected background is computed using ABCD method as discussed in section 8. Therefore for each SR category, a likelihood model is build for each of the A, B, C and D regions seperately as

$$\mathcal{L}_i^m(n_i^m|\vec{\theta}) = \text{Poisson}\left(n_i^m \mid b_i^m(\vec{\theta}) + \mu \cdot s_i^m(\vec{\theta})\right) \cdot p(\vec{\theta}),$$

$$\mathcal{L}_i^D(n_i^D|\vec{\theta}) = \text{Poisson}\left(n_i^D \mid \frac{b_i^B \cdot b_i^C}{b_i^A} + \mu \cdot s_i^D(\vec{\theta})\right) \cdot p(\vec{\theta}), \tag{10.5}$$

where the total likelihood is given by the product of each likelihood category as follow

$$\mathcal{L} = \prod_{i=144} \mathcal{L}_i^A(\vec{\theta}) \mathcal{L}_i^B(\vec{\theta}) \mathcal{L}_i^C(\vec{\theta}) \mathcal{L}_i^D(\vec{\theta}),$$

10.2 Results of the fit to data

The expected number of background events in each of the 48 SR categories is predicted from the data using the ABCD method described in section 8. To be considered in the final signal region D, events must fall within 70 < mass < 90GeV and meet specific thresholds on the displaced jet tagger that are optimized per category, as detailed in section 8.3. The expected background events are obtained by fitting the data from the sideband regions (Asimov data set) using the

likelihood model from equation 10.5. The Asimov dataset, an artificial dataset that assumes perfect agreement between theory and data, serves as a pivotal reference for evaluating the background estimation and testing the methodology's robustness under controlled conditions. The results of a maximum likelihood fit to the observed data are also presented.

The number of yields before and after applying the fit and the observed yields are shown in figure 10.1 per year, and the combination of the three years for boosted and resolved is presented separately in figure 10.2. Two benchmark signal scenarios are overlaid that fall within the expected limits. The first signal sample has an HNL mass of 4.5 GeV and $c\tau = 100$ mm and mainly appears in the displaced boosted categories, which contribute to the majority of sensitivity for this specific benchmark HNL model. The higher mass signal scenario, with $m_{\mathrm{N}} = 10$ GeV and $c\tau = 1$ mm has a smaller displacement and possesses a comparable number of boosted and resolved events. Here, the main sensitivity comes from the displaced, resolved category due to the significantly lower number of background events in that bin compared to the boosted, displaced category.

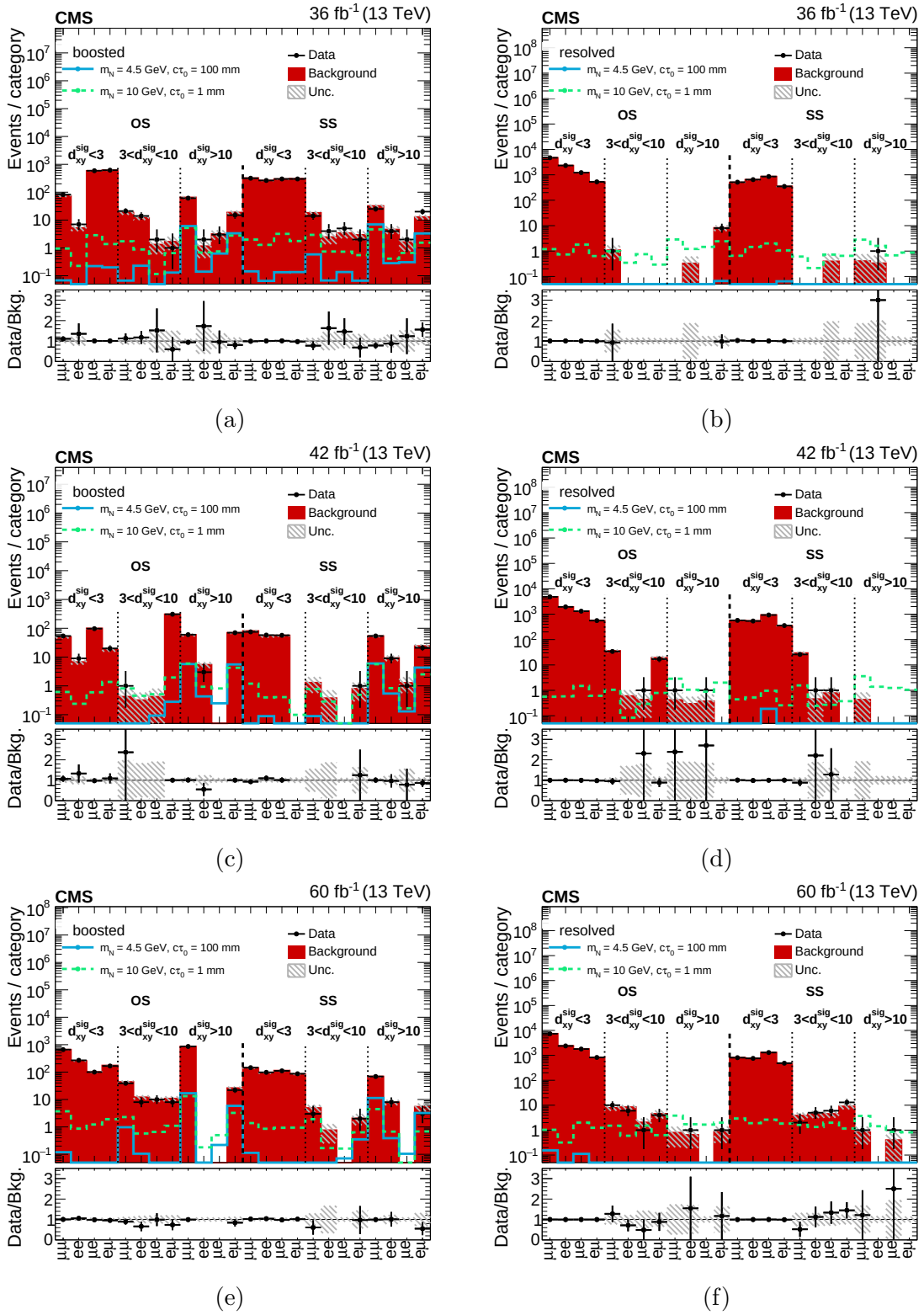

Figure 10.1: Expected background and signal yields for boosted (left) and resolved (right) categories per year and combined obtained from a fit to the Asimov dataset. Two signal Majorana models are superimposed.

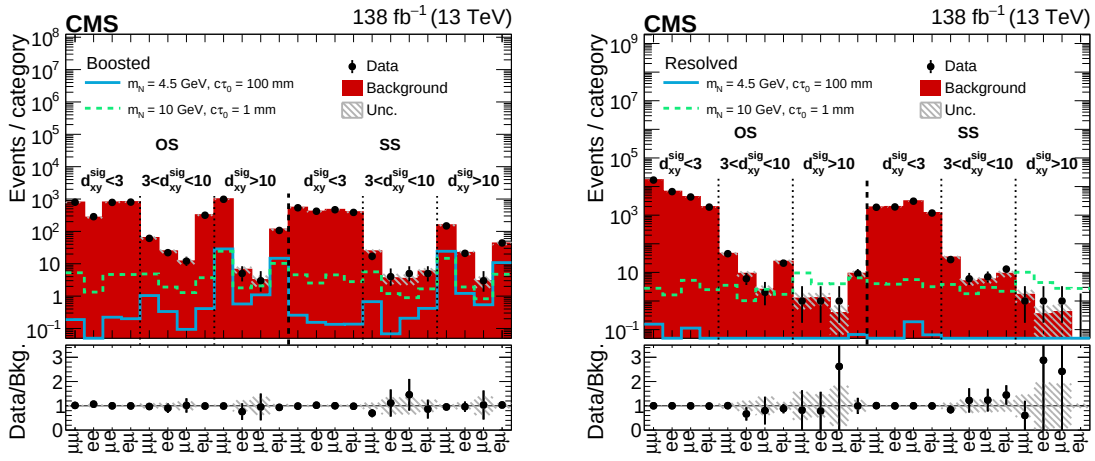

(a) (b)

Figure 10.2: Expected background and signal yields for boosted (left) and resolved (right) categories for combined years obtained from a fit to the Asimov dataset. Two signal Majorana models are superimposed.

10.3 Procedure for deriving the limits

In this section, the approach for deriving the upper limits at 95 % confidence level on the signal strength, is defined. A full detailed procedure is given in [39].

In the following, the parameter of interest (POI) is considered to be the signal strength r. The θ parameter in the fit represents nuisance parameters.

Based on the likelihood model given in equation 10.6, the profiled likelihood ratio is expressed as

$$q(r) = \frac{\mathcal{L}(r, \hat{\theta}(r))}{\mathcal{L}(\hat{r}, \hat{\theta})}, \tag{10.6}$$

Where $\hat{\theta}$ and $\hat{r}$ are the corresponding values of θ and r that maximise the likelihood $\mathcal{L}$. $\hat{\theta}(r)$ is instead the value of θ for a given value of r that maximise the same quantity $\mathcal{L}$. A one sided profile likelihood is used as described in equation 10.7 given $r < 0$ is an unphysical.

$$\tilde{q}(r) = \begin{cases} q(0) r \leq 0, \\ q(r) r > 0. \end{cases} \tag{10.7}$$

An appropriate test statistic defined in equation 10.8 is used for deriving the upper limit on the signal strength r.

$$\tilde{t}_r = \begin{cases} -2 \ln \tilde{q}(r) & \hat{r} \leq r, \\ 0 & \hat{r} > r. \end{cases} \tag{10.8}$$

Based on equation 10.6 and at the maximum likelihood value of r, t_r will be equal to zero. Higher values of t_r leads to lower compatibility of that specific r value with data observed. The level of agreement between the signal strength r and the data is quantified by the p-value p_r defined as

$$p_r = \int_{t_r, obs}^{\infty} f(t_r|r) dt_r, \tag{10.9}$$

where t_r, obs is the observed value, $f(t_r|r)$ is the probability density function that is constructed using pseudo data using the asymptotic approximation as detailed in [39].

The confidential level (CL) discussed in the begining of this section is finally defined as

$$CLs(r) = \frac{p_r}{1 - p_b} \tag{10.10}$$

where the denominator is given as

$$1 - p_b = \int_{t_0,obs}^{\infty} f(t_r, 0) dt_r \tag{10.11}$$

The value of r for which CLs(r) is equal to 0.05 (r_{95}) defines the upper limit on r. Higher values of r are then excluded at 95 % CL while the expected value is defined by considering the median of generated pseudo datasets distribution of r_{95} with signal strength r contribution equal to zero. $\pm 1\sigma$

10.4 Interpretation

The number of observed events is consistent with the SM-only hypothesis ($r = 0$). As a result, no evidence for HNL signal is observed, and the results are used to constrain the phase space of HNL models. The CMS Combine tool is used to set an upper limit (UL) on the HNL production cross section for each HNL mass and coupling hypothesis scenario corresponding to ($m_{\mathrm{N}}, \mid V_\ell \mid^2$). The expected ULs $\sigma_{\mathrm{UL}}(m_{\mathrm{N}}, \mid V_{\ell N} \mid^2)$ are determined by fitting the Asimov data set using an asymptotic approximation [39]. The observed limits are obtained by applying the same fit to the observed data. The UL is compared with the theoretical cross-section, $\sigma_{\mathrm{th}}(m_{\mathrm{N}}, \mid V_{\ell N} \mid^2)$, obtained by using MadGraph at LO. A given signal point is excluded if the signal strength parameter satisfies

$$\mu(m_{\mathrm{N}}, V_\ell^2) = \frac{\sigma_{\mathrm{UL}}(m_{\mathrm{N}}, \mid V_{\ell N} \mid^2)}{\sigma_{\mathrm{th}}(m_{\mathrm{N}}, \mid V_{\ell N} \mid^2)} < 1\,. \tag{10.12}$$

To obtain a complete picture of the limits on HNL production, a 2D grid of $\sigma_{\mathrm{UL}}(m_{\mathrm{N}}, \mid V_{\ell N} \mid^2)$ values is constructed using a 2D interpolation between the available signal points. This allowed us to determine the exclusion contour corresponding to $\mu(m_{\mathrm{N}}, \mid V_{\ell N} \mid^2) = 1$, which is shown in figure 10.3 for various mixing scenarios per year, and in figure 10.4 for the combination of all three years. Our results indicate that the pure-muon coupling scenario provides the best

relative sensitivity, with a maximum excluded coupling strength of $|V_{\mu N}|^2 > 5(4) \times 10^{-7}$ for Dirac (Majorana) HNLs with a mass of 10 GeV.

One interesting trend we observed is that the sensitivity varies with HNL mass. We found that as the HNL mass increases, the sensitivity increases up to a turning point at around 14 GeV, when the HNL is no longer displaced. At higher masses, the sensitivity decreases, and the exclusion line evolves from covering low-mass, displaced scenarios to covering high-mass, prompt scenarios. The displaced categories (i.e. boosted and resolved) are the main source of sensitivity at low-mass regions up to 14 GeV, while the prompt categories become the main source of sensitivity at higher masses, where the number of signal events in the displaced bins becomes nearly zero. This explains why we see different limit shapes at low and high mass regions.

Furthermore, the total decay width for Majorana HNLs is twice as large as for Dirac HNLs, which leads to a higher rate of Majorana events decaying within the tracker volume. However, this also results in a shorter lifetime for Majorana HNLs compared to Dirac HNLs. Additionally, we observed a clear difference in the background between SS and OS categories, particularly for the $\mu\mu$ category. Given these factors, the sensitivity between Dirac and Majorana scenarios is similar, with slightly better sensitivity for the Majorana scenario.

10.5 Impacts and pulls

The impact and pull of a nuisance parameter (NP) are important measures of its significance. The pull quantifies the deviation of the best-fit value of the NP from its pre-fit value in units of the input uncertainty and defined as

$$\text{pull} = \frac{\hat{\theta} - \theta}{\sigma_\theta}\,, \tag{10.13}$$

where $\hat{\theta}$ is the best-fit value of the NP, θ is the initial (pre-fit) value, conventionally set to zero, and σ_θ is the input uncertainty. Meanwhile, the impact of an NP on a parameter of interest (POI) is the shift in the best-fit value of the POI when the NP is fixed to $\pm 1\sigma$ of its nominal value. A low impact indicates that the NP has a negligible effect on the POI.

$$\text{impact} = \Delta\mu^{\pm} = \hat{\hat{\mu}}_{\theta\pm\sigma_\theta} - \hat{\mu}\,. \tag{10.14}$$

An impact plot, as shown in Figure 10.5, displays the impacts of the NPs on the POIs. The highest impacts on the results come from the statistical uncertainty on the background estimation from data A,B,C regions and systematic uncertainties on the loose muon reconstruction SFs and displaced jet tagger SFs.

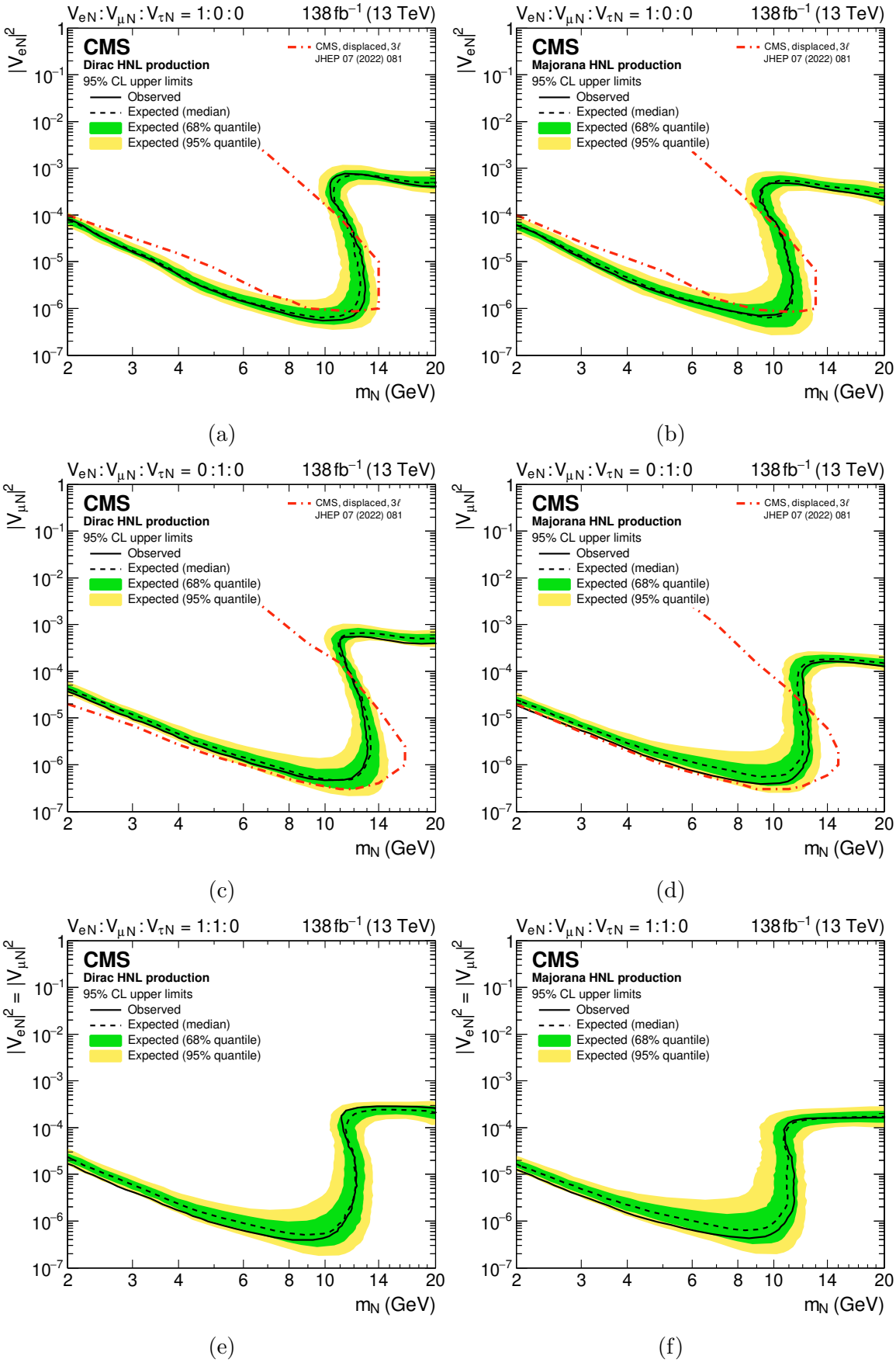

Figure 10.3: Combined limits for Dirac (top) and Majorana(bottom) HNLs for pure and equal muon and electron couplings.

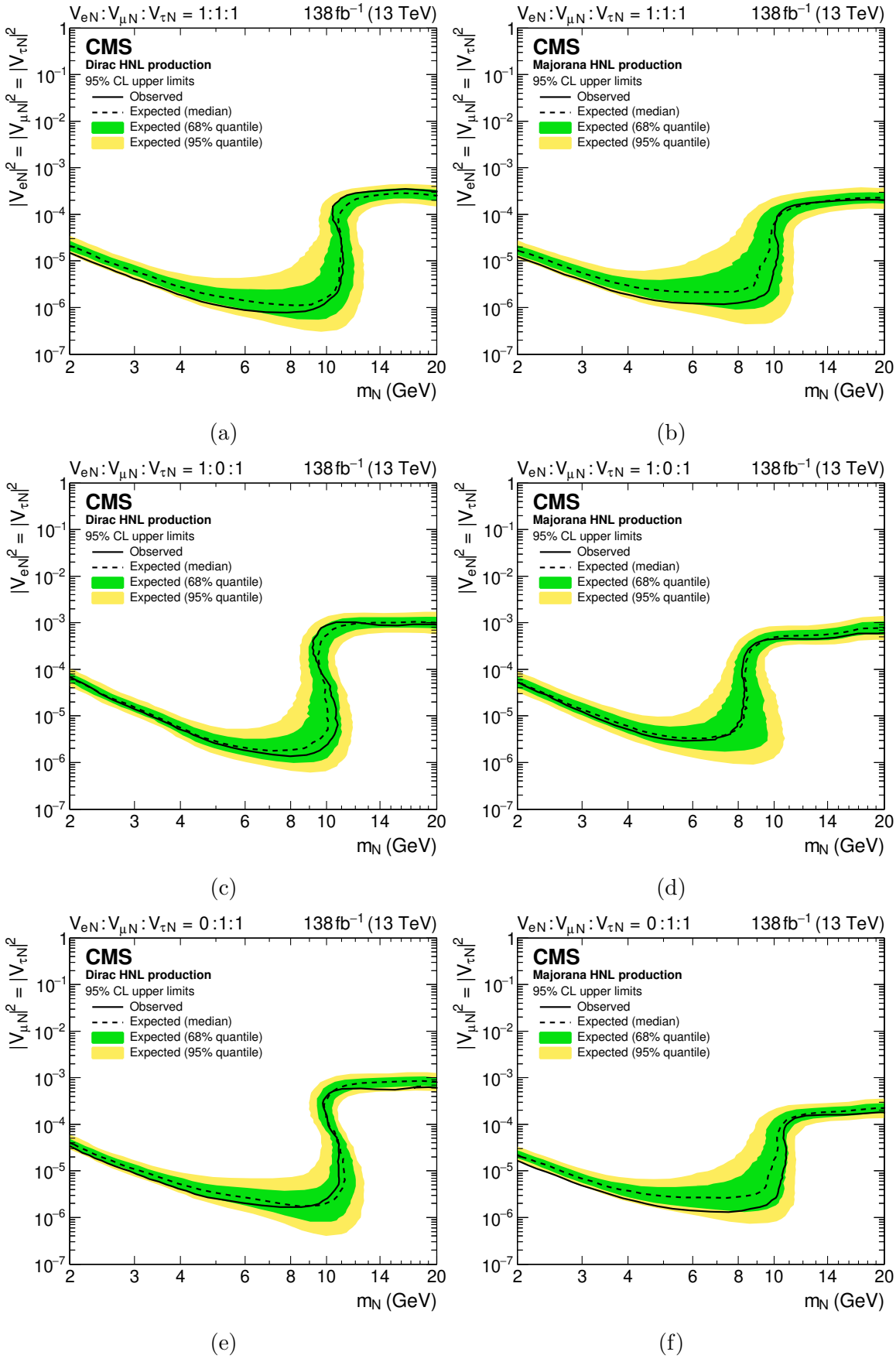

Figure 10.4: Combined limits for Dirac (top) and Majorana(bottom) HNLs for equal coupling to muon and tau, electron and tau, and electron, muon, and tau.

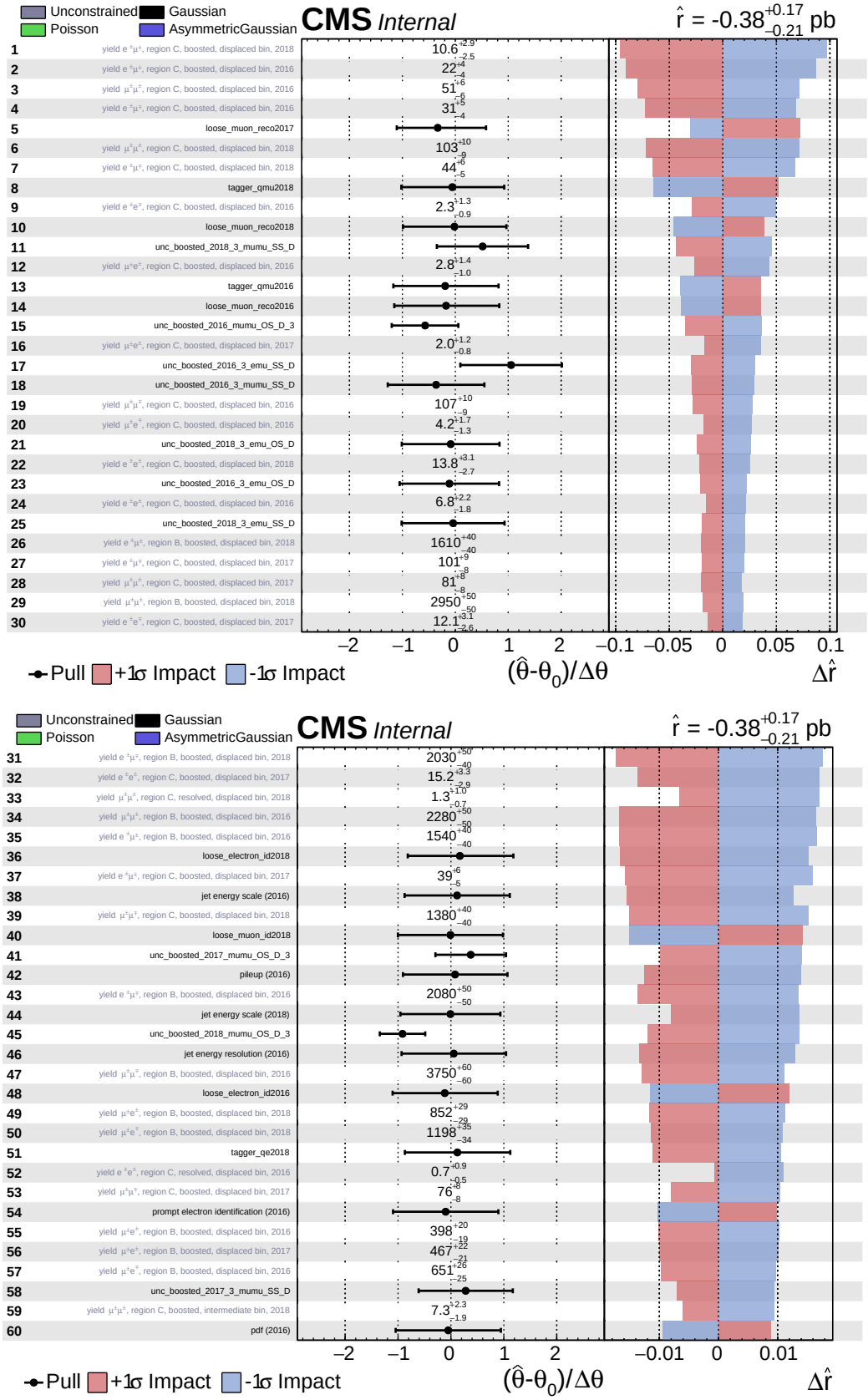

Figure 10.5: Impacts ranked by decreasing significance for the 2016, 2017 and 2018 data-taking scenarios. Only the first sixty are shown. Signal model used: $m_{\mathrm{N}} = 10\mathrm{GeV}$, $c\tau_0 = 1\mathrm{mm}$, $V_\mu = V_e$

10.6 Flavour-dependent limits

The limits on the HNL mass as a function of the relative couplings to the three lepton generations in barycentric space are shown in Figure 10.6 for both Dirac and Majorana HNL scenarios, for a fixed $c\tau_0$ of 0.1 mm (top) or 1 mm (bottom). The color map in the plot represents the maximum excluded HNL mass.

Since $f_{e\mu}$, $f_{e\tau}$, and $f_{\mu\tau}$ are related to the V_e, V_μ, and V_τ couplings by equation 10.15, where A_ℓ is related to the partial width as follows: $\Gamma_\ell = A_\ell(m_N) \times |V_\ell|^2$, a scan over all mass points is performed for each coupling scenario ($f_{e\mu}$, $f_{e\tau}$, $f_{\mu\tau}$) and fixed lifetime to find the maximum excluded mass value such that $\mu(m_N, |\ V_{\ell N}\ |^2) < 1$. The scan is performed for all 67 coupling scenarios. Finally, the cross section is interpolated in 5D parameter space. Similarly, The limits on the HNL proper decay length ($c\tau_0$) is performed and shown in figure 10.7

The best sensitivity is found for pure muon and electron couplings. Since we do not use a τ trigger due to its high threshold, typically 50 GeV compared to electron or muon triggers, we are only sensitive to pure tau coupling when the tau decays leptonically with a high-p_T lepton. This reduces the sensitivity drastically, and therefore, the less sensitive scenario is the pure tau coupling.

$$V_\ell = \lambda \times f_\ell, \lambda^2 = \frac{\Gamma_{\text{tot}}}{A_e \times f_e^2 + A_\mu \times f_\mu^2 + A_\tau \times f_\tau} \tag{10.15}$$

10.7 Summary

This thesis presents the outcomes of a comprehensive search for Heavy Neutral Leptons (HNLs) within the mass range of 2 to 20 GeV, utilizing 138 fb^{-1} of p-p collision data collected from 2016 to 2018. A key contribution of this search is the establishment of Upper Limits at 95% confidence level on the HNL production cross section in the mass and mixing parameter space, significantly expanding the experimental coverage in this region. Additionally, the comparison of these limits with another CMS search for HNLs in the three-lepton final state reveals that the presented results are more stringent for the pure electron coupling scenario, encompassing

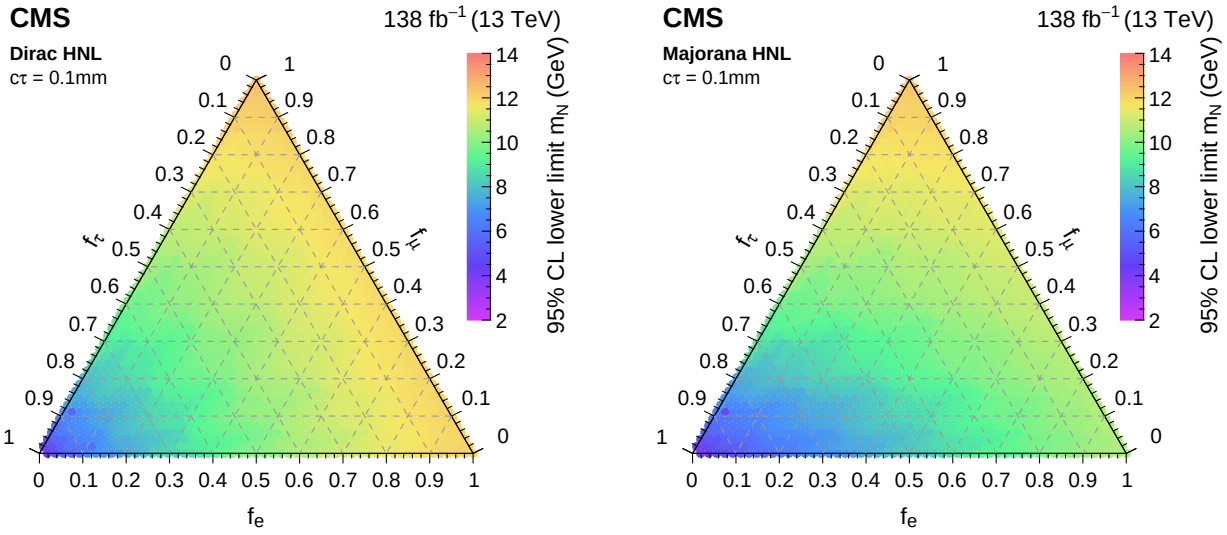

(a)

(b)

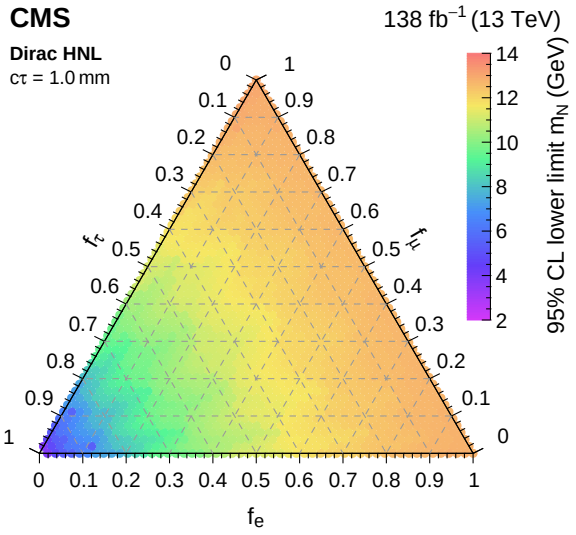

(c)

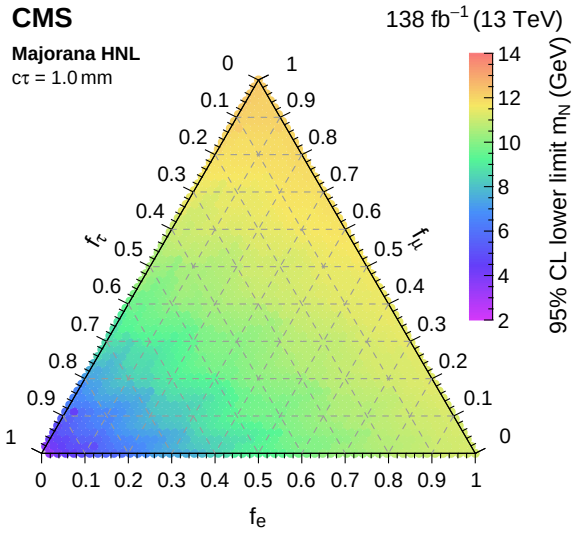

(d)

Figure 10.6: Minimum excluded mass for each flavour combination for Dirac HNLs for (left column) Majorana and (right column) Dirac HNLs with a fixed lifetime of (top row) with $c\tau_0 = 0.1$ mm and (bottom row) $c\tau_0 = 1$ mm.

both Dirac and Majorana HNL nature, while demonstrating comparable outcomes for the pure muon coupling scenarios. This work presents the first results involving a prompt or long-lived Majorana or Dirac HNL that couples to all three lepton generations in the 2 to 20 GeV mass range. The findings of this thesis bear substantial implications for the exploration of new physics beyond the Standard Model.

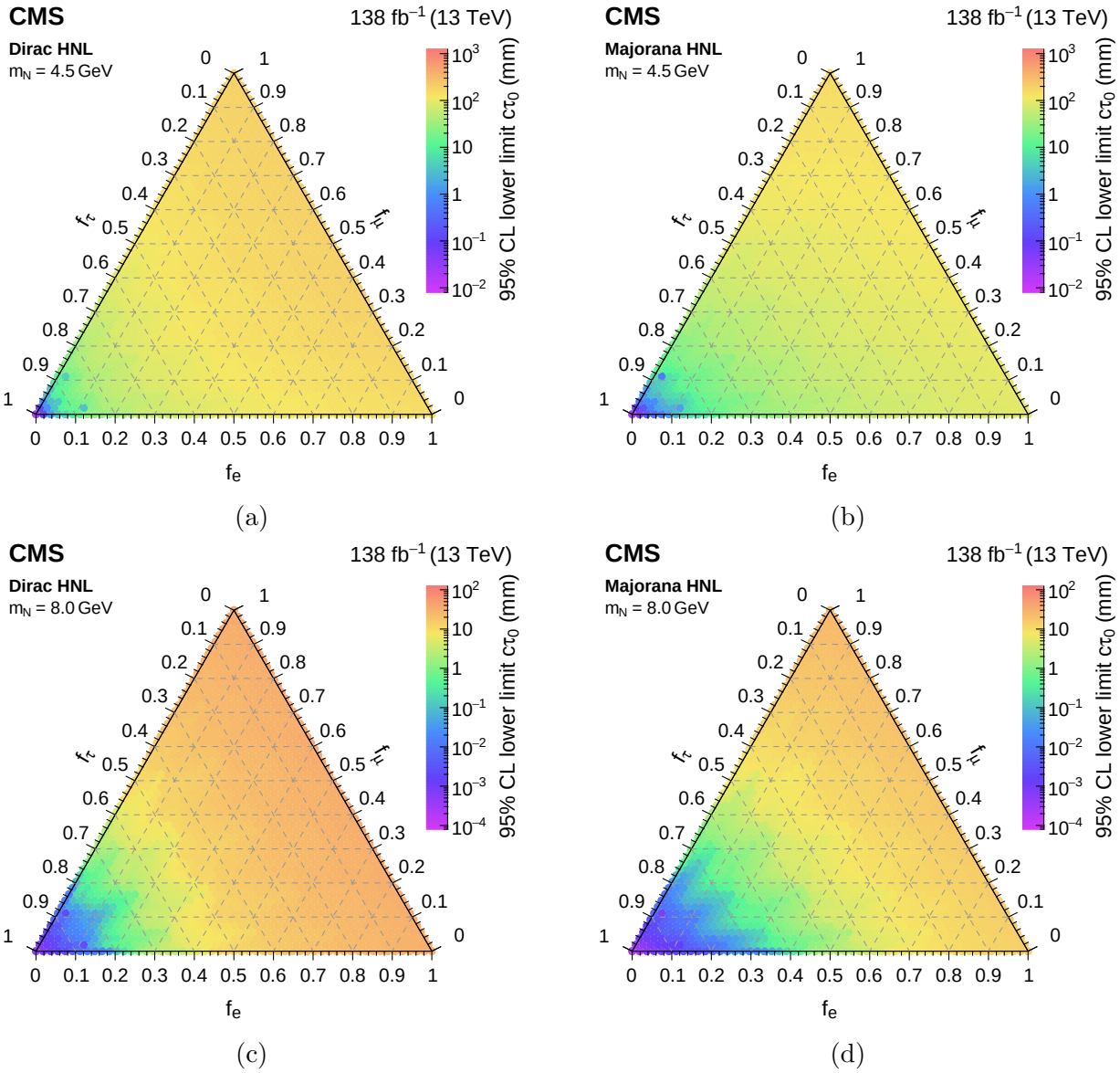

Figure 10.7: Minimum excluded proper lifetime for each flavour combination for (left col- umn) Majorana and (right column) Dirac HNLs with a fixed mass of (top row) 4.5 GeV and (bottom row) 8.0 GeV.

References

[1] LHC Machine. *JINST*, 3:S08001, 2008.

[2] Performance of missing energy reconstruction in 13 TeV pp collision data using the CMS detector. 2016.

[3] G. Aad et al. The ATLAS Experiment at the CERN Large Hadron Collider. *JINST*, 3:S08003, 2008.

[4] G. Aad et al. Search for heavy Majorana neutrinos with the ATLAS detector in pp collisions at $\sqrt{s} = 8$ TeV. *JHEP*, 07:162, 2015.

[5] G. Aad et al. Search for heavy neutral leptons in decays of W bosons produced in 13 TeV pp collisions using prompt and displaced signatures with the ATLAS detector. *JHEP*, 10:265, 2019.

[6] K. Aamodt et al. The ALICE experiment at the CERN LHC. *JINST*, 3:S08002, 2008.

[7] Martín Abadi and al. Tensorflow: Large-scale machine learning on heterogeneous distributed systems. *CoRR*, abs/1603.04467, 2016.

[8] Asli M. Abdullahi et al. The present and future status of heavy neutral leptons. *J. Phys. G*, 50(2):020501, 2023.

[9] P. Abreu et al. Search for neutral heavy leptons produced in Z decays. *Z. Phys. C*, 74:57–71, 1997. [Erratum: Z.Phys.C 75, 580 (1997)].

[10] P. Achard et al. Search for heavy isosinglet neutrino in e^+e^- annihilation at LEP. *Phys. Lett. B*, 517:67–74, 2001.

[11] S. Agostinelli et al. GEANT4–a simulation toolkit. *Nucl. Instrum. Meth. A*, 506:250–303, 2003.

[12] A. Augusto Alves, Jr. et al. The LHCb Detector at the LHC. *JINST*, 3:S08005, 2008.

[13] J. Alwall, R. Frederix, S. Frixione, V. Hirschi, F. Maltoni, O. Mattelaer, H. S. Shao, T. Stelzer, P. Torrielli, and M. Zaro. The automated computation of tree-level and next-to-leading order differential cross sections, and their matching to parton shower simulations. *JHEP*, 07:079, 2014.

[14] Takehiko Asaka and Mikhail Shaposhnikov. The νMSM, dark matter and baryon asymmetry of the universe. *Phys. Lett. B*, 620:17–26, 2005.

[15] C. Bacci et al. Preliminary Result of Frascati (ADONE) on the Nature of a New 3.1-GeV Particle Produced in e+ e- Annihilation. *Phys. Rev. Lett.*, 33:1408, 1974. [Erratum: Phys.Rev.Lett. 33, 1649 (1974)].

[16] V. A. Bednyakov, N. D. Giokaris, and A. V. Bednyakov. On Higgs mass generation mechanism in the Standard Model. *Phys. Part. Nucl.*, 39:13–36, 2008.

[17] Daniele Bertolini, Philip Harris, Matthew Low, and Nhan Tran. Pileup Per Particle Identification. *JHEP*, 10:059, 2014.

[18] Valerio Bertone, Stefano Carrazza, Nathan P. Hartland, Emanuele R. Nocera, and Juan Rojo. A determination of the fragmentation functions of pions, kaons, and protons with faithful uncertainties. *Eur. Phys. J. C*, 77(8):516, 2017.

[19] S. Bethke and A. Wagner. The JADE Experiment at the PETRA e^+e^- collider – history, achievements and revival. *Eur. Phys. J. H*, 47:16, 2022.

[20] Pierre Billoir. Progressive track recognition with a Kalman like fitting procedure. *Comput. Phys. Commun.*, 57:390–394, 1989.

[21] W. Bonivento et al. Proposal to Search for Heavy Neutral Leptons at the SPS. 10 2013.

[22] W. Braunschweig et al. Charged multiplicity distributions and correlations in e+ e- annihilation at PETRA energies. *Z. Phys. C*, 45:193, 1989.

[23] R. Brun and F. Rademakers. ROOT: An object oriented data analysis framework. *Nucl. Instrum. Meth. A*, 389:81–86, 1997.

[24] Andy Buckley, Jonathan Butterworth, David Grellscheid, Hendrik Hoeth, Leif Lonnblad, James Monk, Holger Schulz, and Frank Siegert. Rivet user manual. *Comput. Phys. Commun.*, 184:2803–2819, 2013.

[25] Matteo Cacciari and Gavin P. Salam. Pileup subtraction using jet areas. *Phys. Lett. B*, 659:119–126, 2008.

[26] Matteo Cacciari, Gavin P. Salam, and Gregory Soyez. The anti-k_t jet clustering algorithm. *JHEP*, 04:063, 2008.

[27] Matteo Cacciari, Gavin P. Salam, and Gregory Soyez. FastJet User Manual. *Eur. Phys. J. C*, 72:1896, 2012.

[28] Vilius Cepaitis. Flavour-universal search for heavy neutral leptons with a deep neural network-based displaced jet tagger with the CMS experiment. *Imperial College London*, 2022.

[29] S. Chatrchyan et al. The CMS Experiment at the CERN LHC. *JINST*, 3:S08004, 2008.

[30] Serguei Chatrchyan et al. Energy Calibration and Resolution of the CMS Electromagnetic Calorimeter in *pp* Collisions at $\sqrt{s} = 7$ TeV. *JINST*, 8:P09009, 2013.

[31] Serguei Chatrchyan et al. Description and performance of track and primary-vertex reconstruction with the CMS tracker. *JINST*, 9(10):P10009, 2014.

[32] Serguei Chatrchyan et al. Description and performance of track and primary-vertex reconstruction with the CMS tracker. *JINST*, 9(10):P10009, 2014.

[33] Suyong Choi and Hayoung Oh. Improved extrapolation methods of data-driven background estimations in high energy physics. *Eur. Phys. J. C*, 81(7):643, 2021.

[34] François Chollet et al. Keras. https://keras.io, 2015.

[35] ATLAS Collaboration. Search for heavy neutral leptons in decays of W bosons using a dilepton displaced vertex in $\sqrt{s} = 13$ TeV pp collisions with the ATLAS detector. 4 2022.

[36] CMS Collaboration. The CMS hadron calorimeter project: Technical Design Report. 1997.

[37] G. Cowan. Discovery sensitivity for a counting experiment with background uncertainty. *http://www.pp.rhul.ac.uk/~cowan/stat/medsig/medsigNote.pdf*.

[38] G. Cowan. Discovery sensitivity for a counting experiment with background uncertainty.

[39] Glen Cowan, Kyle Cranmer, Eilam Gross, and Ofer Vitells. Asymptotic formulae for likelihood-based tests of new physics. *Eur. Phys. J. C*, 71:1554, 2011. [Erratum: Eur.Phys.J.C 73, 2501 (2013)].

[40] R.G. de Souza. Tag and probe 2019.

[41] Frank F Deppisch, P S Bhupal Dev, and Apostolos Pilaftsis. Neutrinos and collider physics. *New Journal of Physics*, 17(7):075019, aug 2015.

[42] M. Derrick et al. study of quark fragmentation in e+ e- annihilation at 29-GeV: charged particles multiplicity distributions. 8 1985.

[43] Alexandre Deur, Stanley J. Brodsky, and Guy F. de Teramond. On the Interface between Perturbative and Nonperturbative QCD. *Phys. Lett. B*, 757:275–281, 2016.

[44] S. Dittmaier and M. Schumacher. The Higgs Boson in the Standard Model - From LEP to LHC: Expectations, Searches, and Discovery of a Candidate. *Prog. Part. Nucl. Phys.*, 70:1–54, 2013.

[45] M. Dittmar, A. Santamaria, M.C. Gonzalez-Garcia, and J.W.F. Valle. Production mechanisms and signatures of isosinglet neutral heavy leptons in z0 decays. *Nuclear Physics B*, 332(1):1–19, 1990.

[46] R. Fruhwirth, W. Waltenberger, and P. Vanlaer. Adaptive vertex fitting. *J. Phys. G*, 34:N343, 2007.

[47] Y. Fukuda et al. Evidence for oscillation of atmospheric neutrinos. *Phys. Rev. Lett.*, 81:1562–1567, 1998.

[48] Dmitry Gorbunov and Mikhail Shaposhnikov. How to find neutral leptons of the νMSM? *JHEP*, 10:015, 2007. [Erratum: JHEP 11, 101 (2013)].

[49] Vardan Khachatryan et al. Search for heavy Majorana neutrinos in $\mu^{\pm}\mu^{\pm}$+ jets events in proton-proton collisions at $\sqrt{s} = 8$ TeV. *Phys. Lett. B*, 748:144–166, 2015.

[50] Vardan Khachatryan et al. Jet energy scale and resolution in the CMS experiment in pp collisions at 8 TeV. *JINST*, 12(02):P02014, 2017.

[51] Axel Maas. Brout-Englert-Higgs physics: From foundations to phenomenology. *Prog. Part. Nucl. Phys.*, 106:132–209, 2019.

[52] Maxim Markevitch, A. H. Gonzalez, D. Clowe, A. Vikhlinin, L. David, W. Forman, C. Jones, S. Murray, and W. Tucker. Direct constraints on the dark matter self-interaction cross-section from the merging galaxy cluster 1E0657-56. *Astrophys. J.*, 606:819–824, 2004.

[53] Hinrich Meyer. "e^+e^- annihilation". *https://inis.iaea.org/collection/NCLCollectionStore/_Public/12/626/12626265.pdf*.

[54] Esma Mobs. The CERN accelerator complex. Complexe des accélérateurs du CERN. 2016. General Photo.

[55] R. N. Mohapatra. Seesaw mechanism and its implications. In *SEESAW25: International Conference on the Seesaw Mechanism and the Neutrino Mass*.

[56] Zoltan Nagy and Davison E. Soper. What is a parton shower? *Phys. Rev. D*, 98(1):014034, 2018.

[57] K. Nakabayashi et al. Charged particle multiplicities of quark and gluon jets in e+ e- annihilation at TRISTAN. *Phys. Lett. B*, 413:447–452, 1997.

[58] Keith A. Olive. Dark Energy and Dark Matter. *Conf. Proc. C*, 0908171:257–270, 2009.

[59] J. Rojo P. Skands, S. Carrazza. Tuning PYTHIA 8.1: the Monash 2013 Tune. *https://arxiv.org/pdf/1404.5630.pdf*.

[60] Palash B. Pal. Dirac, Majorana and Weyl fermions. *Am. J. Phys.*, 79:485–498, 2011.

[61] Mikhail Shaposhnikov. A Possible symmetry of the nuMSM. *Nucl. Phys. B*, 763:49–59, 2007.

[62] A. M. Sirunyan et al. Identification of heavy-flavour jets with the CMS detector in pp collisions at 13 TeV. *JINST*, 13(05):P05011, 2018.

[63] A. M. Sirunyan et al. Performance of the CMS muon detector and muon reconstruction with proton-proton collisions at $\sqrt{s} = 13$ TeV. *JINST*, 13(06):P06015, 2018.

[64] Albert M Sirunyan et al. Search for heavy neutral leptons in events with three charged leptons in proton-proton collisions at $\sqrt{s} = 13$ TeV. *Phys. Rev. Lett.*, 120(22):221801, 2018.

[65] Albert M Sirunyan et al. A deep neural network to search for new long-lived particles decaying to jets. *Mach. Learn. Sci. Tech.*, 1:035012, 2020.

[66] Torbjörn Sjöstrand, Stefan Ask, Jesper R. Christiansen, Richard Corke, Nishita Desai, Philip Ilten, Stephen Mrenna, Stefan Prestel, Christine O. Rasmussen, and Peter Z. Skands. An introduction to PYTHIA 8.2. *Comput. Phys. Commun.*, 191:159–177, 2015.

[67] Armen Tumasyan et al. Search for long-lived heavy neutral leptons with displaced vertices in proton-proton collisions at $\sqrt{\mathrm{s}}$ =13 TeV. *JHEP*, 07:081, 2022.

[68] J. A. Tyson, F. Valdes, and R. A. Wenk. Detection of Systematic Gravitational Lens Galaxy Image Alignments: Mapping Dark Matter in Galaxy Clusters. , 349:L1, January 1990.

[69] P. A. Zyla et al. Review of Particle Physics. *PTEP*, (8):083C01, 2020.